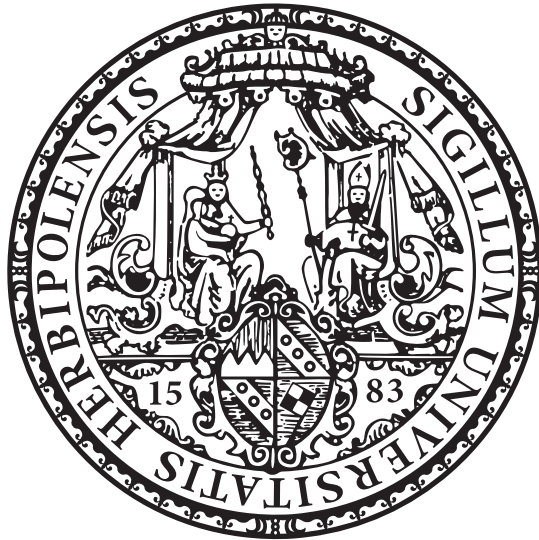


ELECTROCHEMICAL AND MECHANICAL INTERPLAY OF
STATE-OF-THE-ART AND NEXT-GENERATION
LITHIUM-ION BATTERIES



Kumulative Dissertation zur Erlangung des naturwissenschaftlichen Doktorgrades an
der Fakultät für Chemie und Pharmazie der Julius-Maximilians-Universität Würzburg

vorgelegt

von

Philip Daubinger

aus **Habelsee**

Würzburg, im September 2023

 **Fraunhofer**
ISC



Eingereicht bei der Fakultät für Chemie und Pharmazie am

11. September 2023

Gutachter der Dissertation:

1. Gutachter: Prof. Dr. Gerhard Sextl
2. Gutachter: Prof. Dr. Andreas Jossen

Prüfer des öffentlichen Promotionskolloquiums:

1. Prüfer: Prof. Dr. Gerhard Sextl
2. Prüfer: Prof. Dr. Andreas Jossen
3. Prüfer: Dr. Guinevere A. Giffin

Tag des öffentlichen Promotionskolloquiums:

09. Februar 2024

Doktorurkunde ausgehändigt am

The work presented was carried out between October 2018 and September 2022 at the Fraunhofer-Institute for Silicate Research ISC under the supervision of Prof. Dr. Gerhard Sextl, head of Chemical Technology of Materials Synthesis at the Julius-Maximilians-Universität Würzburg, Germany. This cumulative dissertation is an abbreviated presentation of the research results. The detailed results can be found in the following publications:

1. P. Daubinger, F. Ebert, S. Hartmann, and G. A. Giffin, 'Impact of electrochemical and mechanical interactions on lithium-ion battery performance investigated by *operando* dilatometry', *Journal of Power Sources*, vol. 488, p. 229457, 2021, <https://doi.org/10.1016/j.jpowsour.2021.229457>.
2. P. Daubinger, M. Schelter, R. Petersohn, F. Nagler, S. Hartmann, M. Herrmann, and G. A. Giffin, 'Impact of Bracing on Large Format Prismatic Lithium-Ion Battery Cells during Aging', *Advanced Energy Materials*, vol. 44, p. 2102448, 2021, <https://doi.org/10.1002/aenm.202102448>.
3. S. Feiler*, P. Daubinger*, L. Gold, S. Hartmann, and G. A. Giffin, 'Interplay between elastic and electrochemical properties during active material transitions and aging of a lithium-ion battery ', *Batteries & Supercaps*, vol. 6, no. 4, 2023, <https://doi.org/10.1002/batt.202200518>. *S.F. and P.D. contributed equally to this work.
4. P. Daubinger, M. Göttliger, S. Hartmann, and G. A. Giffin, 'Consequences of Different Pressures and Electrolytes on the Irreversible Expansion of Lithium Metal Half Cells', *Batteries & Supercaps*, vol. 6, no. 2, 2023, <https://doi.org/10.1002/batt.202200452>.

Education is the most powerful weapon we can use to change the world.

Nelson Mandela

Contents

List of Figures	ix
List of Tables	xiii
List of Abbreviations	xv
1 Introduction	1
1.1 Motivation	1
1.2 Objectives	2
1.3 Structure of the Thesis	3
2 State of the Art and Theoretical Background	5
2.1 Principles of Lithium-Ion Batteries	5
2.1.1 Thermodynamics and Kinetics	5
2.1.2 Working Principle	8
2.1.3 Negative Electrode	9
2.1.4 Positive Electrode	15
2.1.5 Electrolyte and Separator	19
2.2 Aging Mechanisms	20
2.2.1 Active Cell Components	21
2.2.2 Inactive Cell Components	25
2.3 Characterization Methods	26
2.3.1 Dilatometry	26
2.3.2 X-ray Diffraction (XRD)	27
2.3.3 Electrochemical Impedance Spectroscopy (EIS)	29
2.3.4 Ultrasonic Measurements in Lithium-Ion Batteries	31
3 Materials and Methods: Dilation Cell	39
4 Results and Discussion	41
4.1 Electrochemical and Mechanical Interplay in State-of-the-Art Battery Materials	42
4.1.1 Electrode Level	42
4.1.2 Cell level	47
4.2 Electrochemical and Mechanical Interplay in Next-Generation Battery Materials	57
4.2.1 Electrode Level	57

5 Summary and Outlook	63
5.1 Summary	63
5.2 Outlook	66
6 Zusammenfassung und Ausblick	67
6.1 Zusammenfassung	67
6.2 Ausblick	70
Bibliography	71
Acknowledgement	89
Appendixes	91

List of Figures

2.1	(a) Schematic representation of the activation energy that must be overcome to activate a reaction. (b) Relation between cell polarization and applied discharging current. Three main types of polarization have to be distinguished: ohmic-, activation-, and concentration polarization. Graphs according to [15,19].	7
2.2	Graphical representation of the Butler-Volmer equation. It shows the anodic (oxidation) and cathodic (reduction) reactions and the total reaction as a function of current and overpotential. Graph according to [19].	8
2.3	Schematic working principle of a LIB. The crystal structure of the negative graphite anode and the structure of the positive NCM cathode is shown. During discharging, the lithium ions are extracted from the negative electrode and inserted in the positive electrode. The reverse reaction takes place during charging. Graph according to [16,24].	9
2.4	(a) Schematic drawing of hexagonal graphite with the AB graphene layer stacking. (b) Schematic representation of the Li_xC_6 structure, with the AA graphene layer stacking sequence and the $\alpha\alpha$ intercalated lithium interlayers. Graph according to [25].	11
2.5	(a) Graphite potential over Li_xC_6 compositions during intercalation of lithium ions into graphite. (b) Schematic presentation of staging of lithium ions into graphite. Graphs according to [25,26,51].	12
2.6	(a) Spinel-type LTO structure ($\text{Li}_4\text{Ti}_5\text{O}_{12}$) and (b) rock-salt-type LTO structure ($\text{Li}_7\text{Ti}_5\text{O}_{12}$). Green tetrahedra represent lithium, blue tetrahedra represent disordered lithium and titanium and red spheres represent oxygen. Graphs according to [28,55,57].	13
2.7	Crystal structure of layered NCM. Blue tetrahedra represent the transition metal oxide, yellow spheres represent lithium and red spheres represent oxygen. Graph according to [89].	17
2.8	Crystal structure of LiFePO_4 . The brown octahedras represent the FeO_6 , the purple tetrahedras represent the PO_4 , yellow spheres represent lithium and red spheres represent oxygen. Graph according to [94,95].	18
2.9	Two possible different failure mechanisms of silicon anodes. (a) During lithiation the silicon particle and the SEI is growing and during delithiation of the particles the SEI is breaking. Continuous cycling leads to an increase of the thickness of the SEI. (b) (De)Lithiation results in pulverization of the particles due to the volume changes. Graph according to [117,118].	22

2.10	Schematic failure mechanisms of lithium metal during stripping and plating. Graph according to [34,60].	23
2.11	Schematic degradation mechanisms of NCM and LFP cathodes. The degradation mechanisms (a)-(d) are related to NCM and (a), (c) and (e) are related to LFP.	24
2.12	Schematic presentation of a dilatometer. The expansion is adapted to a graphite anode and a NCM cathode [25,38]. (a) represents the expansion in a fully charged state and (b) in a fully discharged state.	27
2.13	Schematic representation of the Bragg equation.	28
2.14	(a) Schematic representation of a harmonic oscillation and (b) a periodic potentiostatic EIS measurement. Graph according to [162,164].	30
2.15	Schematic representation of ideal EIS and ECM of a LIB. The data is shown in a Nyquist plot. Graph according to [166].	31
2.16	Schematic presentation of (a) longitudinal- and (b) transversal wave. Graph according to [175].	32
2.17	(a) Schematic presentation of a ultrasonic transducer and the signal generation. (b) Impact of damping body on the ultrasound signal. Graph according to [178].	34
2.18	Schematic representation of the sound pressure in the near- (green) and far field (blue) of a transducer. The dashed line (orange) shows the intensity or pressure of the acoustic wave with its maximum at the end of the near field. Graph according to [180].	35
2.19	Schematic presentation of (a) pulse-echo method and (b) transmission method. By using the pulse-echo method the acoustic signal travels twice through the object before it gets to the receiving transducer. Hence the ToF is twice as long in the pulse-echo method compared to the transmission method.	36
2.20	Schematic presentation of ToF determination. The green dot represents the ToF estimated by a threshold equal to 10% of amplitudes maximum and the orange dot is the ToF estimated by 10 times the standard deviation of the signal's noise before the arrival of the first wave package.	37
3.1	(a) Schematic cross section and (b) photograph of the <i>operando</i> dilation cell.	40
3.2	Different upper plunger: (a) Flat plunger and (b) Plunger with step	40
4.1	Formation of graphite vs. NCM111 with an initial 0.1 C cycle, followed by three 0.2 C cycles. Upper graph: Cell potential and anode potential as a function of time. Lower graph: dilation as a function of time. The figure was reprinted from reference [152].	43
4.2	ICA and IDA as a function of anode potential in fourth formation cycle with a current of 0.2 C. The figure was reprinted from reference [152].	44

4.3	Dilation behavior of graphite vs. NCM111, graphite vs. LTO, NCM111 vs. LTO and LFP vs. LTO during cycling. The figure was reprinted from reference [152].	44
4.4	Charge rate capability test. Discharge capacity plotted as a function of the charge rate for (a) the homogeneous pressure distribution (flat plunger) and (b) inhomogeneous pressure distribution (plunger with a step). The figure was reprinted from reference [152].	45
4.5	Anode potential over charging capacity of homogeneous pressure distribution (a) + (b) and inhomogeneous pressure distribution (c) + (d) for CCCV charging rates of 0.5 C and 2 C respectively. The figure was reprinted from reference [152].	46
4.6	a) Cycling of prismatic cells under different external bracing conditions. The capacity is only plotted every 75th cycle for better visibility. b) Thickness change measured every 250 cycles. The figure was reprinted from reference [185].	48
4.7	Photographs of electrodes and separators after cell opening. (a) Cell 1: Unaged reference cell, (b) Cell 2: Aged braced cell and (c) Cell 3: Aged unbraced cell. The figure was reprinted from reference [185].	49
4.8	SEM cross sections of the differently aged cathodes. a) Cell 1, reference, b) Cell 2, braced, c) Cell 3, unbraced, w/o ripples, d) Cell 3, unbraced, w/ ripples. The figure was reprinted from reference [185].	50
4.9	(a) Lithium and (b) transition metal content in anode for reference and aged cells. The lines are a guide for the eye only. The figure was reprinted from reference [185].	50
4.10	Observed (green), calculated (orange), and difference (blue) XRD patterns of the differently aged cathode materials. The figure was reprinted from reference [185].	51
4.11	C-rate-capability test of laboratory electrodes harvested from the prismatic cells. The C-rate relates to the reference cell. The figure was reprinted from reference [185].	52
4.12	0.04 C cycling of a 12 Ah LIB pouch cell. (a) shows the voltage, (b) the cell thickness, (c) the ToF, (d) the SoS and (e) the effective Young's modulus as a function of time. The figure was reprinted from reference [186].	54
4.13	Differential analysis of a) capacity, b) dilation and c) ToF for 0.04 C cycles during RPT over cell voltage. The overlay shows the staging of the graphite anode estimated from harvested three electrode cells. The figure was reprinted from reference [186].	56
4.14	Evolution of ToF (a) and effective Young's modulus (b) as a function of time during RPTs. The figure was reprinted from reference [186].	57

4.15	Dilation behavior of silicon vs. NCM111, lithium vs. LTO and graphite vs. LTO during cycling. Voltage and dilation as a function of cumulative capacity. The figure was reprinted from reference [187].	58
4.16	Pressure dependent dilation of lithium vs. LTO or LFP with three different electrolytes (LP57, LP57 with 5wt% FEC and 1M LiFSI in DME). The figure was reprinted from reference [187].	60
4.17	Specific capacity as a function of cycles for the cycling of lithium vs. LTO or LFP with three different electrolytes (LP57, LP57 with 5wt% FEC and 1M LiFSI in DME) and various external applied pressures (unbraced, 0.5 MPa and 1.0 MPa). The figure was reprinted from reference [187].	61
4.18	Pressure as a function of time for the cells with 0.5 MPa and 1.0 MPa initially applied external pressure. For better visibility, only one representative cell is shown for each parameter. The figure was reprinted from reference [187].	62

List of Tables

2.1	Comparison of specific capacity, nominal potential, volume change and Young's modulus change for positive and negative electrodes. Note that the Young's modulus only refers to the active particles and not to the whole composite electrode and the change is shown from delithiated state to the lithiated state.	10
2.2	Comparison of different key performance indicators for Ni, Co and Mn layered NCM cathodes [73, 84, 86, 87].	16
2.3	Physical and chemical properties typical solvents used for LIB electrolytes [99, 101].	19
2.4	Circuit components, symbols and equations of circuit elements used for LIB. Table according to [164, 165].	31
4.1	Lattice parameters for cathodes obtained from the Rietveld analysis. The table was reprinted from reference [185].	51
4.2	Measured areal capacity, dilation and the dilation per areal related capacity of the investigated cells during lithiation of the negative electrode. The table was reprinted from reference [187].	59

List of Abbreviations

BEV	battery electric vehicle
BMS	battery management system
CCCV	constant current constant voltage
DFT	density functional theory
DMC	dimethyl carbonate
DME	dimethoxyethane
EC	ethylene carbonate
ECD	electrochemical dilatometry
ECM	equivalent circuit modeling
EIS	electrochemical impedance spectroscopy
EMC	ethylmethyl carbonate
EMF	electromotive force
EOL	end of life
FEC	fluorethylene carbonate
GEIS	galvanostatic electrochemical impedance spectroscopy
HF	hydrofluoric acid
HOMO	highest occupied molecular orbital
ICA	incremental capacity analysis
ICE	internal combustion engine
ICP-OES	inductively coupled plasma optical emission spectroscopy
IDA	incremental dilation analysis
LCO	lithium cobalt oxide
LFP	lithium iron phosphate
LIB	lithium-ion battery
LiFSI	lithium bis(fluorosulfonyl)imide
LiPF₆	lithium hexafluorophosphate
LMO	lithium manganese oxide

LP57	1M LiPF ₆ in EC/EMC 3/7 wt%
LTO	lithium titanate
LUMO	lowest unoccupied molecular orbital
NCA	lithium nickel cobalt aluminum oxide
NCM	lithium nickel cobalt manganese oxide
NG	natural graphite
PE	polyethylene
PEEK	polyether ether ketone
PEIS	potentiostatic electrochemical impedance spectroscopy
PP	polypropylene
PTFE	polytetrafluoroethylene
RPT	reference performance test
SEI	solid electrolyte interphase
SEM	scanning electron microscope
SG	synthetic graphite
SoA	state-of-the-art
SoC	state-of-charge
SoH	state-of-health
SoS	speed-of-sound
SSB	solid-state batteries
ToF	time-of-flight
VC	vinylene carbonate
V2G	vehicle-to-grid
XRD	X-ray diffraction

1 Introduction

1.1 Motivation

Climate change is the greatest challenge of our times. The increase of greenhouse gases in the atmosphere over the last 140 years has resulted in an increase of the global average temperature [1,2]. The temperature rise has been accelerating in recent years, with the eight warmest years of all time starting 2015 [3,4]. This shows the urgent need to reduce the greenhouse gas emissions with an energy transition from fossil to renewable energies. This transformation will need to involve the de-carbonization of many sectors such as through the electrification of the transport, buildings and industry (heat production through electricity). This shift will more than double the total electrical power demand in Europe by 2050, where the power production through wind and solar will play a key role [5]. The energy production with wind and solar have the drawback of fluctuations and seasonality. One possible option for solving this problem is energy storage with batteries [5]. The use of battery electric vehicles (BEVs) can combine two major challenges, the electrification and hence the de-carbonization of the transportation sector and the storage of excess energy [6]. The higher efficiency of the electric drive train compared to the conventional internal combustion engine (ICE) can reduce, already today, the greenhouse gas emissions of $\sim 50\%$, depending on the local electricity mix in Europe [7]. The greenhouse gas reduction by using the BEV is expected to decrease even more in the next years as the share of 'green' electricity will rise continuously [5, 7]. To further accelerate the energy transition, the batteries in the BEV could also be used to store excess energy from the grid when the car is not in use. This concept is also known as vehicle-to-grid (V2G). Nevertheless, if the BEV is also used for V2G, the degradation of the battery in terms of capacity loss is increased as the cells experience more cycles. Overall, a long battery life is crucial, both to reduce lifetime greenhouse gas emissions resulting mostly from energy-intensive cell production [7] and to enable batteries to be used as energy storage for the power grid [6].

Today's most promising battery for the BEV is the lithium-ion battery (LIB) due to its high energy and power density compared to other battery chemistries [8]. However, the driving range of today's BEVs is still lower compared to vehicles with an ICE. Thus, the increase of the energy density of LIBs gains more importance, which is also crucial for the widespread acceptance of the BEV by the society. Two possible options are (1) the enhanced utilization of the space within the battery housing by increasing the amount of electrode active materials or (2) the use of electrodes with a higher intrinsic energy density. At first sight, those techniques seem to easily solve this issue but both methods enhance the stress on the battery

components and especially on the electrodes. In comparison to current and temperature, the impact of mechanical parameters and the interplay with the battery's electrochemistry is rather unexplored. Hence, the mechanics in the cell need to be fully understood to obtain a long battery life, which will certainly reduce the ecological footprint and the costs of the batteries.

1.2 Objectives

This thesis aims to give a better understanding of the electrochemical and mechanical interplay in LIB cells. This interplay is crucial for today's state-of-the-art (SoA) but even more for next-generation battery cells. To this purpose, the work is split into two main sections: SoA and next-generation battery materials. In both groups, the electro-mechanical interplay is known to have a significant impact on the lifetime and performance of the LIB and thus needs to be fully understood. To extend this understanding, this PhD thesis addresses the following investigations:

1. Initially, reversible and irreversible dilation of the LIB electrode materials and thus their impact on the battery cell is investigated. Therefore, a laboratory *operando* dilation cell is further developed to study the expansion behavior of various SoA active materials and identify the underlying mechanisms. Additionally, the relation between the (in)homogeneous pressure distribution and the performance of laboratory electrodes will be determined (section 4.1.1).
2. In a further step, the electrochemical and mechanical interplay is studied for commercial large scale LIBs. Here, the impact of bracing on the performance of prismatic cells is studied during an aging and post-mortem study. A new concept of the mechanical state-of-health (SoH) is introduced and addresses the performance reduction with the electrode degradation (section 4.1.2).
3. To deepen the knowledge of the mechanical changes inside the LIB, non-invasive ultrasonic measurements are used to study the mechanics such as the correlation of thickness and Young's modulus change. These changes are studied in dependence of the state-of-charge (SoC)- and SoH (section 4.1.2).
4. Finally, the electrochemical and mechanical interplay of next-generation battery electrode materials is investigated and compared to today's electrodes. Special focus is given to the pressure and electrolyte-dependent performance and expansion of lithium metal (section 4.2.1).

1.3 Structure of the Thesis

The PhD thesis is divided into six main chapters, dealing with the electrochemical and mechanical interplay in LIB cells:

1. Chapter 1 introduces the importance of the topic and describes the thesis' objectives.
2. Chapter 2 provides an overview of the SoA and the theoretical background of the LIB, as well as the most important characterization methods used in this work.
3. Chapter 3 deals with the further development of the *operando* dilation cell.
4. Chapter 4 illustrates and summarizes the main results of this PhD thesis. It deals with the electrochemical and mechanical interplay in LIBs and is divided into three main parts: SoA electrode level, SoA cell level and next-generation electrode level.
5. Chapter 5 and 6 conclude the achievements and give an outlook for future research in this area. Chapter 5 is in English and Chapter 6 is in German.

2 State of the Art and Theoretical Background

This section introduces the LIB and will give a brief overview over the SoA and the concept behind the LIB. In particular, the thermodynamics, the working principle and the aging mechanisms are described. Additionally, the main characterization methods used in this work are explained.

2.1 Principles of Lithium-Ion Batteries

The history of the modern secondary (rechargeable) LIB began in the early 1970s when M. Stanley Whittingham invented the first secondary LIB with lithium as negative electrode and titanium disulfide (TiS_2) as positive electrode [9]. This cell demonstrated a nominal cell voltage of $\sim 2.0 \text{ V}$ vs. Li/Li^+ with a theoretical specific cathodic capacity of almost 240 mAh g^{-1} [9]. The drawback was the need for handling during synthesis under inert conditions due to decomposition of TiS_2 to titanium oxide (TiO_2) and hydrogen sulfide (H_2S) upon the reaction with water [10]. Furthermore, the metallic lithium caused fire incidents [11]. John B. Goodenough exchanged the positive electrode with lithium cobalt oxide (LCO) (LiCoO_2) and improved the average cell voltage up to $\sim 4.0 \text{ V}$ and hence also the power output [12]. In 1985, Akira Yoshino used Goodenough's LCO cathode and replaced lithium with a carbonaceous material, enabling stable and safe cycling [13, 14]. These inventions, among others, led to the commercialization of today's modern LIBs.

2.1.1 Thermodynamics and Kinetics

Before starting with the working principle of LIBs, it is necessary to have a look at the thermodynamics and kinetics of the battery system. The open circuit voltage (E_{OCV}) of a LIB is determined by the difference of the potential of the cathode ($E_{Cathode}$) and anode (E_{Anode}) [15]:

$$E_{OCV} = E_{Cathode} - E_{Anode} \quad (2.1)$$

The voltage during cycling is limited by the electrochemical stability window of the electrolyte. This window is defined by the energy gap between the highest occupied molecular orbital (HOMO) to the lowest unoccupied molecular orbital (LUMO) [16,17].

The basic thermodynamic equation for a reaction is described by the change in Gibbs free energy, or the energy of a reaction available (free) for work, ΔG :

$$\Delta G = \Delta H - T\Delta S \quad (2.2)$$

where ΔH is the enthalpy, or released energy, ΔS is the entropy and T is the absolute temperature [16,18]. The net available free energy from a electrochemical reaction is given by:

$$\Delta G = -nFE \quad (2.3)$$

where n is the number of transferred electrons, F is the Faraday constant and E is the voltage of the cell [18]. Spontaneous reactions have a positive voltage ($E > 0$) and hence the difference of the Gibbs free energy is negative ($\Delta G < 0$). In a chemical reaction:



the relationship between the difference of the free energy (ΔG), the difference of the standard free energy (ΔG°) and the activity products ($a_i^{\nu_i} = \frac{a_C^{\nu_c} a_D^{\nu_d}}{a_A^{\nu_a} a_B^{\nu_b}}$) can be derived as follows:

$$\Delta G = \Delta G^\circ + RT \ln(a_i^{\nu_i}) \quad (2.5)$$

where R is the absolute gas constant [18]. By combining equation 2.3 and 2.5, the Nernst equation is obtained:

$$E = E^\circ + \frac{RT}{nF} \ln(a_i^{\nu_i}) \quad (2.6)$$

where E° is the standard electrode potential [18]. The activity can be approximated by the concentration for low ion concentrations. For solids with a constant composition, an activity of one is assumed for simplicity.

Spontaneous processes have a negative free energy and a positive electromotive force (EMF) with the reaction written in a reversible fashion, which goes in the forward direction. To force the reaction into its backward direction an external voltage has to be applied. This voltage has to overcome kinetic limitations, such as the activation energy E_a , causing a voltage drop (Figure 2.1) [18,19]. The voltage drop during operation of a LIB is not only caused by the activation polarization but also by further effects. Three different kinetic effects for the polarization have to be distinguished:

- Ohmic polarization η_o : Ohmic resistances of individual cell components (electrolyte, active mass, current collectors and tabs) and the contact resistance between active mass and current collector
- Activation polarization η_a : Resistances of the potential difference of electrodes and electrolyte that has to be overcome for charge transfer to occur
- Concentration polarization η_c : Mass transport limitations due to diffusion limitations which arise from concentration gradients at the electrode surface and the bulk

All those polarizations cause a voltage drop of the cell voltage E_p during operation:

$$E_p = E_{OCV} - \eta_o - \eta_a - \eta_c \quad (2.7)$$

where E_{OCV} is the open circuit voltage.

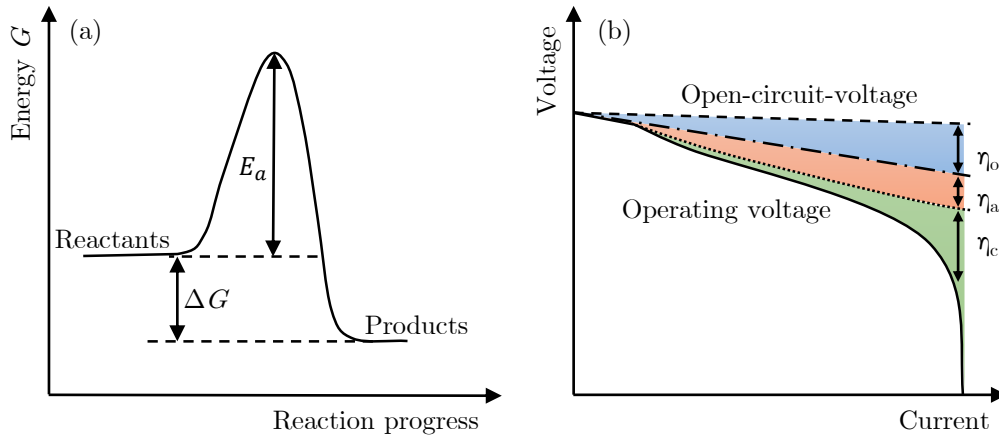


Figure 2.1: (a) Schematic representation of the activation energy that must be overcome to activate a reaction. (b) Relation between cell polarization and applied discharging current. Three main types of polarization have to be distinguished: ohmic-, activation-, and concentration polarization. Graphs according to [15, 19].

The correlation between the current density j of a battery reaction and the activation overpotential (ignoring diffusion and ohmic resistances), is given by the Butler-Volmer equation:

$$j = j_0 \left(\exp\left(\frac{\alpha F n \eta}{RT}\right) - \exp\left(-\frac{(1 - \alpha) F n \eta}{RT}\right) \right) \quad (2.8)$$

with j_0 being the exchange current density and α being the charge transfer coefficient, representing the proportion of oxidation and reduction. The Butler-Volmer equation can be divided into two parts, the forward cathodic reaction (reduction) and the reverse anodic reaction (oxidation) as can be seen in Figure 2.2.

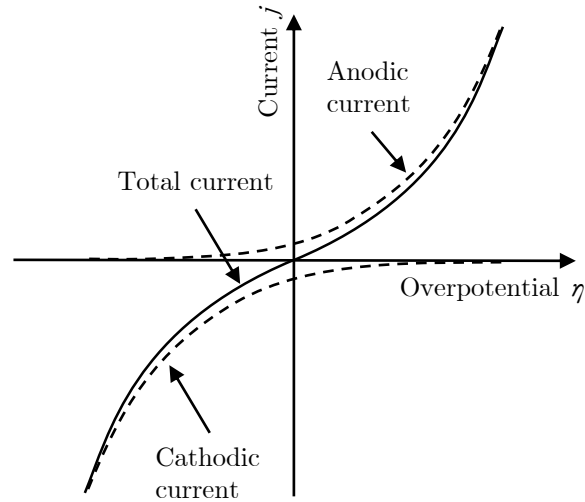


Figure 2.2: Graphical representation of the Butler-Volmer equation. It shows the anodic (oxidation) and cathodic (reduction) reactions and the total reaction as a function of current and overpotential. Graph according to [19].

Another important aspect for the performance and degradation of a LIB is the generated heat (q_{total}) from the chemical reaction. It is the sum of reaction (q_r) and joule (ohmic) (q_j) heats and it is defined by:

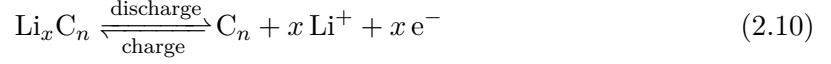
$$q_{total} = q_r + q_j = T\Delta S + I\eta \quad (2.9)$$

where I is the current and η ($= E_{OCV} - E_p$) is the polarization [20, 21, 22, 23]. The reaction heat arises from the intercalation of lithium ions into the host structure of the electrodes and the joule heat is related to the batteries internal resistance and the operating current.

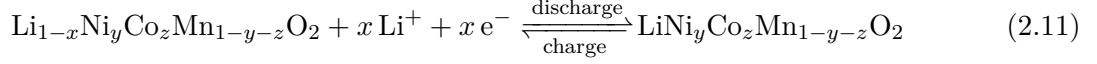
2.1.2 Working Principle

LIBs contain several galvanic cells connected in parallel. Each galvanic cell consists of a positive and a negative electrode separated by a separator (Figure 2.3). These components are soaked with an organic electrolyte, which serves as the medium allowing lithium ion transport. The charging and discharging redox reactions occur on both electrodes (Equations 2.10 - 2.12). During discharging the negative electrode is oxidized (Equation 2.10) and the lithium ions are extracted (deintercalation) from graphite and migrate through the electrolyte to the positive electrode. The corresponding electrons move through an external circuit to the positive electrode where the insertion (intercalation) of the lithium ions occurs. The intercalation of the lithium ions result in a reduction of the transition metals inside the crystal structure (Equation 2.11). As the (de)intercalation reactions occur primarily at the surface of the electrodes, solid-state mass diffusion takes place due to concentration gradients in the active particles. During charging, the reverse reaction occurs. The (de)intercalation of the lithium ions into the host structure results in change of lattice structure which leads to a change in the Young's modulus and the volume.

Negative electrode:



Positive electrode:



Redox reaction:

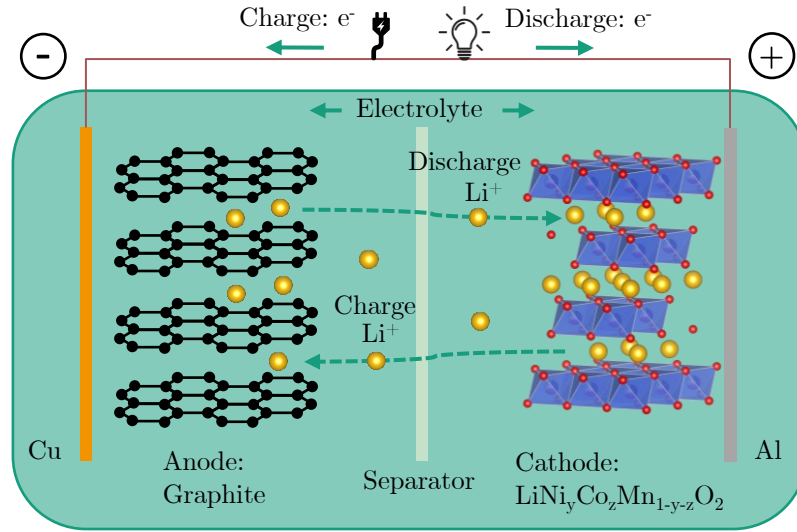
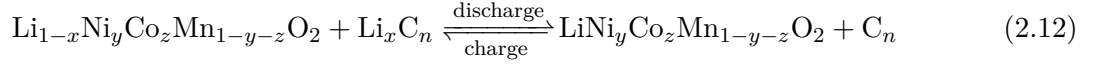


Figure 2.3: Schematic working principle of a LIB. The crystal structure of the negative graphite anode and the structure of the positive NCM cathode is shown. During discharging, the lithium ions are extracted from the negative electrode and inserted in the positive electrode. The reverse reaction takes place during charging. Graph according to [16, 24].

2.1.3 Negative Electrode

For the negative electrode, which is also called anode, three types of storage reactions have to be distinguished: intercalation-, alloying- and conversion reactions.

The intercalation reactions are based on the reversible insertion and extraction of lithium ions in the lattice of the host anode material. The limited number of intercalated lithium ions into the structure result in a low theoretical capacity and small volume changes (Table 2.1) [42, 43]. The most prominent materials for intercalation or insertion reactions are graphite and lithium titanate (LTO). In contrast, alloying type reactions form Li-alloy compounds after lithiation. The specific capacities are about an order of magnitude higher compared to intercalation type reactions due to the multi electron transfer as in silicon and tin. However, the large volumetric expansion during cycling (e.g. $\sim 280\%$ for silicon [31, 32]) can destroy the structure of the electrodes and hinder the practical use of those materials. Conversion

Table 2.1: Comparison of specific capacity, nominal potential, volume change and Young’s modulus change for positive and negative electrodes. Note that the Young’s modulus only refers to the active particles and not to the whole composite electrode and the change is shown from delithiated state to the lithiated state.

Electrode	Spec. cap. / mAh g ⁻¹	Potential / V	ΔV	Young’s mod. / GPa	Ref.
Graphite	372	0.2	10%	32 → 109	[25, 26, 27]
LTO	175	1.55	0.2%	181 → 209	[28, 29, 30]
Si	3579	0.2	280%	96 → 41	[31, 32, 33]
Li	3861	0.0	4.9 μm per mAh cm ⁻²	7.8	[34, 35, 36]
NCM111	150 (pract.)	3.7	1.5%	112 → 143*	[37, 38, 39]
NCM811	200 (pract.)	3.7	1%	112 → 143*	[37, 38, 39]
LFP	170 (pract.)	3.5	5%	125 → 124	[29, 40, 41]

* values for NCM523

reactions store lithium with a high specific capacity through the redox reactions between lithium ions and transition metal cations (M_aX_b , M = Metal, X = O, S, F, N, P) [43, 44]. The downsides are the large voltage hysteresis, poor reversibility and the high volumetric expansion during cycling.

In the following, the negative anode materials used in this work are described briefly.

Graphite

The most prominent material for the negative electrode in the LIB is graphite. The advantages of graphite are the low intercalation potential of the lithium ions into graphite of < 0.3 V vs. Li/Li⁺, the relatively high specific capacity of 372 mAh g⁻¹ and the high reversibility of the (de)intercalation process [25]. The formation of a stable solid electrolyte interphase (SEI) on graphite enables a long cycle life which is not negatively impacted or hindered by the moderate volume change of $\sim 10\%$ [25, 45, 46].

From crystallographic analysis, two different types of graphite with perfect ordered graphene layers can be distinguished: the hexagonal graphite structure with an ABAB stacking (Figure 2.4 (a)) and the less common rhombohedral graphite structure with an ABCABC stacking. The distance between the carbon atoms within the layer is in both cases ~ 0.142 nm and the interlayer spacing ~ 0.336 nm [25, 47]. During lithium intercalation, the structure of the

graphene layers shifts to the AA stacking order (Figure 2.4 (b)) [25,47,48]. The intercalation of lithium ions into the graphite structure leads to an increase of the graphene interlayer distance of around 10% for LiC_6 [25,45,46].

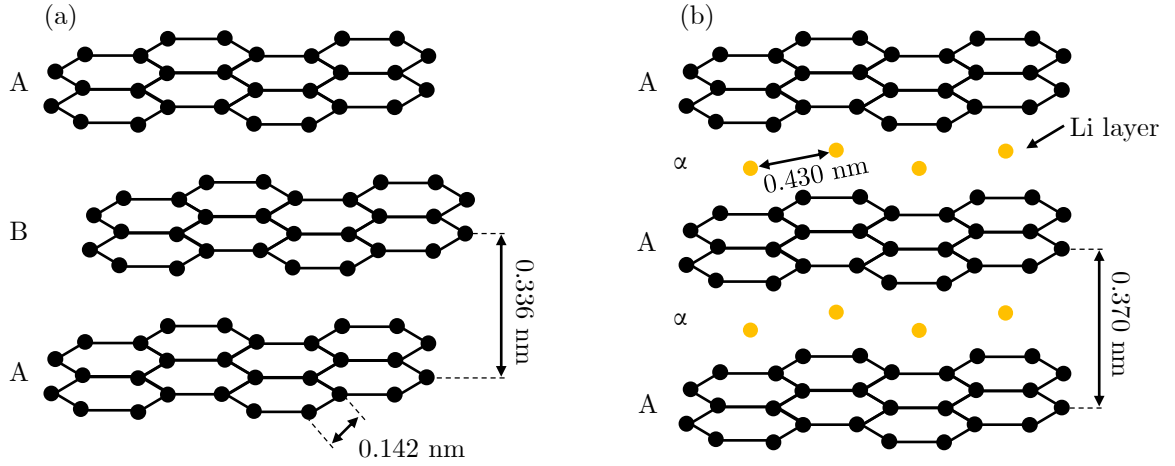


Figure 2.4: (a) Schematic drawing of hexagonal graphite with the AB graphene layer stacking. (b) Schematic representation of the Li_xC_6 structure, with the AA graphene layer stacking sequence and the $\alpha\alpha$ intercalated lithium interlayers. Graph according to [25].

The intercalation of the lithium into graphite is preferred via the edge plane (parallel to the graphene layers). The intercalation over the basal plane (perpendicular to the graphene layers) takes only place at defect sites [49]. Moreover, the lithium ion diffusion coefficient perpendicular to the graphene layers is orders of magnitude smaller ($\sim 8.7 \times 10^{-12} \text{ cm}^2 \text{ s}^{-1}$) than parallel to the graphene layers ($\sim 4.4 \times 10^{-6} \text{ cm}^2 \text{ s}^{-1}$) [50]. The lithium intercalation occurs in stages rather than randomly inserted. The stage index is characterized by the number of graphene layers between two lithium layers, i.e. stage 1 has one graphene layer between two lithium layers (Figure 2.5 (b)) [25,47,48,50,51]. This staging phenomenon is thermodynamically related to the required energy to expand the van-der-Waals gap of the graphene layers and the repulsive interactions of the lithium ions [25]. The transition of the stages can be seen as voltage plateaus in Figure 2.5 (a). The letter 'L' describes imperfectly ordered lithium ions between the graphene layers and thus a rather random, liquid-like organization [26]. The intercalation of the lithium ions in between the graphene layers lead to the aforementioned expansion of $\sim 10\%$. Furthermore, the intercalation, which leads to structural change of the crystal lattice, causes changes of the materials Young's modulus. Table 2.1 sums up the volumetric- and the change of Young's modulus for the materials used in this work.

The intercalation of the lithium ions occurs at graphite potentials $< 0.3 \text{ V}$ vs. Li/Li^+ (Figure 2.5) and thus below the electrochemical stability window of the commonly-used carbonated-based electrolytes [26,52,53]. These low graphite potentials lead to a decomposition of the

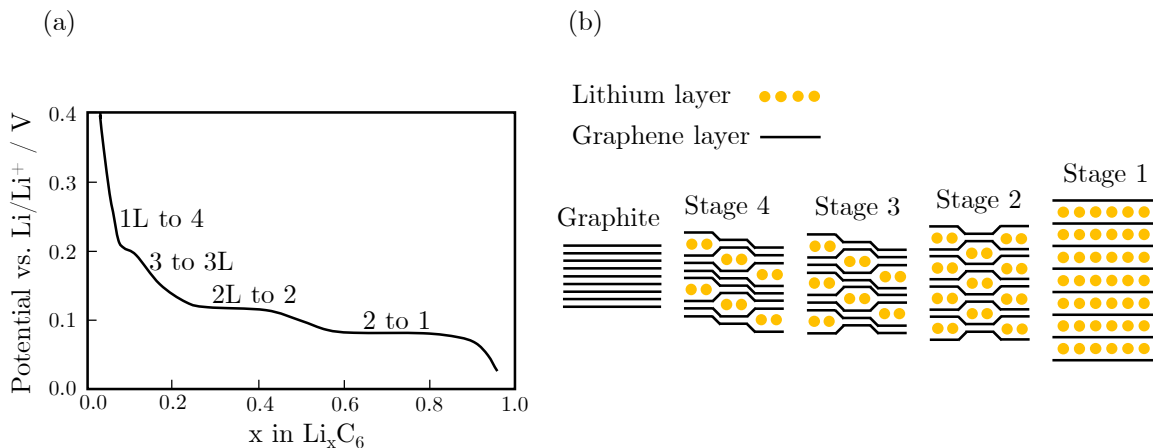


Figure 2.5: (a) Graphite potential over Li_xC_6 compositions during intercalation of lithium ions into graphite. (b) Schematic presentation of staging of lithium ions into graphite. Graphs according to [25, 26, 51].

electrolyte and the SEI is formed on the surface of graphite. The SEI consists of multiple inorganic and organic layers. The compact inorganic layer close to the surface of graphite consists of Li_2O , LiF and Li_2CO_3 . The porous organic layer (polyolephins and semicarbonates) is formed at the outer part of the SEI close to the electrolyte. This SEI layer protects the anode and prevents the electrolyte from further reduction [26, 52, 53]. The downside of the SEI is the consumption of cyclable lithium in the first cycles, which leads to an irreversible capacity loss.

In today's LIB two different types of graphite are used: natural graphite (NG) and synthetic graphite (SG). The difference of both types is the orientation of the single-crystalline parts in the poly-crystalline particles. In NG the orientation of the single-crystals is mostly in the same direction, while in SG the orientation is randomly distributed [26, 54]. The price for SG ($\sim 13 \text{ US\$ kg}^{-1}$) is higher compared to NG ($\sim 8 \text{ US\$ kg}^{-1}$) due to energy intensive production of SG (i.e. graphitization at $\sim 2500 \text{ }^\circ\text{C}$ for several days to weeks) [54]. But the price for SG is expected to drop below $10 \text{ US\$ kg}^{-1}$ in 2025 due to the increasing demand and possible bottlenecks of NG [26]. The advantages of the SG is the higher purity, the lower thermal expansion and better thermal stability [26]. Therefore, although more expensive, SG is predominantly used in BEVs, where long cycle life is essential. NG is used in portable consumer products because a long battery cycle life is not crucial.

Lithium Titanate (LTO)

LTO is an alternative anode material with the advantage of almost no change of the lattice parameters during the (de)intercalation process, resulting in long cycle life. On the other hand, the high operating voltage of $\sim 1.55 \text{ V vs. Li/Li}^+$ and the theoretical specific capacity

of 175 mAh g^{-1} [28, 55, 56] lead to a lower energy density. However, the high voltage results in the absence of a SEI, which compared to graphite lowers the loss of cyclable lithium in the cell.

In the delithiated state, lithium occupies the 8a sites in the spinel type LTO structure (Figure 2.6 (a)). The remaining lithium ions occupy randomly the 16d octahedral sites (1/6), while the rest of the sites (5/6) are filled with Ti^{4+} ions. Oxygen ions fill the 32e sites in the structure. During the intercalation process, the lattice symmetry $Fd\bar{3}m$ remains constant and the external lithium ions move to the 16c octahedral sites (Figure 2.6 (b)). At the same time, the lithium ions which occupy the tetrahedral 8a site move to the neighboring 16c sites. As a consequence, only half of the empty 16c sites in the crystal structure can be filled with external lithium ions. Furthermore, the reduction of Ti^{4+} to Ti^{3+} occurs at the 16d octahedral sites and lead to the transition of the spinel based $\text{Li}_4\text{Ti}_5\text{O}_{12}$ to the rock-salt based $\text{Li}_7\text{Ti}_5\text{O}_{12}$ (Equation 2.13 and Figure 2.6) [28, 55, 56, 57]. The strong covalent bonding between the Ti (16d sites) and O atoms (32e sites) in the crystal structure [58] lead to a negligible volume change of $\sim 0.2\%$ during the two phase transition and hence it has the so called 'zero-strain' characteristics [55, 56]. Nevertheless, the Young's modulus is slightly increasing during lithiation as can be seen in Table 2.1.

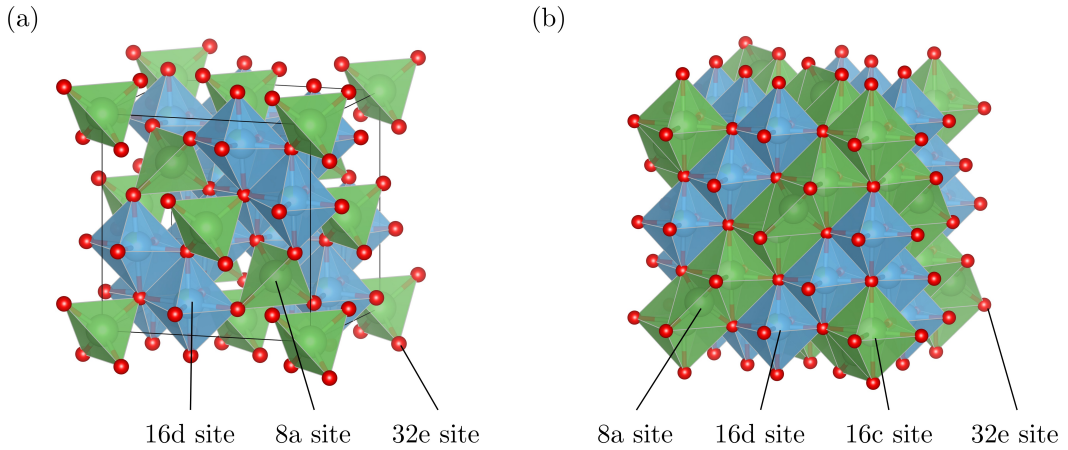
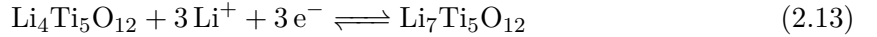


Figure 2.6: (a) Spinel-type LTO structure ($\text{Li}_4\text{Ti}_5\text{O}_{12}$) and (b) rock-salt-type LTO structure ($\text{Li}_7\text{Ti}_5\text{O}_{12}$). Green tetrahedra represent lithium, blue tetrahedra represent disordered lithium and titanium and red spheres represent oxygen. Graphs according to [28, 55, 57].

However, LTO suffers from low intrinsic electronic conductivity ($< 10^{-13} \text{ S cm}^{-1}$) and a low diffusion coefficient ($\sim 10^{-6} \text{ cm}^2 \text{ s}^{-1}$) at room temperature [56, 57]. Moreover the specific capacity is only half the value of graphite and the high operating voltage limit (see also Table

2.1) the practical use of LTO in commercial applications where high specific and volumetric energy densities are required. LTO based anodes have a market share of around 2% in the LIB sector [54].

Lithium

Lithium metal as an anode material is considered as the 'holy-grail' for LIBs. Lithium offers the highest specific capacity of 3860 mAh g^{-1} and the lowest reduction potential of -3.04 V vs. the standard hydrogen electrode of all materials [34, 35, 59, 60]. During cycling, the lithium ions are stripped and plated from and to the surface of the lithium metal. Hereby the theoretical thickness change is $\sim 4.9 \mu\text{m}$ per mAh cm^{-2} [34]. Lithium metal has a body centered cubic structure in the $Im\bar{3}m$ space group [61]. However, even after more than 40 years of research on lithium metal, the main obstacles to the commercialization of lithium metal batteries are still the high reactivity, poor cyclability, safety issues, and volumetric expansion or contraction during stripping or plating [34, 60].

Different attempts with electrolyte or interface engineering try to tackle those aforementioned obstacles. One possible way is to build a homogeneous and stable artificial SEI on the surface of the metal [62, 63]. A different way is to use a framework for lithium stripping and plating. A layered composite of Li and reduced graphene oxide can decrease the volume change below 20% [64] or hollow carbon nanospheres with Au seeds have been designed to facilitate the stripping/plating and to further protect the SEI with the carbon shell [65]. For more detailed information, the reader is referred to the references [34, 59].

The Young's modulus of lithium metal is $\sim 7.8 \text{ GPa}$ [36, 66, 67]. The modulus remains constant during cycling, as there is no change in the crystal structure.

Silicon

A promising material for next-generation anode materials is silicon. The main difference compared to graphite and LTO is the different occurring electrochemical reaction for the storage of the lithium ions. While for graphite and LTO intercalation type reactions take place, alloying reactions occur for the storage of lithium ions in silicon. The alloying reactions result in a theoretical specific capacity of 3579 mAh g^{-1} upon full lithiation ($\text{Li}_{15}\text{Si}_4$) at room temperature [31, 32]. The operating lithiation voltage is relatively low with $\sim 0.2 \text{ V}$ and another advantage is the high abundance of Si element in the earth crust [32, 68]. During the first lithiation, the crystalline silicon undergoes a solid-state amorphization upon reaction with lithium and meta-stable Li-Si phases are formed [69, 70]. At room temperature those Li-Si phases are [71, 72]: LiSi , $\text{Li}_{12}\text{Si}_7$, Li_7Si_3 , $\text{Li}_{13}\text{Si}_4$, $\text{Li}_{15}\text{Si}_4$. The major drawback is the large volume expansion of $\sim 280\%$ during cycling [31, 32].

In contrast to graphite, where the elastic modulus increases during lithiation [27], silicon particles soften during lithiation [33]. The softening of the amorphous silicon particles from around ~ 96 GPa (Si) to ~ 41 GPa ($\text{Li}_{15}\text{Si}_4$) is attributed to the propagation of the ionic Li–Si bonds (during lithiation) that are weaker compared to the covalent Si–Si bonds [33].

2.1.4 Positive Electrode

The positive electrode of the LIB, also called cathode, is mostly a transition metal compound which can be divided in three main structures: Layered, olivine and spinel structures [16,40,73]. Those structures also differ in the dimensionality of the lithium ion transport in the structure. The layered cathodes have a 2D, the olivine cathodes a 1D and the spinel cathodes a 3D lithium ion diffusion path within the structure [74, 75]. The electrochemical reaction of the insertion of the lithium ions is an intercalation type reaction.

The most prominent materials of the layered oxide type cathodes (LiMO_2 , with $M = \text{Ni, Co, Mn, Al}$) are lithium nickel cobalt manganese oxide (NCM), lithium nickel cobalt aluminum oxide (NCA) or lithium cobalt oxide (LCO). The layered materials currently have a dominant market share among the cathode materials [54,76]. For NCM cathode materials, the specific energy density increases with increasing Ni content, but the cycle lifetime and the thermal stability is lowered [54,73]. In contrast Mn increases cycle life and safety of the material. Co is known to enhance the structural stability and to increase the electrical conductivity [73]. The majority of the Co reserves are located in Central Africa, i.e. Democratic Republic of the Congo, a politically unstable country where child labor and severe environmental damage are reportedly occurring [54,77]. Additionally, the high price for Co [54] makes it an ecological and economically unattractive material, which results in attempts to reduce Co as far as possible [78]. Therefore, the exact composition of the layered cathode material is a trade off between energy density, safety, costs and ecological impact. The most commonly used olivine based cathode material is LFP, which was first presented by Padhi et al. in 1997 [41]. The low costs, environmental benignity (non toxic), high thermal stability and the good cyclability [16,40,79] makes LFP an attractive cathode material for LIBs. Recently, LFP is becoming a more and more popular cathode material for small and less expensive electric cars due to the above mentioned reasons [80,81]. The downsides are the specific capacity and the low potential range (Table 2.1), which results in a lower specific energy density compared to layered cathode materials [40,79]. Spinel structured cathode materials like lithium manganese oxide (LMO) have a 3D diffusion network for lithium ions in the crystal structure [16,82]. This material is also environmentally benign, has a high thermal stability, high rate capability and low costs [54,82]. Despite the limited cyclability and capacity fading due to the dissolution of Mn ions and structural instability, LMO is mostly used in cathode material blends in today's LIBs [54,82].

In the following the cathode materials NCM and LFP are described briefly in more detail as they are used in this work.

Lithium Nickel Cobalt Manganese Oxide (NCM)

One of the most used cathode materials in today’s LIBs are the layered NCMs ($\text{LiNi}_y\text{Co}_z\text{Mn}_{1-y-z}\text{O}_2$) of varying compositions. Depending on the exact composition the practical specific capacity is $\sim 150 \text{ mAh g}^{-1}$ for NCM111 ($\text{LiNi}_{0.33}\text{Co}_{0.33}\text{Mn}_{0.33}\text{O}_2$) or $\sim 200 \text{ mAh g}^{-1}$ for NCM811 ($\text{LiNi}_{0.8}\text{Co}_{0.1}\text{Mn}_{0.1}\text{O}_2$) with a nominal voltage of $\sim 3.7 \text{ V}$ vs. Li/Li^+ [37, 54, 83, 84]. The increasing Ni content implies also a higher capacity due to the two electron redox process ($\text{Ni}^{2+/4+}$) [54]. The higher capacity comes at the expense of chemical and structural stability, as can be seen in Table 2.2. Co for example, minimizes the spontaneous reduction of Ni^{3+} to the unstable Ni^{2+} and also inhibits the migration of Ni^{2+} into Li^+ layer, which stabilizes the structure [79, 85]. Mn increases the chemical stability of the layered oxide, as it does not suffer from oxygen release during charging [73]. Ni lies in most of the parameters in Table 2.2 in between Co and Mn, which leads to the trend of high Ni and low Co content to increase capacity while reducing costs.

Table 2.2: Comparison of different key performance indicators for Ni, Co and Mn layered NCM cathodes [73, 84, 86, 87].

Characteristic	Trend
Specific capacity	Ni > Co > Mn
Structural stability	Co > Ni > Mn
Chemical stability	Mn > Ni > Co
Electrical conductivity	Co > Ni > Mn
Abundance	Mn > Ni > Co
Environmental benignity	Mn > Ni > Co
Raw material costs	Co > Ni > Mn

NCM has rhombohedral crystal structure in the $R\bar{3}m$ space group with a stacking of alternating layers (Figure 2.7) [37, 82, 83]. Herein, lithium ions occupy the Wyckoff 3a site, the transition metals, which are statistically distributed, the 3b site and oxygen the 6c site. The oxygen ions are stacked in an O3 sequence to form the other layers [82, 83]. For nickel rich NCM cathode materials ($\text{Ni} \geq 80\%$), several phase transitions occur during cycling. The first transition is from hexagonal to monoclinic (H1 to M), followed by monoclinic to hexagonal (M to H2) and the last is a hexagonal to hexagonal (H2 to H3) transition [37, 83, 88]. For NCM cathodes with a Ni share of $< 80\%$ the M to H2 and the H2 to H3 phase transitions have not been reported [88]. A cation mixing tendency can occur as Ni^{2+} (0.69 \AA) and Li^+ (0.76 \AA) have similar ionic radii [82, 85].

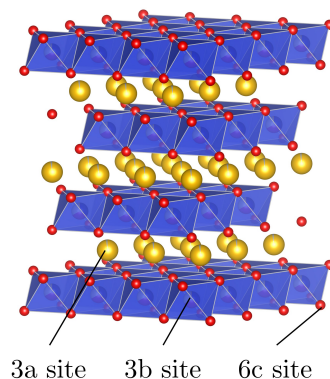


Figure 2.7: Crystal structure of layered NCM. Blue tetrahedra represent the transition metal oxide, yellow spheres represent lithium and red spheres represent oxygen. Graph according to [89].

The thickness change during cycling of the NCM cathodes is $\sim 1.0 - 1.5\%$ [37, 38]. When lithium ions are extracted from the crystal structure electrostatic repulsion between the oxygen ions leads to an expansion of the structure. The less lithium ions the more electrostatic repulsion between the oxygen ions, as lithium is expected to shield the repulsion between the oxygen layers [37, 38].

The mechanical strength of NCM particles is weakening during delithiation. The Young's modulus is decreasing from ~ 143 GPa to ~ 112 GPa (Table 2.1) [39]. This reduction can be explained by a weakening of the bond strength between the transition metals and oxygen, as the atomic charge is increased as a result of the charge compensation process [90]. The oxygen release at high delithiation states can further reduce the mechanical stability. The bond between oxygen and lithium is critical for the out of plane mechanical strength, as the interactions between the transition metals and the oxygen layers depend on the number of lithium ions in the structure. During the delithiation process, the Li–O bonds decrease which weakens the interactions between the transition metal and oxygen, resulting in a decrease of the Young's modulus in the NCM particle [90].

Lithium Iron Phosphate (LFP)

After the discovery in 1997 [41], LFP became a popular cathode material in a wide range of applications. LFP has a specific capacity of ~ 170 mAh g^{-1} with a nominal voltage of ~ 3.5 V vs. Li/Li⁺ [40, 91]. The low electronic conductivity of 10^{-9} S cm^{-1} and the diffusion limitations at the interface of the electrode cause the capacity to be reached only at low currents and elevated temperatures [41, 92, 93]. To overcome those obstacles, carbon-coated LFP was developed. With the carbon-coating the rate capability and the conductivity is improved and hence also the performance [40, 78, 79]. Besides the lower energy density of LFP compared to layered oxides, the low costs, the environmental benignity (non toxic), the high thermal stability and the good cyclability [16, 40, 79] have brought LFP back to more promi-

nence recently. The orthorhombic structure of the olivine LiFePO_4 is a framework of PO_4 complexes sharing one edge and all corners with FeO_6 octahedrons (Figure 2.8) [16, 40, 79]. Both complexes run parallel to the c-axis and propagate along b-axis, thus forming a 3D network. The structure can be viewed as an closed-packed oxygen array with half of the octahedral sites occupied by Fe^{2+} and one-eighth seated with Li^+ [16, 79]. The lithium ions are surrounded by PO_4 tetrahedra complexes and form a conduction channel along the $[010]$ direction [79].

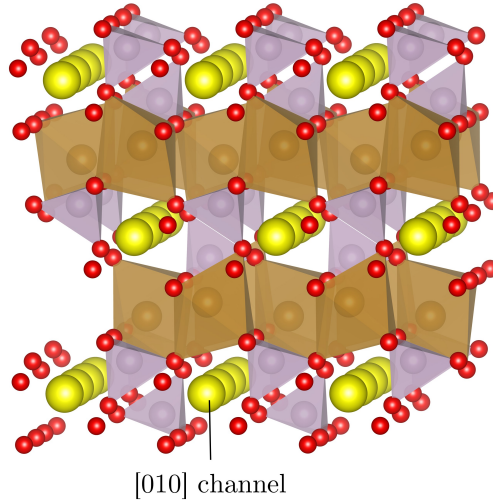


Figure 2.8: Crystal structure of LiFePO_4 . The brown octahedras represent the FeO_6 , the purple tetrahedras represent the PO_4 , yellow spheres represent lithium and red spheres represent oxygen. Graph according to [94, 95].

In contrast to the layered cathode materials, LFP shows a flat potential plateau during cycling. This can be related to the 3D olivine structure, where lithium ions can only be inserted along the $[010]$ channel (Figure 2.8) [91]. This mechanism involves the coexistence of LiFePO_4 and FePO_4 phases [16, 79]. The robust 3D olivine framework shows negligible structural changes retaining almost the same site energy between those two phases, which results in an almost constant electrochemical potential [16]. In addition, the strong covalent P–O bonds result in a high thermal stability compared to the layered oxides, as there is no risk of oxygen release [96, 97].

The volumetric change of the LFP particle during cycling is $\sim 6.0\%$ and the Young’s modulus change is small from 125 GPa to 124 GPa, which corresponds to $< 1\%$ (Table 2.1) [29, 41]. During lithiation, the lattice parameters increase along the $[010]$ (i.e. b-axis) and $[001]$ channel (i.e. c-axis) but decrease along the $[100]$ channel (i.e. a-axis) [29, 98] resulting in the aforementioned thickness change.

2.1.5 Electrolyte and Separator

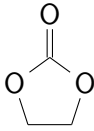
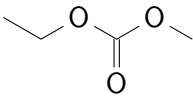
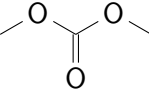
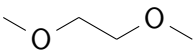
The electrolyte serves as the medium allowing for the lithium ion transport between the anode and the cathode. Today's electrolytes are complex mixtures of different solvents, lithium salts and mostly additives, e.g. 1M lithium hexafluorophosphate (LiPF_6) in a carbonate based solvent like ethylene carbonate (EC) and/or ethylmethyl carbonate (EMC) with the addition of an additive like fluorethylene carbonate (FEC) [99, 100, 101, 102].

The electrolytes' solvent must fulfill the following four main requirements [99, 101]:

1. It should remain liquid in a wide temperature range (low melting- and high boiling point)
2. It should be fluid for the lithium ion transport (low viscosity)
3. The dissolution of lithium salts should be possible in an acceptable concentration (high dielectric constant)
4. The electrolyte should remain inert or should be stable in the potential range of the cell

These requirements, e.g. low viscosity and high dielectric constant, can be achieved by combining different solvents, e.g. EC and EMC, in the electrolyte (Table 2.3).

Table 2.3: Physical and chemical properties typical solvents used for LIB electrolytes [99,101].

Solvent	Structure	Melting point / °C	Boiling point / °C	Viscosity at 25 °C / cP	Dielectric constant ϵ
EC		36	248	1.9 (40°C)	90 (40°C)
EMC		-53	110	0.65	3.0
DMC		4.6	91	0.59	3.1
DME		-58	84	0.46	7.2

In case of polar aprotic organic electrolytes, the lithium conducting agent is a lithium salt. The lithium salt which is added to the solvent should have the following requirements [99,101]:

1. Complete dissolution and dissociation in the organic solvent

2. High electrochemical stability of the anion against reduction at the cathode combined with chemical stability against the organic solvent
3. Compatibility with other cell components, e.g. separator and current collector.

In most of today's LIBs, LiPF_6 is the lithium salt of choice. LiPF_6 has not one outstanding feature, but can be considered as a combination of several positive properties with corresponding trade-offs and limitations. For example, the conductivity is high with $\sim 0.01 \text{ S cm}^{-1}$ (room temperature, 1 M/dm^3) and it is electrochemically stable against lithium up to 4.8 V vs. Li/Li^+ [99, 101]. Moreover, in organic solvents it forms a stable SEI on the graphite anode and protects the aluminum collector from corrosion [99, 100, 101]. The downsides are the low thermal stability ($< 70 \text{ }^\circ\text{C}$) and the formation of hydrofluoric acid (HF) in contact with traces of water. Another salt of interest is lithium bis(fluorosulfonyl)imide (LiFSI) with similar conductivity and stability against lithium compared to LiPF_6 . The advantage is the high thermal stability (up to $200 \text{ }^\circ\text{C}$) and no risk of HF formation. The downsides are the high costs and the corrosion of the aluminum collector at potentials above $\sim 4.0 \text{ V}$ vs. Li/Li^+ [99, 100, 101].

In most electrolytes, additives are used to enhance safety and performance of the LIB. Different additives can be used to enhance the film formation on the electrodes, to stabilize the electrolyte, to improve the safety, increase wettability or to inhibit corrosion [100]. The addition of vinylene carbonate (VC) results in the formation of a stable and homogeneous SEI during formation on the graphitic anode and increases the cycling stability of the LIB [99]. Another promising additive is FEC, which increases the performance of for example Si or Li-containing anodes due to the formation of a more fluorinated SEI layer due to the formation of LiF [100, 103].

The separator is an inactive part within the LIB. However, it plays an import role as it separates anode and cathode electrically and therefore prevents internal short circuits. Further, it provides a porous network for the migration of the lithium ions between the electrodes [104, 105, 106]. Typically the separator is a polyolefin membrane, made from polypropylene (PP) and/or polyethylene (PE), with a thickness $< 25 \mu\text{m}$ and a porosity of $\sim 40\%$ [106]. There are different monolayers and also trilayers as separators on the market. The separator is manufactured either in a wet or a dry process with an extrusion and a stretching step to form the 3D-microporous structure [104, 105].

2.2 Aging Mechanisms

Aging of the LIB refers to the loss of capacity and power due to side reactions in the course of use (cyclic aging) and time (calendar aging). The capacity fading can be described with the state-of-health (SoH), which sets the actual capacity in relation to the nominal capacity. The power fading is related to an impedance increase inside the LIB.

In the following the degradation mechanisms of the active- (negative-, positive electrode and electrolyte) and the inactive cell components (separator and current collector) are described. The main focus in this work is on cyclic aging rather than calendar aging. Calendar aging is mostly affected by temperature and SoC of the LIB. For more details, the reader is referred to [107,108].

2.2.1 Active Cell Components

The aging of the active cell components is crucial and has a direct impact on the capacity losses inside a LIB. In the following section, the aging mechanisms are separated for the negative electrode, positive electrode and electrolyte.

Negative Electrode

With the formation of the solid electrolyte interphase (SEI) on the surface of the electrode in the initial cycles, one of the main degradation mechanisms of graphite, silicon and lithium metal takes place. The low potential at the surface of the electrode leads to a decomposition of the electrolyte and the formation of a protective layer, the SEI (more detailed description in section 2.1.3). The consumption of Li^+ and reduction of the electrolyte leads to a capacity loss of $\sim 10\%$ [109,110,111]. The ideal SEI is permeable for lithium ions but not for the solvent of the electrolyte. However, during cycling the SEI is steadily growing, consuming more and more lithium ions which further reduces the capacity and increases the ionic resistances inside the cell.

Another significant aging mechanisms for graphite and silicon anode is lithium plating. During lithium plating, the lithium ions are not inserted into the electrode's host structure, but are reduced at the anode surface so that they are deposited directly as metallic lithium on the surface of the electrode. This phenomenon is thermodynamically favored when the anode potential drops below 0 V vs. Li/Li^+ [112,113]. As the cell voltage regularly operates above 0 V vs. Li/Li^+ , polarization (ohmic-, charge transfer- and diffusion overpotential) can lead to a voltage drop below 0 V vs. Li/Li^+ . The main reason for the increased overpotentials and hence lithium plating are high SoCs, high currents and low temperatures [112,113]. During rest periods, parts of the plated lithium on the surface of the electrode can partially reintercalate into the anode, but there is also a part of the lithium plating which is irreversible and results in loss of capacity and parasitic side reactions with the electrolyte [111,113]. The parasitic side reactions of the plated lithium and the electrolyte, furthermore, lead to the consumption of lithium and hence reduce the capacity of the cell [111,113]. Moreover lithium plating is also regarded as a safety concern, as forming lithium dendrites can lead to a cell short with exothermic heat generation [113].

The degradation of the electrode itself can also contribute to aging of LIBs. During (de)lithiation of the negative electrode, a thickness change of $\sim 10\%$ for graphite [25,45] and $\sim 280\%$ for silicon particles [31,32] occurs. These thickness changes result in mechanical stress within

the active particles of graphite and/or silicon resulting in reduced particle to particle connection, delamination, cracking [114, 115]. These effects are more pronounced for silicon as the volume changes are significantly higher and can cause destruction of the silicon morphology [32, 68, 116, 117]. The volume changes and destruction can promote self isolation of the active particles (loss of electrical contact), reduction of the electronic conductivity and an unstable SEI formation (Figure 2.9). These above mentioned reasons result in poor cycling efficiency and permanent capacity loss.

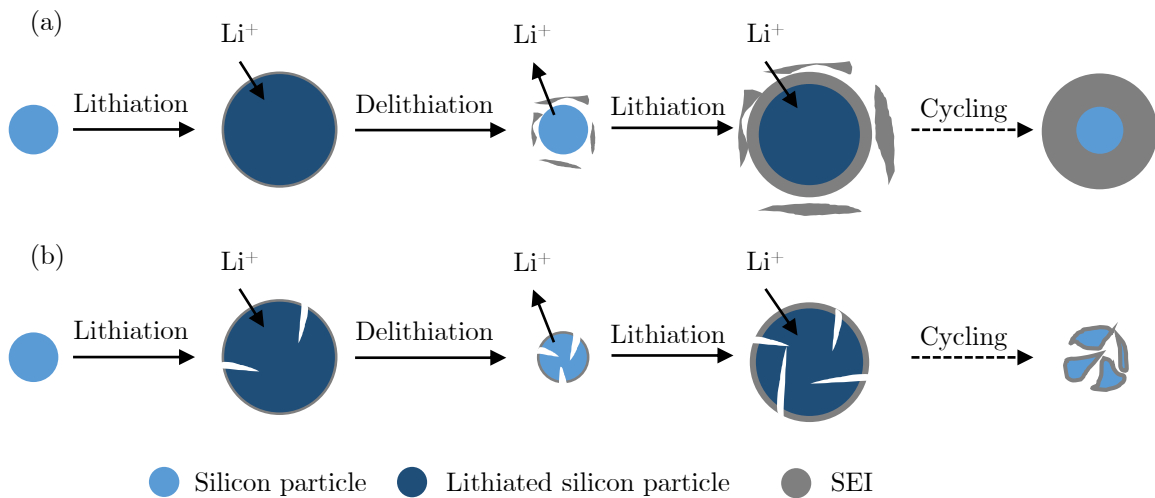


Figure 2.9: Two possible different failure mechanisms of silicon anodes. (a) During lithiation the silicon particle and the SEI is growing and during delithiation of the particles the SEI is breaking. Continuous cycling leads to an increase of the thickness of the SEI. (b) (De)Lithiation results in pulverization of the particles due to the volume changes. Graph according to [117, 118].

Lithium metal electrodes have a high variety of different aging mechanisms, which are briefly described in the following text. The highly negative electrochemical potential of Li/Li^+ leads to the reduction of almost any electrolyte on the lithium surface, resulting in a constant forming and reforming of the SEI. Aurbach et al. indicated that lithium is thermodynamically unstable in organic solvents, which complicates the formation of a stable SEI [119]. During Li plating the large volume expansion of $\sim 4.9 \mu\text{m}$ per mAh cm^{-2} [34] leads to SEI cracks and 'fresh' lithium gets in contact with the electrolyte which further decomposes the electrolyte (see Figure 2.10). Lithium tends to form dendrites during the plating process [34, 60]. These dendrites are a safety risk as they can penetrate the separator and short-circuit the cell and result in thermal runaway and fire hazards. During Li stripping, isolation (loss of electrical contact) of parts of the lithium metal/dendrites and further fractures of the SEI due to volume contraction can occur. During cycling, the thickness of the SEI is drastically increased, the lithium metal electrode becomes porous and a significant amount of lithium is

isolated and not taking part in the electrochemical reactions. The porous part of the lithium metal electrode is called 'mossy lithium' and the isolated part is called 'dead lithium'.

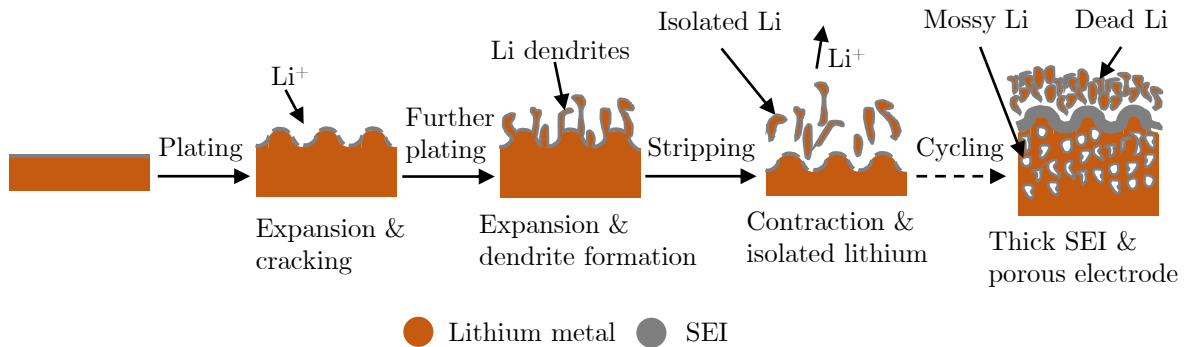


Figure 2.10: Schematic failure mechanisms of lithium metal during stripping and plating. Graph according to [34, 60].

Positive Electrode

The degradation of the positive electrode is mainly focused on the layered NCM and the olivine LFP cathode in this thesis. The main degradation mechanisms for the cathodes are (Figure 2.11):

1. Physical degradation of the electrode structure
2. Phase transitions
3. Electrode material dissolution
4. Cation mixing
5. Formation of surface films

One main aging phenomenon for cathodes is particle cracking due to volume changes. Detachment of the primary particles from secondary particles may occur, leading to a capacity loss [83, 85]. Particle cracking occurs when the electrode is cycled over a long time period, at high currents or to high SoCs [85, 120]. Structural disordering and phase changes during cycling lead to loss of capacity mainly for the NCM cathode [83, 85, 121]. Changes in the phase can occur from layered over spinel to rocksalt structure, accompanied by oxygen release at high SoCs [88, 122]. Those changes mainly occur on the surface of the NCM particles and can form partly electrochemically inactive phases. The formation of the rocksalt structure is also probably more favorable for higher cut-off voltages and also higher Ni content in the NCM cathode [85, 123]. The release of oxygen can lead to the formation of HF due to reactions of the oxygen with the electrolyte. Subsequently, metal dissolution is triggered by surface reactions of the cathode active material with HF [83, 124]. The dissolution occurs especially

at high temperatures and high SoCs [83, 85, 88, 122, 125]. Particularly for the NCM, disproportionated Mn ions ($2\text{Mn}^{3+} \longrightarrow \text{Mn}^{4+} + \text{Mn}^{2+}$) migrate to the anode and are incorporated into the SEI [83, 85]. For LFP, Fe^{2+} is migrating to the anode's SEI [124, 126]. Another degradation mechanism is the cation mixing in the crystal structure of the NCM materials. Here, especially Ni^{2+} ions occupy the lithium sites in the crystal structure due to similar radii (Ni^{2+} : 0.69 Å; Li^+ : 0.76 Å) [37, 127, 128]. This can lead to clogging of the Li^+ diffusion pathways and hence capacity fading, change in interlayer spacing and increasing internal resistance occur [85, 129]. Another essential degradation pathway for the LFP cathodes is the surface film formation. Here, the LFP particles react with HF and form the highly resistive LiF on the surface of the particles [124, 126]. This surface film can cause electrical isolation of the particles and hence reduce the capacity of the cathode.

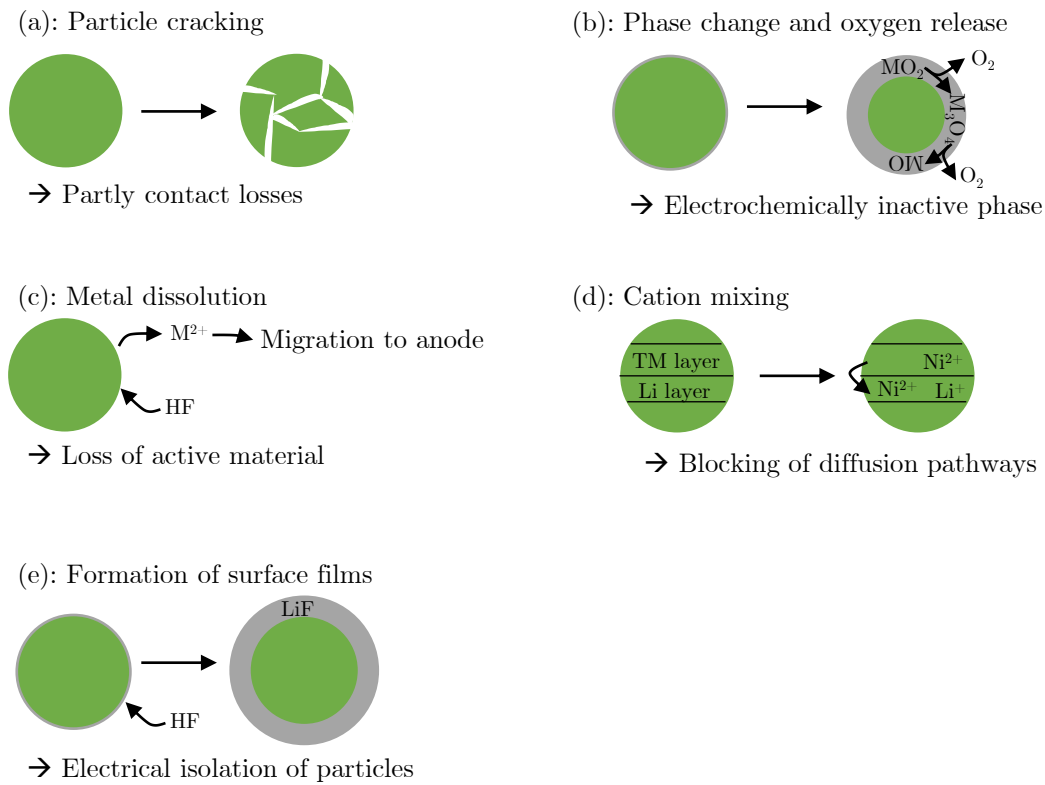


Figure 2.11: Schematic degradation mechanisms of NCM and LFP cathodes. The degradation mechanisms (a)-(d) are related to NCM and (a), (c) and (e) are related to LFP.

Electrolyte

The aging of the electrolyte is often a combination of reactions of the electrolyte with the negative and/or positive electrode (e.g. SEI formation or transition metal dissolution). As the electrolyte is not stable over the whole potential range of the electrodes, the electrolyte gets reduced at the anode and oxidized at the cathode. This results in a reduced ionic conductivity and hence increased ohmic overpotentials, because of the poorly conducting surface

layers [102, 130]. Additionally, the electrolyte can react with traces of water or oxygen and form HF which decomposes the electrodes or current collectors [102]. The ongoing consumption of electrolyte during cycling can cause local dry spots, that cause an inhomogeneous current distribution on the electrodes [111, 131].

Overall, the degradation mechanisms of active cell components in a LIB (e.g. capacity fading, resistance increase) are mostly a combination of various single aging mechanisms of the different parts of the cell. For example, charging a LIB with high currents to high SoCs leads to surface phase changes in NCM cathodes with the result of oxygen release. This oxygen release leads to an electrolyte decomposition due to the reaction of the electrolyte and the oxygen. Thereby HF is formed which results in metal dissolution on the cathode and migration to the anode. At the anode surface the metals react with the SEI, which is growing. Due to the resistance increase, lithium plating is more likely to occur on the anode. Thus, the degradation in a LIB in terms of capacity reduction or resistance increase is mostly a combination of various mechanisms rather than a single aging phenomenon. Due to that, the distinction between the aging phenomena inside a LIB is rather complex.

2.2.2 Inactive Cell Components

Although the separator and the current collectors are not involved in the electrochemical reaction, the aging of those components also have a significant impact on the performance and safety of the LIB.

Separator

The volume changes of the electrodes during cycling result in mechanical stress on the separator causing a porosity reduction and tortuosity increase. These changes lead to a reduced performance of the LIB, due to the hindering of the ionic transport through the pores and the increased internal resistance [132, 133, 134, 135]. Locally-induced stress on the separator can create partial pore clogging in the separator, leading to blocked or extended pathways. Adjacent to those areas high exchange currents occur, which can initiate lithium plating on the anode [136, 137].

Current Collector

On the one hand the current collectors of the anode (copper) and of the cathode (aluminum) can corrode. Copper dissolution is likely to appear at potentials $> 1.5\text{ V}$ vs. Li/Li^+ (over discharge) [138]. The Al collector is stable up to $\sim 5\text{ V}$ vs. Li/Li^+ but during extensive cycling the current collector corrodes due to the reaction with HF [139]. At lower potentials

(<1 V vs. Li/Li⁺) parasitic alloying reaction of aluminum with lithium occur. On the other hand mechanical-induced stress on the current collector, especially for wound electrodes, can lead to deformation and delamination of the electrode or in worst case rupture of the current collector [111,140].

2.3 Characterization Methods

In the following the main characterization methods used in the thesis are described. Particularly the dilatometry, the fundamentals of X-ray diffraction (XRD), electrochemical impedance spectroscopy (EIS) and ultrasonic measurements are explained.

2.3.1 Dilatometry

The electrochemical dilatometry (ECD) is a method to determine the expansion or volume change caused by physical and electrochemical processes of a single electrode or an electrode stack during cycling. Different types of dilatometers are currently used in battery research and the most common are capacitive piston dilatometers [45,141,142,143,144], laser dilatometers [145,146,147], and optical dilatometers [148]. Those different dilatometers are mostly used for different cell levels, e.g. at microscopic electrode level the capacitive piston dilatometer is the system of choice and at macroscopic cell level laser or optical dilatometers are mostly chosen. It should be noted, that at the atomic level, different techniques like XRD [149,150] or density functional theory (DFT) [27,151] calculations are potential methods for approximating electrode expansion.

As the capacitive piston dilatometer is used in this thesis, Figure 2.12 shows schematically the principle of this ECD. By applying a specific homogeneous pressure onto the battery stack with a piston and a spring, it is possible to determine the thickness change of the electrodes during cycling (for thickness change fundamentals see sections 2.1.3 and 2.1.4). The swelling of the electrodes during cycling is measured with a displacement sensor. The knowledge of the thickness change in a LIB is on the one hand important for cell design and on the other hand it is a useful method for distinguishing aging effects inside a LIB. For example the dependency of the aging effects with external applied pressure can be analyzed with an ECD. For more information about the ECD the reader is referred to Chapter 3 and [152].

At battery cell level, the laser triangulation method is a popular distance measurement method. In this method, a laser projects a beam on the surface of an object and the reflected light is sensed in a specific angle by a detector [153,154]. Based on the angle, the distance can be measured.

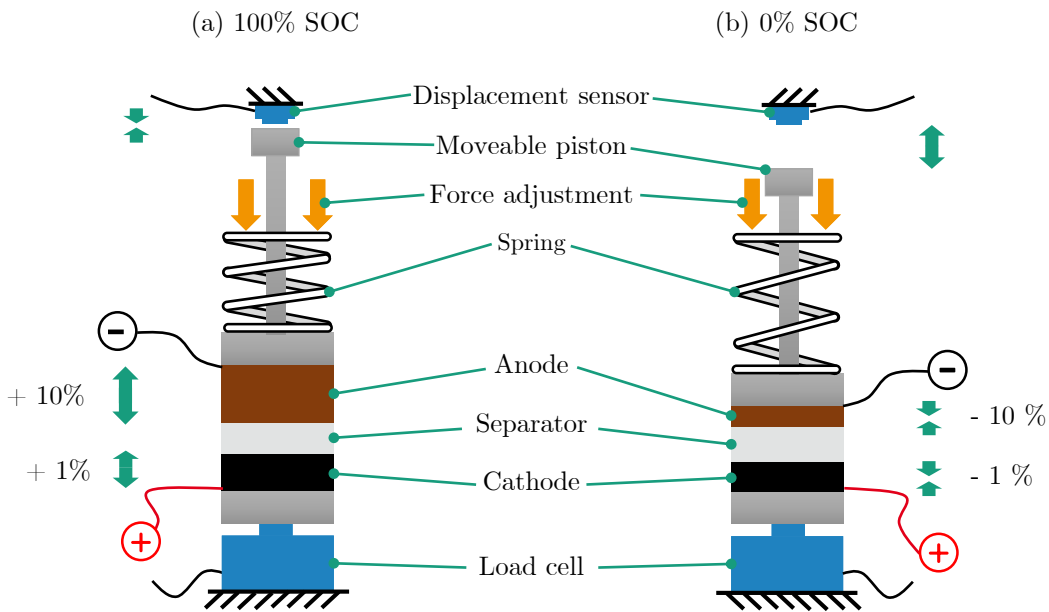


Figure 2.12: Schematic presentation of a dilatometer. The expansion is adapted to a graphite anode and a NCM cathode [25,38]. (a) represents the expansion in a fully charged state and (b) in a fully discharged state.

2.3.2 X-ray Diffraction (XRD)

XRD is a method to analyze the crystalline structure of LIB materials and to obtain information about the phase composition, space group, lattice parameters and site occupancies [155, 156].

The X-ray beam is diffracted at all angles, but at a certain angle θ constructive interference is present and it can be expressed by the Bragg equation:

$$n\lambda = 2d \sin(\theta) \quad (2.14)$$

where n is an integer, λ is the wavelength of the X-ray beam, d is the spacing between the atomic layers and θ is the angle between the atomic layer and the incident and diffracted beam. The equation 2.14 describes Bragg's law and is schematically shown in Figure 2.13. Constructive interference of the X-rays only takes place at angles θ when the path difference of the diffracted X-ray beams at different layers is equal to an integer multiple of the wavelength. Different angles lead to the destructive interference of the X-rays [155, 156]. As the X-ray beam is diffracted at the electron cloud of atoms, elements with more electrons scatter more X-rays compared to elements with less electrons and hence the signal is stronger [157].

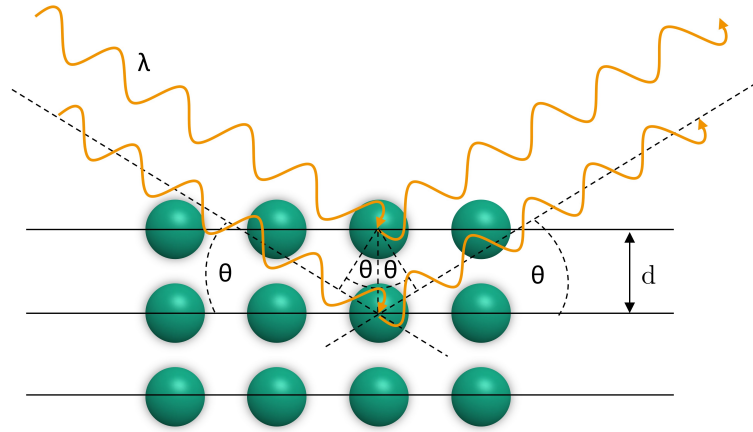


Figure 2.13: Schematic representation of the Bragg equation.

The symmetry of the structure (space group) results in the number of reflections and their positions, which can be analyzed in a XRD pattern. Each diffraction at a lattice plane is described by a reflection, of which the layer distance d , the Miller indices (hkl) and the lattice parameters are defined. Besides the position and the intensities of the peaks, the peak widths, peak shapes, peak asymmetries and the background are used to describe the pattern. The peak width and shape are related to the crystallite size or strain of the particles for example. Another popular method to analyze the XRD patterns is the Rietveld refinement. This method was initially introduced by Hugo M. Rietveld to refine neutron powder diffractions [158] and was later extended to XRD. As the Rietveld method is not a technique for structure determination but for structure refinement, a hypothetical structure is needed that is a good approximation of the final structure. The method uses the mathematical least-square approach, minimizing a weighted residual function S_y :

$$S_y = \sum_i w_i (y_i^{obs} - y_i^{calc})^2 \quad (2.15)$$

where $w_i = 1/y_i^{obs}$ is a weighting factor at each data point i , y_i^{obs} is the observed intensity and y_i^{calc} is the calculated intensity [155, 156, 159]. The calculated intensity y_i^{calc} can be derived by a sum of different factors:

$$y_i^{calc} = s \sum_k L_k m_k |F_k|^2 \Phi(2\theta_i - 2\theta_k) P_k A_k + y_i^{backgr} \quad (2.16)$$

where s is the scaling factor, L_k is the angular dependent Lorentz polarization factor at the k^{th} reflection, m_k is the symmetrically equivalent lattice planes dependent multiplicity factor, F_k is the structure factor which describes the sum of reflection intensities at a particular set of lattice planes (hkl), Φ is the reflection profile function which approximates effects of the instrument as well as specimen features like micro strain or crystallite size, ($2\theta_i -$

$2\theta_k$) is the calculated position of the Bragg reflection at $2\theta_k$, P_k is the preferred orientation function which describes the not randomly orientated crystallites, A_k is the absorption factor and y_i^{backgr} is the background at each data point [155,159]. The factor F_k is of particular importance as it is structure dependent:

$$F_k = F_{hkl} = \sum_{n=1}^N f_n e^{2\pi i(hx_n + ky_n + lz_n)} \quad (2.17)$$

where f_n is the atomic form factor, $(x_n y_n z_n)$ are the fractional coordinates of the unit cell and (hkl) are the indices of lattice planes.

Depending on the structure or the fractional coordinates of the atoms of the unit cell, the diffraction at only specific lattice planes lead to constructive interference of the diffracted X-rays. Thus, the structure factor $F_k \neq 0$ [160].

2.3.3 Electrochemical Impedance Spectroscopy (EIS)

EIS is a non-destructive method to determine the dynamic behavior of a LIB. By applying EIS it is possible to measure different electrochemical and physical properties in-situ without any external influences [161,162,163].

A linear system can be excited with a periodic signal and the output signal is also periodic with the same frequency but a different phase and amplitude [163]. There are two possible ways to apply a signal: (1) potentiostatic electrochemical impedance spectroscopy (PEIS) with an applied potential E_t and an alternating current response I_t or (2) galvanostatic electrochemical impedance spectroscopy (GEIS) with an applied current I_t and a potential response E_t . The following equations describe the PEIS mathematically:

$$E_t = E_0 \sin(\omega t) = E_0 \sin(2\pi f t) \quad (2.18)$$

$$I_t = I_0 \sin(\omega t + \Phi) \quad (2.19)$$

with E_t being the potential at time t , ω the angular frequency and f the frequency. The response signal I_t is also sinusoidal but with different amplitude and phase Φ [161,162,163]. A graphical representation of the equations is shown in Figure 2.14.

Based on Ohm's law, the impedance Z , which is also called the alternating current resistance, can be calculated exemplary for the PEIS, by the ratio of the excitation signal E_t and the output signal I_t .

$$Z = \frac{E_t}{I_t} = \frac{E_0 \sin(\omega t)}{I_0 \sin(\omega t + \Phi)} = Z_0 \frac{\sin(\omega t)}{\sin(\omega t + \Phi)} \quad (2.20)$$

With Euler's formula ($e^{i\varphi} = \cos(\varphi) + i \sin(\varphi)$), the impedance can be expressed as a complex number:

$$Z(\omega) = Z_0 e^{i\Phi} = Z_0 (\cos(\Phi) + i \sin(\Phi)) = Z' + iZ'' \quad (2.21)$$

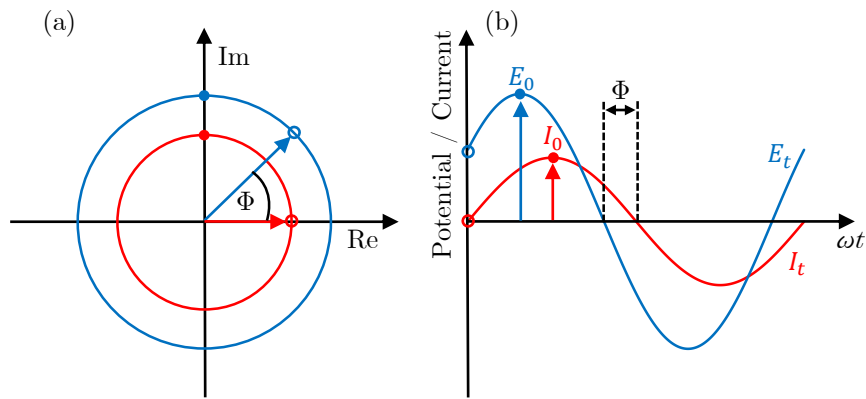


Figure 2.14: (a) Schematic representation of a harmonic oscillation and (b) a periodic potentiostatic EIS measurement. Graph according to [162, 164].

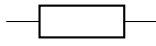
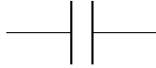
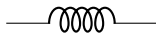

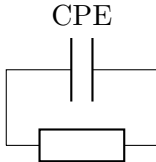
$$Z(\omega) = \text{Re}(Z) + i\text{Im}(Z) \quad (2.22)$$

Subsequently, the impedance has a real and imaginary part. With equation 2.22, the impedance can be plotted in a 'Nyquist diagram', where the real part is plotted on the x-axis and the imaginary part on the y-axis. An alternative representation is the 'Bode diagram', which displays the dependencies of the impedance Z and phase Φ on the frequency ω .

The equivalent circuit modeling (ECM) is a method to model the parameters of the electrochemical system. Furthermore, electrochemical processes which happen inside a LIB are correlated with single impedance components by series or parallel combinations. The most commonly used components are shown in Table 2.4.

Figure 2.15 shows an ideal characteristic impedance spectrum of a LIB in a Nyquist plot. With the ECM, it is possible to correlate the processes with the impedance components (see also Table 2.4). The inductance, which represents the cable inductance, has positive impedance values on the imaginary part. The ohmic resistance of the system can be seen as the intersection with the real axis and the two depressed semicircles, represented by Zarc elements, show the electrode layer resistances. The linear slope at the end represents the diffusion processes inside the electrodes.

Table 2.4: Circuit components, symbols and equations of circuit elements used for LIB. Table according to [164,165].

Circuit component	Symbol	Impedance equation	Description
Resistance		$Z_R = R$	Ohmic resistance, e.g. electrolyte resistance
Capacitance		$Z_C = \frac{1}{i\omega C}$	Capacitance, e.g. double layer capacity
Inductance		$Z_L = i\omega L$	Inductance, e.g. cable inductance
Warburg element		$Z_W = \frac{W}{\sqrt{i\omega}}$	Diffusion controlled process, e.g. solid state diffusion
Zarc element		$Z_{Zarc} = \frac{R}{1 + (i\omega)^a RC}$	Non ideal behavior of porous electrodes

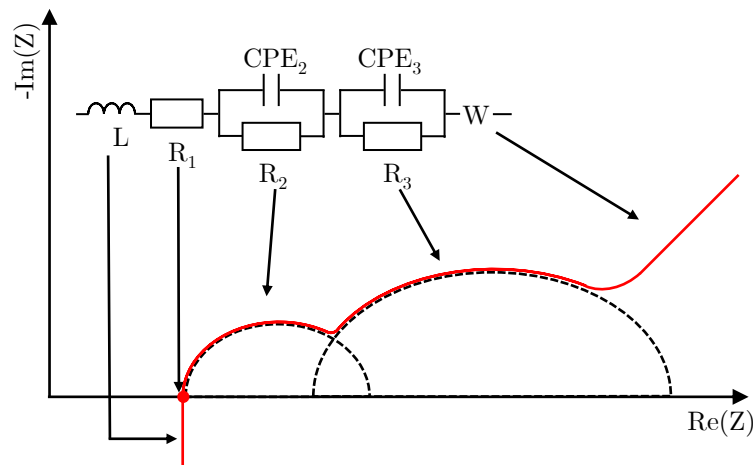


Figure 2.15: Schematic representation of ideal EIS and ECM of a LIB. The data is shown in a Nyquist plot. Graph according to [166].

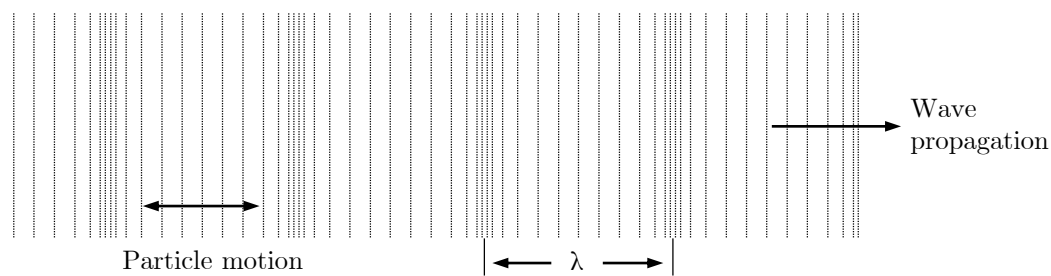
2.3.4 Ultrasonic Measurements in Lithium-Ion Batteries

The development of the non-destructive ultrasonic devices goes back to the beginning of the 20th century. After the sinking of the Titanic and during the first world war, nautical ultrasonic devices were developed to detect icebergs and submarines. In the 1940s, ultrasound was further developed for medical diagnosis and other purposes [167,168]. In the following years, non-destructive ultrasound techniques and imaging were rapidly developed, and in the 2010s ultrasound was used to study the behavior of a LIB (e.g. SoC or SoH) [169,170,171].

Ultrasound in Isotropic Porous Media

The propagation of ultrasound in solid media can be modeled with the aid of mass or particles connected by elastic springs. The displacement of one particle/mass within the chain is coupled to the adjacent mass via the connecting spring. Thereby the displacement propagates as wave along the chain. The generated ultrasonic wave propagates in different modes through a material. The three most commonly used types are the longitudinal-, transversal- and surface waves [172, 173, 174, 175]. Longitudinal, or also called pressure waves, are characterized by the oscillation of the particles in the direction of travel (Figure 2.16 (a)) and transversal or also called shear waves are characterized by the oscillation of the particles perpendicular to the direction of travel (Figure 2.16 (b)). In surface- or Rayleigh waves, the wave propagation is confined to a layer close to the surface of the solid (up to depth of approximately one wavelength) [168]. The surface waves can be used to detect cracks in the surface of a material (e.g. pipes) [174]. For a more detailed description of different wave types the reader is referred to [172, 175].

(a): Longitudinal - or pressure wave



(b): Transversal – or shear wave

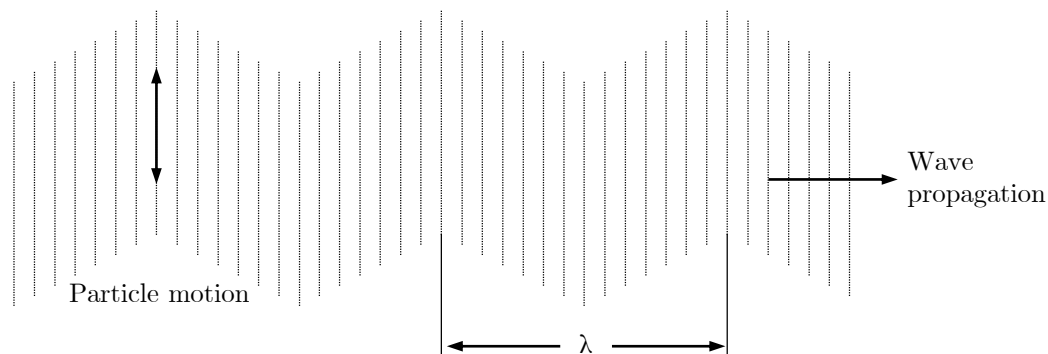


Figure 2.16: Schematic presentation of (a) longitudinal- and (b) transversal wave. Graph according to [175].

The physics of the acoustic wave propagation is described in the next section. The properties of an acoustic wave dependent on the wavelength λ , the phase velocity or sound velocity c and the frequency f [172, 174]. Properties such as wavelength and sound velocity depend on

the frequency - this phenomenon is called dispersion:

$$\lambda = \frac{c}{f} \quad (2.23)$$

The sound velocity of the ultrasound traveling through an isotropic material is dependent on the elastic properties of the material, specifically the Young's modulus E and the Poisson ratio ν (ratio of the transverse strain to the axial strain) [173, 174, 175]. For the three described ultrasonic waves, different sound velocities have to be distinguished:

- Longitudinal velocity c_l :

$$c_l = \sqrt{\frac{E(1-\nu)}{\rho(1+\nu)(1-2\nu)}} \quad (2.24)$$

where ρ is the density.

- Transversal velocity c_t :

$$c_t = \sqrt{\frac{E}{\rho 2(1+\nu)}} = c_l \sqrt{\frac{1-2\nu}{2(1+\nu)}} \quad (2.25)$$

For standard tested solids, the transversal sound velocity is around half of the longitudinal sound velocity [175].

- Rayleigh velocity c_R :

$$c_R = c_t \frac{0.87 + 1.12\nu}{(1+\nu)} \quad (2.26)$$

When ultrasound is propagating through different materials, the reflection between two materials has a high impact on the energy transfer of the acoustic wave between those materials. This impact can be expressed with the acoustic impedance Z_a , which is a measure for the resistance opposed to the propagation of sound waves. The acoustic impedance is defined as the ratio of the acoustic pressure p and the particle velocity u or as a product of density ρ and phase velocity c [176]:

$$Z_a = \frac{p}{u} = \rho c \quad (2.27)$$

When the difference of the acoustic impedance of two materials is very large (e.g. water and air [176]), most of the acoustic energy/wave is reflected at the interface. On the other hand, when the difference of the acoustic impedance is small (e.g. fat and kidney [177]), only a small percentage of the acoustic wave will be reflected at the interface. The ratio between the reflection and the transmitted energy at the interface of adjacent materials is given by the reflectance R_a :

$$R_a = \left(\frac{Z_{a,1} - Z_{a,2}}{Z_{a,1} + Z_{a,2}} \right)^2 \quad (2.28)$$

where $Z_{a,1}$ and $Z_{a,2}$ are the acoustic impedances of both materials at the interface [172,176]. The reflectance R_a at e.g. the water/air interface is 99.89%, meaning 99.89% of the energy is reflected and only 0.11% is transmitted at the interface.

Generation of Ultrasound

One possible way to generate sound waves is the use of a transducer with a piezoceramic disc, which is acting either as an actuator or sensor. Most of these actuators are based on the inverse piezoelectric effect, which is the conversion of electrical energy into mechanical energy. The piezo element starts oscillating (generation of sound waves) when an electrical field is applied. On the other hand, a receiving piezoceramic sensor bases on the inverse effect, where mechanical energy is converted into electrical energy (the vibrating disc generates a voltage signal). The disc is oscillating as a whole, both sides can transfer mechanical energy. The backside damping is required to increase the transferred energy to one side. It also acts as a damper and therefore prevents continued oscillation in resonance (Figure 2.17). The damping body determines the main direction of the sound wave into the specimen as it prevents the oscillation on side of the disc and has an impact on the signal form. The body prevents the piezo from resonating and helps to generate a short and sharp signal (Figure 2.17 (b)).

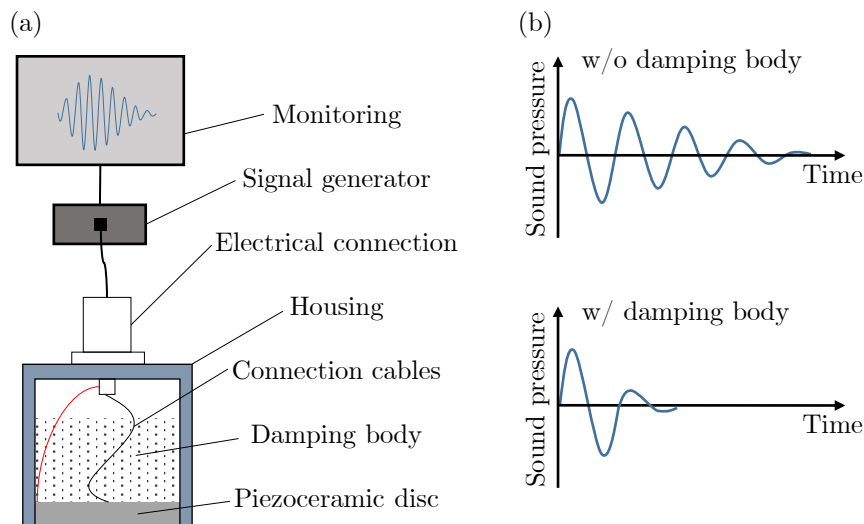


Figure 2.17: (a) Schematic presentation of an ultrasonic transducer and the signal generation. (b) Impact of damping body on the ultrasound signal. Graph according to [178].

The sound pressure profile can be constructed from an infinite number of points on the surface of the transducer (Huygens' principle). This principle states that every point on a wavefront can be the source for a new spherical elementary wave. The superposition of elementary waves creates new wave fronts [175]. In close distance to the surface, this profile is characterized by a number of minima and maxima (radial and lateral distance) (Figure 2.18), which is also

called near field (or Fresnel zone). After the last maximum of the sound intensity at distance N the far field (or Fraunhofer zone) begins:

$$N = \frac{D^2 - \lambda^2}{4\lambda} \quad (2.29)$$

where D is the diameter of the transducer [175, 176, 179]. When the wavelength λ is small compared to the diameter D of the transducer, the equation 2.29 can be simplified to:

$$N = \frac{D^2}{4\lambda} \quad (2.30)$$

This point N is also the natural focus of the piezoelectric transducer with its maximum amplitude (Figure 2.18). In the far field the sound wave is more uniform and the sound intensity decreases approximately quadratically as the beam diameter expands and the energy dissipates [175, 176, 179].

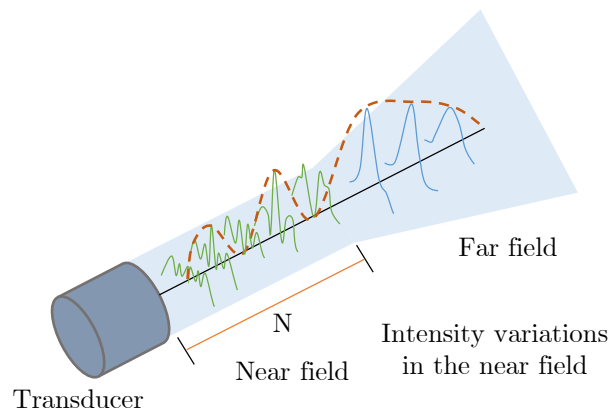


Figure 2.18: Schematic representation of the sound pressure in the near- (green) and far field (blue) of a transducer. The dashed line (orange) shows the intensity or pressure of the acoustic wave with its maximum at the end of the near field. Graph according to [180].

Signal Characteristics

The excited signal can have different forms or characteristics. On the one hand, the excitation can be a single pulse like needle, square wave (rectangle) or step pulse or a more complex excitation like bipolar tone burst, raised cosine, continuous mono frequency, frequency sweeping sinusoidal (chirp) [172, 176]. In this work, the piezo ceramic is excited with a positive rectangle pulse. In simplified terms, one can think of it as hitting a bell with a hammer. The oscillation of the bell is generating the sound wave which travels through air. The generated tone's frequency spectrum largely depends on the shape, e.g. thickness, diameter, size of the bell and the mechanical properties of its material. Very similarly, the ultrasound generated

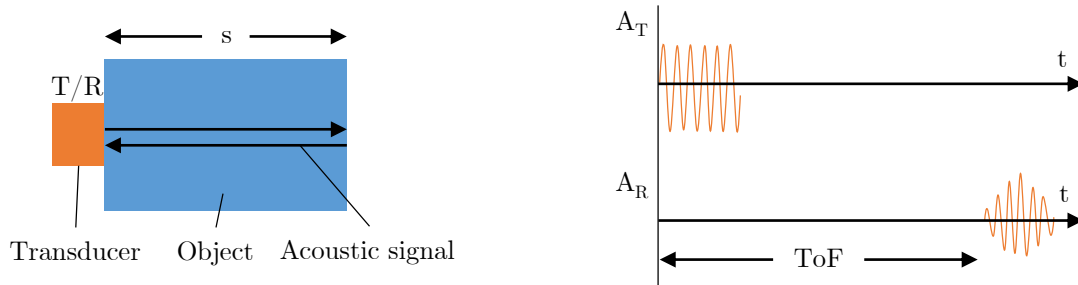
by the piezo electric transducer depends on the inertia of the system, resonance and damping of the piezo.

To determine thickness s of an object, the travel time, which is called time-of-flight (ToF), of the ultrasound signal is measured. By knowing the phase velocity c , the thickness s can easily be calculated [176]:

$$\text{ToF} = \frac{s}{c} \quad (2.31)$$

When the transmitting transducer is also used as a receiving transducer (pulse-echo method), the ToF has to be divided by two to calculate the thickness (Figure 2.19).

(a): Pulse-echo method



(b): Transmission method

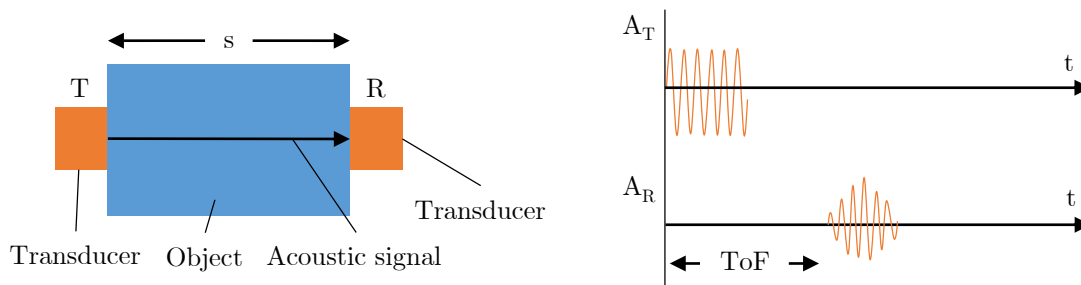


Figure 2.19: Schematic presentation of (a) pulse-echo method and (b) transmission method.

By using the pulse-echo method the acoustic signal travels twice through the object before it gets to the receiving transducer. Hence the ToF is twice as long in the pulse-echo method compared to the transmission method.

A simple way to determine the ToF is the threshold method. The ToF is identified when the signal exceeds a certain threshold [181,182,183]. Possible thresholds are 10% of the amplitude maximum or ten times the standard deviation of the noise in the beginning (Figure 2.20).

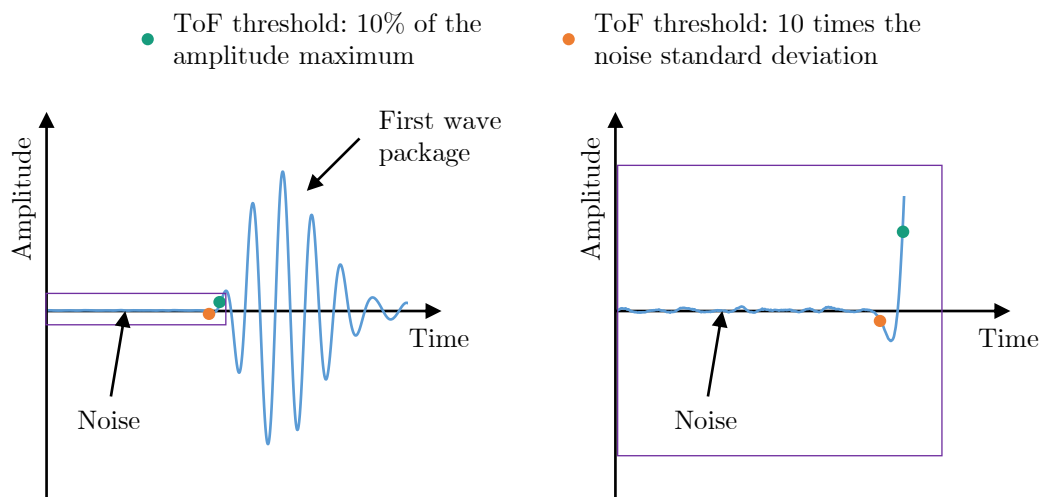


Figure 2.20: Schematic presentation of ToF determination. The green dot represents the ToF estimated by a threshold equal to 10% of amplitudes maximum and the orange dot is the ToF estimated by 10 times the standard deviation of the signal's noise before the arrival of the first wave package.

3 Materials and Methods: Dilation Cell

The materials and methods section focuses on the dilation cell set-up, as it is a self-built device which was further developed during this PhD thesis [152, 184]. Further data for the materials and methods (e.g. electrochemical tests, electrodes, electrolytes, etc.) can be found in the experimental section of the publications [152, 185, 186, 187].

Today only a few *operando* ECD are reported in literature. One system has a fixed glass frit to distinguish between the expansion of the working and counter electrode and to separate the mechanical influence of both electrodes [45, 141, 142]. Another dilatometry system was introduced by Sauerteig et al., which allows pressure adjustment in addition to the measurement of reversible and irreversible dilation, but without the possibility of three-electrode measurements [143, 144]. The dilatometry system used in this PhD thesis has been developed along the lines of that reported by Sauerteig et al. [143], but with the addition of a reference electrode. With the reference electrode, it is possible to distinguish between the half-cell potentials of the anode and the cathode. Furthermore, it is possible to examine the impact of a homogeneous and inhomogeneous pressure distribution onto the electrode stack.

The *operando* dilation cell is shown in Figure 3.1. The main components of the cell are the displacement sensor, the movable piston, the cell housing and the load cell. The contactless capacitive CSH05 displacement sensor with the capaNCDT 6110 amplifier (both Micro-Epsilon GmbH) is used to measure the dilation. The resolution is 1 mV, which corresponds to a dilation of 25 nm. The metallic parts of the movable piston, the screw, the cell housing and the plungers are made of 1.4404 stainless steel to avoid corrosion due to contact with electrolyte. A polyether ether ketone (PEEK) spacer is used for electrical insulation between the two electrodes through the metallic cell body. The force which can be applied on the electrodes is adjusted with a screw and a spring. The screw has a metallic housing with a hollow polytetrafluoroethylene (PTFE) cylinder inside. PTFE is used to avoid stick/slip effects of the piston in the inside of the screw. The spring (22950, SODEMANN Industrifjedre A/S) is used to have more or less constant pressure conditions and to allow the expansion of the electrodes during cycling. The movable piston, which is directly connected with the upper plunger, presses against the electrode stack. The electrode stack is located in an EL-Pat insulation sleeve (EL-Cell GmbH) with an integrated ring-shaped lithium metal reference electrode and a desired separator. The separator can be selected as required which makes the system very flexible. The applied force onto the electrode stack is measured with a KM38-2 kN load cell with an analog GSV-1A signal amplifier (both ME-Systeme GmbH). The applied pressure onto the cell stack can be regarded as more or less constant as the length of the spring is clearly increased compared to the thickness change of the electrodes.

Still, a small pressure change occurs during cycling since the spring constant (30.96 N mm^{-1}) is not infinitely small. The choice of a harder spring is a trade-off between an exact dilation determination and to be able to apply different forces onto the electrode stack without the need of changing the spring. The impact of gassing to the thickness change is negligible in this system as it is an open system and the area of the electrodes is small. However, the open system leads also to the evaporation of the electrolyte and to air infiltration from the outside, which causes fast degradation. Therefore, a PP foil was implemented around the upper plunger to reduce the electrolyte evaporation and the whole dilation cell was integrated into a glovebox to minimize the impact of the ambient atmosphere.

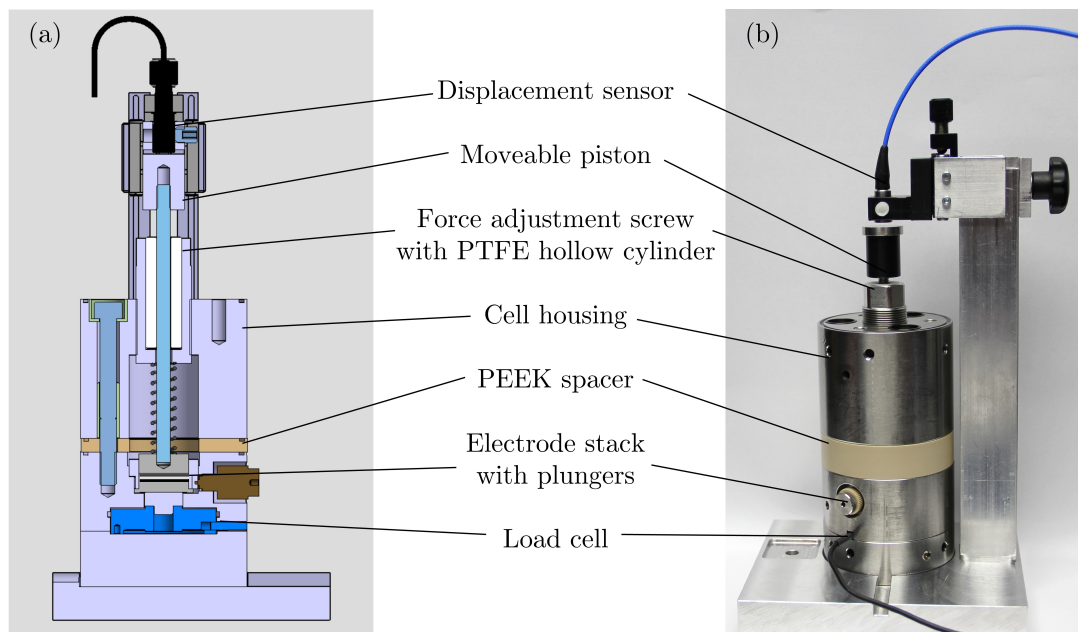


Figure 3.1: (a) Schematic cross section and (b) photograph of the *operando* dilation cell.

Another advantage of this dilatometry system compared to other systems is the choice of the structure of the upper plunger. With the choice of the flat plunger (Figure 3.2 (a)) a homogeneous pressure distribution on the electrode stack is possible. When choosing the plunger with a step ($10 \mu\text{m}$) an inhomogeneous pressure distribution can be imitated. This situation can occur, for instance, when the current collector tab in a round cell presses against an electrode [137].

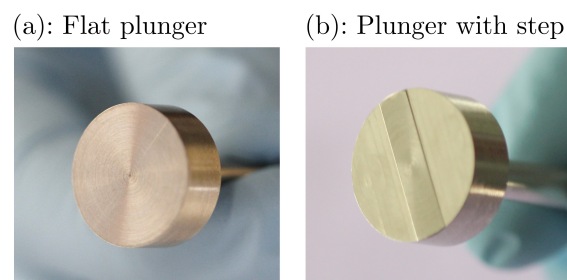


Figure 3.2: Different upper plunger: (a) Flat plunger and (b) Plunger with step

4 Results and Discussion

The following section summarizes excerpts from peer-reviewed published research articles written during the PhD thesis:

1. P. Daubinger, F. Ebert, S. Hartmann, and G. A. Giffin, 'Impact of electrochemical and mechanical interactions on lithium-ion battery performance investigated by *operando* dilatometry', *Journal of Power Sources*, vol. 488, p. 229457, 2021. Text and figures are reprinted (partially adapted) with permission from *Elsevier B.V.* according to reference [152].
2. P. Daubinger, M. Schelter, R. Petersohn, F. Nagler, S. Hartmann, M. Herrmann, and G. A. Giffin, 'Impact of Bracing on Large Format Prismatic Lithium-Ion Battery Cells during Aging', *Advanced Energy Materials*, vol. 44, p. 2102448, 2021. Text and figures are reprinted (partially adapted) with permission from *Wiley-VCH GmbH* according to reference [185].
3. S. Feiler*, P. Daubinger*, L. Gold, S. Hartmann, and G. A. Giffin, 'Interplay between Elastic and Electrochemical Properties during Active Material Transitions and Aging of a Lithium-Ion Battery', *Batteries & Supercaps*, vol. 6, no. 4, 2023. Text and figures are reprinted (partially adapted) with permission from *Wiley-VCH GmbH* according to reference [186]. *S.F. and P.D. contributed equally to this work.
4. P. Daubinger, M. Göttliger, S. Hartmann, and G. A. Giffin, 'Consequences of Different Pressures and Electrolytes on the Irreversible Expansion of Lithium Metal Half Cells', *Batteries & Supercaps*, vol. 6, no. 2, 2023. Text and figures are reprinted (partially adapted) with permission from *Wiley-VCH GmbH* according to reference [187].

For a more detailed version of the articles, the reader is referred to the articles in the appendix or online [152, 185, 186, 187].

The PhD thesis about the electrochemical and mechanical interplay in LIB cells is divided into two main sections: (1) state-of-the-art (SoA) and (2) next-generation battery materials. The SoA part can be further broken down to laboratory scale cells or electrodes and commercial cells. For investigating the expansion behavior of different active materials and electrodes made thereof, a dilation cell is developed first. These investigations are the base for understanding the pressure-dependent aging effects of large commercial automotive cells. Irreversible and reversible volume expansion are not the only mechanical changes within the cells, but also changes in the Young's modulus. Therefore, ultrasonic measurements are used

to examine the mechanical behavior in LIB cells. The results for the next-generation battery materials are examined at laboratory scale cell level. Here, the expansion of lithium and silicon is compared to SoA anode electrodes. Additionally, the impact of pressure and electrolyte on the performance and irreversible expansion of lithium is investigated.

4.1 Electrochemical and Mechanical Interplay in State-of-the-Art Battery Materials

This section about the electro-mechanical interplay is, as already above mentioned, divided into electrode level (section 4.1.1) and cell level (section 4.1.2). In the beginning, an in-house designed *operando* dilation cell is used to study the electro-mechanical impact on electrodes [152,187]. Afterwards, the pressure dependent effects on large format commercial cells is studied [185,186].

4.1.1 Electrode Level

The increasing demand for higher energy densities in LIBs leads to an enhanced utilization of the space within the confinements of the cell housing. This leads to increased mechanical strain inside the cell, which needs to be fully understood to maximize the battery cycle life. Thus, the correlating effects of externally-induced mechanical pressure and dilation of the electrodes on the performance of LIB were investigated using an in-house developed *operando* three-electrode dilation cell. The concept of the dilation cell is based on the system of Sauerteig et al. [143], but with the addition of a reference electrode to differentiate between the positive and negative half-cell potentials [152,184].

Expansion of Different Electrode Materials

Figure 4.1 shows the principle of operation of the dilation cell with graphite vs. NCM111 electrodes during formation, where the cell potential and the anode potential vs. Li/Li^+ are plotted as a function of time. The three intercalation plateaus for lithium in graphite are clearly observable in the anode potential plot and are consistent with the data previously reported in the literature [150,188]. In the initial cycle, a large irreversible dilation of $\sim 7.5\ \mu\text{m}$ ($\sim 8.5\%$ swelling with regard to the graphite electrode film thickness) is visible, which is probably related to the first rearrangement of the lithium-ions within the graphene layers, partial exfoliation and the formation of the initial, thin SEI [52,141,143,189,190]. In the following cycles, the gain of irreversible dilation is decreasing and the reversible dilation is dominant with an expansion of $7.5\ \mu\text{m} - 8.5\ \mu\text{m}$ ($\sim 8\% - 10\%$ swelling with regard to the graphite electrode film thickness) [152]. This is in good agreement with literature [45,46,143,191,192].

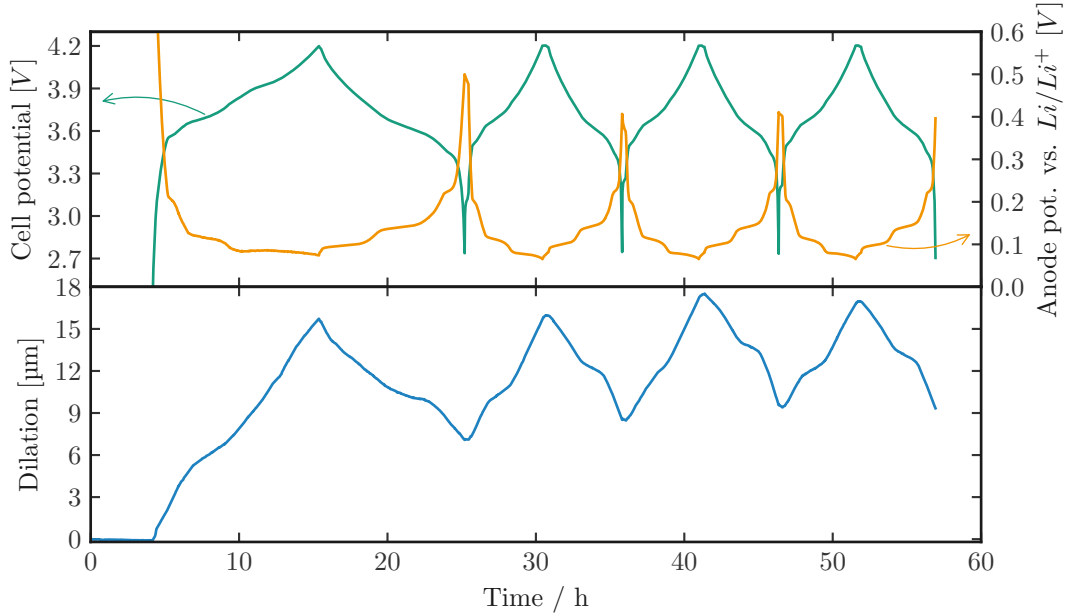


Figure 4.1: Formation of graphite vs. NCM111 with an initial 0.1 C cycle, followed by three 0.2 C cycles. Upper graph: Cell potential and anode potential as a function of time. Lower graph: dilation as a function of time. The figure was reprinted from reference [152].

When looking at the incremental capacity analysis (ICA) and incremental dilation analysis (IDA) as a function of the anode potential for one cycle (Figure 4.2), it can be seen that the peaks of the ICA correlate with the peaks of the IDA. This indicates that the voltage plateaus of the graphite correspond to dilation and hence the expansion can be mainly attributed to the graphite electrodes [152].

The assumption that the graphite is the main reason for the overall expansion in today's LIB was studied with further SoA electrodes (Figure 4.3). With the zero-strain electrode LTO it can be shown that NCM111 has only a negligible expansion of $\sim 0.1 \mu\text{m}$ ($\sim 0.1\%$ swelling with regard to the NCM111 electrode film thickness) during charging and discharging, while graphite shows a significant change of $\sim 3.3 \mu\text{m}$ ($\sim 4.7\%$ swelling with regard to the graphite electrode film thickness) during cycling. The expansion of the graphite is a lower compared to the theoretical value of $\sim 10\%$ as the capacity is not fully utilized ($\sim 78\%$) [25]. LFP has, in contrast to NCM111, a considerable dilation of $\sim 1.0 \mu\text{m}$ ($\sim 1.1\%$ swelling with regard to the LFP electrode film thickness) during cycling [187]. It should be noted that the expansion or contraction for nickel-rich NCM electrode material (e.g. NCM811 or NCA) is more significant compared to NCM111 [37, 186, 193, 194]. The H2 to H3 phase transition of the crystal structure occurs for the nickel-rich material at high voltages, which leads to a significant decline of the c lattice parameter in the rhombohedral crystal structure (see also section 2.1.4) [37, 88]. It can be concluded that for the most common cathode choices in

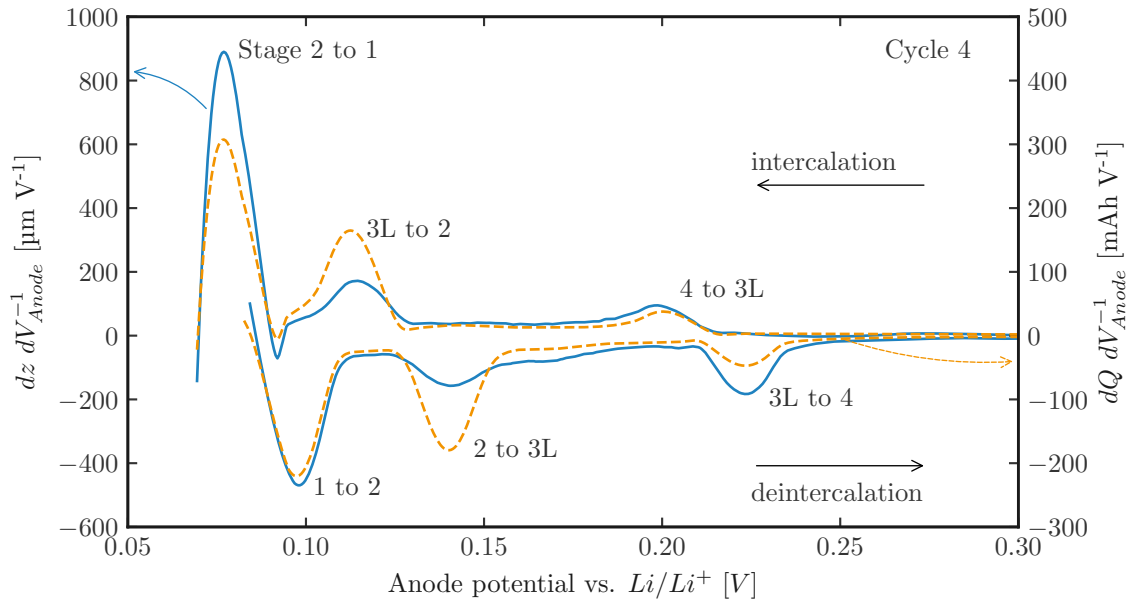


Figure 4.2: ICA and IDA as a function of anode potential in fourth formation cycle with a current of 0.2 C. The figure was reprinted from reference [152].

today's LIBs, the anode contributes most to the total expansion. When silicon is added to the graphite anode, the expansion is even more dominant [194].

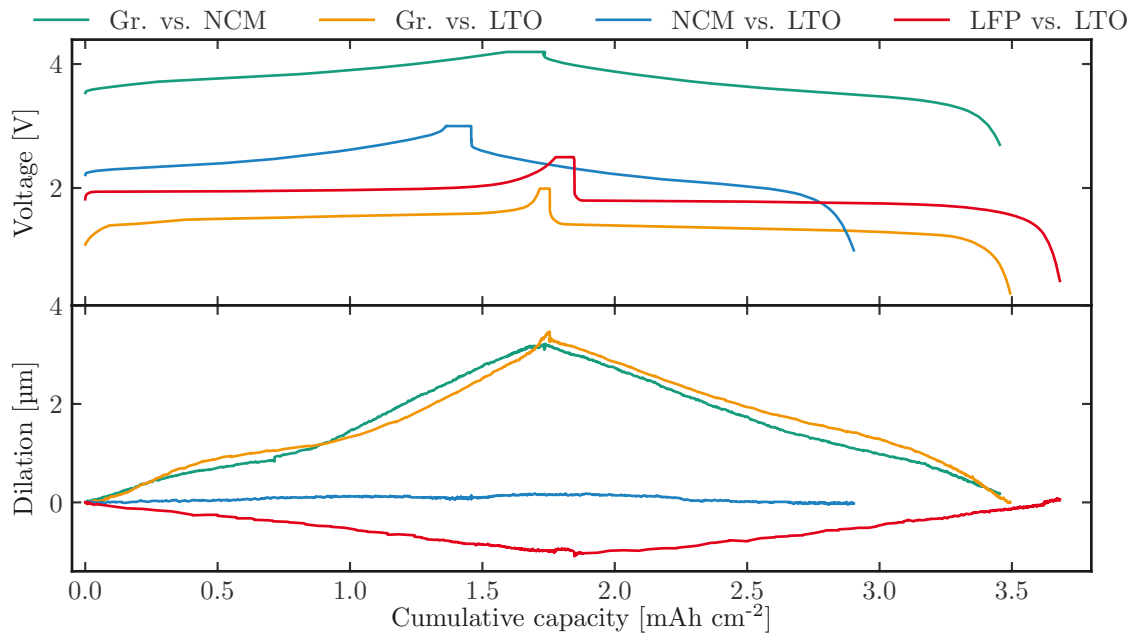


Figure 4.3: Dilation behavior of graphite vs. NCM111, graphite vs. LTO, NCM111 vs. LTO and LFP vs. LTO during cycling. The figure was reprinted from reference [152].

Impact of Mechanical Stress on Battery Performance

After investigating the expansion of different electrodes, the effect of pressure and its distribution on the performance of the electrodes is studied. The reversible volume expansion during cycling results in mechanical stress onto the electrodes due to the limitation of the rigid battery housing. The stress is even more enhanced when the electrodes are exposed to irreversible dilation or inhomogeneous pressure distribution (e.g. due to current collector [137]). Hence, the effect of pressure onto the electrodes during cycling and its impact on the performance is studied with the dilation cell. This is possible as the dilation cell has different upper plungers (Figure 3.2) to imitate different pressure distributions onto the electrodes. In this work, a flat plunger is used for homogeneous pressure distribution and a plunger with a 10 μm step for the inhomogeneous pressure distribution.

Figure 4.4 shows the influence of different mechanical forces on the lithium-ion cell performance during a rate capability test. The cells with the homogeneous pressure distribution (Figure 4.4 (a)) do not show any capacity fading regardless of the applied pressure and charging current and show a discharging capacity of $\sim 3.5 \text{ mAh cm}^{-2}$. When looking at the cells with the inhomogeneous pressure distribution (Figure 4.4 (b)), a significant lower discharging capacity with $\sim 3.2 \text{ mAh cm}^{-2}$ is seen and a severe capacity reduction (1.1 mAh cm^{-2} at the final charging rate of 0.2 C) is visible for the cells with the highest applied force.

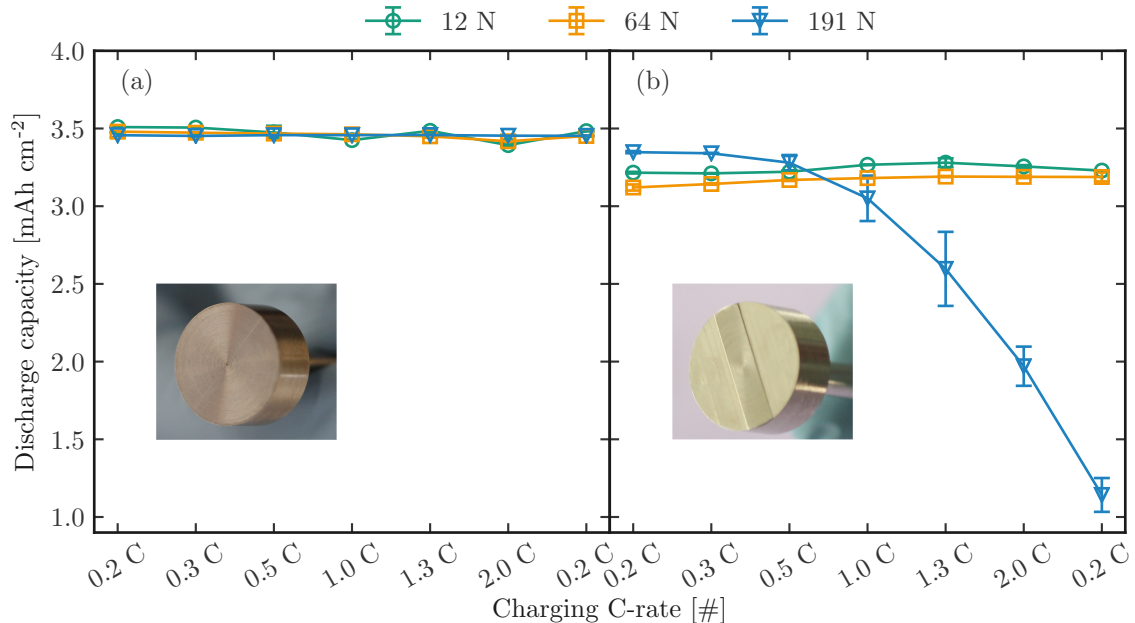


Figure 4.4: Charge rate capability test. Discharge capacity plotted as a function of the charge rate for (a) the homogeneous pressure distribution (flat plunger) and (b) inhomogeneous pressure distribution (plunger with a step). The figure was reprinted from reference [152].

When having a closer look at the electrochemical potential of graphite during constant current constant voltage (CCCV) charging (Figure 4.5), the impact of pressure and its distribution can be seen. For the cells with homogeneous pressure distribution, a pressure dependency is observed, with the graphite potential being more negative the higher the pressure due to increasing polarization. This is even more pronounced for increased currents. Regardless of the lithium plating (especially at high currents and pressures), the cells do not show any capacity fading (Figure 4.4). This indicates that the amount of lithium plating is relatively small with no significant impact on the performance during this C-rate test. If the cells would be cycled for a longer time at high currents, it can be assumed that the effect of lithium plating would make a difference in terms of performance. When looking at the graphite potential of the cells with the inhomogeneous pressure distribution, the effects of lithium plating are significantly more pronounced compared to the cells with the homogeneous distribution. Even for the lowest force and the low current, the graphite potential drops below 0 V vs. Li/Li^+ and hence lithium plating occurs. These effects are even more pronounced for higher applied forces and currents [152].

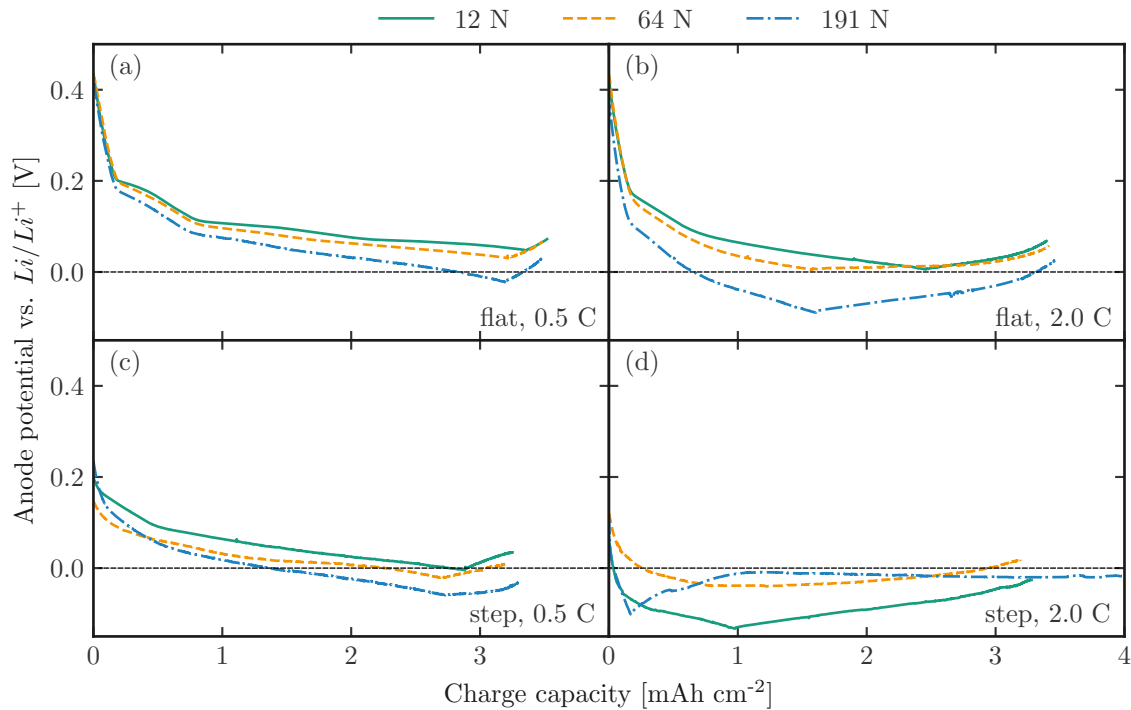


Figure 4.5: Anode potential over charging capacity of homogeneous pressure distribution (a) + (b) and inhomogeneous pressure distribution (c) + (d) for CCCV charging rates of 0.5 C and 2 C respectively. The figure was reprinted from reference [152].

Overall, for SoA electrodes the dilation is mostly related to the anode. The reversible and irreversible expansion during cycling results in mechanical stress on the battery electrodes. The mechanical stress in terms of pressure and pressure distribution negatively affects the

capacity and leads to larger overpotentials inside the cell. With high pressures or inhomogeneous pressure distribution, the overpotential in the cells is increased. The high overpotentials cause lithium plating, which leads to capacity degradation.

4.1.2 Cell level

After gaining knowledge about the effects of pressure and (in)homogeneous pressure distribution in a laboratory scale dilation cell, the effect of pressure on large format LIB cells is studied in this section. Therefore, the impact of mechanical bracing on the lifetime of large format 94 Ah prismatic cells during an accelerated aging test is examined. Furthermore, a new concept, the 'mechanical state of health' (mechanical SoH) is introduced and discussed. The mechanical SoH is a concept which is used to demonstrate the impact of mechanical forces on the performance of the cell or electrodes [185]. Furthermore, to obtain a deeper knowledge on the mechanical characteristics and changes inside a battery, 12 Ah LIB pouch cells are examined more precisely with ultrasonic transducer in a further study. The changes of mechanical characteristics (e.g. Young's modulus or thickness change) in the battery cell are studied and correlated with the SoC and SoH [186].

Accelerated Aging Test of the Prismatic Automotive Cells

To examine the impact of pressure or bracing on large format 94 Ah LIB cells, two cells were cycled with bracing and two cells without bracing for more than 7000 cycles. The external bracing was applied with two form-fitted metal plates at the front and back of the battery cell. The bracing was a fixed bracing, where the expansion of the cells was limited. Figure 4.6 shows the discharge capacity during the aging test, where all cells show similar capacity reduction in the initial 3000 cycles. Afterwards, the unbraced cells have an accelerated capacity fading compared to the braced cells, reaching the 80% SoH threshold 900 cycles earlier. The unbraced cells also see a thickness change of 22% (~ 10 mm) at end of life (EOL), whereas the braced cells show only a small thickness increase of around 2.5% (~ 1.1 mm) after 7000 cycles. This indicates that the unbraced cells experience more severe degradation mechanisms inside the cell compared to the braced cells especially in the region of 80% SoH. Another indication is the capacity recovery of $\sim 12\%$ after a 5 week cycling break after more than 7000 cycles for the braced cells. The unbraced cells do not show any capacity recovery after this break, indicating irreversible capacity loss [185].

Post-Mortem Analysis of Three Different Aged Cells

For a deeper understanding of the different degradation mechanisms within the cells and to examine the cause of the capacity fading and thickness increase, post-mortem investigations were conducted on three different cells. The first cell (Cell 1) is the reference cell that has

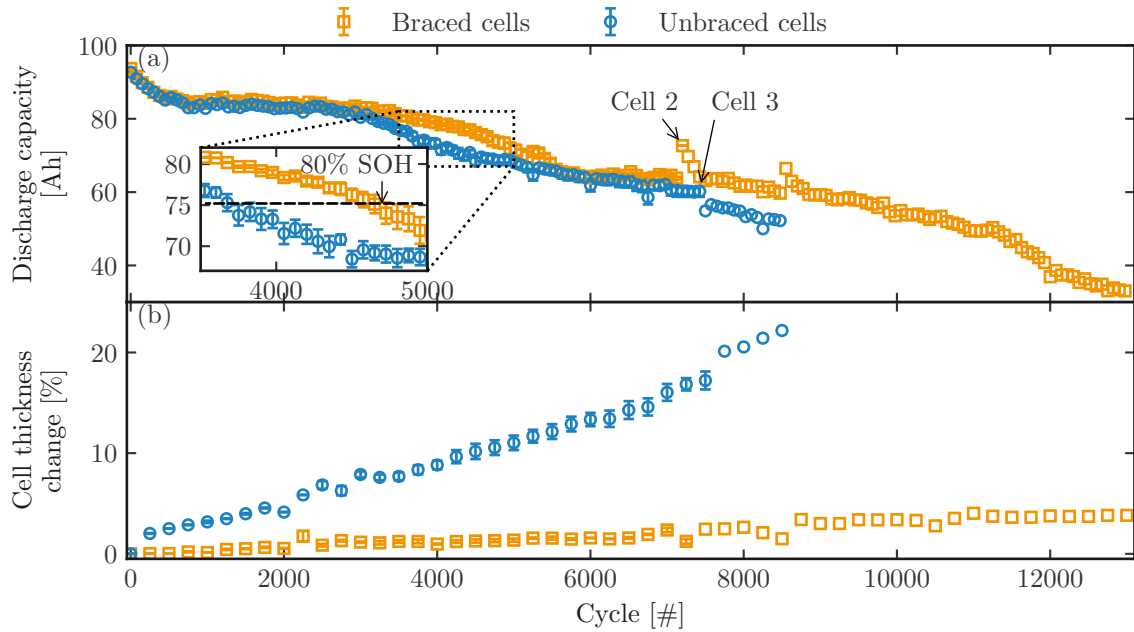


Figure 4.6: a) Cycling of prismatic cells under different external bracing conditions. The capacity is only plotted every 75th cycle for better visibility. b) Thickness change measured every 250 cycles. The figure was reprinted from reference [185].

not been cycled (only formation cycles), the second cell is a braced cell after 7250 cycles (Cell 2) and the third cell is an unbraced cell after 7500 cycles (Cell 3).

The photographs of the electrodes and separator during cell opening reveal only slight degradation in terms of delamination or lithium plating for the aged braced cell in comparison with the unaged reference cell. The cell opening of the aged unbraced cell revealed a different picture. Here, severe degradation mechanisms are visible in terms of widespread lithium plating on the anode, ripples on the cathode and sticking junks of lithium metal on the separator. These results suggest that lithium plating on the anode plays a significant role in the capacity degradation and thickness increase of especially the unbraced cells. In contrast, the external bracing leads to a more homogeneous pressure distribution and hence also reduced contact losses between anode, separator and cathode. Lithium plating is pronounced only in areas with high pressure inhomogeneity, e.g. at the winding of the jelly roll [185]. This is in agreement with the investigations of the (in)homogeneous pressure distribution in the laboratory dilation cell [152].

The morphology of the electrodes is further studied in the following. Whereas the anode has no considerable changes in the morphology in terms of cracking, the aged cathodes show a significant increase in cracking compared to the unaged reference cathode (Figure 4.8). The amount of cracks is increasing from the unbraced cathode in the area without ripples (Figure 4.8 (c)) over the braced cathode (Figure 4.8 (b)) to the unbraced cathode in the area with ripples (Figure 4.8 (d)). This indicates that not only the anode suffers from degradation due

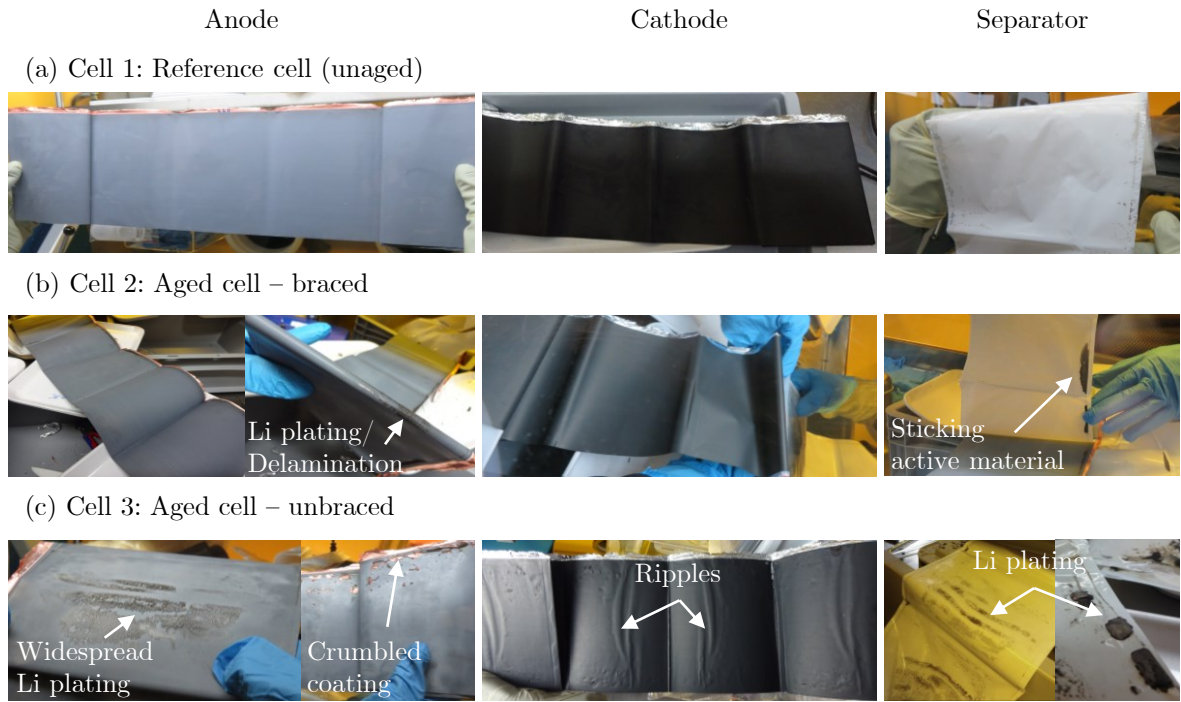


Figure 4.7: Photographs of electrodes and separators after cell opening. (a) Cell 1: Unaged reference cell, (b) Cell 2: Aged braced cell and (c) Cell 3: Aged unbraced cell. The figure was reprinted from reference [185].

to lithium plating, but also the cathode due to cracking. The cracking can lead to isolation of particles or the loss of percolation paths, which reduces the capacity [185].

To further examine the anode and cathode degradation inductively coupled plasma optical emission spectroscopy (ICP-OES) is performed on different anode samples (Figure 4.9). The lithium content in the aged cells ($\sim 1.4 \text{ mAh cm}^{-2}$ and $\sim 1.5 \text{ mAh cm}^{-2}$ respectively) is significantly higher as in the reference anode ($\sim 0.5 \text{ mAh cm}^{-2}$), which confirms the assumption of loss of lithium inventory due to lithium plating. Another significant degradation method is the SEI increase and hence also loss of lithium inventory. The transition metal dissolution in the cathode and the transport to the anode leads to a thickening of the SEI. This SEI thickening can also be seen in the increase of the transition metal content in the anode. For example, the nickel content is increasing from $\sim 2.6 \text{ nmol cm}^{-2}$ in the reference cell to $\sim 17.3 \text{ nmol cm}^{-2}$ in the aged braced cell and $\sim 23.9 \text{ nmol cm}^{-2}$ in the aged unbraced cell respectively. The unbraced samples show in total a higher lithium and transition metal content compared to the braced cell, which further confirms the positive impact of bracing on the aging of the 94 Ah LIB cells [185].

To get a deeper look into the cathode degradation, XRD with Rietveld refinement were performed for the different cathode samples (Figure 4.10 and Table 4.1). For all tested cathode samples, no considerable phase changes can be seen in the diffractograms. The obtained

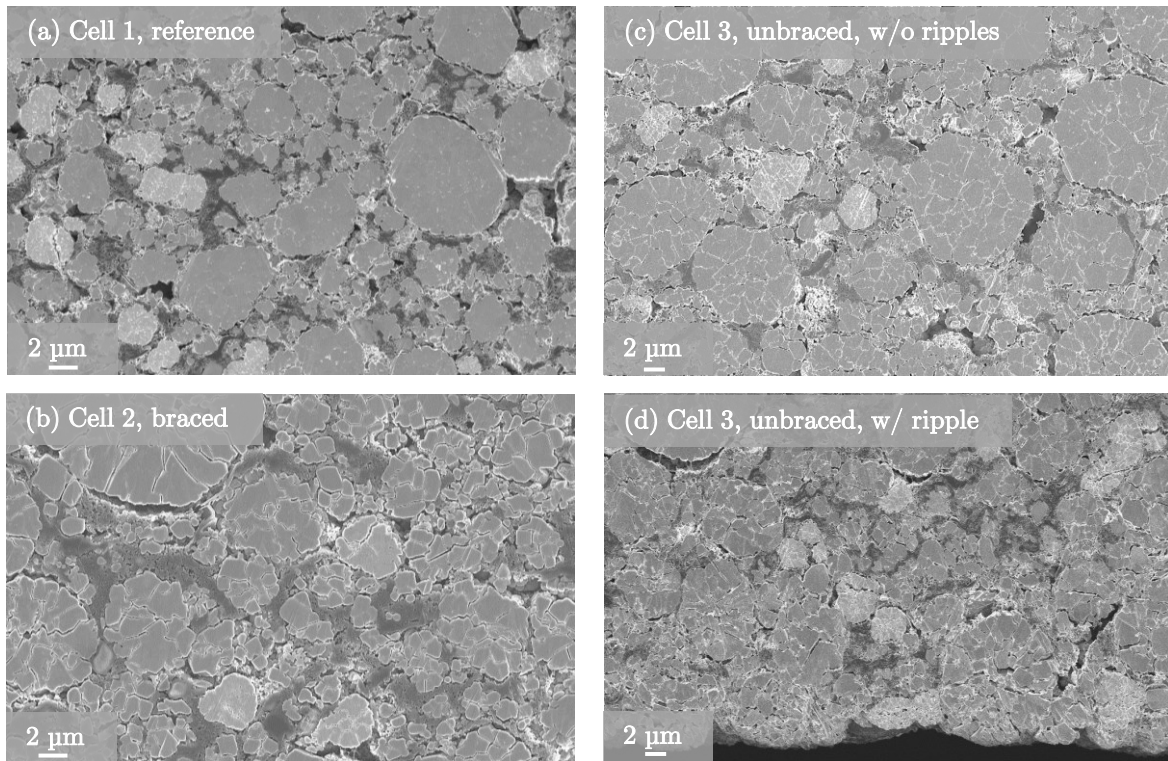


Figure 4.8: SEM cross sections of the differently aged cathodes. a) Cell 1, reference, b) Cell 2, braced, c) Cell 3, unbraced, w/o ripples, d) Cell 3, unbraced, w/ ripples. The figure was reprinted from reference [185].

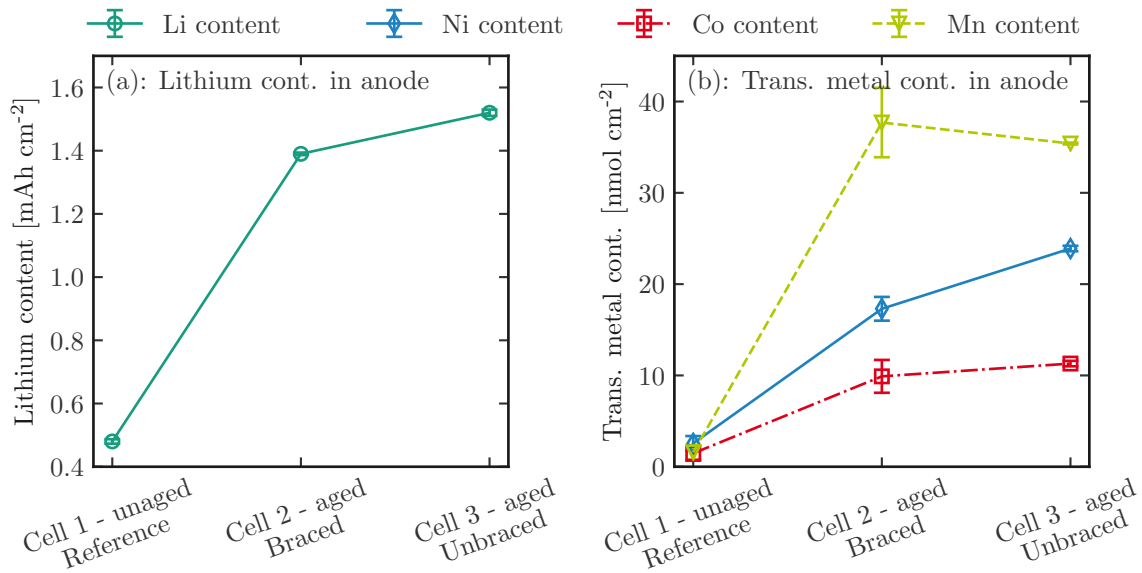


Figure 4.9: (a) Lithium and (b) transition metal content in anode for reference and aged cells. The lines are a guide for the eye only. The figure was reprinted from reference [185].

lattice parameter, e.g. crystallite size, from the Rietveld refinement indicate an enhanced degradation of the cathodes which have been exposed to higher pressures. The cathode with

Table 4.1: Lattice parameters for cathodes obtained from the Rietveld analysis. The table was reprinted from reference [185].

Cell	c [Å]	$R:(I(006)+I(102))$ $/I(101)$	Crystallite size [Å]	Lattice strain [%]
Cell 1: unaged, reference	14.250	0.74	1357	0.08
Cell 2: aged, braced	14.308	0.92	388	0.11
Cell 3: aged, unbraced, w/o ripples	14.304	0.73	994	0.06
Cell 3: aged, unbraced, w/ ripples	14.327	0.88	387	0.1

external bracing and the unbraced cathode in the area with ripples (counterfacing widespread lithium plating) have the highest lattice parameter c , highest intensity ratio R (indication for increased cation mixing), lowest crystallite size and highest lattice strain (Table 4.1). This proves that high pressure results in a structural degradation in terms of cracking (crystallite size) and cation mixing (intensity ratio R). The unbraced cathode without ripples shows minor aging effects compared to the cathodes exposed to high pressure [185].

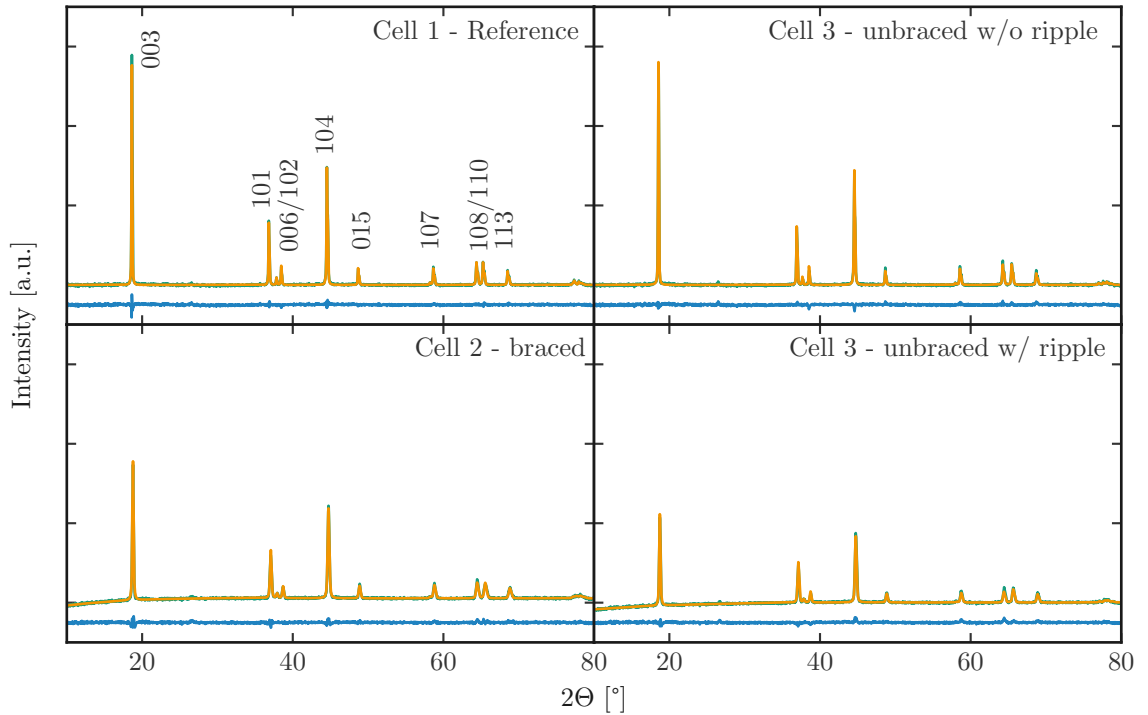


Figure 4.10: Observed (green), calculated (orange), and difference (blue) XRD patterns of the differently aged cathode materials. The figure was reprinted from reference [185].

To confirm the physicochemical characterizations, electrochemical testing of harvested electrodes from the prismatic LIB was done in laboratory cells. The results (Figure 4.11) show that the capacity reduction is primarily attributed to the loss of lithium inventory. The degradation of the electrodes itself plays a minor role. The loss of lithium inventory is caused by lithium plating on the anode and the thickening of the SEI. Nevertheless, the anode itself suffers only little from capacity reduction, e.g. at 1.1 C current rate. The anode samples from the reference cell show only a slightly higher capacity of $\sim 2.7 \text{ mAh cm}^{-2}$ compared to the aged electrodes with $\sim 2.6 \text{ mAh cm}^{-2}$ for the braced samples and $\sim 2.4 \text{ mAh cm}^{-2}$ for the unbraced samples. The electrochemical performance of the cathode proves that high pressure or structural degradation also leads to reduced capacities or increased aging effects. Here, the cathode samples in the area without ripples from the unbraced cells ($\sim 2.3 \text{ mAh cm}^{-2}$ at 1.1 C) show a better performance compared to the braced samples ($\sim 2.2 \text{ mAh cm}^{-2}$ at 1.1 C). However, the effect of cathode degradation, as compared to the loss of lithium inventory, has a minor impact on the overall cell degradation. It can be concluded that external bracing is beneficial for the electrochemical performance of large format prismatic LIB. The bracing results in decreased anode degradation even if the cathode suffers more from the high pressure. The external bracing leads to mostly homogeneous pressure distribution and hence also less severe lithium plating compared to the unbraced cells. Here, the inhomogeneous pressure distribution leads to a variety of different degradation mechanisms like lithium plating, ripples or crumbled coatings [185].

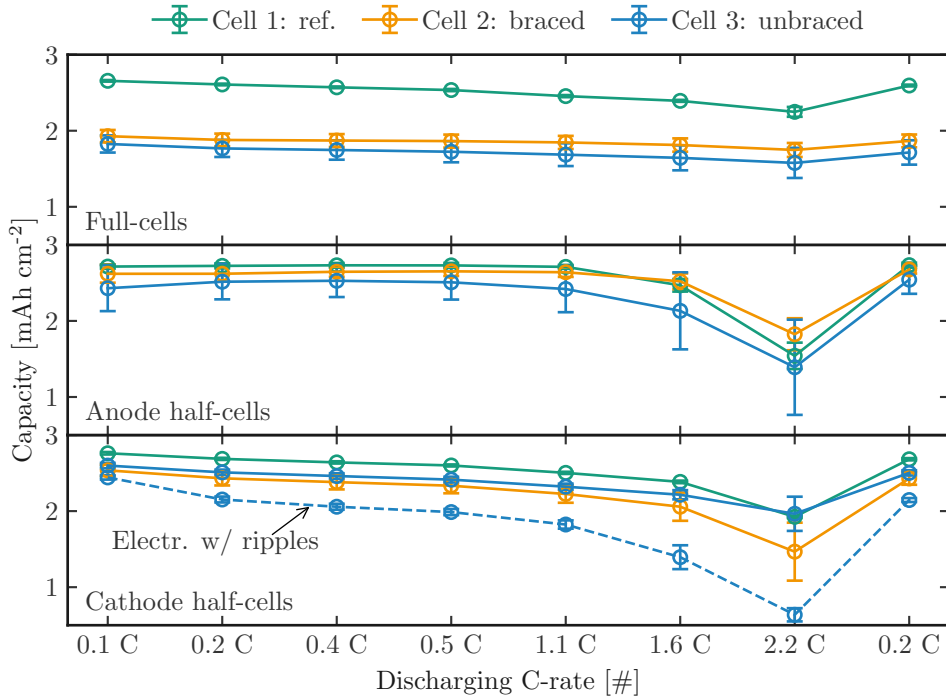


Figure 4.11: C-rate-capability test of laboratory electrodes harvested from the prismatic cells. The C-rate relates to the reference cell. The figure was reprinted from reference [185].

Mechanical State of Health

In addition to the aging study, a new concept of the mechanical SoH will be introduced in the following section. It shall be used to correlate the capacity reduction with the mechanical degradation of, for example, the electrode particles or other cell components. Even if these aspects also play a role in the more general term 'state-of-health', the concept of mechanical SoH is intended to focus more on the mechanical characteristics of the materials and cell components and their influence on the capacity reduction. The mechanical effects on the lifetime of a LIB are rather unexplored compared to temperature and current. However, the impact of the mechanics on the lifetime of batteries play a vital role, particularly as the volumetric energy density (related to the space for the battery) is continually increased. The mechanical SoH results from the processes inside the battery cell/electrodes, e.g. particle cracking or volumetric expansion/contraction, etc. Thus electrodes with a good mechanical SoH should have low structural and irreversible volume changes and also a low capacity reduction. In contrast, electrodes with a poor mechanical SoH have large structural changes, e.g., particle cracking, high irreversible volumetric growth, together with a significant capacity fading. In this sense, changes in mechanical SoH are not directly triggered by external effects like applied pressure, etc., but they are certainly affected by them [185].

In this work, it could be shown that the mechanical SoH can be used as an indication for the degradation of the electrode material. In particular, the cathode suffers from a low mechanical SoH due to large structural changes in combination with the capacity fading. For the anode, the change in mechanical SoH is less significant compared to the cathode. Nevertheless, the irreversible thickness increase of the anode leads to a decrease of the mechanical SoH. However, further studies need to be conducted for a deeper understanding of the correlation between mechanical characteristics and capacity reduction of the electrodes [185].

Ultrasound as a Possible Method for Detecting Mechanical Changes

With the results obtained from the aging study in commercial batteries, another method is needed to get more insights into the mechanics of the battery. One possible method to examine the mechanical changes *operando* during cycling is the use of ultrasound [170, 195]. 12 Ah LIB pouch cells are cycled and *operando* ultrasonic in combination with dilation measurements are performed (Figure 4.12). During charging of the cell, the cell is thickening ~ 0.13 mm, which corresponds to 2.0% of the total cell thickness (~ 6.5 mm), as the graphite anode is expanding [152]. Although the cell is getting thicker and the signal needs to take a longer pathway, the time-of-flight (ToF) is decreasing $\sim 2.5\%$ during charging (Figure 4.12 (c)). This is related to an increase of the sound velocity inside the battery cell, which is caused by an increase of the effective elastic modulus ($\sim 9\%$) during charging (Figure 4.12 (d) + (e)).

The change in the elastic modulus is mostly related to the graphite stage transition 1L to 4 and the cathodic phase transition H2 to H3. Overall, the change in mechanical parameters inside a LIB cells can be detected by the ultrasonic transducer [186].

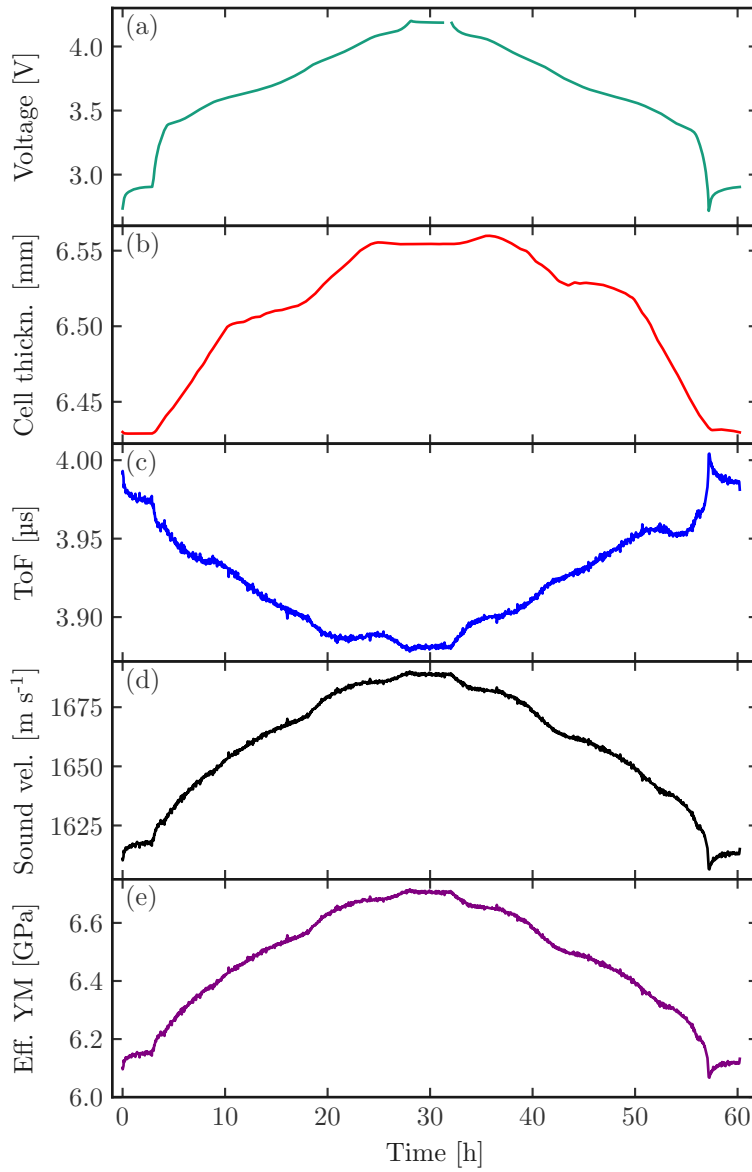


Figure 4.12: 0.04 C cycling of a 12 Ah LIB pouch cell. (a) shows the voltage, (b) the cell thickness, (c) the ToF, (d) the SoS and (e) the effective Young's modulus as a function of time. The figure was reprinted from reference [186].

Mechanical Changes During Aging

After evaluating the mechanical changes during one cycle, the pouch cells are cycled and studied for 1000 cycles. Figure 4.13 shows the differential analysis of the capacity, dilation and ToF during the reference performance test (RPT) cycles. Four peaks are observed in all graphs where the first peak (I, Figure 4.13) can mainly be attributed to the transition

of graphite stages 1L to 4. The next two peaks are a superposition of the cathodic phase transition H1 to M plus the graphite stage transition 3 to 2 (II) and the M to H2 plus the 2 to 1 (III), respectively. The last peak (IV) can be ascribed exclusively to the cathodic H2 to H3 phase transition [88]. Figure 4.13 (a) shows that most of the capacity reduction is related to the loss of lithium inventory, which is in agreement with the previous study in the prismatic cells [185]. The loss of lithium inventory can be seen as the incremental capacity peaks are shifting to higher voltages and decrease in magnitude. The reversible dilation of the cell is also declining, mostly during the graphitic stage transitions 1L to 3, i.e. ~ 3.4 V - 3.5 V (Figure 4.13 (b)). This is assumed to be related to cracking of the cathode and/or SEI formation on the anode, resulting in higher porosity of the electrodes where the reversible expansion can grow into. Figure 4.13 (c) shows that the differential change in ToF during the RPT is mostly related to the graphite stage transitions 1L to 4 (I), at the beginning of 2 to 1 (III) and the H2 to H3 phase transition of the NCM cathode (IV). At those transitions or peaks in the differential ToF, the mechanical changes inside the electrodes, due to changes in the lattice structure and/or stage or phase transitions, are dominant. The second peak (II) mainly stems from a voltage plateau that mathematically leads to a larger absolute $d\text{ToF} dV^{-1}$, rather than a significant change in ToF. The graphitic peaks (I and III) are caused by a stiffening of the electrode and not by a decrease in thickness as the graphite anode is expanding in those voltage areas. The fourth peak, which can be attributed to the NCM cathode, is caused in part by the thickness decrease (Figure 4.13 (b)), but most part of the ToF change is related to the stiffening of the cell. During aging the differential change in the ToF is declining, which is mostly caused by the graphite anode. Here, the transitions 1L to 4 and 2 to 1 shift to higher voltages due to the loss of lithium inventory and the magnitude of the peaks is decreasing. The last peak at ~ 4.1 V is attributed to the cathodic H2 to H3 phase transition and it is not affected by any ToF change during aging [186].

The decrease of the differential ToF magnitude during the RPT over aging is accompanied by an increase of the overall ToF (Figure 4.14). The ToF is increasing from ~ 4.0 μs at the initial cycle at SoC 0% to ~ 4.4 μs at cycle 1000, which is on the one hand related to the irreversible thickness change of $\sim 4\%$ (~ 0.25 mm) in the cell during aging and on the other hand due to the softening of the cell. The irreversible thickness change accounts for $\sim 33\%$, assuming a constant sound velocity, of the increase of the ToF during aging. Hence, the rest of the ToF increase is related to the reduction of the overall cell stiffness (Figure 4.14 (b)). The effective modulus of the cell is declining $\sim 11\%$ - 12% , which can mostly be related to the thickening and more porous SEI. The thicker and more porous SEI layer lead to a decreased sound velocity as larger pores deform easier under stress [196, 197]. Thus, the SEI is getting softer and the sound velocity is decreasing [186].

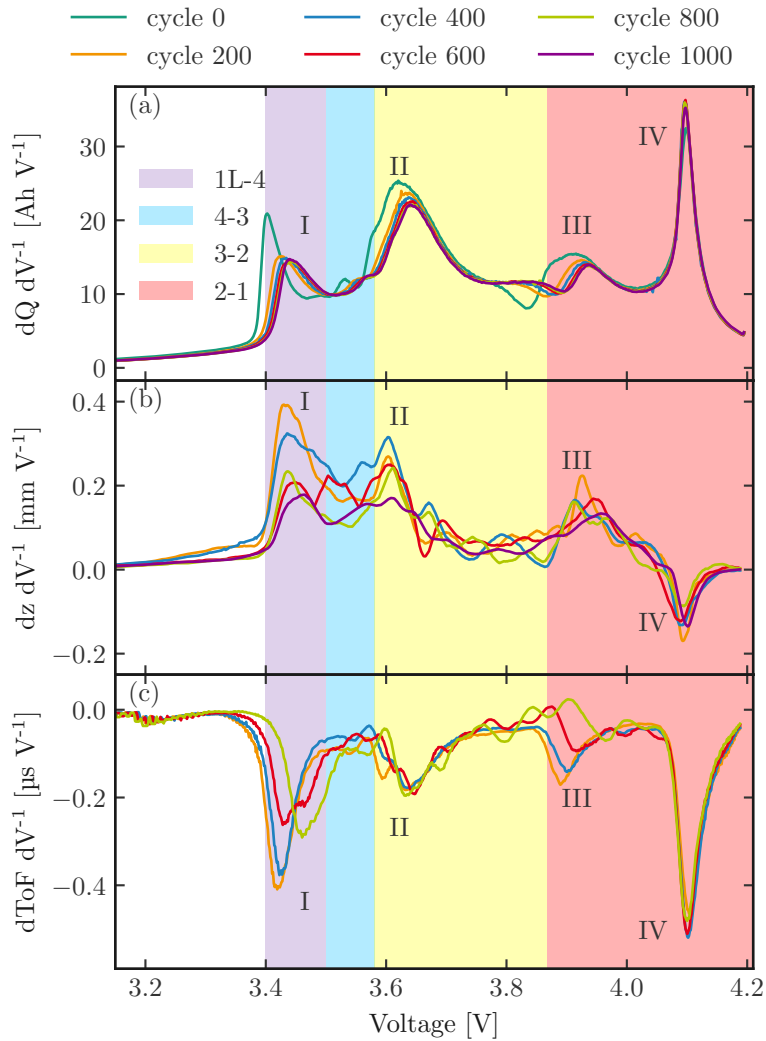


Figure 4.13: Differential analysis of a) capacity, b) dilation and c) ToF for 0.04 C cycles during RPT over cell voltage. The overlay shows the staging of the graphite anode estimated from harvested three electrode cells. The figure was reprinted from reference [186].

Overall, it is shown that with ultrasonic measurements mechanical characteristics of a LIB can be determined. During cycling, the effective Young's modulus is changing $\sim 9\%$, which is related, in large part, to the stage transitions of the lithium ions in the graphite and the H2 to H3 phase transition of the nickel-rich NCM cathode. During aging, the stiffness of the cell is decreasing $\sim 11\% - 12\%$, which can be explained by a thicker and more porous SEI on the anode. The cathode shows negligible stiffness changes during aging.

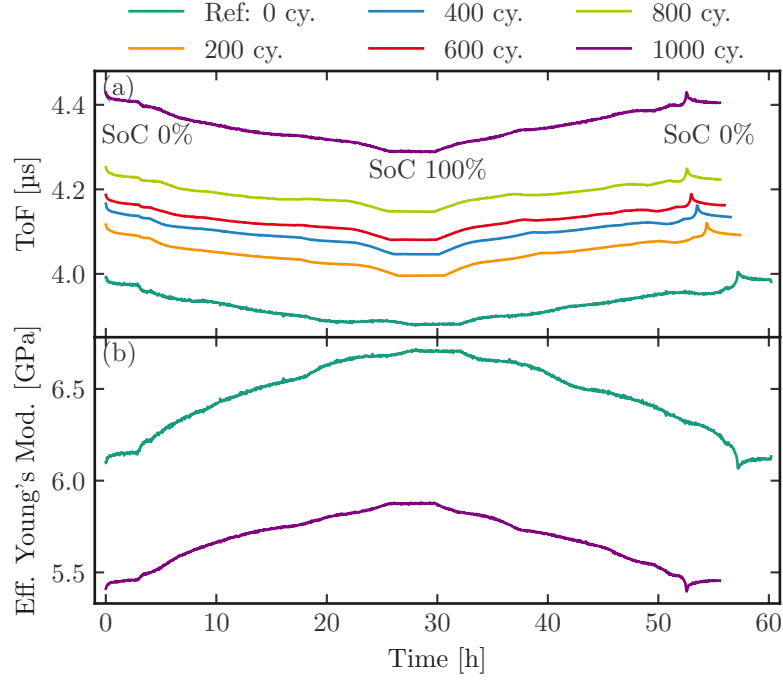


Figure 4.14: Evolution of ToF (a) and effective Young's modulus (b) as a function of time during RPTs. The figure was reprinted from reference [186].

4.2 Electrochemical and Mechanical Interplay in Next-Generation Battery Materials

After evaluating the electrochemical and mechanical interplay in SoA battery materials, the interplay is also examined using next-generation battery materials. In this work the expansion of lithium metal and silicon is compared to SoA electrode material. Afterwards, the (ir)reversible expansion of lithium metal during cycling is investigated for different electrolytes and different applied external pressures.

4.2.1 Electrode Level

Two possible ways to increase the energy density in LIB is to increase the share of the active material by either increasing the utilization of the active electrode area in the same battery housing or to use electrodes with a higher specific energy density. Both methods result in increasing stress on the electrodes, whereas the impact of stress on SoA electrodes was studied in section 4.1. In this section, the effect of using new anode materials on the dilation and performance is examined. Two promising anode materials are silicon and lithium metal as both have higher specific capacities compared to graphite [25, 31, 35].

Expansion of Lithium Metal and Silicon

Figure 4.15 and Table 4.2 show that silicon and lithium have tremendously increased expansion compared to graphite ($\sim 3.3 \mu\text{m}$ or $\sim 4.7\%$ respectively). Silicon has an electrode film thickness change of $\sim 50\%$, which is lower than the expected theoretical value of 280% [31,32]. This can be explained with the high electrode porosity of $\sim 75\%$ and also the limited utilization of the full capacity with only $\sim 72\%$. The expansion is even more distinct for the lithium metal with $\sim 7.9 \mu\text{m per mAh cm}^{-2}$ compared to $\sim 4.9 \mu\text{m per mAh cm}^{-2}$ of silicon and $\sim 2.0 \mu\text{m per mAh cm}^{-2}$ of graphite respectively. This expansion is significant larger than the theoretical expansion of the metal during plating with $4.9 \mu\text{m per mAh cm}^{-2}$ (calculated by using Faraday's law, assuming the deposition of a dense, homogeneous lithium layer) [34]. The further thickness increase is associated with the SEI and with the deposition of less dense, i.e. dendritic or mossy, lithium. During stripping the contraction is $\sim -5.4 \mu\text{m per mAh cm}^{-2}$, which also is larger than theoretically expected, thus implying stripping of mossy lithium. This enormous expansion indicates that for future LIBs the mechanics, such as external bracing, will play an even more important role than today. This can also be seen when looking at the irreversible dilation of the silicon or lithium electrode. While silicon has a small but still considerable irreversible dilation for one cycle, the irreversible dilation for lithium metal is very large with $\sim 2.5 \mu\text{m per mAh cm}^{-2}$ in one cycle. The irreversible dilation is determined from the difference between the two half cycles, and is related to the SEI growth and the formation of dead lithium [187].

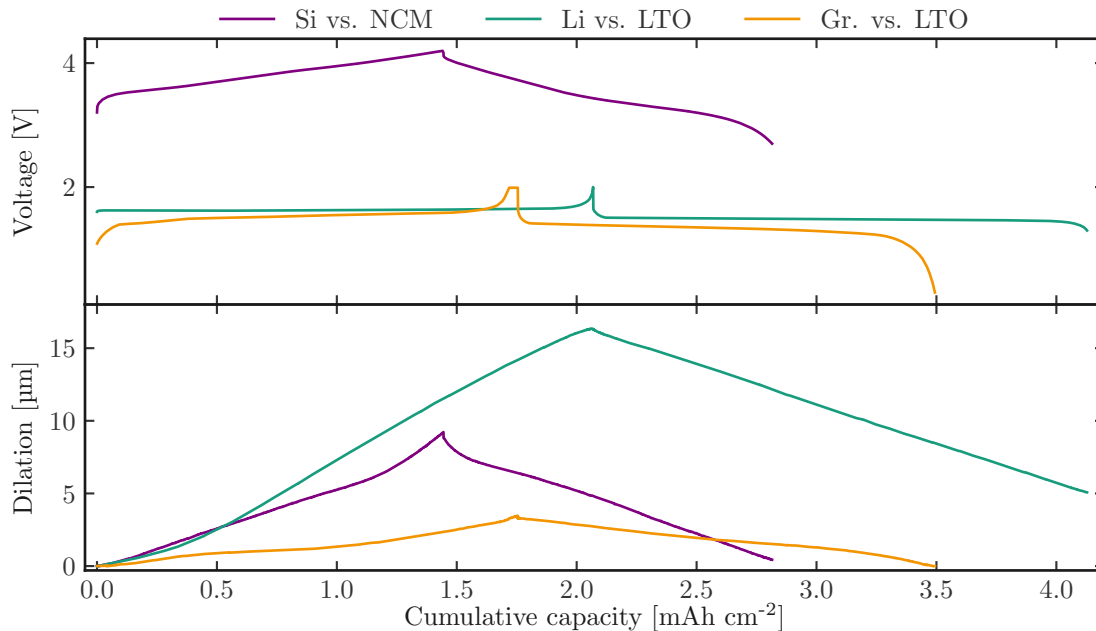


Figure 4.15: Dilation behavior of silicon vs. NCM111, lithium vs. LTO and graphite vs. LTO during cycling. Voltage and dilation as a function of cumulative capacity. The figure was reprinted from reference [187].

Table 4.2: Measured areal capacity, dilation and the dilation per areal related capacity of the investigated cells during lithiation of the negative electrode. The table was reprinted from reference [187].

Cell	Areal lithiation capacity [mAh cm ⁻²]	Lithiation dilation [μm]	Areal capacity related dilation [$\mu\text{m per mAh cm}^{-2}$]
Lithium vs. LTO	2.07	16.30	7.89
Silicon vs. NCM111	1.83	8.90	4.87
Graphite vs. LTO	1.75	3.44	1.96

Irreversible Expansion of Lithium Metal during Cycling

To get a closer examination of the irreversible dilation in lithium metal battery cells, a pressure and electrolyte dependent study is performed. Three different pressures (i.e., 0.05 MPa, 0.5 MPa and 1.0 MPa) and three different electrolytes (i.e., 1M LiPF₆ in EC/EMC 3/7 wt% (LP57), LP57 with 5wt% FEC and 1M LiFSI in dimethoxyethane (DME)) were chosen for this study. Figure 4.16 shows the dilation of the different cell configurations during testing. It should be noted that the total cell dilation of the lithium vs. LTO cells is initially decreasing as the LTO electrode is lithiated at the beginning of the formation. Hence, the lithium ions get stripped from the lithium metal electrode which reduces the thickness. The lithium vs. LFP show an initial increasing dilation as the LFP is delithiated and hence the lithium ions are plated on the lithium metal electrode. This increases the thickness of the cell. In Figure 4.16, it can be seen that the cells with the carbonate-based LP57 electrolyte show the highest irreversible dilation during the cycling experiments. This is expected as organic carbonates are not chemically stable versus lithium and do not form relatively stable SEI phases on the lithium [34, 198]. When adding FEC to the carbonate-based electrolyte (LP57), the performance is enhanced and the irreversible expansion is reduced (e.g. 8.2 μm compared to 33.2 μm at the end of the test at 0.5 MPa). The decomposition of the electrolyte, when FEC is present, is mostly related to FEC, as it decomposes earlier compared to EC or EMC [103, 199, 200]. This results in a thicker but more stable SEI, when FEC is present. When using the ether-based electrolyte (1M LiFSI in DME) almost no considerable irreversible expansion is seen at elevated pressures, which is also caused by a stable SEI. Furthermore, a pressure dependency is seen. The cells show the largest irreversible expansion at the lowest pressure with $> 47 \mu\text{m}$ for all electrolytes and only little expansion at the highest pressure with $\sim 18 \mu\text{m}$ for the cells with LP57 and $\sim 0 \mu\text{m}$ for the other cells. This indicates that one of the main degradation mechanisms of lithium (formation of mossy and dead lithium) is significantly reduced when applying an increased pressure. High pressure results in better electrical contact of the mossy and the bulk lithium. Overall this shows that the electrolyte and also the pressure are critical for the cycling of lithium metal cells [187]. For

the implementation of new anode materials into commercial batteries the reversible cycling is crucial and hence the irreversible expansion of the electrodes should be limited.

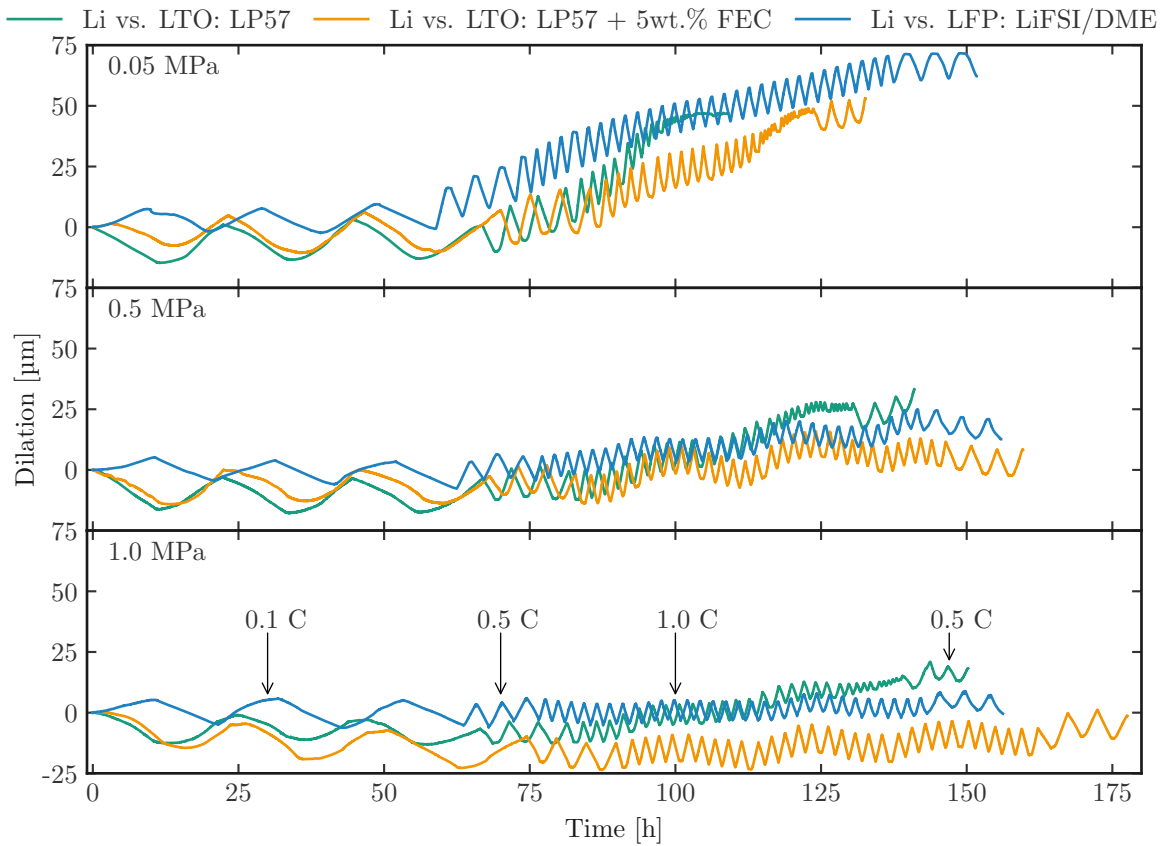


Figure 4.16: Pressure dependent dilation of lithium vs. LTO or LFP with three different electrolytes (LP57, LP57 with 5wt% FEC and 1M LiFSI in DME). The figure was reprinted from reference [187].

In addition to the experiments in the dilation cell, cycling tests are conducted in laboratory pouch cells with an external bracing device to study the pressure and electrolyte impact for a longer time period. Figure 4.17 shows the performance of the different cells. Regardless of the applied pressure, the cells with the standard LP57 show limited cycling, reaching the 80% SoH threshold after only ~ 60 cycles. With the addition of FEC, the cells' performances increase, up to over 300 cycles. It can also be seen that the cells with the highest applied external pressure of 1.0 MPa show the best performance, followed by cells with 0.5 MPa and at the end the unbraced cells. This confirms the assumption of the more stable SEI when FEC is present and the better electrical contact between the mossy and the bulk lithium at elevated pressures. The lithium metal cells with the ether-based electrolyte show stable cycling with a high capacity retention (98%) for ~ 100 cycles, proving a stable SEI. After around 100 cycles, the capacity of the individual cells starts to scatter, which is probably mostly related to drying due to consumption of the electrolyte. The consumption of the electrolyte, which in this case leads to gassing, is a significant degradation mechanism, which

makes it difficult to cycle the cells longer than 100 cycles. In total, it can be concluded that the impact of the counter electrode on the performance of the lithium metal cells is small, but the choice of the electrolyte and the applied external pressure play a significant role [187]. When looking at the pressure evolution in the pouch cells (Figure 4.18), it can be seen that the cells with LP57 have a significant pressure increase during cycling, e.g. by a factor of ~ 2 for the cells with initially 0.5 MPa external pressure. This is mostly related to the irreversible swelling of the lithium electrode due to the formation of mossy and dead lithium. The cells with LP57 with 5wt% FEC have a reduced pressure increase compared to the cells with pure LP57 (w/o FEC). After 1000 hours of cycling, the pressure on the electrodes increased only up to ~ 0.8 MPa (initially 0.5 MPa) and ~ 1.1 MPa (initially 1.0 MPa). This confirms that FEC is limiting the irreversible expansion due to a more stable SEI of the cells. Nevertheless, the cells with 1M LiFSI in DME have the most significant pressure increase of ~ 1.7 MPa and ~ 1.9 MPa respectively at end of testing, but which is probably mostly related to the gassing and not to the irreversible expansion of the mossy and dead lithium. A pressure dependency is also seen as the cells with initially 0.5 MPa show a considerable larger pressure increase compared to the cells with an initial external pressure of 1.0 MPa. This shows that elevated pressures reduce the formation of dead lithium due to better electrical contact and hence also the irreversible cell expansion [187].

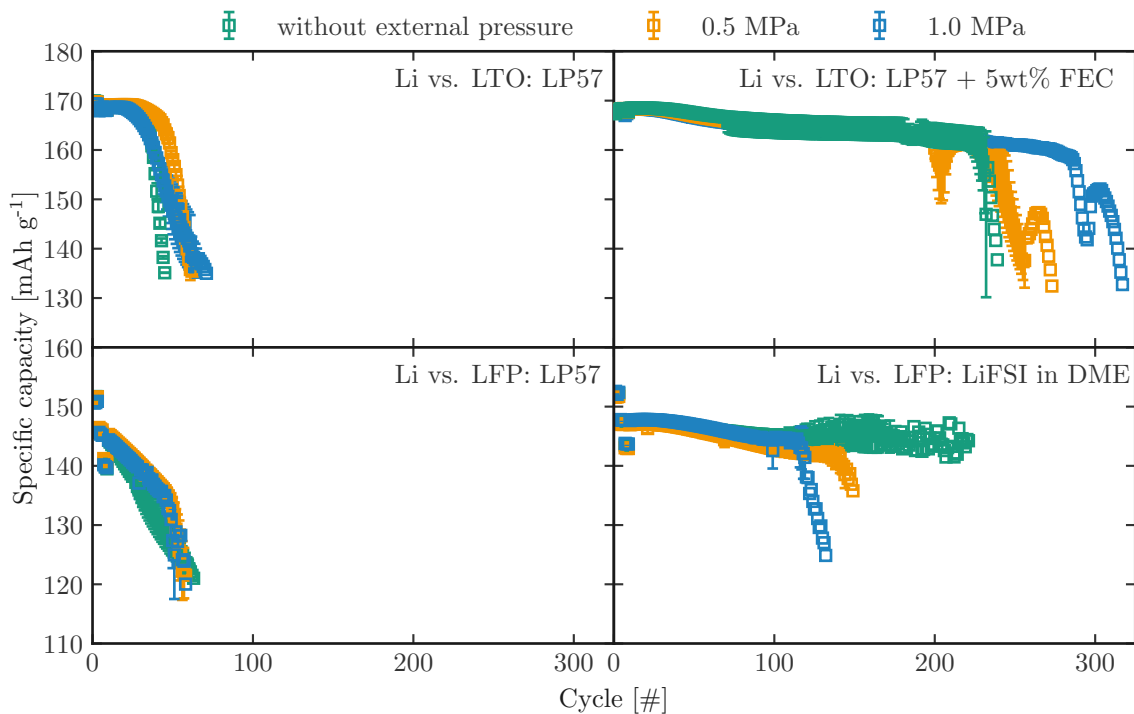


Figure 4.17: Specific capacity as a function of cycles for the cycling of lithium vs. LTO or LFP with three different electrolytes (LP57, LP57 with 5wt% FEC and 1M LiFSI in DME) and various external applied pressures (unbraced, 0.5 MPa and 1.0 MPa). The figure was reprinted from reference [187].

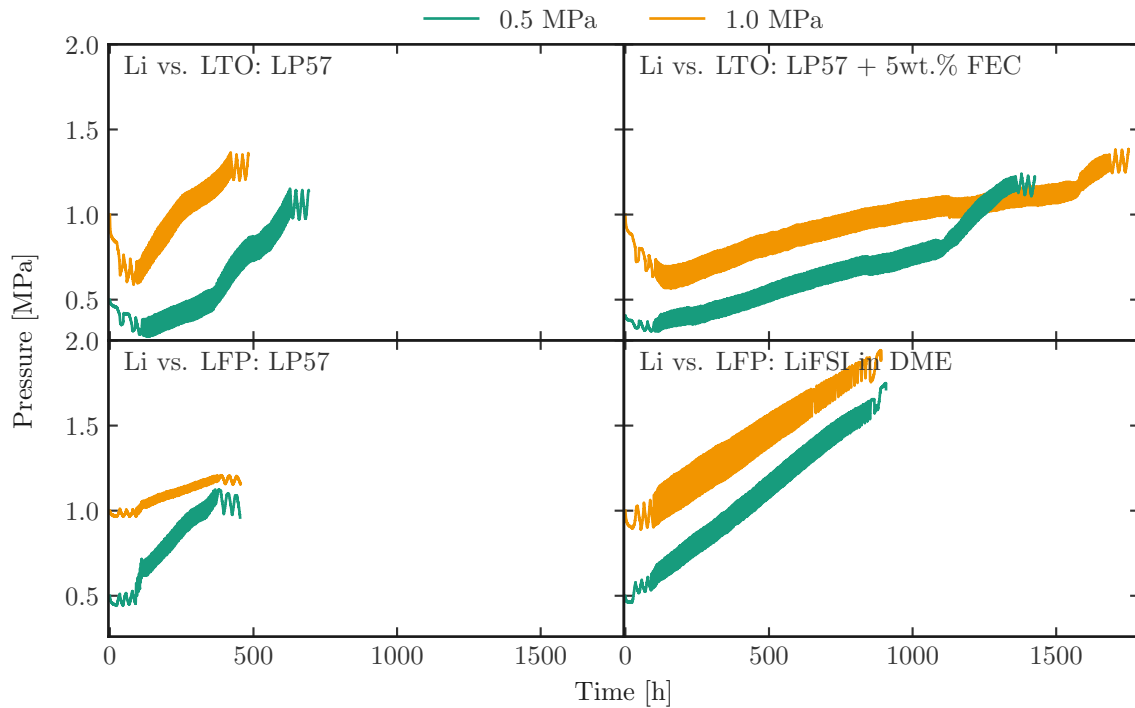


Figure 4.18: Pressure as a function of time for the cells with 0.5 MPa and 1.0 MPa initially applied external pressure. For better visibility, only one representative cell is shown for each parameter. The figure was reprinted from reference [187].

The research on next generation anode materials has shown that these materials have a tremendously increased expansion during cycling compared to graphite. This expansion can cause significant increased stress on the electrodes. Another issue is the irreversible expansion of those electrodes during cycling. It could be shown that not only the choice of the electrolyte but also the pressure have a substantial impact on the performance and irreversible expansion of lithium metal electrodes. High pressure and the addition of FEC significantly reduces the irreversible swelling and increases the performance. This is not only important for future batteries but also for today's LIBs, as often lithium metal electrodes are used in laboratory half-cells. Here, the limitations of the lithium electrode should be considered, especially when cycling the cells for a longer time period and a low external pressure is applied. [187]. The increased pressure not only shows beneficial effects on lithium metal, as it also has positive effects on silicon electrodes. It was shown that elevated external pressure reduces the irreversible swelling due to cracking or delamination and also increases the performance [201].

5 Summary and Outlook

5.1 Summary

The demand for LIB with enhanced energy densities leads to increased utilization of the space within the confinements of the battery housing or to the use of electrode material with increased intrinsic specific energy densities. Both requirements result in more stress on the battery electrodes and separator during cycling or aging. However, the effect of mechanical strain on the cell's electrochemistry and thus the performance of batteries is rather unexplored compared to the impact of current or temperature, for example. The objective of this thesis was to give a better understanding of the electrochemical and mechanical interplay in current- and next-generation lithium based battery cells. Therefore, the thesis was structured into the investigations on SoA and next-generation LIBs. For SoA LIBs, the investigations of the interplay started at laboratory scale. Here, the expansion of various electrodes and also the impact of mechanical pressure and its distribution on the performance of the cells were studied (1). The investigations at laboratory scale was followed by an examination of the electrochemical and mechanical interactions on large format commercial LIBs which are used in BEVs. Accordingly, the effect of bracing and its effect on the performance was studied in an aging and post-mortem study (2). To gain a deeper understanding of the mechanical changes in LIBs, an ultrasonic study was performed for pouch cells. Here, the mechanical changes were further investigated in dependence of SoC and SoH (3). The effects of the mechanical stress on the performance for next-generation batteries were studied at laboratory scale. In the beginning, the expansion of next-generation anode materials such as silicon and lithium was compared with today's anode materials. Furthermore, the effect of mechanical pressure and electrolyte on the irreversible dilation and performance was investigated for lithium metal cells (4). Overall, it was shown that pressure has a significant effect on the performance of today's and also future LIBs. The interplay of the electrochemical and mechanical effects inside a LIB has a considerable impact on the lifetime, capacity fading and impedance increase of the batteries.

The most important results are summarized in the following.

1. A laboratory dilation cell was developed to obtain a deeper understanding of the dilation or expansion behavior of the battery electrodes at laboratory level. With the cell, the expansion behavior of a graphite anode vs. a NCM111 cathode was analyzed. It was shown that graphite has a significant irreversible dilation ($\sim 8.5\%$, with regard to

graphite film thickness) in the initial formation cycle due to the first arrangement of the lithium ions in the graphene layers, SEI formation, partial exfoliation and graphene layer spacing. After the initial cycle, the irreversible dilation decreases and the reversible dilation ($\sim 8\%$ - 10% , with regard to graphite film thickness) is dominant. Here, most of the expansion comes from the graphite 2 to 1 stage transition. It was further shown that in today's batteries most of expansion is caused by the anode as the cathode materials show a lower impact on the overall cell expansion (around one order of magnitude).

In addition to the dilation study, it was also possible to evaluate the macroscopic impact of pressure and its distribution on the performance of the cell. Here, it was revealed that especially an inhomogeneous pressure distribution and/or high pressure cause a considerable capacity reduction and polarization of laboratory cells. Thus, lithium plating on the anode was found to be the most relevant aging factor.

2. The effect of pressure on cell performance was examined using different bracing methods for large scale 94 Ah prismatic LIB cells. In an accelerated aging study (> 7000 cycles), it was demonstrated that the cells without external bracing suffer from enhanced capacity reduction, especially in the region of 80% SoH, reaching the threshold 900 cycles earlier. Post-mortem investigations showed that the unbraced cell had severe visible degradation phenomena (lithium plating on the anode as well as ripple formation on the cathode) all over the cell, whereas the braced cell exhibited lithium plating in some areas with inhomogeneous pressure distribution (e.g. windings of the jelly rolls). Further analytic investigations revealed that the anode suffers from loss of lithium inventory due to lithium plating and also thickening of the SEI. The cathode shows a pressure dependency, where the electrodes which see a high pressure have an increased structural degradation in terms of crystallite size and cation mixing. For example, the unaged reference cell has in comparison to the aged braced cell a crystallite size of 1357 \AA and an intensity ratio R value ($(I(006)+I(102))/I(101)$) of 0.74 compared to 388 \AA and 0.92 respectively. Nevertheless, the impact of the electrodes itself on capacity reduction was rather small compared to the main degradation mechanism being the loss of lithium inventory.

Moreover, a new concept of the mechanical SoH was introduced, correlating the capacity decline with the mechanical degradation of the electrodes or other cell components. It was shown that the cathode suffers from a lower mechanical SoH, and hence greater mechanical degradation compared to the anode.

3. For a better understanding of the individual mechanical characteristics inside a commercial LIB, ultrasonic measurements were used as a non-invasive characterization method. It was shown that mostly changes of the ToF and stiffness occurring during cycling in a graphite vs. nickel rich NCM cell is coming from the graphite stage transitions 1L to

4, 2 to 1 and the phase transition of the nickel-rich NCM from H2 to H3 during cycling. In an extensive aging study, it was further proven that the ToF is increasing $\sim 10\%$ and the Young's modulus of the cell is decreasing $\sim 11\%$ over aging. The differential ToF magnitude during the RPT is also decreasing with cell aging. The change is caused by the irreversible thickening of the cell of $\sim 4\%$ due to SEI growth, cracking, lithium plating and porosity increase. The additional layers (e.g. SEI and lithium plating) have an increased porosity which reduces the sound velocity. Hence, the overall stiffness is decreasing with $\sim 11\%$ over aging.

4. The study of the electrochemical and mechanical interplay in next-generation LIBs was done in laboratory cells. First results showed that lithium metal and silicon anodes have a tremendously enhanced expansion in comparison to graphite anodes by a factor of ~ 4 and 2.5 respectively. Not only the reversible expansion but also the irreversible expansion, i.e. mossy and dead lithium, is dramatically increased, which causes fast capacity fading. Thus, the effect of pressure and electrolyte on the irreversible expansion and performance of lithium metal was studied. It was examined that an elevated pressure (0.5 MPa and 1.0 MPa respectively) and also the use of additives like FEC with a carbonate-based electrolyte or the use of ether-based electrolytes can significantly reduce the formation of mossy and dead lithium. With that, the cycling performance of the lithium metal half-cells was enhanced by a factor of 2 to 5 . These results are also relevant for today's battery electrode testing in half-cells, as lithium metal is also used as a counter electrode. Particularly when the cells are cycled at high current rates ($> \sim 1$ mA cm $^{-2}$) or for a longer time ($> \sim 20$ cycles).

In total, the studies performed in this thesis reveal that the electrochemical and mechanical interplay has a significant impact on the performance of SoA and next-generation LIB cells. For the SoA batteries, the cell expansion of especially the anode cause stress on the electrodes. In combination with inhomogeneous pressure distribution on the electrodes, major degradation mechanisms like lithium plating, SEI growth or particle cracking occur. A homogeneous pressure distribution reduces the amount of lithium plating, but particle cracking on the cathode increases. These aging effects, especially irreversible thickness change on the anode, cause a softening of the overall cell stiffness which is important to know for the integration of pouch cells within a battery system. The SEI and the lithium plating layer are more porous and hence the total stiffness is decreasing. Moreover, the new concept of the mechanical SoH was introduced to correlate capacity reduction with the mechanical degradation of the electrodes. For the next-generation batteries the effect of pressure is probably even more important as for SoA LIBs, as the electrodes exhibit an enormous expansion during cycling. This expansion is combined with a large irreversible expansion, which can significantly be reduced at elevated external pressure and has to be considered when designing next-generation battery modules and systems. To conclude, the electrochemical and mechanical interplay is

an important parameter, regardless if for SoA or next-generation batteries, for an elongated cycle life.

5.2 Outlook

The presented thesis provides a further step for the understanding of the electrochemical and mechanical interplay in LIBs. However, there are still ongoing challenges in this field to be solved:

1. The mechanical characteristic or changes needs to be investigated for different SoA chemistries. How does the addition of silicon into the graphite-based anode effect the stiffness change? What's the impact of different SEI chemistries on the stiffness?
2. Further studies with specialized sensors are needed to validate the mechanical SoH and to be possibly integrated into the battery management system (BMS). A reliable separation between anode and cathode characteristic would be helpful.
3. The dilation of solid-state batteries (SSB) with lithium metal as the anode is still mostly unknown and important for commercialization of those batteries. Furthermore, the impact of inhomogeneous pressure distribution on the performance of SSB is also an important factor to be addressed.

6 Zusammenfassung und Ausblick

6.1 Zusammenfassung

Mit der steigenden Nachfrage nach Lithium-Ionen-Batterien (LIB) mit hoher Energiedichte geht eine effizientere Nutzung des Raumes innerhalb des Batteriegehäuses oder die Verwendung von Elektrodenmaterial mit erhöhter intrinsischer Energiedichte einher. Durch beide Maßnahmen steigt die mechanische Belastung auf die Batterieelektroden und den Separator während eines Zyklus oder im Zuge der Alterung. Deren Auswirkungen auf die elektrochemischen Reaktionen der Elektroden und damit auf die Leistung der Batterien ist jedoch im Vergleich zu den Auswirkungen von Strom oder Temperatur eher unerforscht. Das Ziel dieser Doktorarbeit ist es, ein besseres Verständnis für das elektrochemische und mechanische Zusammenspiel in heutigen und zukünftigen Lithium-Batteriezellen zu entwickeln. Daher wurde die Arbeit in die Untersuchungen von heutigen und zukünftigen LIBs gegliedert. Für heutige LIBs begannen die Untersuchungen des elektrochemisch-mechanischen Zusammenspiels im Labormaßstab. Hier wurde die Ausdehnung unterschiedlicher Elektroden sowie der Einfluss des mechanischen Drucks und seiner Verteilung auf die Leistung der Batteriezellen untersucht (1). Aufbauend auf den Untersuchungen im Labormaßstab folgte eine Untersuchung der elektrochemischen und mechanischen Wechselwirkungen an großformatigen kommerziellen LIBs, die in BEVs verwendet werden. Dafür wurde der Einfluss von mechanischer Verspannung auf die Leistung der Batterien in einer Alterungs- und Post-Mortem-Studie untersucht (2). Um ein vertieftes Verständnis der mechanischen Veränderungen innerhalb der LIBs zu entwickeln, wurden kommerzielle Pouch-Zellen mittels Ultraschalluntersuchungen analysiert. Hierbei wurden die mechanischen Veränderungen in Abhängigkeit des Ladezustands und der Alterung weiter untersucht (3). Die Auswirkungen der mechanischen Belastung auf die Leistung von zukünftigen Batteriesystemen wurde im Labormaßstab untersucht. Zunächst wurde die Ausdehnung von Anodenmaterialien der nächsten Generation wie Silicium und Lithium mit heutigen Anodenmaterialien verglichen. Außerdem wurde der Einfluss von mechanischem Druck und des Elektrolyten auf die irreversible Dilatation und die Performance von Lithium-Metall Zellen untersucht (4).

Insgesamt zeigt diese Arbeit, dass der Druck einen erheblichen Einfluss auf die Leistung heutiger und auch zukünftiger LIBs hat. Das Zusammenspiel der elektrochemischen und mechanischen Effekte in einer LIB hat einen erheblichen Einfluss auf die Lebensdauer, den Kapazitätsabfall und die Impedanzerhöhung der Batterien. Die wichtigsten Ergebnisse sind im Folgenden zusammengefasst.

1. Zunächst wurde eine Dilatationszelle weiterentwickelt und aufgebaut, um ein besseres Verständnis des Dilatations- oder Ausdehnungsverhalten der Batterieelektroden zu erhalten. Mit der Messzelle wurde das Ausdehnungsverhalten einer Graphitanode gegenüber einer NCM111 Kathode analysiert. Es konnte gezeigt werden, dass Graphit eine signifikante irreversible Dilatation im initialen Formierzyklus aufweist (8,5 %, bezogen auf Graphitschichtdicke). Dies kommt aufgrund der initialen Anordnung der Lithium-Ionen in den Graphenschichten, der SEI Bildung, der partiellen Exfoliation und der Ausdehnung der Graphenschichtabstände zustande. Nach dem ersten Zyklus nimmt die irreversible Dilatation ab und die reversible Dilatation (8 - 10 %, bezogen auf die Graphitschichtdicke) dominiert. Der größte Teil der Ausdehnung ist dabei auf den Graphitstufenübergang von Stufe 2 auf 1 zurückzuführen. Es wurde außerdem gezeigt, dass bei heutigen Batteriezellen der größte Teil der Ausdehnung von der Anode verursacht wird. Kathodenmaterialien haben um etwa eine Größenordnung geringeren Einfluss auf die Gesamtausdehnung der Zelle.

Zusätzlich zu den Ausdehnungsuntersuchungen wurden die makroskopischen Auswirkungen des Drucks und seiner Verteilung auf die Performance der Elektroden mit der Dilatationszelle getestet. Hier zeigte sich, dass insbesondere eine inhomogene Druckverteilung und/oder ein hoher Druck zu einem erheblichen Kapazitätsrückgang und Anstieg der Widerstände in den Laborzellen führte. Lithium Plating auf der Anode war dabei die dominanteste Degradationsursache.

2. Der Einfluss von Druck auf die Performance von kommerziellen großformatigen prismatischen 94 Ah LIB Zellen wurde mithilfe unterschiedlicher Verspannungen untersucht. In einer beschleunigten Alterungsstudie (> 7000 Zyklen) wurde gezeigt, dass die Zellen ohne externe Verspannung unter einem verstärkten Kapazitätsrückgang leiden, insbesondere im Bereich von 80 % SoH. Die Grenze von 80 % SoH erreichen die unverspannten Zellen \sim 900 Zyklen früher als die verspannten Zellen. Anschließende Post-Mortem Untersuchungen zeigten, dass die unverspannte Zelle deutlich sichtbare Degradationen (Lithium Plating auf der Anode sowie Wellentäler und -berge auf der Kathode) in der gesamten Zelle aufweisen, während die verspannte Zelle nur in einigen Bereichen mit inhomogener Druckverteilung (z.B. Ränder der Jelly Rolls) Lithium Plating zeigte. Weitere Untersuchungen ergaben, dass die Degradation der Anode hauptsächlich von Lithium Plating und SEI Wachstum dominiert wird. Die Kathode zeigt eine Druckabhängigkeit, wobei die Elektroden, die einem hohen Druck ausgesetzt sind, eine erhöhte strukturelle Degradation in Bezug auf die Kristallitgröße und Kationenmischung aufweisen. Die nicht gealterte Referenzzelle hat zum Beispiel eine Kristallitgröße von 1357 Å und ein Intensitätsverhältnis $R ((I(006)+I(102))/I(101))$ von 0,74 im Vergleich zu 388 Å und 0,92 der gealterten verspannten Zelle. Dennoch war der Einfluss der Elektroden selbst auf die Kapazitätsrückgang im Vergleich zum Hauptdegradationsmechanismus, nämlich dem Verlust von zyklisierbaren Lithiums, eher gering.

Darüber hinaus wurde ein neues Konzept des mechanischen SoH eingeführt, das den

Kapazitätsrückgang mit der mechanischen Degradation der Elektroden oder anderer Zellkomponenten korreliert. Es wurde gezeigt, dass die Kathode einen geringeren mechanischen SoH im Vergleich zur Anode hat und damit mehr mechanische Degradation erfährt.

3. Für ein besseres Verständnis der individuellen mechanischen Eigenschaften der Elektroden innerhalb einer kommerziellen LIB wurden Ultraschallmessungen als zerstörungsfreie Charakterisierungsmethode eingesetzt. Dabei konnte gezeigt werden, dass die größte Änderung der ToF (Flugzeit) und Steifigkeit während eines Zyklus in einer Graphit- und einer nickelreichen NCM Zelle, von den Graphitphasenübergängen 1L zu 4, 2 zu 1 und dem Phasenübergang des nickelreichen NCM von H2 zu H3 während des Zyklus herrühren. In einer ausgedehnten Alterungsstudie wurde außerdem nachgewiesen, dass die ToF während der Alterung um $\sim 10\%$ zunimmt und das Elastizitätsmodul der Gesamtzelle im Laufe der Alterung um $\sim 11\%$ abnimmt.

Die ToF Änderung während eines Zyklus nimmt während des RPT (Referenzzyklus) ebenfalls mit der Zellalterung ab. Diese Verringerung wird durch das irreversible Dickewachstum der Zelle von $\sim 4\%$ aufgrund von SEI-Wachstum, Rissbildung in den Elektroden, Lithium Plating und Porositätszunahme verursacht. Die zusätzlichen Schichten (z.B. SEI und Lithium Plating) haben eine erhöhte Porosität, die die Schallgeschwindigkeit verringert. Folglich nimmt die Gesamtsteifigkeit um 11% über die Alterung ab.

4. Das elektrochemische und mechanische Zusammenspiel in zukünftigen LIBs wurde in Laborzellen untersucht. Erste Ergebnisse zeigten, dass Lithium- und Siliciumanoden eine im Vergleich zu Graphitanoden um den Faktor 4 bzw. 2,5 höhere Ausdehnung aufweisen. Nicht nur die reversible Ausdehnung, sondern auch die irreversible Ausdehnung, d. h. 'moosartiges' und 'totes' Lithium, ist dramatisch erhöht, was einen schnellen Kapazitätsabfall verursacht. Darauf aufbauend wurden die Auswirkungen von Druck und der Wahl des Elektrolyts auf die irreversible Ausdehnung und die Performance von Lithiummetall analysiert. Es wurde gezeigt, dass ein erhöhter Druck (0.5 MPa und 1.0 MPa) und die Verwendung von Zusätzen wie FEC im karbonatbasierten Elektrolyten oder die Verwendung von etherbasierten Elektrolyten die Bildung von moosartigen und totem Lithium deutlich reduziert. Dadurch konnte die Zyklenstabilität der Lithium-Metall Halbzellen um einen Faktor von 2 bis 5 verbessert werden. Diese Ergebnisse sind auch für heutige Elektrodentests in Halbzellen relevant, da hier Lithium oft als Gegenelektrode verwendet wird. Insbesondere wenn die Zellen mit hohen Strömen zyklisiert werden ($> \sim 1 \text{ mA cm}^{-2}$) oder über einen längeren Zeitraum ($> \sim 20$ Zyklen) getestet werden, muss die Degradation der Lithiumelektrode mit berücksichtigt werden.

Insgesamt zeigen die in dieser Arbeit durchgeführten Untersuchungen, dass das elektrochemische und mechanische Zusammenspiel einen erheblichen Einfluss auf die Performance von heutigen und zukünftigen LIBs hat. Bei den heutigen Batterien verursacht die Zellexpansion

sion, insbesondere der Anode, Stress auf die Elektroden. In Kombination mit einer inhomogenen Druckverteilung auf die Elektroden können Degradationsmechanismen wie Lithium Plating, SEI-Wachstum oder Partikelrissbildung auftreten. Eine homogene Druckverteilung reduziert die Menge an Lithium Plating, aber die Partikelrisse in den Kathodenpartikeln nehmen zu. Diese Alterungseffekte, insbesondere die irreversible Dickenänderung der Anode, führen zu einer Verringerung der Gesamtsteifigkeit der Zelle, was für die Integration von Pouch Zellen in ein Batteriesystem wichtig ist. Die SEI und das geplattete Lithium sind poröser und infolgedessen nimmt die Gesamtsteifigkeit ab. Außerdem wurde ein neues Konzept des mechanischen SoH eingeführt, um die Kapazitätsverringerng mit der mechanischen Degradation der Elektroden zu korrelieren. Bei den Batterien der nächsten Generation ist der Einfluss des Drucks wahrscheinlich noch wichtiger als bei heutigen LIBs, da die Elektroden während des Zyklus eine enorme Ausdehnung aufweisen. Diese Ausdehnung ist mit einer großen irreversiblen Ausdehnung verbunden und muss bei der Entwicklung von zukünftigen Batteriemodulen berücksichtigt werden. Die Ergebnisse der vorliegenden Arbeit zeigen, dass das elektrochemische und mechanische Zusammenspiel ein wichtiger Parameter für eine lange Lebensdauer ist, unabhängig davon ob es sich um heutige oder zukünftige LIBs handelt.

6.2 Ausblick

Die vorliegende Arbeit ist ein weiterer Schritt zum verbesserten Verständnis des elektrochemischen und mechanischen Zusammenspiels in LIBs. Allerdings gibt es auf diesem Gebiet immer noch Herausforderungen, die es zu lösen gilt:

1. Die mechanischen Eigenschaften oder Veränderungen müssen für verschiedene Elektroden-Chemien untersucht werden. Wie wirkt sich die Zugabe von Silicium in einer Graphit-basierte Anode auf die Steifigkeit aus? Welchen Einfluss haben die verschiedenen SEI Zusammensetzungen auf die Steifigkeit der Batterie?
2. Weitere Studien mit speziellen Sensoren sind erforderlich, um den mechanischen SoH zu validieren und möglicherweise in das BMS zu integrieren. Eine zuverlässige Differenzierung zwischen Anode und Kathode wäre hilfreich.
3. Die Ausdehnung von Festkörperbatterien (SSBs) mit Lithiummetall als Anode ist noch weitgehend unbekannt und wichtig für die Kommerzialisierung dieser Batterien. Außerdem ist die Auswirkung einer inhomogenen Druckverteilung auf die Leistung der SSB ein weiterer wichtiger Faktor, den es zu untersuchen gilt.

Bibliography

- [1] J. Hansen, R. Ruedy, M. Sato, and K. Lo, “GLOBAL SURFACE TEMPERATURE CHANGE,” *Reviews of Geophysics*, vol. 48, no. 4, 2010.
- [2] N. J. L. Lenssen, G. A. Schmidt, J. E. Hansen, M. J. Menne, A. Persin, R. Ruedy, and D. Zyss, “Improvements in the GISTEMP Uncertainty Model,” *Journal of Geophysical Research: Atmospheres*, vol. 124, no. 12, pp. 6307–6326, 2019.
- [3] NOAA National Centers for Environmental Information, “State of the Climate: Monthly Global Climate Report for Annual 2021,” 2022. <https://www.ncei.noaa.gov/access/monitoring/monthly-report/global/202113>, last accessed on 03.08.2022.
- [4] World Meteorological Organization, “WMO Provisional State of the Global Climate 2022,” 2022. https://library.wmo.int/index.php?lvl=notice_display&id=22156#.Y4XTVnbMJPZ, last accessed on 29.11.2022.
- [5] Goldman Sachs Research, “Carbonomics: Re-Imagining Europe’s Energy System,” 2022. <https://www.goldmansachs.com/insights/pages/gs-research/carbonomics-re-imagining-europes-energy-system/report.pdf>, last accessed on 03.08.2022.
- [6] S. S. Ravi and M. Aziz, “Utilization of Electric Vehicles for Vehicle-to-Grid Services: Progress and Perspectives,” *Energies*, vol. 15, no. 2, p. 589, 2022.
- [7] D. Hall and N. Lutsey, “Effects of battery manufacturing on electric vehicle life-cycle greenhouse gas emissions,” 2018. <https://theicct.org/publications/EV-battery-manufacturing-emissions>, last accessed on 03.08.2022.
- [8] B. Diouf and R. Pode, “Potential of lithium-ion batteries in renewable energy,” *Renewable Energy*, vol. 76, pp. 375–380, 2015.
- [9] M. S. Whittingham, “Electrical energy storage and intercalation chemistry,” *Science*, vol. 192, no. 4244, pp. 1126–1127, 1976.
- [10] F. Schipper and D. Aurbach, “A brief review: Past, present and future of lithium ion batteries,” *Russian Journal of Electrochemistry*, vol. 52, no. 12, pp. 1095–1121, 2016.
- [11] B. Scrosati, “History of lithium batteries,” *Journal of Solid State Electrochemistry*, vol. 15, no. 7-8, pp. 1623–1630, 2011.

- [12] K. Mizushima, P. C. Jones, P. J. Wiseman, and J. B. Goodenough, "Li_xCoO₂ (0 < x < 1): A new cathode material for batteries of high energy density," *Materials Research Bulletin*, vol. 15, no. 6, pp. 783–789, 1980.
- [13] A. Yoshino, "The birth of the lithium-ion battery," *Angewandte Chemie (International ed. in English)*, vol. 51, no. 24, pp. 5798–5800, 2012.
- [14] A. Yoshino, K. Sanekika, and T. Nakajima, "US4668595A - Secondary battery," 1987.
- [15] D. Linden and T. B. Reddy, *Handbook of Batteries*. McGraw-Hill handbooks, New York, NY: McGraw-Hill, 3. ed. ed., 2002.
- [16] C. Liu, Z. G. Neale, and G. Cao, "Understanding electrochemical potentials of cathode materials in rechargeable batteries," *Materials Today*, vol. 19, no. 2, pp. 109–123, 2016.
- [17] J. B. Goodenough and K.-S. Park, "The Li-ion rechargeable battery: A Perspective," *Journal of the American Chemical Society*, vol. 135, no. 4, pp. 1167–1176, 2013.
- [18] M. Winter and R. J. Brodd, "What are batteries, fuel cells, and supercapacitors?," *Chemical reviews*, vol. 104, no. 10, pp. 4245–4269, 2004.
- [19] C. Breitkopf and K. Swider-Lyons, eds., *Springer Handbook of Electrochemical Energy*. Springer Handbooks, Berlin, Heidelberg: Springer, 1st ed. 2017 ed., 2017.
- [20] G. Liu, M. Ouyang, L. Lu, J. Li, and X. Han, "Analysis of the heat generation of lithium-ion battery during charging and discharging considering different influencing factors," *Journal of Thermal Analysis and Calorimetry*, vol. 116, no. 2, pp. 1001–1010, 2014.
- [21] N. Sato, "Thermal behavior analysis of lithium-ion batteries for electric and hybrid vehicles," *Journal of Power Sources*, vol. 99, no. 1-2, pp. 70–77, 2001.
- [22] K. E. Thomas and J. Newman, "Thermal Modeling of Porous Insertion Electrodes," *Journal of Power Sources*, vol. 150, no. 2, p. A176, 2003.
- [23] K. Smith and C.-Y. Wang, "Power and thermal characterization of a lithium-ion battery pack for hybrid-electric vehicles," *Journal of Power Sources*, vol. 160, no. 1, pp. 662–673, 2006.
- [24] X.-L. Wang, K. An, L. Cai, Z. Feng, S. E. Nagler, C. Daniel, K. J. Rhodes, A. D. Stoica, H. D. Skorpenske, C. Liang, W. Zhang, J. Kim, Y. Qi, and S. J. Harris, "Visualizing the chemistry and structure dynamics in lithium-ion batteries by in-situ neutron diffraction," *Scientific reports*, vol. 2, p. 747, 2012.
- [25] M. Winter, J. O. Besenhard, M. E. Spahr, and P. Novák, "Insertion Electrode Materials for Rechargeable Lithium Batteries," *Advanced Materials*, vol. 10, no. 10, pp. 725–763, 1998.

-
- [26] J. Asenbauer, T. Eisenmann, M. Kuenzel, A. Kazzazi, Z. Chen, and D. Bresser, “The success story of graphite as a lithium-ion anode material – fundamentals, remaining challenges, and recent developments including silicon (oxide) composites,” *Sustainable Energy & Fuels*, vol. 4, no. 11, pp. 5387–5416, 2020.
- [27] Y. Qi, H. Guo, L. G. Hector, and A. Timmons, “Threefold Increase in the Young’s Modulus of Graphite Negative Electrode during Lithium Intercalation,” *Journal of Power Sources*, vol. 157, no. 5, p. A558, 2010.
- [28] C. P. Sandhya, B. John, and C. Gouri, “Lithium titanate as anode material for lithium-ion cells: a review,” *Ionics*, vol. 20, no. 5, pp. 601–620, 2014.
- [29] Y. Qi, L. G. Hector, C. James, and K. J. Kim, “Lithium Concentration Dependent Elastic Properties of Battery Electrode Materials from First Principles Calculations,” *Journal of The Electrochemical Society*, vol. 161, no. 11, pp. F3010–F3018, 2014.
- [30] T.-F. Yi, Y. Xie, Y.-R. Zhu, J. Shu, A.-N. Zhou, and H.-B. Qiao, “Stabilities and electronic properties of lithium titanium oxide anode material for lithium ion battery,” *Journal of Power Sources*, vol. 198, pp. 318–321, 2012.
- [31] M. N. Obrovac and V. L. Chevrier, “Alloy negative electrodes for Li-ion batteries,” *Chemical reviews*, vol. 114, no. 23, pp. 11444–11502, 2014.
- [32] K. Feng, M. Li, W. Liu, A. G. Kashkooli, X. Xiao, M. Cai, and Z. Chen, “Silicon-Based Anodes for Lithium-Ion Batteries: From Fundamentals to Practical Applications,” *Small*, vol. 14, no. 8, 2018.
- [33] V. B. Shenoy, P. Johari, and Y. Qi, “Elastic softening of amorphous and crystalline Li-Si Phases with increasing Li concentration: A first-principles study,” *Journal of Power Sources*, vol. 195, no. 19, pp. 6825–6830, 2010.
- [34] D. Lin, Y. Liu, and Y. Cui, “Reviving the lithium metal anode for high-energy batteries,” *Nature nanotechnology*, vol. 12, no. 3, pp. 194–206, 2017.
- [35] M. Winter, B. Barnett, and K. Xu, “Before Li Ion Batteries,” *Chemical reviews*, vol. 118, no. 23, pp. 11433–11456, 2018.
- [36] A. Masias, N. Felten, R. Garcia-Mendez, J. Wolfenstine, and J. Sakamoto, “Elastic, plastic, and creep mechanical properties of lithium metal,” *Journal of Materials Science*, vol. 54, no. 3, pp. 2585–2600, 2019.
- [37] L. de Biasi, A. O. Kondrakov, H. Geßwein, T. Brezesinski, P. Hartmann, and J. Janek, “Between Scylla and Charybdis: Balancing Among Structural Stability and Energy Density of Layered NCM Cathode Materials for Advanced Lithium-Ion Batteries,” *The Journal of Physical Chemistry C*, vol. 121, no. 47, pp. 26163–26171, 2017.

- [38] F. B. Spingler, S. Kücher, R. Phillips, E. Moyassari, and A. Jossen, “Electrochemically Stable In Situ Dilatometry of NMC, NCA and Graphite Electrodes for Lithium-Ion Cells Compared to XRD Measurements,” *Journal of The Electrochemical Society*, vol. 168, no. 4, p. 040515, 2021.
- [39] R. Xu, H. Sun, L. S. de Vasconcelos, and K. Zhao, “Mechanical and Structural Degradation of $\text{LiNi}_x\text{Mn}_y\text{Co}_z\text{O}_2$ Cathode in Li-Ion Batteries: An Experimental Study,” *Journal of The Electrochemical Society*, vol. 164, no. 13, pp. A3333–A3341, 2017.
- [40] M. S. Whittingham, “Lithium batteries and cathode materials,” *Chemical reviews*, vol. 104, no. 10, pp. 4271–4301, 2004.
- [41] A. K. Padhi, K. S. Nanjundaswamy, and J. B. Goodenough, “Phospho-olivines as Positive-Electrode Materials for Rechargeable Lithium Batteries,” *Journal of The Electrochemical Society*, vol. 144, no. 4, pp. 1188–1194, 1997.
- [42] K. Cao, T. Jin, L. Yang, and L. Jiao, “Recent progress in conversion reaction metal oxide anodes for Li-ion batteries,” *Materials Chemistry Frontiers*, vol. 1, no. 11, pp. 2213–2242, 2017.
- [43] Y. Lu, Le Yu, and X. W. Lou, “Nanostructured Conversion-type Anode Materials for Advanced Lithium-Ion Batteries,” *Chem*, vol. 4, no. 5, pp. 972–996, 2018.
- [44] N. Mahmood, T. Tang, and Y. Hou, “Nanostructured Anode Materials for Lithium Ion Batteries: Progress, Challenge and Perspective,” *Advanced Energy Materials*, vol. 6, no. 17, p. 1600374, 2016.
- [45] M. Hahn, H. Buqa, P. W. Ruch, D. Goers, M. E. Spahr, J. Ufheil, P. Novák, and R. Kötz, “A Dilatometric Study of Lithium Intercalation into Powder-Type Graphite Electrodes,” *Journal of Power Sources*, vol. 11, no. 9, p. A151, 2008.
- [46] D. Billaud, F. X. Henry, M. Lelaurain, and P. Willmann, “Revisited structures of dense and dilute stage II lithium-graphite intercalation compounds,” *Journal of Physics and Chemistry of Solids*, vol. 57, no. 6-8, pp. 775–781, 1996.
- [47] H. Shi, J. Barker, M. Y. Saïdi, R. Koksang, and L. Morris, “Graphite structure and lithium intercalation,” *Journal of Power Sources*, vol. 68, no. 2, pp. 291–295, 1997.
- [48] A. Senyshyn, O. Dolotko, M. J. Mühlbauer, K. Nikolowski, H. Fuess, and H. Ehrenberg, “Lithium Intercalation into Graphitic Carbons Revisited: Experimental Evidence for Twisted Bilayer Behavior,” *Journal of The Electrochemical Society*, vol. 160, no. 5, pp. A3198–A3205, 2013.
- [49] T. Tran and K. Kinoshita, “Lithium intercalation/deintercalation behavior of basal and edge planes of highly oriented pyrolytic graphite and graphite powder,” *Journal of Electroanalytical Chemistry*, vol. 386, no. 1-2, pp. 221–224, 1995.

-
- [50] K. Persson, V. A. Sethuraman, L. J. Hardwick, Y. Hinuma, Y. S. Meng, A. van der Ven, V. Srinivasan, R. Kostecki, and G. Ceder, “Lithium Diffusion in Graphitic Carbon,” *The Journal of Physical Chemistry Letters*, vol. 1, no. 8, pp. 1176–1180, 2010.
- [51] D. Allart, M. Montaru, and H. Gualous, “Model of Lithium Intercalation into Graphite by Potentiometric Analysis with Equilibrium and Entropy Change Curves of Graphite Electrode,” *Journal of The Electrochemical Society*, vol. 165, no. 2, pp. A380–A387, 2018.
- [52] S. J. An, J. Li, C. Daniel, D. Mohanty, S. Nagpure, and D. L. Wood, “The state of understanding of the lithium-ion-battery graphite solid electrolyte interphase (SEI) and its relationship to formation cycling,” *Carbon*, vol. 105, no. 4, pp. 52–76, 2016.
- [53] E. Peled and S. Menkin, “Review—SEI: Past, Present and Future,” *Journal of The Electrochemical Society*, vol. 164, no. 7, pp. A1703–A1719, 2017.
- [54] R. Schmich, R. Wagner, G. Hörpel, T. Placke, and M. Winter, “Performance and cost of materials for lithium-based rechargeable automotive batteries,” *Nature Energy*, vol. 3, no. 4, pp. 267–278, 2018.
- [55] H. Yan, D. Zhang, Qilu, X. Duo, and X. Sheng, “A review of spinel lithium titanate ($\text{Li}_4\text{Ti}_5\text{O}_{12}$) as electrode material for advanced energy storage devices,” *Ceramics International*, vol. 47, no. 5, pp. 5870–5895, 2021.
- [56] B. Zhao, R. Ran, M. Liu, and Z. Shao, “A comprehensive review of $\text{Li}_4\text{Ti}_5\text{O}_{12}$ -based electrodes for lithium-ion batteries: The latest advancements and future perspectives,” *Materials Science and Engineering: R: Reports*, vol. 98, pp. 1–71, 2015.
- [57] X. Sun, P. V. Radovanovic, and B. Cui, “Advances in spinel $\text{Li}_4\text{Ti}_5\text{O}_{12}$ anode materials for lithium-ion batteries,” *New Journal of Chemistry*, vol. 39, no. 1, pp. 38–63, 2015.
- [58] C. Sousa and F. Illas, “Ionic-covalent transition in titanium oxides,” *Physical Review B*, vol. 50, no. 19, pp. 13974–13980, 1994.
- [59] A. Varzi, K. Thanner, R. Scipioni, D. Di Lecce, J. Hassoun, S. Dörfler, H. Altheus, S. Kaskel, C. Prehal, and S. A. Freunberger, “Current status and future perspectives of lithium metal batteries,” *Journal of Power Sources*, vol. 480, no. 3–4, p. 228803, 2020.
- [60] W. Xu, J. Wang, F. Ding, X. Chen, E. Nasybulin, Y. Zhang, and J.-G. Zhang, “Lithium metal anodes for rechargeable batteries,” *Energy Environ. Sci.*, vol. 7, no. 2, pp. 513–537, 2014.
- [61] K. Schubert, “Ein Modell für die Kristallstrukturen der chemischen Elemente,” *Acta Crystallographica Section B Structural Crystallography and Crystal Chemistry*, vol. 30, no. 1, pp. 193–204, 1974.

- [62] M. Wu, Z. Wen, Y. Liu, X. Wang, and L. Huang, "Electrochemical behaviors of a Li_3N modified Li metal electrode in secondary lithium batteries," *Journal of Power Sources*, vol. 196, no. 19, pp. 8091–8097, 2011.
- [63] G. A. Umeda, E. Menke, M. Richard, K. L. Stamm, F. Wudl, and B. Dunn, "Protection of lithium metal surfaces using tetraethoxysilane," *J. Mater. Chem.*, vol. 21, no. 5, pp. 1593–1599, 2011.
- [64] D. Lin, Y. Liu, Z. Liang, H.-W. Lee, J. Sun, H. Wang, K. Yan, J. Xie, and Y. Cui, "Layered reduced graphene oxide with nanoscale interlayer gaps as a stable host for lithium metal anodes," *Nature nanotechnology*, vol. 11, no. 7, pp. 626–632, 2016.
- [65] K. Yan, Z. Lu, H.-W. Lee, F. Xiong, P.-C. Hsu, Y. Li, J. Zhao, S. Chu, and Y. Cui, "Selective deposition and stable encapsulation of lithium through heterogeneous seeded growth," *Nature Energy*, vol. 1, no. 3, p. 359, 2016.
- [66] S. Tariq, K. Ammigan, P. Hurh, R. Schultz, P. Liu, and J. Shang, "LI material testing-fermilab antiproton source lithium collection lens," *Proceedings of the 2003 particle accelerator conference*, pp. 1452–1454, 2003.
- [67] W. M. Robertson and D. J. Montgomery, "Elastic Modulus of Isotopically-Concentrated Lithium," *Physical Review*, vol. 117, no. 2, pp. 440–442, 1960.
- [68] X. Su, Q. Wu, J. Li, X. Xiao, A. Lott, W. Lu, B. W. Sheldon, and J. Wu, "Silicon-Based Nanomaterials for Lithium-Ion Batteries: A Review," *Advanced Energy Materials*, vol. 4, no. 1, p. 1300882, 2014.
- [69] P. Limthongkul, Y.-I. Jang, N. J. Dudney, and Y.-M. Chiang, "Electrochemically-driven solid-state amorphization in lithium-silicon alloys and implications for lithium storage," *Acta Materialia*, vol. 51, no. 4, pp. 1103–1113, 2003.
- [70] J. Li and J. R. Dahn, "An In Situ X-Ray Diffraction Study of the Reaction of Li with Crystalline Si," *Journal of Power Sources*, vol. 154, no. 3, p. A156, 2007.
- [71] S.-M. Liang, F. Taubert, A. Kozlov, J. Seidel, F. Mertens, and R. Schmid-Fetzer, "Thermodynamics of Li-Si and Li-Si-H phase diagrams applied to hydrogen absorption and Li-ion batteries," *Intermetallics*, vol. 81, pp. 32–46, 2017.
- [72] C. J. Wen and R. A. Huggins, "Chemical diffusion in intermediate phases in the lithium-silicon system," *Journal of Solid State Chemistry*, vol. 37, no. 3, pp. 271–278, 1981.
- [73] A. Manthiram, "A reflection on lithium-ion battery cathode chemistry," *Nature communications*, vol. 11, no. 1, p. 1550, 2020.
- [74] J. B. Goodenough, "Design considerations," *Solid State Ionics*, vol. 69, no. 3-4, pp. 184–198, 1994.

- [75] C. Julien, A. Mauger, K. Zaghib, and H. Groult, “Comparative Issues of Cathode Materials for Li-Ion Batteries,” *Inorganics*, vol. 2, no. 1, pp. 132–154, 2014.
- [76] S.-T. Myung, F. Maglia, K.-J. Park, C. S. Yoon, P. Lamp, S.-J. Kim, and Y.-K. Sun, “Nickel-Rich Layered Cathode Materials for Automotive Lithium-Ion Batteries: Achievements and Perspectives,” *ACS Energy Letters*, vol. 2, no. 1, pp. 196–223, 2017.
- [77] Bundesanstalt für Geowissenschaften und Rohstoffe, *Analyse des artisanalen Kupfer-Kobalt-Sektors in den Provinzen Haut-Katanga und Lualaba in der Demokratischen Republik Kongo*. Hannover: BGR, 2019.
- [78] M. S. Whittingham, “Ultimate limits to intercalation reactions for lithium batteries,” *Chemical reviews*, vol. 114, no. 23, pp. 11414–11443, 2014.
- [79] Z. Chen, W. Zhang, and Z. Yang, “A review on cathode materials for advanced lithium ion batteries: microstructure designs and performance regulations,” *Nanotechnology*, vol. 31, no. 1, p. 012001, 2020.
- [80] Y. Sun and B. Goh, “Tesla wins China approval to build Model 3 vehicles with LFP batteries: ministry,” 2020. <https://www.reuters.com/article/us-tesla-china-electric-batteries/tesla-wins-china-approval-to-build-model-3-vehicles-with-lfp-batteries-ministry-idUSKBN23IOVT>, last accessed on 28.12.2021.
- [81] A. Home, “Column: Volkswagen powers up for the electric vehicle revolution,” 2021. <https://www.reuters.com/business/energy/volkswagen-powers-up-electric-vehicle-revolution-andy-home-2021-03-24/>, last accessed on 28.12.2021.
- [82] W. Lee, S. Muhammad, C. Sergey, H. Lee, J. Yoon, Y.-M. Kang, and W.-S. Yoon, “Advances in the Cathode Materials for Lithium Rechargeable Batteries,” *Angewandte Chemie (International ed. in English)*, vol. 59, no. 7, pp. 2578–2605, 2020.
- [83] L. de Biasi, B. Schwarz, T. Brezesinski, P. Hartmann, J. Janek, and H. Ehrenberg, “Chemical, Structural, and Electronic Aspects of Formation and Degradation Behavior on Different Length Scales of Ni-Rich NCM and Li-Rich HE-NCM Cathode Materials in Li-Ion Batteries,” *Advanced Materials*, vol. 31, no. 26, p. e1900985, 2019.
- [84] N. Nitta, F. Wu, J. T. Lee, and G. Yushin, “Li-ion battery materials: present and future,” *Materials Today*, vol. 18, no. 5, pp. 252–264, 2015.
- [85] P. Teichert, G. G. Eshetu, H. Jahnke, and E. Figgemeier, “Degradation and Aging Routes of Ni-Rich Cathode Based Li-Ion Batteries,” *Batteries*, vol. 6, no. 1, p. 8, 2020.
- [86] InvestmentMine, “Base Metals,” 09.04.2021. <https://www.mining.com/markets/commodity/group/base-metals/#>, last accessed on 09.04.2021.

- [87] S. Ahmed, P. A. Nelson, K. G. Gallagher, N. Susarla, and D. W. Dees, "Cost and energy demand of producing nickel manganese cobalt cathode material for lithium ion batteries," *Journal of Power Sources*, vol. 342, pp. 733–740, 2017.
- [88] R. Jung, M. Metzger, F. Maglia, C. Stinner, and H. A. Gasteiger, "Oxygen Release and Its Effect on the Cycling Stability of $\text{LiNi}_x\text{Mn}_y\text{Co}_z\text{O}_2$ (NMC) Cathode Materials for Li-Ion Batteries," *Journal of The Electrochemical Society*, vol. 164, no. 7, pp. A1361–A1377, 2017.
- [89] S.-C. Yin, Y.-H. Rho, I. Swainson, and L. F. Nazar, "X-ray/Neutron Diffraction and Electrochemical Studies of Lithium De/Re-Intercalation $\text{Li}_{1-x}\text{Co}_{1/3}\text{Ni}_{1/3}\text{Mn}_{1/3}\text{O}_2$ ($x = 0 - 1$)," *Chemistry of Materials*, vol. 18, no. 7, pp. 1901–1910, 2006.
- [90] K. Min and E. Cho, "Intrinsic origin of intra-granular cracking in Ni-rich layered oxide cathode materials," *Physical chemistry chemical physics : PCCP*, vol. 20, no. 14, pp. 9045–9052, 2018.
- [91] J. Yang and J. S. Tse, "Li ion diffusion mechanisms in LiFePO_4 : an ab initio molecular dynamics study," *The journal of physical chemistry. A*, vol. 115, no. 45, pp. 13045–13049, 2011.
- [92] A. Yamada, S. C. Chung, and K. Hinokuma, "Optimized LiFePO_4 for Lithium Battery Cathodes," *Solid State Ionics*, vol. 148, no. 3, p. A224, 2001.
- [93] A. S. Andersson, "Thermal Stability of LiFePO_4 -Based Cathodes," *Electrochemical and Solid-State Letters*, vol. 3, no. 2, p. 66, 1999.
- [94] Y. Janssen, D. Santhanagopalan, D. Qian, M. Chi, X. Wang, C. Hoffmann, Y. S. Meng, and P. G. Khalifah, "Reciprocal Salt Flux Growth of LiFePO_4 Single Crystals with Controlled Defect Concentrations," *Chemistry of Materials*, vol. 25, no. 22, pp. 4574–4584, 2013.
- [95] K. Jensen, M. Christensen, C. Tyrsted, and B. Brummerstedt Iversen, "Real-time synchrotron powder X-ray diffraction study of the antisite defect formation during sub- and supercritical synthesis of LiFePO_4 and $\text{LiFe}_{1-x}\text{Mn}_x\text{PO}_4$ nanoparticles," *Journal of Applied Crystallography*, vol. 44, no. 2, pp. 287–294, 2011.
- [96] K. Zaghib, A. Guerfi, P. Hovington, A. Vijh, M. Trudeau, A. Mauger, J. B. Goodenough, and C. M. Julien, "Review and analysis of nanostructured olivine-based lithium rechargeable batteries: Status and trends," *Journal of Power Sources*, vol. 232, pp. 357–369, 2013.
- [97] B. Scrosati and J. Garche, "Lithium batteries: Status, prospects and future," *Journal of Power Sources*, vol. 195, no. 9, pp. 2419–2430, 2010.

-
- [98] T. Maxisch and G. Ceder, “Elastic properties of olivine Li_xFePO_4 from first principles,” *Physical Review B*, vol. 73, no. 17, p. 1101, 2006.
- [99] R. Korthauer, ed., *Handbuch Lithium-Ionen-Batterien*. Berlin, Heidelberg and s.l.: Springer Berlin Heidelberg, 2013.
- [100] T. R. Jow, K. Xu, O. Borodin, and M. Ue, eds., *Electrolytes for Lithium and Lithium-Ion Batteries*, vol. 58 of *Modern Aspects of Electrochemistry*. New York, NY and s.l.: Springer New York, 2014.
- [101] K. Xu, “Nonaqueous liquid electrolytes for lithium-based rechargeable batteries,” *Chemical reviews*, vol. 104, no. 10, pp. 4303–4417, 2004.
- [102] K. Xu, “Electrolytes and interphases in Li-ion batteries and beyond,” *Chemical reviews*, vol. 114, no. 23, pp. 11503–11618, 2014.
- [103] E. Markevich, G. Salitra, F. Chesneau, M. Schmidt, and D. Aurbach, “Very Stable Lithium Metal Stripping–Plating at a High Rate and High Areal Capacity in Fluoroethylene Carbonate-Based Organic Electrolyte Solution,” *ACS Energy Letters*, vol. 2, no. 6, pp. 1321–1326, 2017.
- [104] X. Huang, “Separator technologies for lithium-ion batteries,” *Journal of Solid State Electrochemistry*, vol. 15, no. 4, pp. 649–662, 2011.
- [105] H. Lee, M. Yanilmaz, O. Toprakci, K. Fu, and X. Zhang, “A review of recent developments in membrane separators for rechargeable lithium-ion batteries,” *Energy Environ. Sci.*, vol. 7, no. 12, pp. 3857–3886, 2014.
- [106] M. F. Lagadec, R. Zahn, and V. Wood, “Characterization and performance evaluation of lithium-ion battery separators,” *Nature Energy*, vol. 4, no. 1, pp. 16–25, 2019.
- [107] A. Barré, B. Deguilhem, S. Grolleau, M. Gérard, F. Suard, and D. Riu, “A review on lithium-ion battery ageing mechanisms and estimations for automotive applications,” *Journal of Power Sources*, vol. 241, no. 9, pp. 680–689, 2013.
- [108] M. Dubarry, N. Qin, and P. Brooker, “Calendar aging of commercial Li-ion cells of different chemistries – A review,” *Current Opinion in Electrochemistry*, vol. 9, no. 10, pp. 106–113, 2018.
- [109] Y.-X. Lin, Z. Liu, K. Leung, L.-Q. Chen, P. Lu, and Y. Qi, “Connecting the irreversible capacity loss in Li-ion batteries with the electronic insulating properties of solid electrolyte interphase (SEI) components,” *Journal of Power Sources*, vol. 309, pp. 221–230, 2016.

- [110] S. H. Ng, C. Vix-Guterl, P. Bernardo, N. Tran, J. Ufheil, H. Buqa, J. Dentzer, R. Gadiou, M. E. Spahr, D. Goers, and P. Novák, “Correlations between surface properties of graphite and the first cycle specific charge loss in lithium-ion batteries,” *Carbon*, vol. 47, no. 3, pp. 705–712, 2009.
- [111] P. Keil, *Aging of Lithium-Ion Batteries in Electric Vehicles*. PhD thesis, Technische Universität München, München, 2017.
- [112] N. Legrand, B. Knosp, P. Desprez, F. Lopicque, and S. Raël, “Physical characterization of the charging process of a Li-ion battery and prediction of Li plating by electrochemical modelling,” *Journal of Power Sources*, vol. 245, pp. 208–216, 2014.
- [113] T. Waldmann, B.-I. Hogg, and M. Wohlfahrt-Mehrens, “Li plating as unwanted side reaction in commercial Li-ion cells – A review,” *Journal of Power Sources*, vol. 384, pp. 107–124, 2018.
- [114] D. Aurbach, B. Markovsky, I. Weissman, E. Levi, and Y. Ein-Eli, “On the correlation between surface chemistry and performance of graphite negative electrodes for Li ion batteries,” *Electrochimica Acta*, vol. 45, no. 1-2, pp. 67–86, 1999.
- [115] V. A. Sethuraman, L. J. Hardwick, V. Srinivasan, and R. Kostecki, “Surface structural disordering in graphite upon lithium intercalation/deintercalation,” *Journal of Power Sources*, vol. 195, no. 11, pp. 3655–3660, 2010.
- [116] C. K. Chan, H. Peng, G. Liu, K. McIlwrath, X. F. Zhang, R. A. Huggins, and Y. Cui, “High-performance lithium battery anodes using silicon nanowires,” *Nature nanotechnology*, vol. 3, no. 1, pp. 31–35, 2008.
- [117] H. Wu, G. Chan, J. W. Choi, I. Ryu, Y. Yao, M. T. McDowell, S. W. Lee, A. Jackson, Y. Yang, L. Hu, and Y. Cui, “Stable cycling of double-walled silicon nanotube battery anodes through solid-electrolyte interphase control,” *Nature nanotechnology*, vol. 7, no. 5, pp. 310–315, 2012.
- [118] X. Zuo, J. Zhu, P. Müller-Buschbaum, and Y.-J. Cheng, “Silicon based lithium-ion battery anodes: A chronicle perspective review,” *Nano Energy*, vol. 31, no. 4, pp. 113–143, 2017.
- [119] D. Aurbach, “A short review of failure mechanisms of lithium metal and lithiated graphite anodes in liquid electrolyte solutions,” *Solid State Ionics*, vol. 148, no. 3-4, pp. 405–416, 2002.
- [120] C. R. Birkl, M. R. Roberts, E. McTurk, P. G. Bruce, and D. A. Howey, “Degradation diagnostics for lithium ion cells,” *Journal of Power Sources*, vol. 341, no. 1, pp. 373–386, 2017.

- [121] S. Hwang, E. Jo, K. Y. Chung, K. S. Hwang, S. M. Kim, and W. Chang, "Structural Evolution of $\text{Li}_x\text{Ni}_y\text{Mn}_z\text{Co}_{1-y-z}\text{O}_2$ Cathode Materials during High-Rate Charge and Discharge," *The Journal of Physical Chemistry Letters*, vol. 8, no. 23, pp. 5758–5763, 2017.
- [122] R. Jung, P. Strobl, F. Maglia, C. Stinner, and H. A. Gasteiger, "Temperature Dependence of Oxygen Release from $\text{LiNi}_{0.6}\text{Mn}_{0.2}\text{Co}_{0.2}\text{O}_2$ (NMC622) Cathode Materials for Li-Ion Batteries," *Journal of The Electrochemical Society*, vol. 165, no. 11, pp. A2869–A2879, 2018.
- [123] E. Hu, X. Wang, X. Yu, and X.-Q. Yang, "Probing the Complexities of Structural Changes in Layered Oxide Cathode Materials for Li-Ion Batteries during Fast Charge-Discharge Cycling and Heating," *Accounts of chemical research*, vol. 51, no. 2, pp. 290–298, 2018.
- [124] M. Koltypin, D. Aurbach, L. Nazar, and B. Ellis, "More on the performance of LiFePO_4 electrodes—The effect of synthesis route, solution composition, aging, and temperature," *Journal of Power Sources*, vol. 174, no. 2, pp. 1241–1250, 2007.
- [125] S.-K. Jung, H. Gwon, J. Hong, K.-Y. Park, D.-H. Seo, H. Kim, J. Hyun, W. Yang, and K. Kang, "Understanding the Degradation Mechanisms of $\text{LiNi}_{0.5}\text{Co}_{0.2}\text{Mn}_{0.3}\text{O}_2$ Cathode Material in Lithium Ion Batteries," *Advanced Energy Materials*, vol. 4, no. 1, p. 1300787, 2014.
- [126] M. Dubarry and B. Y. Liaw, "Identify capacity fading mechanism in a commercial LiFePO_4 cell," *Journal of Power Sources*, vol. 194, no. 1, pp. 541–549, 2009.
- [127] R. D. Shannon, "Revised effective ionic radii and systematic studies of interatomic distances in halides and chalcogenides," *Acta Crystallographica Section A*, vol. 32, no. 5, pp. 751–767, 1976.
- [128] H. Xie, K. Du, G. Hu, Z. Peng, and Y. Cao, "The Role of Sodium in $\text{LiNi}_{0.8}\text{Co}_{0.15}\text{Al}_{0.05}\text{O}_2$ Cathode Material and Its Electrochemical Behaviors," *The Journal of Physical Chemistry C*, vol. 120, no. 6, pp. 3235–3241, 2016.
- [129] R. Xiong, Y. Pan, W. Shen, H. Li, and F. Sun, "Lithium-ion battery aging mechanisms and diagnosis method for automotive applications: Recent advances and perspectives," *Renewable and Sustainable Energy Reviews*, vol. 131, p. 110048, 2020.
- [130] M. S. Ding, K. Xu, S. S. Zhang, K. Amine, G. L. Henriksen, and T. R. Jow, "Change of Conductivity with Salt Content, Solvent Composition, and Temperature for Electrolytes of LiPF_6 in Ethylene Carbonate-Ethyl Methyl Carbonate," *Journal of The Electrochemical Society*, vol. 148, no. 10, p. A1196, 2001.

- [131] B. P. Matadi, S. Geniès, A. Delaille, T. Waldmann, M. Kasper, M. Wohlfahrt-Mehrens, F. Aguesse, E. Bekaert, I. Jiménez-Gordon, L. Daniel, X. Fleury, M. Bardet, J.-F. Martin, and Y. Bultel, “Effects of Biphenyl Polymerization on Lithium Deposition in Commercial Graphite/NMC Lithium-Ion Pouch-Cells during Calendar Aging at High Temperature,” *Journal of The Electrochemical Society*, vol. 164, no. 6, pp. A1089–A1097, 2017.
- [132] J. Cannarella and C. B. Arnold, “Ion transport restriction in mechanically strained separator membranes,” *Journal of Power Sources*, vol. 226, pp. 149–155, 2013.
- [133] J. Cannarella, X. Liu, C. Z. Leng, P. D. Sinko, G. Y. Gor, and C. B. Arnold, “Mechanical Properties of a Battery Separator under Compression and Tension,” *Journal of The Electrochemical Society*, vol. 161, no. 11, pp. F3117–F3122, 2014.
- [134] G. Y. Gor, J. Cannarella, C. Z. Leng, A. Vishnyakov, and C. B. Arnold, “Swelling and softening of lithium-ion battery separators in electrolyte solvents,” *Journal of Power Sources*, vol. 294, no. 10, pp. 167–172, 2015.
- [135] C. Peabody and C. B. Arnold, “The role of mechanically induced separator creep in lithium-ion battery capacity fade,” *Journal of Power Sources*, vol. 196, no. 19, pp. 8147–8153, 2011.
- [136] F. Ebert, A. Oberbauer, M. A. Cabañero, G. Sestl, and M. Lienkamp, “Simulation of Lithium Plating Due to Spatial Inhomogeneous Separator Strain in Lithium-Ion-Cells,” *International Journal of Automotive Engineering*, vol. 10, no. 2, pp. 242–248, 2019.
- [137] T. C. Bach, S. F. Schuster, E. Fleder, J. Müller, M. J. Brand, H. Lorrman, A. Jossen, and G. Sestl, “Nonlinear aging of cylindrical lithium-ion cells linked to heterogeneous compression,” *Journal of Energy Storage*, vol. 5, pp. 212–223, 2016.
- [138] P. Arora, R. E. White, and M. Doyle, “Capacity Fade Mechanisms and Side Reactions in Lithium-Ion Batteries,” *Journal of The Electrochemical Society*, vol. 145, no. 10, pp. 3647–3667, 1998.
- [139] S.-T. Myung, Y. Hitoshi, and Y.-K. Sun, “Electrochemical behavior and passivation of current collectors in lithium-ion batteries,” *J. Mater. Chem.*, vol. 21, no. 27, p. 9891, 2011.
- [140] T. Waldmann, S. Gorse, T. Samtleben, G. Schneider, V. Knoblauch, and M. Wohlfahrt-Mehrens, “A Mechanical Aging Mechanism in Lithium-Ion Batteries,” *Journal of The Electrochemical Society*, vol. 161, no. 10, pp. A1742–A1747, 2014.
- [141] M. Bauer, M. Wachtler, H. Stöwe, J. V. Persson, and M. A. Danzer, “Understanding the dilation and dilation relaxation behavior of graphite-based lithium-ion cells,” *Journal of Power Sources*, vol. 317, no. 11, pp. 93–102, 2016.

- [142] B. Rieger, S. Schlueter, S. V. Erhard, J. Schmalz, G. Reinhart, and A. Jossen, “Multi-scale investigation of thickness changes in a commercial pouch type lithium-ion battery,” *Journal of Energy Storage*, vol. 6, no. 9, pp. 213–221, 2016.
- [143] D. Sauerteig, S. Ivanov, H. Reinshagen, and A. Bund, “Reversible and irreversible dilation of lithium-ion battery electrodes investigated by in-situ dilatometry,” *Journal of Power Sources*, vol. 342, no. 10, pp. 939–946, 2017.
- [144] S. Ivanov, D. Sauerteig, A. Dimitrova, S. Krischok, and A. Bund, “Irreversible dilation of graphite composite anodes influenced by vinylene carbonate,” *Journal of Power Sources*, vol. 457, p. 228020, 2020.
- [145] B. Rieger, S. F. Schuster, S. V. Erhard, P. J. Osswald, A. Rheinfeld, C. Willmann, and A. Jossen, “Multi-directional laser scanning as innovative method to detect local cell damage during fast charging of lithium-ion cells,” *Journal of Energy Storage*, vol. 8, no. 2, pp. 1–5, 2016.
- [146] J. Sturm, F. B. Spingler, B. Rieger, A. Rheinfeld, and A. Jossen, “Non-Destructive Detection of Local Aging in Lithium-Ion Pouch Cells by Multi-Directional Laser Scanning,” *Journal of The Electrochemical Society*, vol. 164, no. 7, pp. A1342–A1351, 2017.
- [147] F. B. Spingler, W. Wittmann, J. Sturm, B. Rieger, and A. Jossen, “Optimum fast charging of lithium-ion pouch cells based on local volume expansion criteria,” *Journal of Power Sources*, vol. 393, no. 5, pp. 152–160, 2018.
- [148] G. Bohn, J. Taub, A. Linke, S. Bayer, D. Oeser, A. Ziegler, P. Ettl, and A. Ackva, “High-resolution Interferometric Measurement of Thickness Change on a Lithium-Ion Pouch Battery,” *IOP Conference Series: Earth and Environmental Science*, vol. 281, no. 1, p. 012030, 2019.
- [149] J. R. Dahn, “Phase diagram of Li_xC_6 ,” *Physical Review B*, vol. 44, no. 17, pp. 9170–9177, 1991.
- [150] T. Ohzuku, Y. Iwakoshi, and K. Sawai, “Formation of Lithium-Graphite Intercalation Compounds in Nonaqueous Electrolytes and Their Application as a Negative Electrode for a Lithium Ion (Shuttlecock) Cell,” *Journal of The Electrochemical Society*, vol. 140, no. 9, pp. 2490–2498, 1993.
- [151] T. Zhang, D. Li, Z. Tao, and J. Chen, “Understanding electrode materials of rechargeable lithium batteries via DFT calculations,” *Progress in Natural Science: Materials International*, vol. 23, no. 3, pp. 256–272, 2013.
- [152] P. Daubinger, F. Ebert, S. Hartmann, and G. A. Giffin, “Impact of electrochemical and mechanical interactions on lithium-ion battery performance investigated by operando dilatometry,” *Journal of Power Sources*, vol. 488, p. 229457, 2021.

- [153] Micro-Epsilon, “Laser triangulation.” <https://www.micro-epsilon.com/service/glossar/Laser-Triangulation.html?sLang=us>, last accessed on 07.01.2022.
- [154] W. Pastorius, “Triangulation Sensors - An Overview.” https://tu-dresden.de/bu/umwelt/geo/ipf/photogrammetrie/ressourcen/dateien/elearning/documents_content/elearn_triangulsensor?lang=de, last accessed on 07.01.2022.
- [155] C. Hammond, *The basics of crystallography and diffraction*, vol. 21 of *International Union of Crystallography book series*. Oxford and New York: Oxford University Press, fourth edition, reprinted (with corrections) ed., 2016.
- [156] W. Massa, *Kristallstrukturbestimmung*. Studienbücher Chemie, Wiesbaden: Springer Fachmedien Wiesbaden, 8., überarb. Aufl. ed., 2015.
- [157] I. H. Buchberger, *Electrochemical and structural investigations on lithium-ion battery materials and related degradation processes*. PhD thesis, Technische Universität München, München, 2016.
- [158] H. M. Rietveld, “A profile refinement method for nuclear and magnetic structures,” *Journal of Applied Crystallography*, vol. 2, no. 2, pp. 65–71, 1969.
- [159] R. A. Young, *The Rietveld method*, vol. 5 of *Oxford science publications*. Oxford: Oxford Univ. Press, 1993.
- [160] F. Nagler, *Investigations of component stabilities within cathode composites of novel battery systems*. Master thesis, Technische Universität Darmstadt, Darmstadt, 2020.
- [161] T. P. Heins, *Entwicklung Impedanzspektroskopie-basierter Methoden zur mechanistischen Untersuchung der Bildung von Oberflächenfilmen auf Lithium-Ionen-Elektroden*. PhD thesis, Technischen Universität Carolo-Wilhelmina zu Braunschweig, Braunschweig, 2015.
- [162] M. E. Orazem and B. Tribollet, *Electrochemical impedance spectroscopy*. The Electrochemical Society series, Hoboken, NJ: Wiley, 2008.
- [163] U. Tröltzsch, *Entwurf von physikalischen und chemischen Modellen für die Impedanzspektroskopie*. Habilitation, Technische Universität Chemnitz, Chemnitz, 2015.
- [164] P. Daubinger, *Fabrication and Characterization of Magnesium Powder Anodes for High Energy Batteries*. Master thesis, Universität Stuttgart, Stuttgart, 2018.
- [165] D. U. Sauer, “Impedanzspektroskopie – Eine Methode, viele Anwendungen,” *Technische Mitteilungen*, no. 99, pp. 7–11, 2006.

-
- [166] D. Andre, M. Meiler, K. Steiner, H. Walz, T. Soczka-Guth, and D. U. Sauer, “Characterization of high-power lithium-ion batteries by electrochemical impedance spectroscopy. II: Modelling,” *Journal of Power Sources*, vol. 196, no. 12, pp. 5349–5356, 2011.
- [167] D. Kane, W. Grassi, R. Sturrock, and P. V. Balint, “A brief history of musculoskeletal ultrasound: ‘From bats and ships to babies and hips’,” *Rheumatology (Oxford, England)*, vol. 43, no. 7, pp. 931–933, 2004.
- [168] G. L. Workman, D. Kishoni, and P. O. Moore, eds., *Ultrasonic testing*, vol. Vol. 7 of *Nondestructive testing handbook*. Columbus, Ohio: American Society for Nondestructive Testing, 3. ed. ed., 2007.
- [169] G. Davies, K. W. Knehr, B. van Tassell, T. Hodson, S. Biswas, A. G. Hsieh, and D. A. Steingart, “State of Charge and State of Health Estimation Using Electrochemical Acoustic Time of Flight Analysis,” *Journal of The Electrochemical Society*, vol. 164, no. 12, pp. A2746–A2755, 2017.
- [170] L. Gold, T. Bach, W. Virsik, A. Schmitt, J. Müller, T. E. Staab, and G. SEXTL, “Probing lithium-ion batteries’ state-of-charge using ultrasonic transmission – Concept and laboratory testing,” *Journal of Power Sources*, vol. 343, pp. 536–544, 2017.
- [171] A. G. Hsieh, S. Bhadra, B. J. Hertzberg, P. J. Gjeltema, A. Goy, J. W. Fleischer, and D. A. Steingart, “Electrochemical-acoustic time of flight: in operando correlation of physical dynamics with battery charge and health,” *Energy Environ. Sci.*, vol. 8, no. 5, pp. 1569–1577, 2015.
- [172] L. Gold, *Methods for the state estimation of lithium-ion batteries*. PhD thesis, Julius-Maximilians-Universität Würzburg, Würzburg, 2023.
- [173] H. Baule and E. Müller, “Messung elastischer Eigenschaften von Gesteinen,” in *Geophysik I / Geophysics I* (S. Flüge and J. Bartels, eds.), vol. 10 / 47 of *Handbuch der Physik / Encyclopedia of Physics*, pp. 169–201, Berlin, Heidelberg: Springer Berlin Heidelberg, 1956.
- [174] M. Lowe, “ULTRASONICS,” in *Encyclopedia of vibration* (S. Braun, D. J. Ewins, and S. S. Rao, eds.), pp. 1437–1441, San Diego: Academic Press, 2001.
- [175] J. Krautkrämer and H. Krautkrämer, *Werkstoffprüfung mit Ultraschall*. Berlin and Göttingen and Heidelberg: Springer, 1961.
- [176] P. Regtien and E. Dertien, “Acoustic sensors,” in *Sensors for mechatronics* (P. Regtien and E. Dertien, eds.), vol. 11, pp. 267–303, Amsterdam and Oxford and Cambridge, MA: Elsevier, 2018.

- [177] J. E. Aldrich, “Basic physics of ultrasound imaging,” *Critical Care Medicine*, vol. 35, no. 5 Suppl, pp. 131–137, 2007.
- [178] J.-S. Lee and J. Carlos Santamarina, “P-Wave Reflection Imaging,” *Geotechnical Testing Journal*, vol. 28, no. 2, p. 12595, 2005.
- [179] A. Hijazi, “Ultrasonic Testing,” 2021. <https://sites.google.com/view/alahijazi/classes/non-destructive-testing-ndt>, last accessed on 04.01.2022.
- [180] Olympus, “Ultrasonic Flaw Detection Tutorial - Beam Characteristics.” <https://www.olympus-ims.com/en/ndt-tutorials/flaw-detection/beam-characteristics/>, last accessed on 05.01.2022.
- [181] B. Barshan, “Fast processing techniques for accurate ultrasonic range measurements,” *Measurement Science and Technology*, vol. 11, no. 1, pp. 45–50, 2000.
- [182] L. H. Le, “An investigation of pulse-timing techniques for broadband ultrasonic velocity determination in cancellous bone: a simulation study,” *Physics in medicine and biology*, vol. 43, no. 8, pp. 2295–2308, 1998.
- [183] L. Svilainis, “Review of high resolution time of flight estimation techniques for ultrasonic signals,” in *International Conference on NDT*, pp. 1–12, 2013.
- [184] F. G. Ebert, *Analyse und Optimierung elektrochemisch-mechanischer Effekte bei Lithium-Ionen-Zellen*. Düren: Shaker Verlag GmbH, 2022.
- [185] P. Daubinger, M. Schelter, R. Petersohn, F. Nagler, S. Hartmann, M. Herrmann, and G. A. Giffin, “Impact of Bracing on Large Format Prismatic Lithium-Ion Battery Cells during Aging,” *Advanced Energy Materials*, vol. 44, p. 2102448, 2021.
- [186] S. Feiler, P. Daubinger, L. Gold, S. Hartmann, and G. A. Giffin, “Interplay between Elastic and Electrochemical Properties during Active Material Transitions and Aging of a Lithium-Ion Battery,” *Batteries & Supercaps*, vol. 6, no. 4, 2023.
- [187] P. Daubinger, M. Göttlinger, S. Hartmann, and G. A. Giffin., “Consequences of Different Pressures and Electrolytes on the Irreversible Expansion of Lithium Metal Half Cells,” *Batteries & Supercaps*, vol. 6, no. 2, 2023.
- [188] M. D. Levi and D. Aurbach, “The mechanism of lithium intercalation in graphite film electrodes in aprotic media. Part 1. High resolution slow scan rate cyclic voltammetric studies and modeling,” *Journal of Electroanalytical Chemistry*, vol. 421, no. 1-2, pp. 79–88, 1997.
- [189] L. Zheng, J. Zhu, D. D.-C. Lu, G. Wang, and T. He, “Incremental capacity analysis and differential voltage analysis based state of charge and capacity estimation for lithium-ion batteries,” *Energy*, vol. 150, pp. 759–769, 2018.

- [190] J. O. Besenhard, M. Winter, J. Yang, and W. Biberacher, "Filming mechanism of lithium-carbon anodes in organic and inorganic electrolytes," *Journal of Power Sources*, vol. 54, no. 2, pp. 228–231, 1995.
- [191] K. R. Kganyago and P. E. Ngoepe, "Structural and electronic properties of lithium intercalated graphite LiC_6 ," *Physical Review B*, vol. 68, no. 20, 2003.
- [192] J. Cannarella and C. B. Arnold, "Stress evolution and capacity fade in constrained lithium-ion pouch cells," *Journal of Power Sources*, vol. 245, pp. 745–751, 2014.
- [193] H. Pegel, O. von Kessel, P. Heugel, T. Deich, J. Tübke, K. P. Birke, and D. U. Sauer, "Volume and thickness change of NMC811 | SiO_x -graphite large-format lithium-ion cells: from pouch cell to active material level," *Journal of Power Sources*, vol. 537, p. 231443, 2022.
- [194] P. Kargl, V. Drews, P. Daubinger, O. Schweighofer, M. Marinaro, G. A. Giffin, M. Wohlfahrt-Mehrens, and A. Thaler, "Investigation of voltage and expansion hysteresis of Si-alloy-C/NMC622 pouch cells using dilatometry," *Journal of Power Sources*, vol. 548, p. 232042, 2022.
- [195] K. W. Knehr, T. Hodson, C. Bommier, G. Davies, A. Kim, and D. A. Steingart, "Understanding Full-Cell Evolution and Non-chemical Electrode Crosstalk of Li-Ion Batteries," *Joule*, vol. 2, no. 6, pp. 1146–1159, 2018.
- [196] C. M. Sayers and L. D. den Boer, "Porosity variation of elastic wave velocities in clean sandstones," *Geophysical Prospecting*, vol. 69, no. 8-9, pp. 1733–1744, 2021.
- [197] M. R. J. Wyllie, A. R. Gregory, and L. W. Gardner, "ELASTIC WAVE VELOCITIES IN HETEROGENEOUS AND POROUS MEDIA," *Geophysics*, vol. 21, no. 1, pp. 41–70, 1956.
- [198] M. Ue and K. Uosaki, "Recent progress in liquid electrolytes for lithium metal batteries," *Current Opinion in Electrochemistry*, vol. 17, pp. 106–113, 2019.
- [199] R. Jung, M. Metzger, D. Haering, S. Solchenbach, C. Marino, N. Tsiouvaras, C. Stinner, and H. A. Gasteiger, "Consumption of Fluoroethylene Carbonate (FEC) on Si-C Composite Electrodes for Li-Ion Batteries," *Journal of The Electrochemical Society*, vol. 163, no. 8, pp. A1705–A1716, 2016.
- [200] X.-Q. Zhang, X.-B. Cheng, X. Chen, C. Yan, and Q. Zhang, "Fluoroethylene Carbonate Additives to Render Uniform Li Deposits in Lithium Metal Batteries," *Advanced Functional Materials*, vol. 27, no. 10, p. 1605989, 2017.
- [201] M. Göttlinger, P. Daubinger, W. Stracke, S. Hartmann, and G. A. Giffin, "Influence of external pressure on silicon electrodes in lithium-ion cells," *Electrochimica Acta*, vol. 419, p. 140354, 2022.

Acknowledgement

First of all, I would like to thank Prof. Dr. Gerhard Sextl for giving me the opportunity to conduct my PhD thesis at the Fraunhofer ISC in Würzburg. I would also like to thank him for the supervision and the discussions throughout the thesis.

For the review of this dissertation, I want to thank Prof. Dr. Gerhard Sextl and Prof. Dr. Andreas Jossen for their time and interest in my research.

Furthermore, I would like to thank Dr. Sarah Hartmann and Dr. Guinevere A. Giffin for their valuable support and guidance during this time. Without your patience and the numerous discussions, this work would not have been possible. You helped me to improve myself on a professional and personal level.

This work would not have been possible without the active support of my colleagues at Fraunhofer R&D Center for Electromobility (FZEB). I would especially like to thank Vilija Anfimovaite, Elena Fleder, Ajana Gebel and Franziska Stahl for their support in the lab. Without your help, a lot of work in the lab would certainly not have been possible.

Moreover, I would like to thank all my PhD student colleagues, Dr. Begüm Bozkaya, Lisa Brändler, Selma Dahms, Dr. Fabian Ebert, Simon Feiler, Dr. Lukas Gold, Mara Göttlinger, Dr. Michael Hofmann, Felix Nagler, Dr. Lukas Niklaus, Dr. Sven Macher, Matthias Rumpel, Razieh Sarani, Mario Weller, Andreas 'Junior' Wolf, Dr. Paul Wulfert-Holzmann and Simon Ziegler for the numerous discussions and the various after-work drinks. I would like to emphasize Mara, Fabian, Felix and Simon, as I collaborated closely with them. I hope you enjoyed it as much as I did.

Not to be forgotten are all the other colleagues at FZEB and Center Smart Materials and Adaptive Systems (CeSMA) and especially Andreas Gronbach. Thanks for all the things I learned from you.

I also want to thank my two students Benedikt Herbert and Yazan Sweiss for their great support during their project work and internship. I wish you all the best for your future.

My special thanks goes out to Dr. Matthias Herrmann, Ronny Petersohn and Dr. Matthias Schelter from the Intilion GmbH for their great support and cooperation in the investigations of the effect of bracing on the aging of prismatic LIB battery cells.

I gratefully acknowledge the funding received during this thesis from the Federal Ministry for Economic Affairs and Climate Action through the project ReViSEDBatt and from the European Union's Horizon 2020 Research & Innovation programme through the project SPARTACUS.

Last but not least, I would like to thank my love Sina, my parents and all the rest of my family for your endless love and support. You helped me to get through the challenging times in the last years. Thanks for brightening up my life. Danke Sina, Mama, Papa, Patrick, Nele und Finn!

Appendixes

Research Articles

1. P. Daubinger, F. Ebert, S. Hartmann, and G. A. Giffin, 'Impact of electrochemical and mechanical interactions on lithium-ion battery performance investigated by operando dilatometry', *Journal of Power Sources*, vol. 488, p. 229457, 2021, <https://doi.org/10.1016/j.jpowsour.2021.229457>.
2. P. Daubinger, M. Schelter, R. Petersohn, F. Nagler, S. Hartmann, M. Herrmann, and G. A. Giffin, 'Impact of Bracing on Large Format Prismatic Lithium-Ion Battery Cells during Aging', *Advanced Energy Materials*, vol. 44, p. 2102448, 2021, <https://doi.org/10.1002/aenm.202102448>. The paper was also featured as front cover: P. Daubinger, M. Schelter, R. Petersohn, F. Nagler, S. Hartmann, M. Herrmann, and G. A. Giffin, 'Impact of Bracing on Large Format Prismatic Lithium-Ion Battery Cells during Aging (Adv. Energy Mater. 10/2022)', *Advanced Energy Materials*, 12(10), 2270039, <https://doi.org/10.1002/aenm.202270039>.
3. S. Feiler*, P. Daubinger*, L. Gold, S. Hartmann, and G. A. Giffin, 'Interplay between Elastic and Electrochemical Properties during Active Material Transitions and Aging of a Lithium-Ion Battery', *Batteries & Supercaps*, vol. 6, no. 4, 2023, <https://doi.org/10.1002/batt.202200518>. *S.F. and P.D. contributed equally to this work.
4. P. Daubinger, M. Göttliger, S. Hartmann, and G. A. Giffin, 'Consequences of Different Pressures and Electrolytes on the Irreversible Expansion of Lithium Metal Half Cells', *Batteries & Supercaps*, vol. 6, no. 2, 2023, <https://doi.org/10.1002/batt.202200452>.

Other Publications

1. M. Göttliger, P. Daubinger, W. Stracke, S. Hartmann, and G. A. Giffin, 'Influence of external pressure on silicon electrodes in lithium-ion cells', *Electrochimica Acta*, vol. 419, p. 140354, 2022, <https://doi.org/10.1016/j.electacta.2022.140354>.
2. P. Kargl, V. Drews, P. Daubinger, O. Schweighofer, M. Marinaro, G. A. Giffin, M. Wohlfart-Mehrens and A. Thaler, 'Investigation of voltage and expansion hysteresis of Si-alloy-C/NMC622 pouch cells using dilatometry', *Journal of Power Sources*, vol. 548, p. 232042, 2022, <https://doi.org/10.1016/j.jpowsour.2022.232042>.

Conference Contribution

Presentation

1. P. Daubinger, R. Petersohn, F. Nagler, S. Hartmann, M. Herrmann, and G. A. Giffin, 'Bracing dependent aging phenomena of large format automotive prismatic cells', *Batterieforum Deutschland*, Online Conference, 2021.
2. P. Daubinger, M. Göttliger, L. Gold, S. Hartmann and G. A. Giffin, 'Pressure dependent aging mechanisms in lithium-ion cells', *72nd Annual Meeting of the International Society of Electrochemistry*, Online Conference, 2021.
3. P. Daubinger, M. Göttliger, S. Hartmann and G. A. Giffin, 'Silicon-Based Anodes for Lithium-Ion Batteries – Dilatometry and Influence of External Pressure', *Workshop Si-Based Anodes*, Online Conference, 2021.
4. P. Daubinger, M. Göttliger, S. Hartmann and G. A. Giffin, 'Impact of External Pressure on the Performance and Expansion of State-of-the-Art and Next-Generation Battery Materials using Operando Dilatometry', *241st Electrochemical Society Meeting*, Vancouver, Canada, 2022.
5. P. Daubinger, M. Schelter, R. Petersohn, F. Nagler, S. Hartmann, M. Herrmann, and G. A. Giffin, 'Mechanical Effects Occurring inside Large Format 94 Ah Prismatic Lithium-Ion Cells at different Bracing during Aging', *241st Electrochemical Society Meeting*, Vancouver, Canada, 2022.

Poster

1. P. Daubinger, F. Ebert, S. Hartmann, G. A. Giffin and G. Sextl, 'Impact of volume changes on lithium ion battery cycling and aging', *Advanced Lithium Batteries for Automotive Applications (ABAA)*, Ulm, Germany, 2019.
2. P. Daubinger, R. Petersohn, F. Nagler, S. Hartmann, M. Herrmann, and G. A. Giffin, 'Bracing dependent aging phenomena of large format automotive prismatic cells', *Batterieforum Deutschland*, Online Conference, 2021.
3. P. Daubinger, F. Ebert, S. Hartmann and G. A. Giffin, 'Impact of inhomogeneous pressure distribution on the performance of graphite using operando dilatometry', *Swiss Battery Days*, Online Conference, 2021.
4. P. Daubinger, M. Göttliger, S. Hartmann and G. A. Giffin, 'Effects of (in)homogeneous pressure distribution on the performance of battery materials using operando dilatometry', *Kraftwerk Batterie/ Advanced Battery Power*, Online Conference, 2021.
5. P. Daubinger, S. Feiler, L. Gold, S. Hartmann and G. A. Giffin, 'State-of-Charge Dependent Change of the Young's Modulus in Lithium-Ion Batteries', *241st Electrochemical Society Meeting*, Vancouver, Canada, 2022.

Manuscripts



Impact of electrochemical and mechanical interactions on lithium-ion battery performance investigated by *operando* dilatometry

Philip Daubinger^a, Fabian Ebert^{a,b}, Sarah Hartmann^a, Guinevere A. Giffin^{a,*}

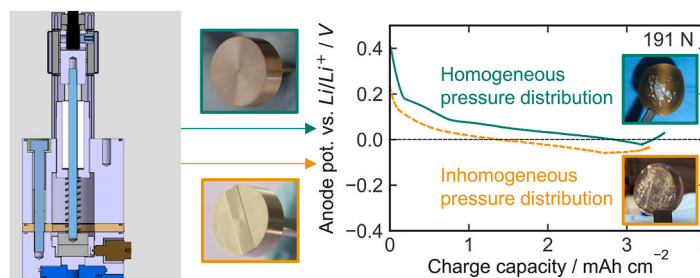
^a Fraunhofer R&D Center Electromobility, Fraunhofer Institute for Silicate Research, Neunerplatz 2, 97082, Wuerzburg, Germany

^b Institute of Automotive Technology, Technical University of Munich TUM, Boltzmannstraße 15, 85748, Garching, Germany

HIGHLIGHTS

- Investigation of electrode expansion using a three-electrode dilatometry set-up.
- Most irreversible dilation observed for initial Li⁺ intercalation into graphite.
- High applied pressure accelerates aging mainly at the anode.
- Correlation between applied pressure and expansion of the electrodes.
- Inhomogeneous pressure distribution leads to accelerated aging and lithium plating.

GRAPHICAL ABSTRACT



ARTICLE INFO

Keywords:

Dilatometry
Mechanical stress
Graphite
Lithium-ion battery
Expansion
Pressure distribution

ABSTRACT

The demand for higher energy densities in lithium-ion batteries leads to an increased utilization of the space within the confinements of the cell housing for the electrodes, resulting in increased electrochemical/mechanical interactions and stress inside the cells. In this study, the correlating effects of externally-induced mechanical stress and dilation of the electrodes on the performance of LIBs were investigated using an *operando* three-electrode dilatometry cell. The results demonstrate that most of the initial irreversible dilation in a graphite/LiNi_{0.33}Co_{0.33}Mn_{0.33}O₂ (NCM111) cell occurs during the initial lithium intercalation at the anode during the transition from stage 2 to 1, i.e. LiC₁₂ to LiC₆, due to SEI formation, particle rearrangement and graphene layer spacing. Moreover, high applied pressure, which leads to a reduction of the porosity inside the separator and therefore increased ionic transport resistance, tortuosity and overpotential, results in a hastened degradation mainly at graphite anode. These effects are more pronounced with an inhomogeneous pressure distribution and lithium plating is identified as the main cause of degradation. This dilatometry cell is a powerful tool for studying the electrode/active material expansion and electrochemical/mechanical effects for a homogeneous and inhomogeneous pressure distribution.

1. Introduction

One of the biggest obstacles to the widespread adoption of fully

electrified vehicles is the limited volumetric/gravimetric energy density of lithium-ion batteries (LIBs) necessary to have driving ranges comparable to vehicles with internal combustion engines. Improving the

* Corresponding author.

E-mail address: guinevere.giffin@isc.fraunhofer.de (G.A. Giffin).

<https://doi.org/10.1016/j.jpowsour.2021.229457>

Received 7 October 2020; Received in revised form 15 December 2020; Accepted 3 January 2021

Available online 15 January 2021

0378-7753/© 2021 Elsevier B.V. All rights reserved.

state-of-the-art LIB technology offers an alternative to developing new cell chemistries as a way to increase the energy density in the next decade [1,2]. Such an improvement can be made by increasing the electrode thickness and thus the amount of active material [3–6] or by adding small amounts of silicon (Si) into a carbon (C)-based anode (Si/C) [7–9]. Additionally, the space within the confinements of the cell housing has to be utilized as much as possible for the electrodes. The optimized packing leads to increases in the pressure within the cell due to reversible and irreversible volume changes of the electrodes during cycling and aging [2,9].

The anode is particularly prone to volume changes during cycling. A graphite anode has a volumetric expansion of ~10% [10–13] while that of a Si/C anode, depending on the amount of Si in C, has anywhere from ca. 14% [14] to 300% (for Si only) [7–9]. In the next few years, the amount of Si in commercial anode applications will likely increase due to the higher energy density of Si compared to graphite, but this will also increase the volumetric expansion of the anode. In comparison, the swelling of most NCM cathode materials is <2% [15–18]. The expansion of the electrodes is constrained by the cell housing which results in high pressure on electrodes and on the separator. The Young's modulus of the separator (<440 MPa, dependent on the specific separator) [15,19–21] is relatively small in comparison to that of graphite (~28–109 GPa) [13] or NCM111 (~200 GPa) [22]. Therefore, the high pressure inside the cell results mainly in compression of the separator. It should be noted that the Young's modulus of the composite electrodes is up to two orders of magnitude smaller than that of pure active materials due to the binder and conductive carbon, but it is still higher than that of the separator [15,23]. Uneven compression of the separator results in local distortion or reduction of separator porosity [24,25]. This reduced porosity increases the local current density which can lead to a drop of the anode potential below 0 V vs. Li/Li⁺. Below 0 V, the formation of metallic lithium is energetically favored and lithium plating occurs on the anode [26,27]. These depositions also lead to inhomogeneous pressure distribution which further accelerate aging and, in the worst case, can result in internal short circuits [25]. Both experiments and simulations have shown that a homogeneous pressure distribution across the electrode surface is necessary to decrease aging phenomena [25,28–30].

Electrode dilation, especially of the anode, is one of the key factors for local plating phenomena and as such must be understood in detail. The impact of the cathode on the total dilation of cell is of minor relevance in comparison to that of the anode [31–33]. There are different approaches to detect the dilation of electrodes or battery cells. At the macroscopic or cell level, dilatometry [16,34,35] or 3D displacement measurements [36] can be used. At the microscopic or atomic level, X-ray diffraction [37,38] or density functional theory (DFT) calculations [13,39] are potential methods for approximating electrode expansion.

To date, only few *operando* dilation measurement systems have been reported. One such system has a fixed glass frit to separate the mechanical influence of working and counter electrodes [12,34,36]. One of the disadvantages of this system is that the applied pressure is fixed and cannot be varied, e.g. to investigate material strain-dependent effects. Another system introduced by Sauerteig et al. [16,18] allows the pressure to be adjusted in addition to the measurement of reversible and irreversible dilation, but without the possibility of three-electrode measurements. The *operando* dilatometry measuring cell used in this work has been developed along the lines of that reported by Sauerteig et al. [16], but with the addition of a reference electrode to distinguish the anode and cathode potentials. With the differentiation of the two half-cell potentials it is possible to non-destructively monitor electrode degradation phenomena such as lithium plating, since the anode potential drops below 0 V vs. Li/Li⁺ during lithium plating [26,27].

This study investigates the effects of mechanical stress and dilation of the electrodes on the electrochemical performance using an *operando* three-electrode dilation cell. By using state-of-the-art electrodes, separator and electrolyte, the stack dilation is studied under representative conditions. First, the cell is benchmarked with other laboratory cells,

and then the dilation processes during the formation of the electrodes is discussed. Additionally, the reversible and irreversible dilation under defined mechanical pressure and pressure distribution is examined. In particular, the influence of high currents and (in)homogeneous pressure distribution on aging is investigated, since both are known to accelerate aging. Using these results, the correlation between mechanical stress, electrode expansion and aging are explored.

2. Experimental

2.1. Dilation cell design

The schematic cross section, a picture of the cell and the two different plungers of the *operando* dilatometry setup are shown in Fig. 1.

The metallic cell housing and the plungers of the measurement cell are made of 1.4404 stainless steel. Electrical insulation between the cell body and the electrodes is ensured by a polyether ether ketone spacer. The pressure can be adjusted via a hollow screw and a spring in the upper section of the cell. The dilation rod is housed in polytetrafluoroethylene to avoid slip/stick effects. The mechanical pressure is measured with a KM38-2 kN load cell with an analog GSV-1A signal amplifier (both ME-Systeme GmbH). The dilation is measured via a contactless capacitive CSH05 displacement sensor with a capaNCDDT 6110 amplifier (both Micro-Epsilon GmbH) which gives a resolution of 1 mV corresponding to a dilation of 25 nm. An EL-Pat insulation sleeve (EL-Cell GmbH) with an integrated ring-shaped lithium metal reference electrode, located on the side of the electrode stack, is used. This insulation sleeve can be fit with almost any separator, which makes the system flexible. The cell may be fitted with either a flat plunger or a structured plunger with a step (Fig. 1 (c) and (d)) which results in either a homogeneous or an inhomogeneous pressure distribution on the electrode stack, respectively. The structured plunger allows local pressure inhomogeneities on the electrodes, e.g. due to current collector tabs [28], to be simulated.

2.2. Cell stack material

Graphite and NCM111 (CUSTOMCELLS Itzehoe GmbH) were used as the anode and cathode respectively. The graphite anode (96% active material content) has an areal capacity of 3.8 mAh cm⁻² with a thickness of ~102 μm including 14 μm Cu as the current collector and a porosity of

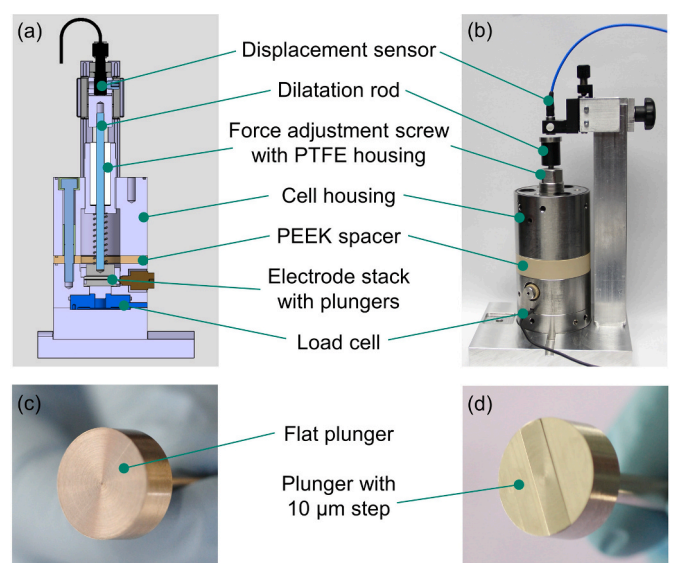


Fig. 1. (a) Schematic cross section and (b) photograph of the *operando* dilation cell. Photograph of the plungers used in the cell: (c) flat and (d) with a 10 μm step.

38%. The NCM111 cathode (90% active material content) has an areal capacity of 3.5 mAh cm^{-2} with a thickness of $\sim 109 \text{ }\mu\text{m}$ including $20 \text{ }\mu\text{m}$ Al current collector foil and a porosity of 35%. The electrode foils were cut into 18 mm disks and dried in a vacuum oven at $120 \text{ }^\circ\text{C}$ overnight. CG2500 (Celgard LLC) with a thickness of $25 \text{ }\mu\text{m}$ and a porosity of 55% was used as the separator and LP57 (1 M LiPF_6 in EC/EMC 3/7 wt%, Gotion Inc.) was used as electrolyte. The separator was dried under vacuum at $50 \text{ }^\circ\text{C}$ overnight.

2.3. Electrochemical measurements and post-mortem analysis

In the dilation cell set-up, the anode was in contact with the upper plunger and $200 \text{ }\mu\text{l}$ of electrolyte was used. Three different force magnitudes (12 N, 64 N and 191 N) were applied onto the cell stack with two different types of plungers as described above (Fig. 1 (c) + (d)). The resulting pressure on the electrodes depends on the plunger used. The applied forces result in operating pressures of 0.05 MPa, 0.25 MPa and 0.75 MPa for the flat plunger and 0.18 MPa, 0.88 MPa and 2.63 MPa for the plunger with a $10 \text{ }\mu\text{m}$ step. The pressure is 3.5 times higher for the plunger with the step than for the flat plunger due to the smaller area (72 to 254 mm^2). The selection of the external forces was based on previous studies [29,40–42] and the limitations of the spring (i.e. maximum load), as only one spring was used during the experiments. The choice to apply the same force on the stack with the two different plungers was used to simulate realistic conditions on the battery cell level. The force exerted on the electrodes, i.e. by cell housing or module bracing, remains constant regardless of the (in)homogeneous pressure distribution on the electrodes, e.g. by current collector tabs [28].

Cell assembly and cycling was performed inside an argon-filled glovebox (MBraun, H_2O and $\text{O}_2 < 1 \text{ ppm}$). The electrochemical measurements were performed with a ModuLab XM MTS System (Solartron Analytical). The full cell potential, the anode and cathode potential, the applied force and the dilation were recorded. The C-rate was related to the theoretical areal mass loading of NCM111 and corresponds to 8.9 mA for 1 C. The temperature was maintained at $25 \text{ }^\circ\text{C}$ using a self-built temperature device.

If not noted otherwise, the formation of the cells (initial cycle with 0.1 C followed by three 0.2 C cycles between $2.7 \text{ V} - 4.2 \text{ V}$) was started after a rest period of 12 h. The applied force during the formation was 12 N for both plungers. Following the formation, either a charge rate capability test or a cycling procedure was started. In the rate capability test, the charge current was varied (two cycles at each rate in the following sequence: 0.2C, 0.3C, 0.5 C, 1.0 C, 1.3 C and 2.0 C), while the discharge current was held constant at 0.2 C. Unlike most rate tests shown in the literature, the charge current was varied to stress the system and accelerate aging in the electrodes. The rate test was carried out at the three different forces noted above. In the cycling test, the charge and discharge current was 0.75 C and the force was 12 N. The charge step was performed in constant current constant voltage (CCCV) mode. The cut-off criterion in the voltage step was a current $I < 0.04 \text{ C}$ at 4.2 V . All data with standard deviation shown were obtained from at least two independently assembled cells.

Electrochemical impedance spectroscopy (EIS) was conducted in a frequency range of $200 \text{ kHz} - 30 \text{ mHz}$ with a 10 mV root-mean-square perturbation. The EIS spectrum was collected at 100% state of charge (SOC) in an open circuit condition with a rest time of 15 min before the measurement. This SOC was chosen such that electrodes were at a state of maximum expansion and thus the pressure inside the cell was the highest.

Post-Mortem analysis of the electrodes was done at 100% SOC. The electrodes were immersed in dimethyl carbonate (DMC) for 2 h. The solvent was exchanged after 1 h.

2.4. Dilatometry measurements

During a single cycle, the total dilation is divided into two parts, the

reversible and irreversible dilation. The total dilation of a cycle is defined as the maximum increase in the electrode thickness, whereas the irreversible dilation is obtained from the difference between the change in the electrode thickness during the discharge half cycle and the total dilation. The reversible dilation is the difference between the total and the irreversible dilation.

Previous dilation studies showed that the reversible volume change of NCM111 is $< 1\%$ [15,16] and therefore about an order of magnitude smaller than that of graphite ($\sim 10\%$) [10–12,16,43]. Nagayama et al. did not observe any expansion of NCM111 during cycling [31]. Based on these studies, when considering the expansion behavior of the electrode stack, the expansion of NCM111 is neglected in this work because its influence is small compared to that of graphite.

For the investigation of lithium intercalation into graphite, incremental capacity analysis (ICA) dQ/dV is often implemented. In an ICA, the peaks correspond to voltage plateaus (coexistence of lithium intercalation stages in graphite) [44–47]. From the dilation measurements, an incremental dilation analysis (IDA) dz/dV can be conducted. The IDA is adapted from the ICA. In the IDA, the peaks correlate with the changes in the slope of the dilation signal due to the lithium (de)intercalation processes into graphite. Positive values of dz/dV represent the intercalation process and the negative values arise during the deintercalation process. The voltage step size for dV was 2.5 mV .

3. Results and discussion

3.1. Validation of dilation cell

The cell performance in the dilation cell is validated via comparison with that of two other laboratory-scale cell types: El-cells and pouch cells. The electrode stack construction was the same for all three cell types, except the amount of electrolyte was different in the reference cells than in the dilation cell (El-Cells: $100 \text{ }\mu\text{l}$ and pouch cell: $250 \text{ }\mu\text{l}$). Fig. 2 (a) and (b) shows a comparison of the discharge capacity during the formation cycles with standard deviation of three cells each and an exemplary potential profile in the fourth cycle of a representative cell. The different cell types have comparable potential profiles and capacities. All cells reach the theoretical capacity of 3.5 mAh cm^{-2} by the fourth cycle (if not earlier). Only the first discharge cycle in the dilation cell differs from that in the other cells. The capacity is lower, which could be due to a slower settling of the pressure in this system.

In Figure Supplementary 1, the functionality of the dilation cell is demonstrated over an extended period of time. The capacity retention at 0.75 C is 97.2% and the coulombic efficiency (CE) approaches one after the formation cycles. The irreversible dilation is relatively large in the first four cycles and then decreases to approximately $0 \text{ }\mu\text{m}$ during the cycling at 0.75 C. The reversible dilation of the system also varies in the first cycles but stabilizes at around $6.7 \text{ }\mu\text{m} \pm 0.2 \text{ }\mu\text{m}$ after the formation processes are completed. Overall, the applicability of the dilation cell is shown over a longer period of time ($\sim 200 \text{ h}$) and its use is not limited to short-term investigations.

3.2. Reversible and irreversible dilation of graphite during formation

In Fig. 3 (a), the cell potential and the anode potential vs. Li/Li^+ are plotted as a function of time. The three intercalation plateaus for lithium in graphite are clearly observable in the anode potential plot and are consistent with the data previously reported in the literature [38,48].

In Fig. 3 (b) an initial total dilation of $\sim 18\%$ and a large irreversible dilation of $\sim 8.5\%$ (both dilations referring to the graphite electrode film thickness) can be seen. This total and irreversible dilation are related to the first rearrangement of the lithium-ions within the graphene layers, the formation of the initial, thin SEI [16,34], the initial co-intercalation of solvated lithium ions and partial exfoliation of graphite at the surface [49–53].

These exfoliation processes can cause cracking and splitting of the

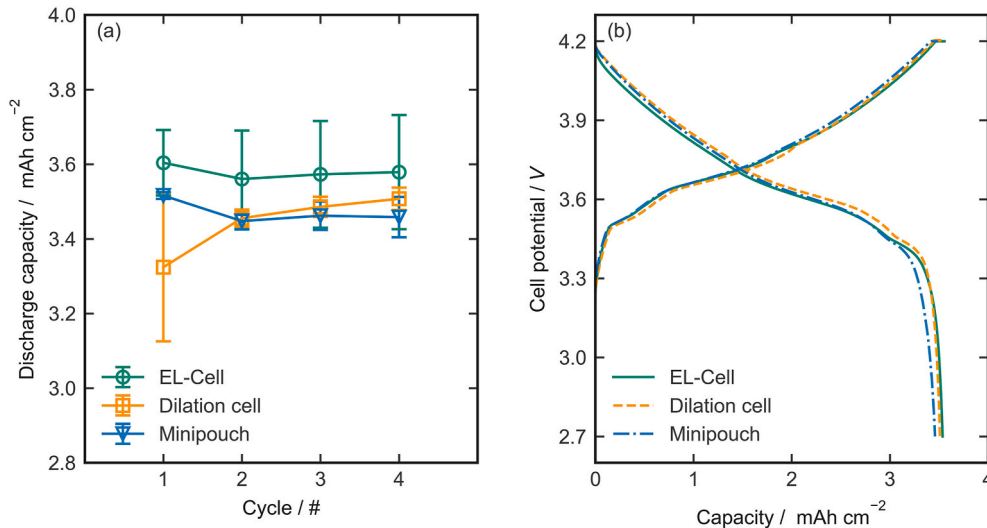


Fig. 2. Comparison of dilation cell with standard laboratory test cells. (a) Discharge capacity with standard deviation of three cells each during the formation cycles and (b) potential profile in the fourth formation cycle of a representative cell.

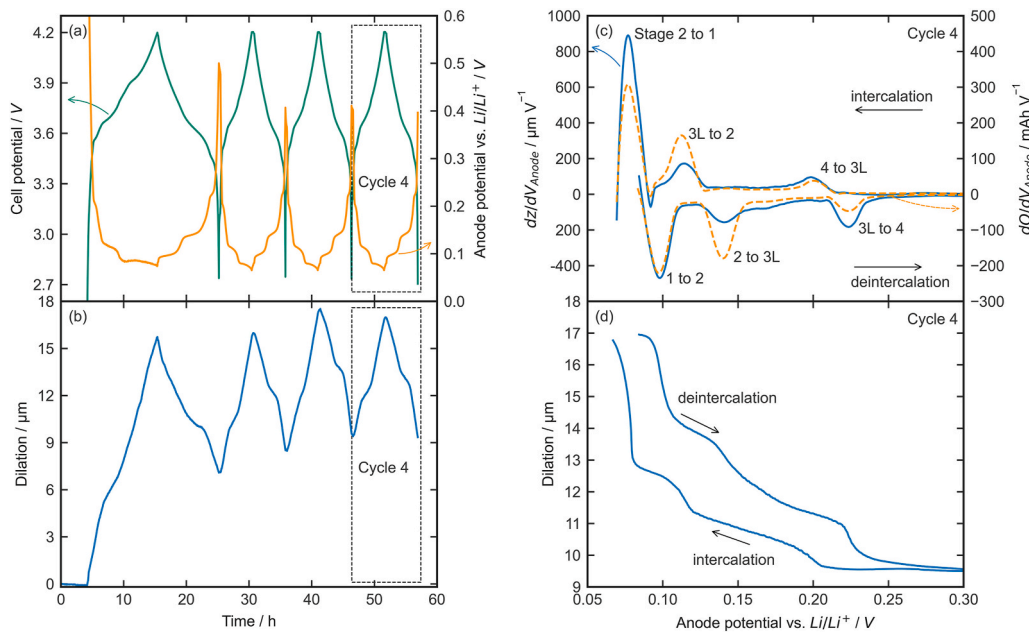


Fig. 3. Formation of graphite vs. NCM111 with an initial 0.1 C cycle, followed by three 0.2 C cycles. (a) Cell potential, anode potential and (b) dilation as a function of time. (c) ICA, IDA and (d) dilation as a function of anode potential in fourth cycle.

graphite particles, which changes the structure, orientation [54,55] and hence the thickness of the electrode. This leads to an expansion of the graphene layers which is more pronounced than for lithium-ion intercalation only [50,56–58]. In the following cycles, the total and irreversible dilation decrease. This can be attributed to a small amount of particle rearrangement and shallow solid electrolyte interphase (SEI) formation [16,34]. The reversible expansion of the electrode stack is between 7.5 μm and 8.5 μm (~8%–10% swelling with regard to the graphite electrode film thickness) during formation cycles. This is in good agreement with literature [10–12,16,43]. The influence of the evolution of gas during the initial formation cycles on the dilation is negligible as the dilation cell has a large dead volume inside the housing due to upper plunger and spring. As a result, the gas generated can move into the dead volume of the cell and is not trapped in the electrode stack. Furthermore, the impact of the sensor drift on the total dilation is minor, as can be seen in Fig. 3 (b). The dilation within the cell deviates by about

0.05 μm around its mean value after a pressure relaxation period during the open circuit potential before the initial formation cycle; the relaxation phase is not shown in the figure.

Fig. 3 (c) shows the ICA and IDA as a function of the anode potential in the fourth formation cycle. The peaks of the ICA correlate with the peaks of the IDA, indicating that voltage plateaus correspond to dilation. The increase of the expansion can be mainly attributed to the graphite electrode. The slope changes of the dilation signal can be used as an alternative method for detecting the stage transitions for lithium intercalation into graphite.

A detailed view of the irreversible dilation of the first cycles is shown in Fig. 4. A change in the slope of the dilation signal is observed in the potential range of ~1.1 V–~0.7 V (inset Fig. 4 (a)). In this range, the onset of SEI formation, depending on solvent and salt used, is typically reported [44,49,56,59,60]. As the expansion in this range is ~800 nm, the slope change cannot be ascribed to the SEI formation alone. In this

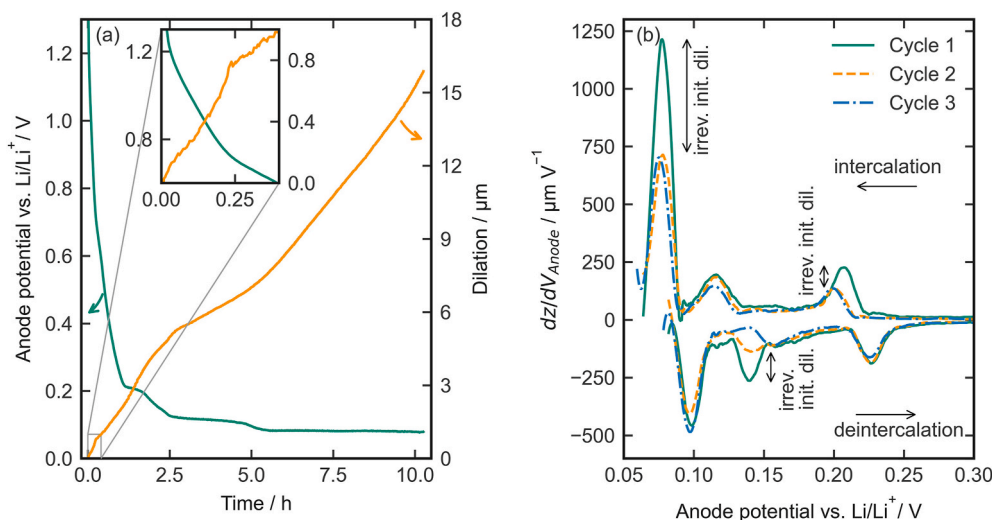


Fig. 4. (a) Anode potential and dilation as a function of time in the first charge cycle (lithium intercalation into graphite). (b) IDA profile of three 0.1 C formation cycles.

voltage range, solvent co-intercalation and/or partial exfoliation of the graphene layers is also possible. Hence, the high dilation in this range is possibly attributed to SEI formation and additionally to solvent co-intercalation and partial exfoliation.

In Fig. 4 (b), the IDA of three 0.1 C formation cycles is plotted as a function of the anode potential. Most of the graphite dilation during intercalation can be observed at ~ 0.08 V and is associated with a transition of the lithiation process from stage 2 (LiC_{12}) to 1 (LiC_6). The contribution of the other stage transition peaks to the total dilation is smaller. When comparing the individual cycles, the intensity of the $\text{dz/dV}_{\text{Anode}}$ peaks at ~ 0.08 V is around 60% higher and at ~ 0.20 V almost 100% times higher in the first cycle as compared to the following cycles. This is related to the initial irreversible dilation of the electrodes and electrolyte decomposition. At ~ 0.20 V (transition from stage 4 (LiC_{36}) to 3L (LiC_{27})), the initial intercalation of lithium ions and SEI formation takes place within the graphene layers. At ~ 0.08 V, further SEI formation occurs because of the decomposition of the electrolyte. At low anode potentials and the accompanying high cathode potentials, electrolyte reduction at the anode surface and electrolyte oxidation at the cathode surface is more pronounced [60,61]. During the initial charge, the $\text{dQ/dV}_{\text{Anode}}$ peak of stage transition 2 (LiC_{12}) to 1 (LiC_6) is around 26% higher than the peak in the following cycles (Figure Supplementary 2). A small loss of capacity results in a comparatively large dilation. No differences can be seen for the peaks at 0.12 V (stage transition 3L (LiC_{27}) to 2 (LiC_{12})).

The irreversible dilation decreases from the initial to the following cycles. This is attributed to the increase of the average graphite interlayer distance in the first cycle as previously described by Dahn and Dahn et al. [37,62]. Atomic force microscopy investigations by Campana et al. showed an increase in the irreversible graphene layer spacing of $24\% \pm 7\%$ for the first cycle [58]. In this work, the initial irreversible dilation is 8.5% (referring to the graphite electrode film thickness) in the first formation cycle (Fig. 3 (b)). The dilation is smaller than in the study by Campana et al. [58] since the complete composite electrode including the porous structure, binder and conductive materials is measured here rather than only the graphite particles. The initial irreversible dilation of the electrodes is higher than that reported by other similar studies [12, 18,34] due to the high mass loading and low porosity of the electrodes used here. The loading of the graphite electrodes in those studies were in the range from 1.8 mAh cm^{-2} [12,34] up to 3.0 mAh cm^{-2} [18] and the initial irreversible dilation from $\sim 2.5\%$ [12,34] to $\sim 5\%$ [18]. It should be noted that Bauer et al. [34] only charged the graphite to 75% SOC and therefore the irreversible dilation might be larger if they would have

charged up to higher SOCs. In graphite electrodes with a high loading, the initial irreversible expansion of the interlayer has an increased influence as compared to electrodes that are more porous and have lower loadings [16].

It can be observed that the peak intensities of the single cycles during the deintercalation differ from the peaks during intercalation. The peak intensities at ~ 0.10 V and ~ 0.23 V are in the same range for the deintercalation in the first cycle and that in the subsequent cycles, indicating that most of the particle rearrangement occurs during the initial half cycle. In contrast, the peak at ~ 0.14 V corresponding to the stage transition 2 to 3L is higher for the first cycle than for the following cycles. For cycle 3, the peak is shifted to ~ 0.15 V. The irreversible dilation during deintercalation occurs only in the stage transition 2 to 3L, while the other stages only undergo irreversible dilation during intercalation. Up to now, this effect is not completely clear, but might be related to further particle rearrangement and the reduction of co-intercalated solvated lithium ions.

3.3. Impact of mechanical stress on battery performance

Fig. 5 shows the influence of mechanical stress on the lithium-ion cell performance in terms of rate capability. As noted in Section 2.3 above, the rate was held constant for the discharge step, but varied for the charge step to accelerate the aging and to enhance the impact of the mechanical pressure on the graphite anode. With a homogeneous applied force, i.e. with the flat plunger, the discharge capacity is constant around 3.5 mAh cm^{-2} (theoretical loading of cathode: 3.5 mAh cm^{-2}) for the applied C-rates. This suggests that with a homogeneous pressure distribution (Fig. 5 (c)), the mechanical stress-induced capacity reduction, at least at the pressures investigated, is minimal.

With an inhomogeneous applied force, i.e. the plunger with step, the initial capacity is as much as 0.4 mAh cm^{-2} lower than that with a homogeneous applied force. This effect can be mainly attributed to an insufficient electrical contact between the anode and plunger over the complete electrode area. For the cells with the lower applied forces of 12 N and 64 N (0.18 MPa and 0.88 MPa at the step), there is no further losses in the capacity during the rate test. The cells with the highest applied force of 191 N (2.63 MPa at the step) initially have a higher capacity than those with lower applied forces. This may be attributed to the improved electrical contact of the electrodes with the plunger [27] in combination with the slow kinetics of the processes occurring in the cell. At high charge rates (0.5 C and above), the discharge capacity drops dramatically and the electrodes are irreversible damaged. At the end of

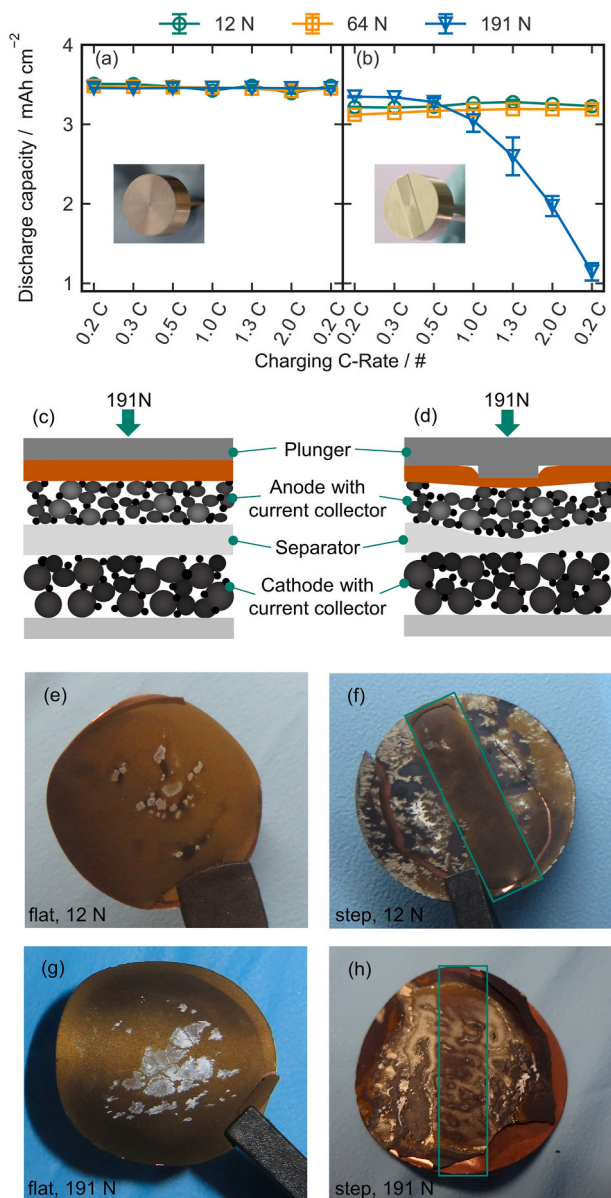


Fig. 5. Charge rate capability test. Discharge capacity plotted as a function of the charge rate for (a) the homogeneous pressure distribution (flat plunger) and (b) inhomogeneous pressure distribution (plunger with a step). Impact of the high force (191 N) onto the electrode stack for (c) the flat plunger and (d) the plunger with step. Graphite electrodes after cycling. (e) + (g) show the electrodes with the homogeneous pressure distribution and (f) + (h) the electrodes with the inhomogeneous pressure distribution. A force of 12 N is applied for (e) + (f) and 191 N for (g) + (h) respectively. Cell opening is performed at 100% SOC.

the rate test with the low C-rate of 0.2 C, there is no recovery of the discharge capacity indicating a continuous degradation in terms of irreversible capacity loss and hence also irreversible damage to the electrode. There may be increased delamination of the electrode mass from current collector next to the step due to shear forces resulting from the inhomogeneous pressure distribution (Fig. 5 (d), (f) + (h)). As shown in Fig. 5 (d), the uneven pressure distribution on the separator leads to a decrease in porosity of the polyolefin separator in the area of high pressure. This results in an increased tortuosity and thus, an increased ionic transport resistance inside the separator [15,30]. The combination of localized high pressure, increased tortuosity and ionic transport resistance, insufficient electrical contact and the high currents lead to

lithium plating on the anode (Fig. 5 (e)–(h)).

The electrode stack with a load of 191 N (Fig. 5 (g): homogeneous pressure distribution) shows more lithium plating as compared to the electrode with 12 N (Fig. 5 (e)). Both electrodes with the non-uniform pressure distribution (Fig. 5 (f) + (h)) exhibit more lithium plating than the electrodes with the flat plunger. This is mainly related to the higher local pressure at the electrode due to the step and the insufficient contact between both electrodes, which increases the overpotential in the cell. When the plunger with the step is used in combination with low applied forces (12 N), lithium plating (silver/white areas in Fig. 5 (f)) mainly takes place next to the step. In addition to the areas with lithium plating, further areas (black areas) occur next to the step that are less- or non-lithiated. This supports the hypothesis that there is insufficient electrical contact and/or delamination next to the step and thus areas with high local current densities (as the overall current remains constant). Lithium plating is favored in these areas due to the localized high balancing currents. When a high applied force of 191 N (Fig. 5 (h)) is used in combination with a non-uniform pressure distribution, lithium plating is found all over the electrode. The high force results in compression of the separator, leading to decreased porosity, increased tortuosity and ionic transport resistance [25]. This loss of cyclable lithium due to lithium plating causes a reduction of the capacity.

Fig. 6 shows the influence of pressure distribution and applied pressure on the electrochemical potential of graphite during CCCV charging. The beginning of the CV step can be identified as the change from a decreasing to increasing anode potential. With a homogeneous pressure distribution (Fig. 6 (a) + (b)), the potential plateaus are visible for 0.5 C and 12 N. The capacity is close to the theoretical capacity of 3.5 mAh cm^{-2} . However, for higher currents or applied forces, the charge potential curve shows little evidence of plateaus due to increased overpotentials, which can be seen by a shift of the potential to lower values during intercalation. For the cell with the highest applied force (191 N) the potential drops below 0 V, causing lithium plating already at a charge capacity of 2.8 mAh cm^{-2} (82% SOC) and 0.7 mAh cm^{-2} (19% SOC) for 0.5 C and 2.0 C, respectively.

For cells with a non-uniform pressure distribution, shown in Fig. 6 (c) and (d), the effects of accelerated aging and higher overpotentials are enhanced. The potential plateaus have mostly vanished. Even for the low applied force of 12 N at C-rate 0.5 C, the anode potential drops below 0 V at a charged capacity of 2.8 mAh cm^{-2} (85% SOC). These effects are further intensified for the higher applied forces and currents.

Fig. 7 shows EIS before and after cycling of the full cells with homogeneous and inhomogeneous pressure distribution. The individual spectrum of the full cells consist of four features which can be ascribed as follows: a high-frequency intercept due to ohmic resistances in the cell, a semicircle at high frequencies related to the surface films (SEI) on the particles, a second semicircle at low frequencies correlated to the charge transfer resistances and inclined line related to solid-state diffusion. These four features are fitted with an appropriate model (Fig. 7 (e)).

The high pressure results in increased interfacial kinetics, mass transport in the electrodes, ionic pore resistance and ohmic resistance [30,42]. This can be seen in EIS data (Fig. 7 (a)) as an increase of the diameter of the semicircle and length of the diffusion tail for the cells with the high applied pressure. The ohmic resistance is increased due to the higher tortuosity and ionic transport resistance in the separator [15, 30] and can be seen as a shift of the intercept at high frequencies (flat plunger: $2.5 \Omega \text{ cm}^2$ at 12 N to $3.4 \Omega \text{ cm}^2$ at 191 N).

The change of the resistances of the electrodes before and after cycling for the homogenous pressure distribution can be seen in the Nyquist plot, where, for example, the charge transfer resistances at low frequencies are increased after cycling (Fig. 7 (b) and Table Supplementary 1). While the cell with a 12 N force has an increase in the charge transfer resistance from $2.8 \Omega \text{ cm}^2$ to $4.3 \Omega \text{ cm}^2$, that for the cell with 191 N increases from $2.2 \Omega \text{ cm}^2$ to $5.2 \Omega \text{ cm}^2$. The impact of the cathode on the impedance increase after cycling is probably minor for the homogenous pressure distribution, as the cathode potentials at EIS

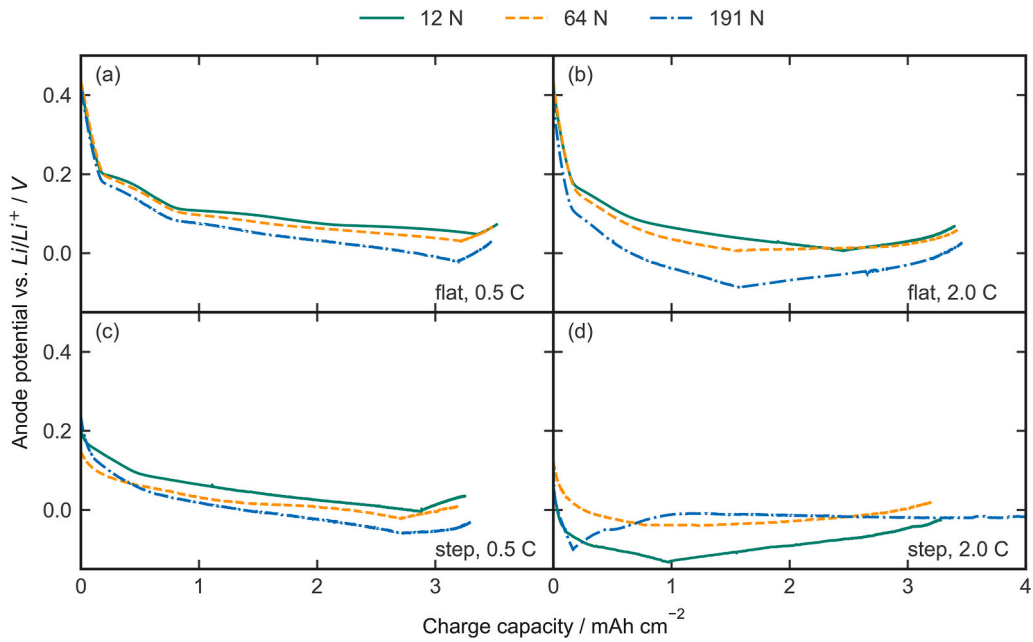


Fig. 6. Anode potential over charging capacity of homogeneous pressure distribution (a)+(b) and inhomogeneous pressure distribution (c)+(d) for CCCV charging rates of 0.5 C and 2.0 C respectively.

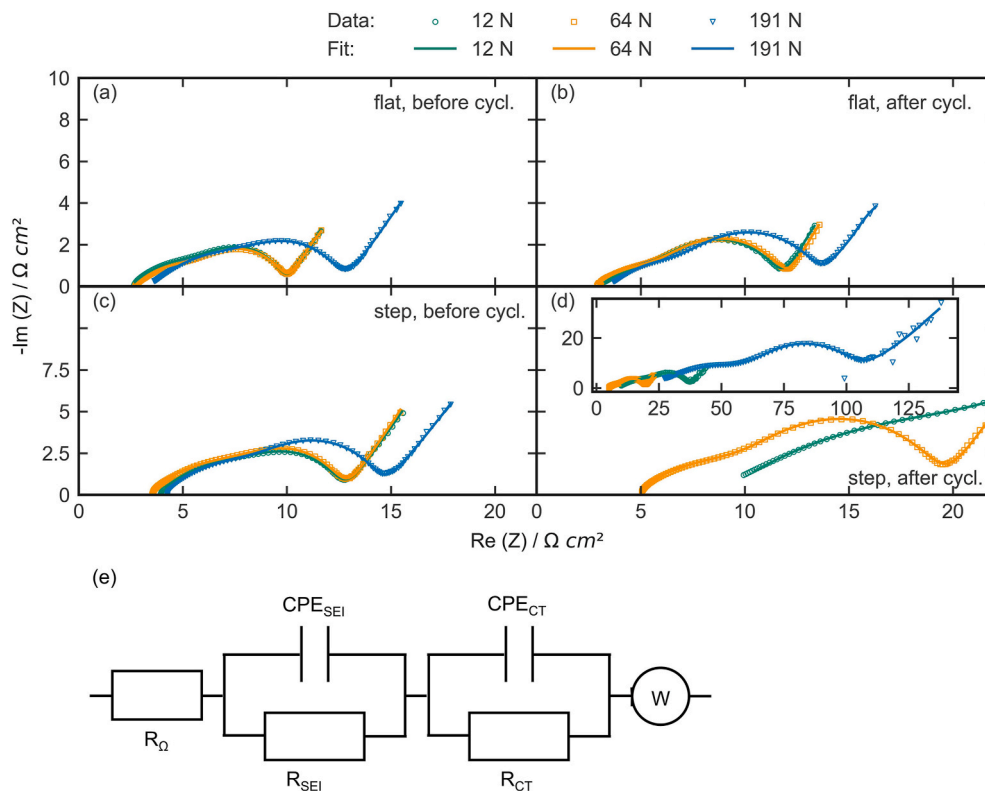


Fig. 7. (a)–(d) Nyquist plot for cells before and after C-rate capability testing for the flat (a) + (b) and (c) + (d) plunger with step. (e) Equivalent circuit model used for fitting.

before and after cycling are in a similar range. For the inhomogeneous pressure distribution the electrodes have increased resistances and lithium plating compared to the cells with a homogeneous pressure distribution (Fig. 7 (c) + (d) and Table Supplementary 1). In particular, the ohmic resistance and the charge transfer resistance increase during cycling; the cell with the highest applied force also shows the highest

increase in resistance. Here, the impact of the cathode on the impedance increase after cycling is more significant as the cathode potentials at EIS differ slightly before and after cycling (i.e. 4.24 V before and 4.16 V after cycling for the 12 N cells). This confirms the accelerated aging of the electrodes with a non-uniform pressure distribution and high applied forces. These effects combined with the high currents lead to

degradation in terms of increased resistance and decreased performance due to lithium plating of the graphite electrode. The cathode (not shown here) shows no visible and morphological degradation regardless of the pressure distribution.

In summary, the electrodes with the homogeneous pressure distribution undergo only slight degradation with regard to resistance increase and performance reduction with low applied forces of 12 N or 64 N during the C-rate test. For the highest applied force of 191 N, the electrodes show significant resistance increase but similar discharge capacities during the C-rate test. This can be related to an increased capacity in the CV step during charging (Figure Supplementary 3) which increases the charge and thus also the discharge capacity. The influence of the CV step will be discussed in the following section in more detail. The cells with an inhomogeneous pressure distribution show accelerated aging, which is most pronounced at high currents due to lithium plating.

The overpotential and hence the degradation of the cell can also be seen from the proportion of the capacity in CV step during charge. The duration of the CV step is an indication of the internal diffusion processes of the active material and the aging of the electrodes [63,64]. For low degradation, most lithium ions are intercalated into the anode during the CC charge step and consequently the CV step is short, accounting only for a small amount of the lithium intercalation. Figure Supplementary 3 shows the proportion of the CV charging step in comparison to the CC step for different forces and plungers (theoretical capacity of electrodes: 3.5 mAh cm⁻²). The share of the CV step with respect to the total capacity increases with higher forces and currents. Furthermore, the CV step share is higher for the inhomogeneous pressure distribution compared to the homogeneous distribution. Low pressure and even pressure distribution lead to a short CV step at 0.5 C and accounts for 4.3% of the total charge capacity. At higher currents (2.0 C), the slow kinetics of the electrodes hinder the lithium intercalation resulting in increased capacity in CV step (26.6%). For the cell with the 10 μm step plunger and the lowest applied force (12 N), the CV step accounts for up to 11.4% at 0.5 C and up to 70.1% at 2.0 C. The cell with the highest applied force of 191 N has a total charge capacity of 5.95 mAh cm⁻² due to lithium plating. These results clearly indicate increasing overpotentials with increasing C-rates which is even more pronounced with increased force and non-uniformity of the pressure.

The cumulative irreversible dilation during the initial formation cycles and the C-rate test is shown in Fig. 8 for the homogeneous and

inhomogeneous pressure distribution. The irreversible dilation for the inhomogeneous pressure distribution is significantly smaller than that with the homogeneous pressure distribution. This might be related to the lower overall capacity with the cells with the inhomogeneous pressure distribution (Fig. 5). The decreased capacity is a result of decreased transition of the lithiation process in graphite from stage 2 (LiC₁₂) to stage 1 (LiC₆) compared to the cells with a homogeneous pressure distribution. As previously shown in Fig. 4 (b), most of the irreversible dilation occurs during the transition from stage 2 to stage 1 and hence the cumulative irreversible dilation is lower for the inhomogeneous pressure distribution. After the initial cycles, the cumulative irreversible dilation reaches a plateau for both pressure distributions.

For the cells with the homogeneous pressure distribution, the irreversible dilation varies within the error bars around the same level as it reached after formation. Hence, the irreversible dilation is independent of applied current in this test procedure for the homogeneous applied pressure. For the inhomogeneous pressure distribution the irreversible dilation also fluctuates around the cumulative irreversible dilation as it reached after formation for low currents (<1.0 C). The cells with the lowest applied force show slightly increasing irreversible dilation with increasing currents up to 2.0 C which decreases again during the final 0.2 C step. This might be related to increased lithium plating on the graphite anode for high currents, followed by at least of partial consumption of this lithium at the low current rate (0.2 C) at the end of the C-rate test. The cells with higher inhomogeneous pressure distribution, mainly the cells with 191 N applied force, show only slightly increased irreversible dilation starting at the highest current (2.0 C). However, the cumulative irreversible dilation increases considerably in the low current cycles after the C-rate test. This may be attributed to an irreversible degradation of the graphite electrode due to lithium plating at high currents and results in continued lithium plating during the following low current cycles (Fig. 5 (f) + (h)).

For the reversible dilation during the C-rate test, regardless of the pressure distribution, higher pressure results in lower mean reversible dilation, i.e. 7.9 μm for the 12 N cells and 6.7 μm for the 191 N cells with a homogeneous pressure distribution. Furthermore, the reversible dilation for the inhomogeneous pressure distribution is smaller than the cells with a homogeneous pressure distribution, i.e. 7.3 μm for the 12 N cells and 5.6 μm for the 191 N cells with an inhomogeneous pressure distribution. This can be related to the lower capacity delivered, as most

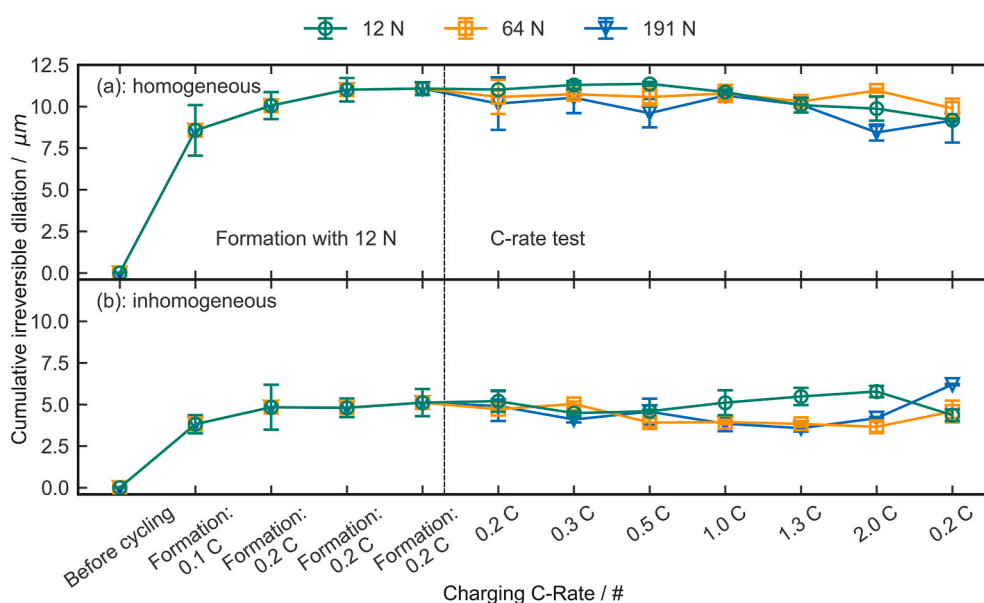


Fig. 8. Evolution of cumulative irreversible dilation for (a) the homogeneous pressure distribution and (b) inhomogeneous pressure distribution with an applied force of 12 N, 64 N and 191 N. During the formation the applied force was 12 N for all cells.

of the capacity and reversible dilation occurs during the transition from stage 2 to 1 (Fig. 4 (b)). The reversible dilation during this C-rate test is independent of applied current due to the prolonged CV step at the charging step.

All these results show the importance of a homogeneous and low pressure distribution on the cell stack. These findings show the trend towards higher overpotentials with increased pressure and uneven pressure distribution. Even small deviations in the pressure distribution combined with high currents can lead to a fast degradation of the graphite anode. The loss of cyclable lithium occurs mainly at the graphite electrode due to lithium plating and SEI formation and hence the main driver of the cell degradation.

4. Conclusion

The use of a three-electrode *operando* dilation set-up, which shows a comparable electrochemical performance to typical laboratory cells, enabled the reversible and irreversible dilation of electrodes under different mechanical loads to be investigated. Graphite/NCM111 cells show a high initial irreversible dilation of 8.5% most likely due to SEI formation, particle rearrangement and graphene layer spacing in the graphite anode during formation. Most of the initial irreversible dilation in the graphite anode was assigned to the transition from stage 4 to 3L (LiC₃₆ to LiC₂₇) and stage 2 to 1 (LiC₁₂ to LiC₆) of the lithium-ion intercalation process. After the formation cycles, the irreversible dilation approached zero, suggesting that the SEI formation and particle rearrangement were completed for this system. The reversible dilation of the graphite/NCM111 system has been determined to be between 8% and 10%, which is consistent with previous literature.

This study also focused on the relationship between applied pressure and cell degradation. High applied pressure, which leads to a reduction of the porosity inside the separator and therefore increased ionic transport resistance, tortuosity and overpotential, results in an accelerated degradation mainly at the graphite anode. For an inhomogeneous pressure distribution, these effects are more pronounced, and lithium plating is identified as the main degradation cause. Localized exchange currents lead to higher local currents next to the areas of high pressure initiating lithium plating. During CCCV charging, the anode potential drops below 0 V, causing lithium plating at earlier state of charges for the inhomogeneous pressure distribution than for homogeneous pressure distribution. Moreover, the capacity share of the CV step as compared to the CC step during charge illustrates the electrode degradation. The CV step share is increased with high applied forces/pressures and/or an inhomogeneous pressure distribution, reflecting accelerated aging.

A homogeneous pressure distribution in batteries is one of the most important prerequisites for good long-term cell performance. Inhomogeneous pressure distributions and high applied pressure significantly accelerate the aging of the electrodes. This study uses the graphite/NCM111 system as an example to demonstrate the mechanical impact on the electrode performance. Further investigations regarding the mechanical impact of different active materials are ongoing.

CRedit authorship contribution statement

Philip Daubinger: Conceptualization, paper, Methodology, Investigation, Validation, Visualization, Writing - original draft. **Fabian Ebert:** Conceptualization, test cell, Methodology, Investigation, Writing - review & editing. **Sarah Hartmann:** Investigation, Supervision, Writing - review & editing. **Guinevere A. Giffin:** Investigation, Supervision, Writing - review & editing.

Declaration of competing interest

The authors declare that they have no known competing financial interests or personal relationships that could have appeared to influence

the work reported in this paper.

Acknowledgement

The authors gratefully acknowledge the funding of this work by the Federal Ministry for Economic Affairs and Energy (BMWi) of Germany in the project ReViSEDBatt (grant number 03ETE004A). The authors further acknowledge the following coworkers in the Fraunhofer R&D Center for Electromobility at Fraunhofer ISC: Lukas Gold for fruitful scientific discussions and support; Ajana Gebel, Vilija Anfimovaite, Franziska Stahl and Elena Fleder for technical support.

Appendix A. Supplementary data

Supplementary data to this article can be found online at <https://doi.org/10.1016/j.jpowsour.2021.229457>.

References

- [1] R. Schmich, R. Wagner, G. Höppl, T. Placke, M. Winter, *Nat Energy* 3 (2018) 267–278, <https://doi.org/10.1038/s41560-018-0107-2>.
- [2] M. Li, J. Lu, Z. Chen, K. Amine, *Adv. Mater.* (2018), e1800561, <https://doi.org/10.1002/adma.201800561>.
- [3] L.S. Kremer, A. Hoffmann, T. Danner, S. Hein, B. Prifling, D. Westhoff, C. Dreer, A. Latz, V. Schmidt, M. Wohlfahrt-Mehrens, *Energy Technol.* 8 (2020), 1900167, <https://doi.org/10.1002/ente.201900167>.
- [4] S.-H. Park, P.J. King, R. Tian, C.S. Boland, J. Coelho, C. Zhang, P. McBean, N. McEvoy, M.P. Kremer, D. Daly, J.N. Coleman, V. Nicolosi, *Nat Energy* 4 (2019) 560–567, <https://doi.org/10.1038/s41560-019-0398-y>.
- [5] X. Wu, S. Xia, Y. Huang, X. Hu, B. Yuan, S. Chen, Y. Yu, W. Liu, *Adv. Funct. Mater.* 29 (2019), 1903961, <https://doi.org/10.1002/adfm.201903961>.
- [6] L. Zolin, M. Chandresris, W. Porcher, B. Lestriez, *Energy Technol.* 7 (2019), 1900025, <https://doi.org/10.1002/ente.201900025>.
- [7] Y. Cao, M. Li, J. Lu, J. Liu, K. Amine, *Nat. Nanotechnol.* 14 (2019) 200–207, <https://doi.org/10.1038/s41565-019-0371-8>.
- [8] X. Shen, Z. Tian, R. Fan, Le Shao, D. Zhang, G. Cao, L. Kou, Y. Bai, *J. Energy Chem.* 27 (2018) 1067–1090, <https://doi.org/10.1016/j.jechem.2017.12.012>.
- [9] X. Zeng, M. Li, D. Abd El-Hady, W. Alshitari, A.S. Al-Bogami, J. Lu, K. Amine, *Adv. Energy Mater.* 9 (2019), 1900161, <https://doi.org/10.1002/aenm.201900161>.
- [10] D. Billaud, F.X. Henry, M. Lelaurain, P. Willmann, *J. Phys. Chem. Solid.* 57 (1996) 775–781, [https://doi.org/10.1016/0022-3697\(95\)00348-7](https://doi.org/10.1016/0022-3697(95)00348-7).
- [11] K.R. Kganayo, P.E. Ngoepe, *Phys. Rev. B* 68 (2003), <https://doi.org/10.1103/PhysRevB.68.205111>.
- [12] M. Hahn, H. Buqa, P.W. Ruch, D. Goers, M.E. Spahr, J. Ufheil, P. Novák, R. Kötz, *Electrochem. Solid State Lett.* 11 (2008) A151, <https://doi.org/10.1149/1.2940573>.
- [13] Y. Qi, H. Guo, L.G. Hector, A. Timmons, *J. Electrochem. Soc.* 157 (2010) A558, <https://doi.org/10.1149/1.3327913>.
- [14] D. Lee, A. Kondo, S. Lee, S. Myeong, S. Sun, I. Hwang, T. Song, M. Naito, U. Paik, *J. Power Sources* 457 (2020), 228021, <https://doi.org/10.1016/j.jpowsour.2020.228021>.
- [15] D. Sauersteig, N. Hanselmann, A. Arzberger, H. Reinshagen, S. Ivanov, A. Bund, *J. Power Sources* 378 (2018) 235–247, <https://doi.org/10.1016/j.jpowsour.2017.12.044>.
- [16] D. Sauersteig, S. Ivanov, H. Reinshagen, A. Bund, *J. Power Sources* 342 (2017) 939–946, <https://doi.org/10.1016/j.jpowsour.2016.12.121>.
- [17] L. de Biasi, A.O. Kondrakov, H. Geßwein, T. Brezesinski, P. Hartmann, J. Janek, *J. Phys. Chem. C* 121 (2017) 26163–26171, <https://doi.org/10.1021/acs.jpcc.7b06363>.
- [18] S. Ivanov, D. Sauersteig, A. Dimitrova, S. Krischok, A. Bund, *J. Power Sources* 457 (2020), 228020, <https://doi.org/10.1016/j.jpowsour.2020.228020>.
- [19] J. Cannarella, X. Liu, C.Z. Leng, P.D. Sinko, G.Y. Gor, C.B. Arnold, *J. Electrochem. Soc.* 161 (2014) F3117–F3122, <https://doi.org/10.1149/2.019141jes>.
- [20] I.C. Halalay, M.J. Lukitsch, M.P. Balogh, C.A. Wong, *J. Power Sources* 238 (2013) 469–477, <https://doi.org/10.1016/j.jpowsour.2013.04.036>.
- [21] A. Sheidaei, X. Xiao, X. Huang, J. Hitt, *J. Power Sources* 196 (2011) 8728–8734, <https://doi.org/10.1016/j.jpowsour.2011.06.026>.
- [22] E.J. Cheng, K. Hong, N.J. Taylor, H. Choe, J. Wolfenstine, J. Sakamoto, *J. Eur. Ceram. Soc.* 37 (2017) 3213–3217, <https://doi.org/10.1016/j.jeurceramsoc.2017.03.048>.
- [23] V.A. Sethuraman, N. van Winkle, D.P. Abraham, A.F. Bower, P.R. Guduru, *J. Power Sources* 206 (2012) 334–342, <https://doi.org/10.1016/j.jpowsour.2012.01.036>.
- [24] J. Cannarella, C.B. Arnold, *J. Electrochem. Soc.* 162 (2015) A1365–A1373, <https://doi.org/10.1149/2.1051507jes>.
- [25] F. Ebert, A. Oberbauer, M.A. Cabañero, G. Sextl, M. Lienkamp, *Int. J. Artif. Intell. Expt. Syst.* 10 (2019) 242–248, <https://doi.org/10.20485/jsaeijae.10.2.242>.
- [26] M. Tang, P. Albertus, J. Newman, *J. Electrochem. Soc.* 156 (2009) A390, <https://doi.org/10.1149/1.3095513>.
- [27] M. Petzl, M.A. Danzer, *J. Power Sources* 254 (2014) 80–87, <https://doi.org/10.1016/j.jpowsour.2013.12.060>.

- [28] T.C. Bach, S.F. Schuster, E. Fleder, J. Müller, M.J. Brand, H. Lormann, A. Jossen, G. Sextl, *J. Energy Storage* 5 (2016) 212–223, <https://doi.org/10.1016/j.est.2016.01.003>.
- [29] F. Ebert, G. Sextl, M. Lienkamp, Effect of a Flexible Battery Module Bracing on Cell Aging, *IEEE, Piscataway, NJ*, 2017.
- [30] V. Müller, R.-G. Scurtu, M. Memm, M.A. Danzer, M. Wohlfahrt-Mehrens, *J. Power Sources* 440 (2019), 227148, <https://doi.org/10.1016/j.jpowsour.2019.227148>.
- [31] M. Nagayama, K. Ariyoshi, Y. Yamamoto, T. Ohzuku, *J. Electrochem. Soc.* 161 (2014) A1388–A1393, <https://doi.org/10.1149/2.0981409jes>.
- [32] Y. Koyama, N. Yabuuchi, I. Tanaka, H. Adachi, T. Ohzuku, *J. Power Sources* 151 (2004) A1545, <https://doi.org/10.1149/1.1784823>.
- [33] Y. Koyama, I. Tanaka, H. Adachi, Y. Makimura, T. Ohzuku, *J. Power Sources* 119–121 (2003) 644–648, [https://doi.org/10.1016/S0378-7753\(03\)00194-0](https://doi.org/10.1016/S0378-7753(03)00194-0).
- [34] M. Bauer, M. Wachtler, H. Stöwe, J.V. Persson, M.A. Danzer, *J. Power Sources* 317 (2016) 93–102, <https://doi.org/10.1016/j.jpowsour.2016.03.078>.
- [35] W. Biberacher, A. Lerf, J.O. Besenhard, H. Möhwald, T. Butz, *MRS Bull.* 17 (1982) 1385–1392, [https://doi.org/10.1016/0025-5408\(82\)90223-9](https://doi.org/10.1016/0025-5408(82)90223-9).
- [36] B. Rieger, S. Schlueter, S.V. Erhard, J. Schmalz, G. Reinhart, A. Jossen, *J. Energy Storage* 6 (2016) 213–221, <https://doi.org/10.1016/j.est.2016.01.006>.
- [37] J.R. Dahn, *Phys. Rev. B* 44 (1991) 9170–9177, <https://doi.org/10.1103/PhysRevB.44.9170>.
- [38] T. Ohzuku, *J. Electrochem. Soc.* 140 (1993) 2490, <https://doi.org/10.1149/1.2220849>.
- [39] T. Zhang, D. Li, Z. Tao, J. Chen, *Prog. Nat. Sci.: Mater. Int.* 23 (2013) 256–272, <https://doi.org/10.1016/j.pnsc.2013.04.005>.
- [40] J. Cannarella, C.B. Arnold, *J. Power Sources* 245 (2014) 745–751, <https://doi.org/10.1016/j.jpowsour.2013.06.165>.
- [41] M. Wünsch, J. Kaufman, D.U. Sauer, *J. Energy Storage* 21 (2019) 149–155, <https://doi.org/10.1016/j.est.2018.11.019>.
- [42] A.S. Mussa, M. Klett, G. Lindbergh, R.W. Lindström, *J. Power Sources* 385 (2018) 18–26, <https://doi.org/10.1016/j.jpowsour.2018.03.020>.
- [43] T. Palaniselvam, M. Goktas, B. Anothumakkool, Y.-N. Sun, R. Schmich, L. Zhao, B.-H. Han, M. Winter, P. Adelhelm, *Adv. Funct. Mater.* 29 (2019), 1900790, <https://doi.org/10.1002/adfm.201900790>.
- [44] M. Winter, J.O. Besenhard, M.E. Spahr, P. Novák, *Adv. Mater.* 10 (1998) 725–763, [https://doi.org/10.1002/\(SICI\)1521-4095\(199807\)10:10<725:AID-ADMA725>3.0.CO;2-Z](https://doi.org/10.1002/(SICI)1521-4095(199807)10:10<725:AID-ADMA725>3.0.CO;2-Z).
- [45] A. Mukhopadhyay, B.W. Sheldon, *Prog. Mater. Sci.* 63 (2014) 58–116, <https://doi.org/10.1016/j.pmatsci.2014.02.001>.
- [46] C. Weng, Y. Cui, J. Sun, H. Peng, *J. Power Sources* 235 (2013) 36–44, <https://doi.org/10.1016/j.jpowsour.2013.02.012>.
- [47] L. Zheng, J. Zhu, D.D.-C. Lu, G. Wang, T. He, *Energy* 150 (2018) 759–769, <https://doi.org/10.1016/j.energy.2018.03.023>.
- [48] M.D. Levi, D. Aurbach, *J. Electroanal. Chem.* 421 (1997) 79–88, [https://doi.org/10.1016/S0022-0728\(96\)04832-2](https://doi.org/10.1016/S0022-0728(96)04832-2).
- [49] S.J. An, J. Li, C. Daniel, D. Mohanty, S. Nagpure, D.L. Wood, *Carbon* 105 (2016) 52–76, <https://doi.org/10.1016/j.carbon.2016.04.008>.
- [50] J.O. Besenhard, M. Winter, J. Yang, W. Biberacher, *J. Power Sources* 54 (1995) 228–231, [https://doi.org/10.1016/0378-7753\(94\)02073-C](https://doi.org/10.1016/0378-7753(94)02073-C).
- [51] G.-C. Chung, H.-J. Kim, S.-I. Yu, S.-H. Jun, J.-w. Choi, M.-H. Kim, *J. Electrochem. Soc.* 147 (2000) 4391, <https://doi.org/10.1149/1.1394076>.
- [52] E. Peled, S. Menkin, *J. Electrochem. Soc.* 164 (2017) A1703–A1719, <https://doi.org/10.1149/2.1441707jes>.
- [53] A.N. Dey, B.P. Sullivan, *J. Electrochem. Soc.* 117 (1970) 222, <https://doi.org/10.1149/1.2407470>.
- [54] D. Aurbach, M.D. Levi, E. Levi, A. Schechter, *J. Phys. Chem. B* 101 (1997) 2195–2206, <https://doi.org/10.1021/jp962815t>.
- [55] D. Aurbach, B. Markovsky, I. Weissman, E. Levi, Y. Ein-Eli, *Electrochim. Acta* 45 (1999) 67–86, [https://doi.org/10.1016/S0013-4686\(99\)00194-2](https://doi.org/10.1016/S0013-4686(99)00194-2).
- [56] D. Aurbach, M. Koltypin, H. Teller, *Langmuir* 18 (2002) 9000–9009, <https://doi.org/10.1021/la020306e>.
- [57] S.-K. Jeong, M. Inaba, T. Abe, Z. Ogumi, *J. Electrochem. Soc.* 148 (2001) A989, <https://doi.org/10.1149/1.1387981>.
- [58] F.P. Campana, R. Kötz, J. Vetter, P. Novák, H. Siegenthaler, *Electrochem. Commun.* 7 (2005) 107–112, <https://doi.org/10.1016/j.elecom.2004.11.015>.
- [59] N.A. Kaskhedikar, J. Maier, *Adv. Mater.* 21 (2009) 2664–2680, <https://doi.org/10.1002/adma.200901079>.
- [60] P. Lu, C. Li, E.W. Schneider, S.J. Harris, *J. Phys. Chem. C* 118 (2014) 896–903, <https://doi.org/10.1021/jp4111019>.
- [61] S.J. An, J. Li, Z. Du, C. Daniel, D.L. Wood, *J. Power Sources* 342 (2017) 846–852, <https://doi.org/10.1016/j.jpowsour.2017.01.011>.
- [62] J.R. Dahn, R. Fong, M.J. Spoon, *Phys. Rev. B* 42 (1990) 6424–6432, <https://doi.org/10.1103/PhysRevB.42.6424>.
- [63] A. Eddahech, O. Briat, J.-M. Vinassa, *J. Power Sources* 258 (2014) 218–227, <https://doi.org/10.1016/j.jpowsour.2014.02.020>.
- [64] R. Jung, R. Morasch, P. Karayaylali, K. Phillips, F. Maglia, C. Stinner, Y. Shao-Horn, H.A. Gasteiger, *J. Electrochem. Soc.* 165 (2018) A132–A141, <https://doi.org/10.1149/2.0401802jes>.

Impact of electrochemical and mechanical interactions on lithium-ion battery performance investigated by *operando* dilatometry

Philip Daubinger ^a, Fabian Ebert ^{a,b}, Sarah Hartmann ^a, Guinevere A. Giffin ^{a,*}

^aFraunhofer R&D Center Electromobility, Fraunhofer Institute for Silicate Research, Neunerplatz 2, 97082 Wuerzburg, Germany

^bInstitute of Automotive Technology, Technical University of Munich TUM, Boltzmannstraße 15, 85748 Garching, Germany

*Corresponding author. Phone: +49 931 4100 959. E-mail address: guinevere.giffin@isc.fraunhofer.de

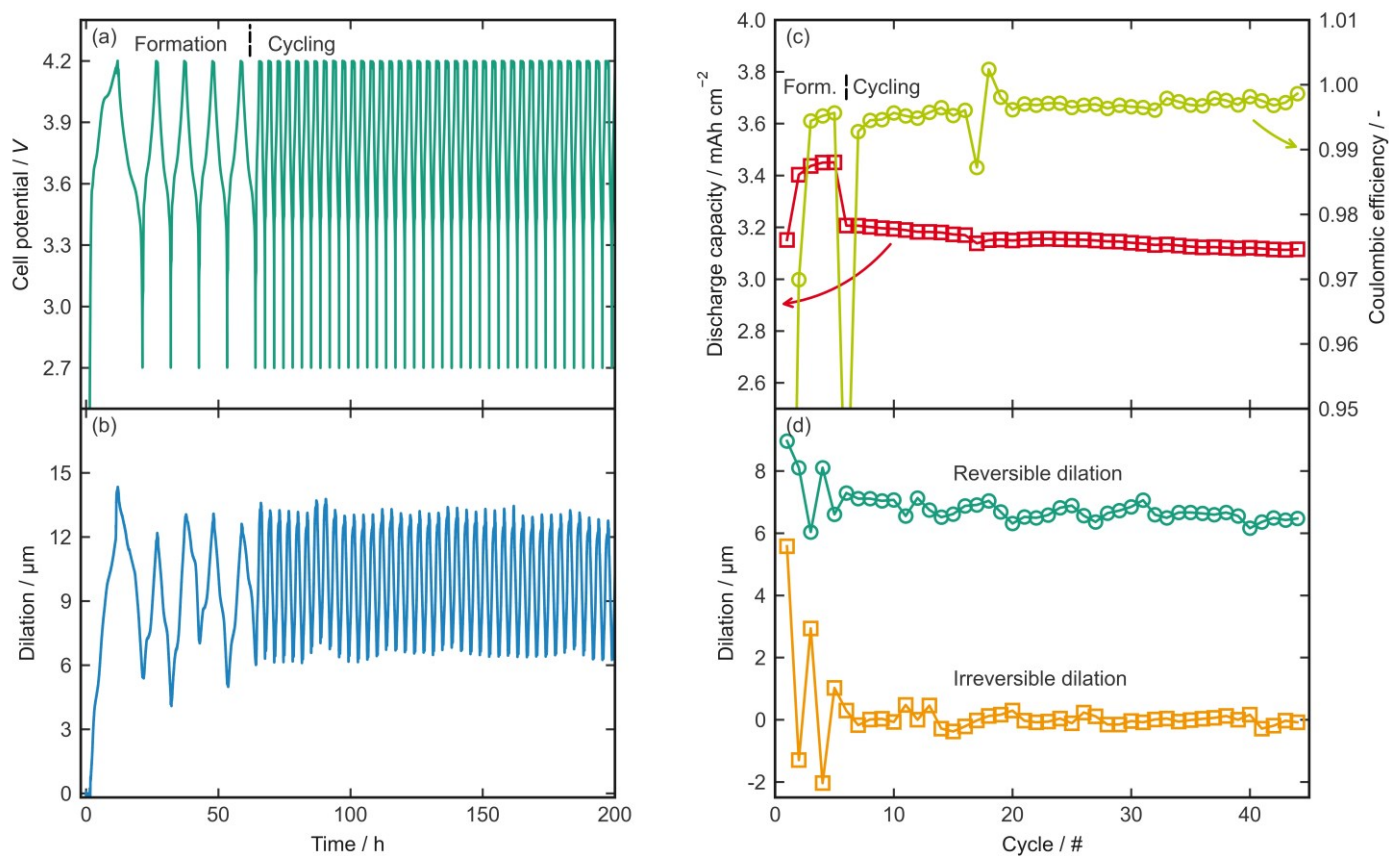


Figure Supplementary 1: Cycling of graphite vs. NCM111 with one initial 0.1 C cycle and four 0.2 C cycles (formation procedure), followed by further cycling at 0.75 C. (a) Cell potential and (b) dilatation as a function of time and (c) discharge capacity, coulombic efficiency and (d) reversible and irreversible dilatation as a function of cycle number. Reversible and irreversible dilatation of graphite during formation.

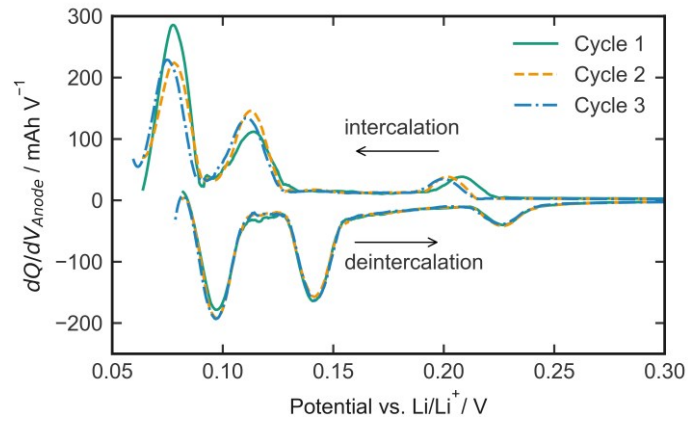


Figure Supplementary 2: ICA of three 0.1 C formation cycles.

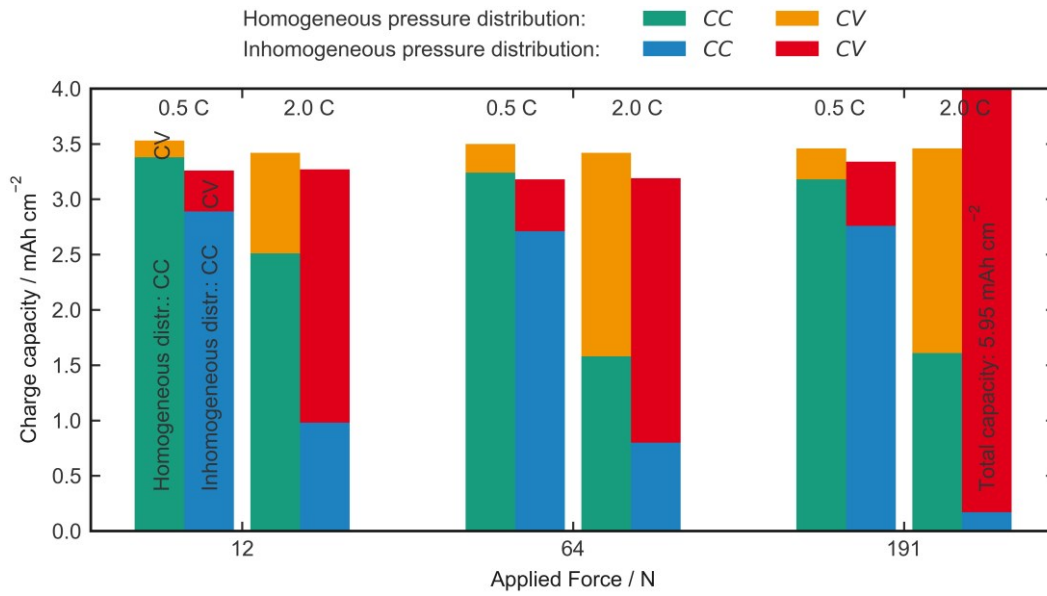


Figure Supplementary 3: Overview of the proportion of CC step to CV step during charging for different pressure distributions, C-rates and forces.

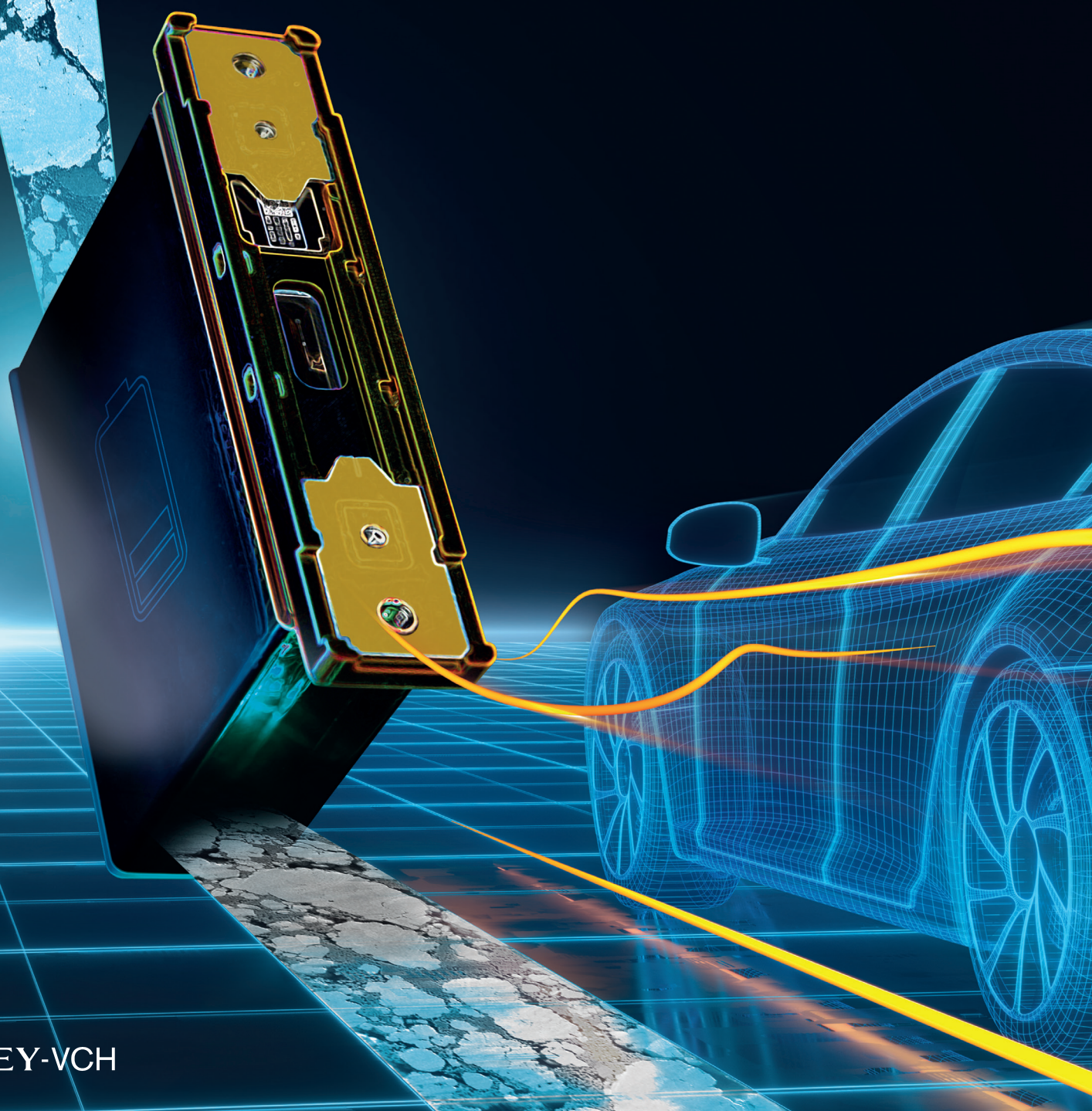
Table Supplementary 1: Change in resistance and characteristic frequency before and after cycling.

Plunger	Force / N	$\Delta R_{\Omega} /$ $\Omega \text{ cm}^2$	$\Delta R_{\text{SEI}} /$ $\Omega \text{ cm}^2$	$\Delta R_{\text{CT}} /$ $\Omega \text{ cm}^2$	$\Delta f_{\text{SEI}} /$ Hz	$\Delta f_{\text{CT}} /$ Hz
flat	12	0.5	-0.2	1.5	-60	-10
10 μm step	12	5.0	12.4	6.8	73	-23
flat	64	0.1	0.1	1.9	48	-8
10 μm step	64	1.4	0.0	5.2	298	-16
flat	191	0.1	-2.4	3.0	204	-12
10 μm step	191	18.9	38.4	27.5	874	-12

Vol. 12 • No. 10 • March 10 • 2022

www.advenergymat.de

ADVANCED ENERGY MATERIALS



WILEY-VCH

RESEARCH ARTICLE

Impact of Bracing on Large Format Prismatic Lithium-Ion Battery Cells during Aging

Philip Daubinger, Matthias Schelter, Ronny Petersohn, Felix Nagler, Sarah Hartmann, Matthias Herrmann, and Guinevere A. Giffin*

To reduce the ecological footprint and to increase the lifetime of lithium-ion batteries (LIBs), it is necessary to understand aging phenomena inside the cells during cycling. In this study, the positive effect of external pressure through bracing the cells on aging is investigated for automotive battery cells with more than 7000 cycles. After cycling, the aged cells are studied by using post-mortem analysis. It is shown that bracing does not affect the anode and cathode in the same manner. A lack of external pressure results in lithium plating due to contact losses on the anode. Such a loss of lithium inventory plays only a small role in the braced cells. However, the structural and morphological degradation, such as particle cracking at the cathode, is significant. Half-cell tests of aged and unaged anode samples extracted from the automotive cells confirm the post-mortem findings, where only minimal differences can be seen for the braced cell. In contrast, the aged cathodes from braced cells demonstrate substantial capacity fade in half-cell measurements as compared to the cathodes extracted from the unbraced cell. Finally, a new concept of the mechanical state of health (mechanical SOH) is introduced to correlate mechanical effects with electrode degradation.

lower emissions and higher efficiency of the electric drive trains (30–66% lower emissions over lifetime depending the source of the electricity used).^[1,2] Lithium-ion batteries (LIB) play a key role in the electromobility because of their high specific energy and high efficiency (well-to-wheel efficiency: BEV ≈70% compared to ICE ≈25%).^[3–6] Nonetheless, there remain several limitations such as the high initial costs,^[4,7,8] the limited recycling scheme,^[9–13] material bottlenecks, particularly for cobalt and lithium^[14–17] and the safety concerns.^[18–21] Due to these economic and ecological reasons, a long battery cell lifetime is essential for the widespread acceptance by the society and to reduce the ecological footprint and the costs.

Today, there are different cell geometries used in BEV or HEV. The three most common cell types are the pouch cell, the round or cylindrical cell (e.g., 18 650- or 21 700 type) and the prismatic

cell.^[22,23] The pouch cell has the highest specific energy of all cell types, but has a low mechanical stiffness of the laminate casing.^[24] However, this low mechanical stiffness is compensated with the use of external bracing, which is known to reduce aging.^[25,26] Pouch cells are part of the battery system of, e.g., the VW ID.3^[27] or the Porsche Taycan.^[28] The battery of the Tesla Model S/3 contains round/cylindrical cells^[29,30] while other BEVs use prismatic cells in their battery packs such as BMW i3^[31] or Mazda MX-30.^[32] The advantages of prismatic cells are the dense packaging, the simple module design and the high energy density in modules.^[24] However, they age faster than cylindrical cells due to a number of reasons including the lower pressure or mechanical stability inside the cell.^[33] As a result of reversible and irreversible volume changes of the anode and the cathode during cycling,^[34–38] low compression can result in insufficient contact between the components within an electrode stack.

There are several publications that have examined the influence of external mechanical pressure on cell aging. Most of the studies deal with either cylindrical^[39] or pouch cells^[25,40–43] with a small nominal capacity of <6 Ah. Hahn et al.^[44] and Wuensch et al.^[26] investigated the effect of different types of bracing on automotive lithium-ion pouch cells with a capacity of 40 Ah, respectively 37 Ah. There are a few reports about the aging effects in prismatic cells^[45–50] but only little about the impact of bracing on the cells' cycling performance.

1. Introduction

The change from conventional internal combustion engines (ICE) to electric motors in battery electric vehicles (BEV) or in some hybrid electric vehicles (HEV) is underway due to the

P. Daubinger, F. Nagler, S. Hartmann, G. A. Giffin
Fraunhofer R&D Center Electromobility
Fraunhofer Institute for Silicate Research
Neunerplatz 2, 97082 Wuerzburg, Germany
E-mail: guinevere.giffin@isc.fraunhofer.de

M. Schelter, R. Petersohn, M. Herrmann
Intilion GmbH
Dr.-Sinsteden-Strasse 8, 08056 Zwickau, Germany
G. A. Giffin
Chemical Technology of Materials Synthesis
Faculty of Chemistry and Pharmacy
Julius-Maximilians-University Wuerzburg
Roentgenring 11, 97070 Wuerzburg, Germany

 The ORCID identification number(s) for the author(s) of this article can be found under <https://doi.org/10.1002/aenm.202102448>.

© 2021 The Authors. Advanced Energy Materials published by Wiley-VCH GmbH. This is an open access article under the terms of the Creative Commons Attribution License, which permits use, distribution and reproduction in any medium, provided the original work is properly cited.

DOI: 10.1002/aenm.202102448

In this study, the impact of mechanical bracing on the lifetime of large format 94 Ah prismatic cells during an accelerated aging test is examined. In the first part, the electrochemical results of the aging tests, where the cells were cycled for more than 7000 cycles under different bracing conditions, are presented. In the second part, the degradation of the cells using different post-mortem analysis techniques is examined. Furthermore, a new concept, the “mechanical state of health” (mechanical SOH) is introduced and discussed. The mechanical SOH is used to demonstrate the impact of mechanical forces, for example, external pressure or cell casing, on the performance of the cell or electrodes.

2. Results and Discussion

Figure 1 shows the master chart of all tests conducted in this study. Physical and electrical tests of the large format prismatic LIBs (with and without external pressure, i.e., bracing) are shown in Section 2.1. After the tests on the prismatic cells, the cells were opened and a post-mortem analysis was conducted (Section 2.2). This included an optical inspection (Section 2.2.1) and a physicochemical characterization to examine the morphology, the thickness, the chemical composition, and the structure of the electrodes as discussed in Section 2.2.2. Finally, the

electrodes harvested electrodes after cell opening are characterized with electrochemical measurements in laboratory cells as in Section 2.2.3. In addition to the master chart in Figure 1a, Table S1, Supporting Information, has been included with a summary of the measurements and the main result from each one.

2.1. Accelerated Aging Test of the Prismatic Automotive Cells

The cell performance during the accelerated aging test of the different cells is shown in Figure 2. All the cells show similar aging in the beginning with a significant capacity loss in the first 700 cycles followed by a plateau at ≈ 84 Ah, which corresponds to 90% state of health (SOH), for up to 3000 cycles (Figure 2a). Starting at ≈ 3000 cycles, the unbraced cells show a larger drop in capacity compared to the braced cells. The critical threshold of 80% SOH was reached for the unbraced cells at ≈ 3800 cycles and at ≈ 4700 cycles for the braced cell. After ≈ 7420 cycles for the unbraced cells and after ≈ 7170 cycles for the braced cells, the cycling of the cells was paused for five weeks to see the relaxation behavior of the cells. The unbraced cells showed no capacity recovery after the break. In contrast, the braced cells regained $\approx 12\%$ of the discharge capacity when comparing the last five cycles before and the first five cycles after the break. These observations indicate

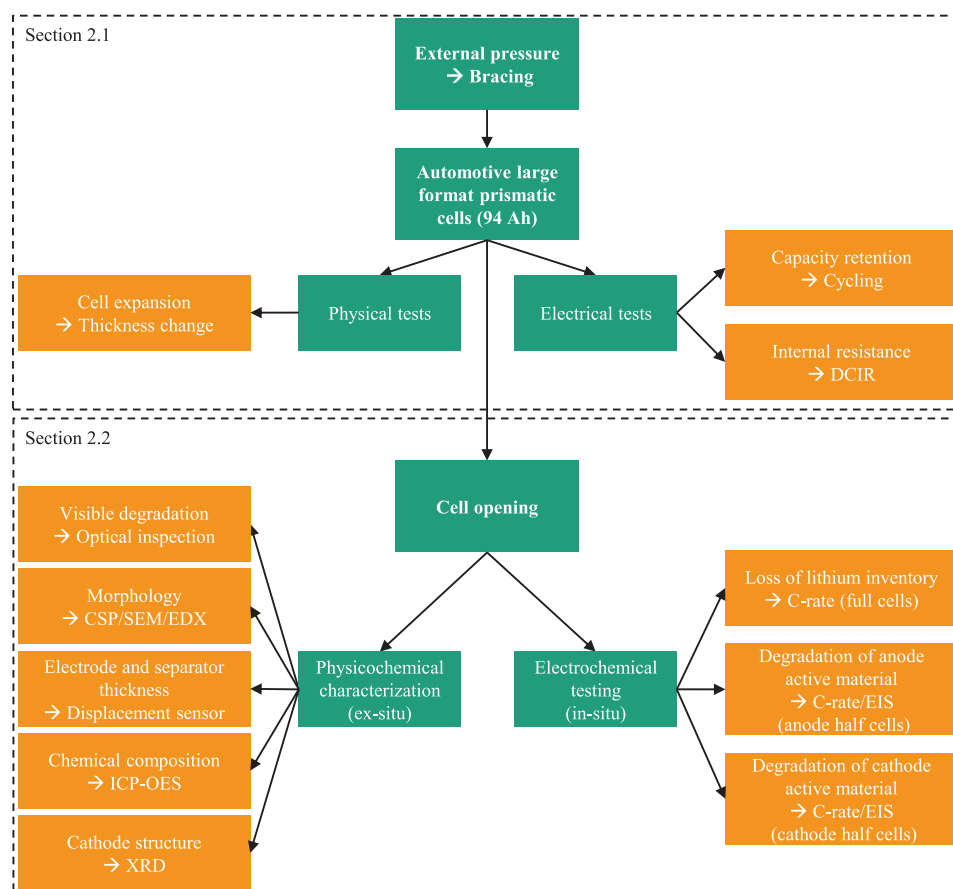


Figure 1. Master chart of the experiments conducted in this work. Section 2.1 deals with the aging of the prismatic lithium-ion cells and Section 2.2 with the subsequent post-mortem study.

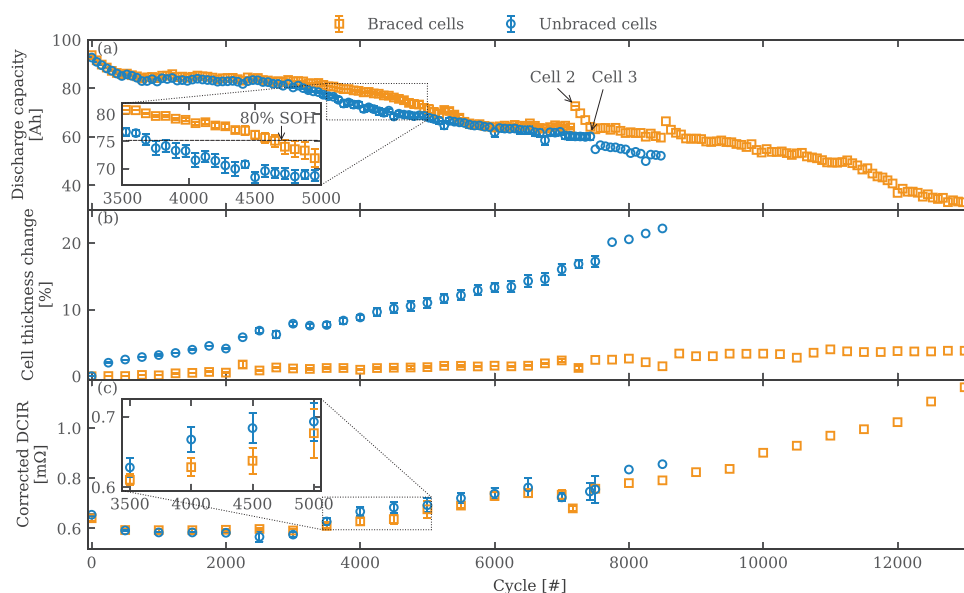


Figure 2. a) Cycling of prismatic cells under different external bracing conditions. The capacity is only plotted every 75th cycle for better visibility. b) Thickness change measured every 250 cycles and c) corrected DCIR determined every 500 cycles at 100% SOC with a discharging current rate of 2 C.

a reversible capacity loss in the braced cell and an irreversible capacity loss in the unbraced cell. After the pause step, the cells were cycled for ≈ 80 cycles and then one of each unbraced and braced cells was used for post-mortem analysis while the other cells were cycled until 8500 cycles (unbraced cell) and 13 000 cycles (braced cell), with nearly linear capacity fading.

A difference in the thickness change between the unbraced and braced cells can be seen in Figure 2b and Figure S1, Supporting Information. The unbraced cells have a relatively linear thickness increase during the aging test with a total increase of 22% (≈ 10 mm) at end of life (EOL). This might be attributed to lithium plating on the anode, electrode swelling, delamination, and/or layer depositions on the electrodes. After the 5 week cycling pause after ≈ 7420 cycles, no decline in thickness is observed, which might be related to irreversible lithium plating and thus an irreversible loss of capacity. It should be noted that a plastic deformation of the aluminum housing might also be a reason for the unchanged thickness after the pause. The braced cells show only a small thickness increase of $\approx 2.5\%$ (≈ 1.1 mm) after 7000 cycles compared to the initial thickness of the cell. Interestingly, the thickness change decreased by $\approx 45\%$ (≈ 0.5 mm) after the cycling pause compared to the thickness change before the break. This might be related to reversible lithium plating on the surface of the anodes which intercalates into the graphite structure at steady state conditions.

The corrected direct current internal resistance (DCIR) was determined every 500 cycles for Cell 2 (braced) and Cell 3 (unbraced) (Figure 2c). The initial resistance (after initial charging) of the unbraced cell is comparable to the braced cell (i.e., 0.65 and 0.64 m Ω , respectively). After the initial cycles, the DCIR decreases for both cells as the formation reactions are completed^[51] and then remains, more or less, stable until 3000 cycles. The larger increase of the resistance of the unbraced cell between 3500 and 4500 cycles (Figure 2c inset) is related to the increased capacity loss compared to the braced cell (Figure 2a inset). After the cycling break, the DCIR of the braced cells decreases by $\approx 5.0\%$, while the drop is negligible for

the unbraced cell. This is a further indication that reversible lithium plating or capacity loss occurs in the braced cell.

The unbraced cells show increased aging during cycling compared to the braced cells. The unbraced cells reach the threshold of 80% SOH, which is a typical value for the minimum usable capacity for BEV/HEV cells,^[52–54] ≈ 900 cycles earlier than the braced cells with the same aging procedure.

2.2. Post-Mortem Analysis of Three Different Aged Cells

For a deeper understanding of the different degradation mechanisms within the cells and to examine the cause of the thickness increase, post-mortem investigations were conducted on three of the cells. The first cell (Cell 1) is the reference cell without being cycled (only formation cycles), the second cell is the braced cell (Cell 2), and the third cell is the unbraced cell (Cell 3).

2.2.1. Cell Opening

Figure 3 shows photographs of the electrodes and separators after cell opening inside the glovebox. The unaged electrodes of Cell 1 (Figure 3a: Cell 1: Reference cell [unaged]) show no visible degradation (e.g., depositions, delamination, or cracks) and the electrode layers appear homogeneous. The appearance of separator indicates no visible degradation and no electrode material sticks to the separator. The components extracted from Cell 2 (Figure 3b: Cell 2: aged cell, braced) shows only little visible degradation. Overall the anode looks homogeneous except at some spots adjacent to the current collector. Some windings (area at the edge of a jelly rolls [JR], where the electrodes are wrapped around) indicate minor lithium plating and delamination. Next to the current collector, the current is higher due to the ohmic potential drop along the negative current collector.^[55,56] Therefore the current is higher, which promotes lithium plating. At the windings, the inhomogeneous pressure distribution

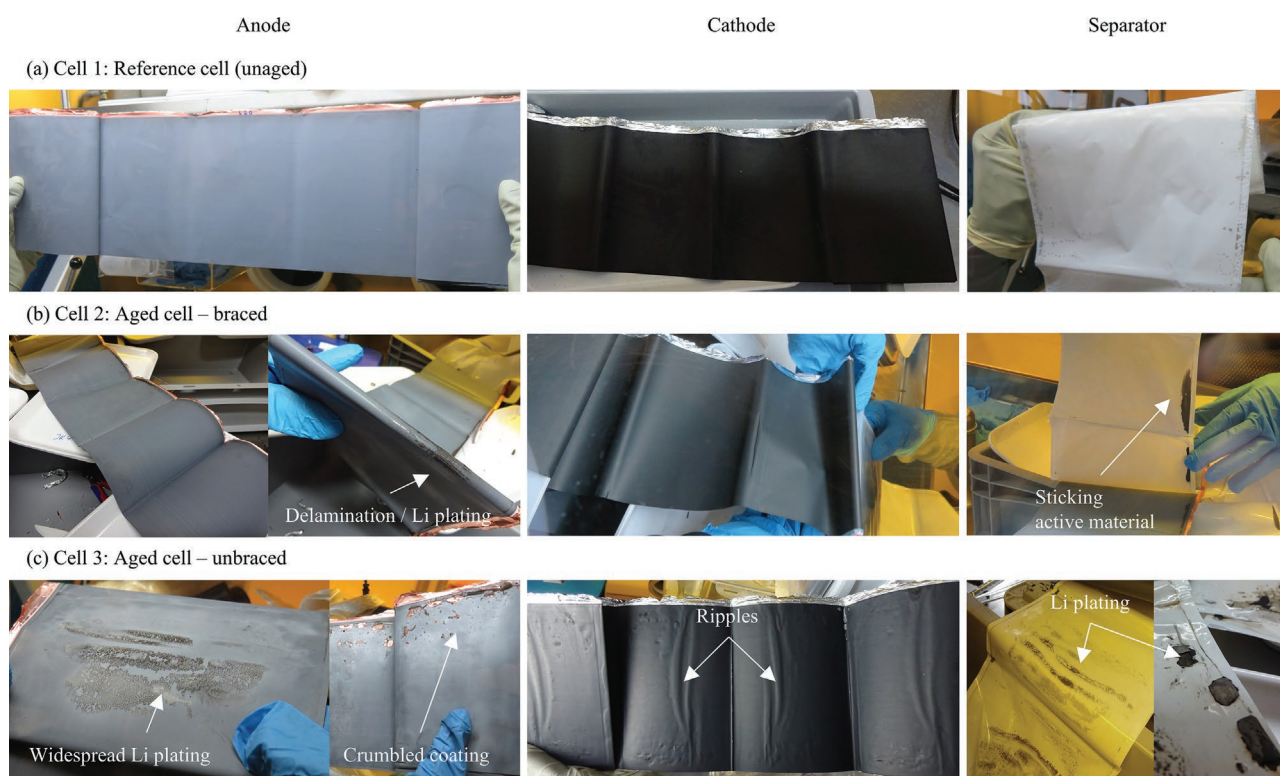


Figure 3. Photographs of electrodes and separators after cell opening. a) Cell 1: unaged reference cell, b) Cell 2: aged braced cell, and c) Cell 3: aged unbraced cell.

leads to a reduction of the separator porosity and thus, high exchange currents drive lithium plating.^[57] The cathode looks homogeneous with no visible deposition layers, for example, due to electrolyte decomposition, and only some cracks are found at the winding of the electrodes. This might be an artefact resulting from unwinding and separation of the electrodes and not from electrochemical aging effects. The appearance of the separator is consistent with the results from the electrodes and shows no obvious alteration, except for few spots adjacent to the current collector where anode material can be found sticking on the separator. The electrodes and separator of Cell 3 (Figure 3c: Cell 3: aged cell, unbraced) show significant degradation. Lithium plating is visible over a large area of the anode, mainly at windings, next to current collector and also in some areas spread over the flat face of the electrode sheet. Next to the current collector, there are also areas with crumbled coating and even small holes/perforations of the anode. The cathode shows little visible degradation in terms of deposition layers or cracks, but ripple formation is found in some stretches of the cathode. These ripples become more pronounced when moving from the outside layers to the inner layers of the JR. Extensive lithium plating can be found on the anodes facing those rippled areas (see Figure S2, Supporting Information). The peaks and troughs of the rippled areas demonstrate contact losses between anode, separator, and cathode and/or local separator deformation. This favors lithium plating on the anode due to high exchange currents. It remains unclear if the ripples initiate the areal contact losses and thus the lithium plating on the anode or vice versa. The obvious degradation and loss of

lithium inventory also becomes evident when examining the separator. Here pieces of plated lithium are found as well as anode material (imprints of the ripples). Furthermore, melted areas of the separator are found close to material deposits.

These results show that for the braced cell there are only few areas showing visible degradation, such as lithium plating at some windings. In contrast, lithium plating in unbraced Cell 3 is pronounced and seems to be the predominant cause of degradation in the unbraced cells. At areas with high pressure inhomogeneity (e.g., windings) and high currents (close to current collector), lithium plating is even more pronounced. The external bracing leads to a more homogeneous pressure distribution over the cell which reduces the contact losses between the electrodes (e.g., cathode ripples) and hence also the degradation (e.g., lithium plating). The small amount of lithium plating also supports the theory of reversible lithium plating. During the 5 week pause in cycling (described in Section 2.1), plated lithium can re-intercalate into the graphite structure during steady-state conditions in the braced cell, which increases the capacity and decreases the thickness and the internal resistance of the cell.

2.2.2. Physicochemical Analysis

After cell opening, the surface of the electrodes was examined with scanning electron microscopy (SEM) (Figure 4 and Figure S3, Supporting Information). The morphology of the anode surface of Cell 1 (reference cell) shows a uniform Al_2O_3 particle coating on the graphite. This particulate surface layer is also observed

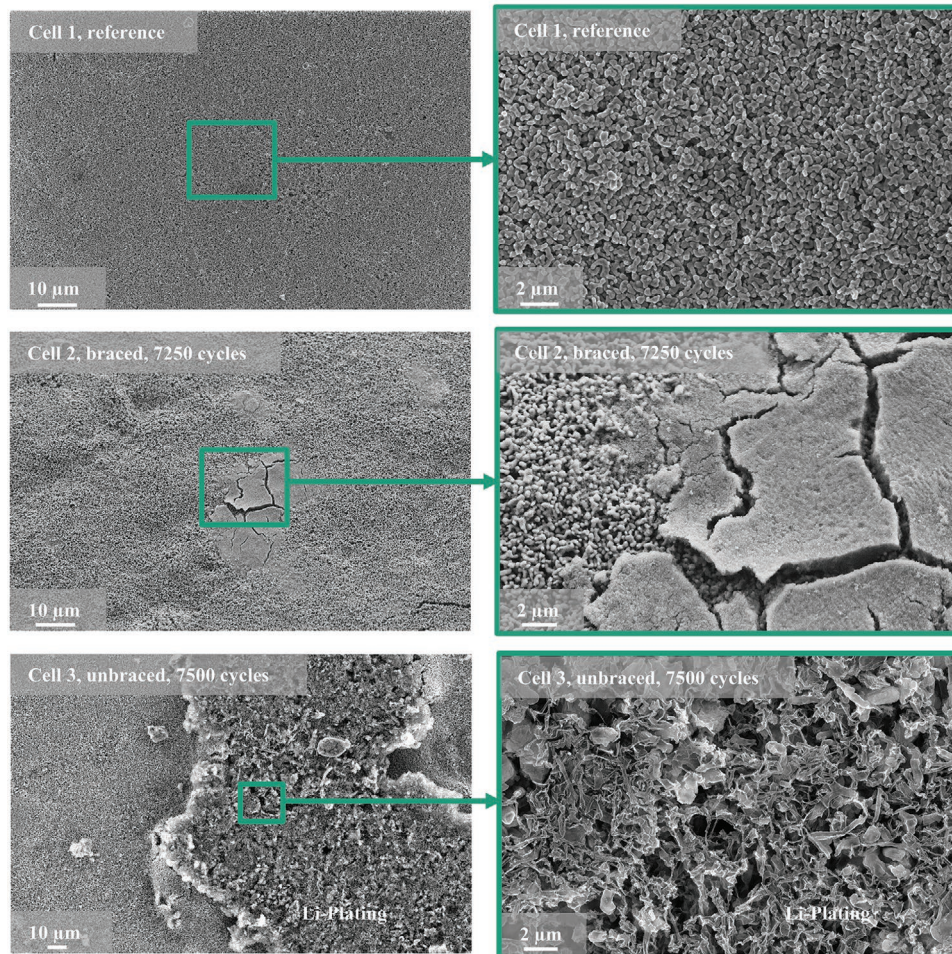


Figure 4. SEM pictures of anode surfaces of the reference and aged cells.

for Cell 2 (braced), but shows additional spots of deposition which can be decomposition products of the electrolyte. The anode surface of Cell 3 (unbraced) shows extensive areas with deposits, which can be attributed to plated lithium.

The SEM investigations of the cathode surfaces (Figure S3, Supporting Information) show no significant differences between Cells 1, 2, and 3. There is evidence of particle segregation with aging (Cells 2 and 3), which is not as pronounced for the cathode of the reference cell (Cell 1). However, neither major cracks nor delamination are found. The cathode samples from Cell 3 extracted from regions with and without ripple peaks and ripple troughs (Figure 3c: cathode) show no difference in surface morphology in the SEM images. Overall, there is neither formation of additional layers on the cathode surface due to aging nor delamination, indicating that the capacity reduction of the cell during cycling is largely associated with the anode and, for example, lithium plating. This aspect is discussed in more detail in the following sections.

For a closer analysis, the cross section of the electrodes is examined. The anodes of all cells consist of non-spherical graphite particles with a 2–6 μm thick Al_2O_3 particle coating. The total thickness of the double-sided graphite anodes ranges between $\approx 151 \mu\text{m}$ for Cell 1 and $\approx 177 \mu\text{m}$ for Cell 3, which includes the $\approx 7 \mu\text{m}$ thick Cu current collector (Table 1). The

analysis of the cross section (Figure S4, Supporting Information) reveals only marginal morphological changes, if any, between the reference cell (Cell 1) and the aged cells (Cells 2 and 3) in terms of cracks inside the particles. Nevertheless, the total thickness of the graphite electrode increases during aging (Table 1), which might be attributed to partial exfoliation and solid electrolyte interphase (SEI) formation. Most of the anode surfaces are covered by a uniform Al_2O_3 particle coating. Only for Cell 3, the unbraced aged cell, defects in the coating can be detected. It is at these locations that there is direct contact with the graphite particles and thus lithium plating occurs (Figure S4(d), Supporting Information). This finding is confirmed by the SEM- energy dispersive X-ray

Table 1. Mean thickness and standard deviation of double-sided coated electrodes and separators. The copper current collector (anode) is $\approx 7 \mu\text{m}$ thick and the aluminum current collector (cathode) $\approx 12 \mu\text{m}$.

	Anode thickness [μm]	Separator thickness [μm]	Cathode thickness [μm]
Cell 1: unaged, reference	150.7 ± 0.7	20.1 ± 0.4	131.2 ± 0.3
Cell 2: aged, braced	168.5 ± 1.9	20.0 ± 0.8	134.6 ± 1.3
Cell 3: aged, unbraced	176.8 ± 6.5	19.7 ± 0.7	142.3 ± 1.8

(EDX) measurements (Figure 5). Oxygen is detected over the complete surface of the graphite electrode, but aluminum, associated with the Al_2O_3 coating layer, is only detected in the center of the image. This indicates that there is lithium plating at the edges of the picture as the metallic lithium reacts with the oxygen of the air (e.g., Li_2O) during the cross-section polisher (CSP) sample preparation. Lithium plating starts at a defect site within the Al_2O_3 coating layer, which then further destroys the layer in adjacent areas and directly deposits on the graphite particles.

The SEM cross-sections of the cathodes are shown in Figure 6. The double-sided cathode is $\approx 131 \mu\text{m}$, including the $\approx 12 \mu\text{m}$ Al current collector, for Cell 1 and expands up to $\approx 142 \mu\text{m}$ for Cell 3 (Table 1). The cathode consists of secondary particles with diameters up to $\approx 12 \mu\text{m}$. The secondary particles of the reference cell (Figure 6a) exhibit only few cracks, whereas the secondary particles of the aged Cells 2 and 3 show significant particle cracking along the grain boundaries. These cracks are accompanied by volumetric changes in combination with external pressure on the electrodes. By cracking, “fresh” cathode/NCM active material comes into contact with electrolyte, which can cause undesirable side reactions along with the loss of ionic and electronic pathways within the electrode.^[58–60]

The amount of cracks in the case of Cell 2 is only slightly higher than Cell 3: without ripples (Figure 6b,c). In contrast, the amount of visible cracks is significantly higher in areas of the Cell 3 cathode with ripples compared to areas without ripples (Figure 6c,d). For Cell 3: with ripples (Figure 6d), there is a gradient where the gap size between the cracks increases from the current collector towards the surface of the electrode. These cracks can lead to contact losses between the particles especially at the surface of the electrode resulting in enhanced morphological degradation or increased overpotentials of the electrode in those areas. Additionally, the cracks cause a volumetric expansion of the particles, what can be seen in a thickness

increase of the cathode (Table 1). The smaller cathode thickness of Cell 2 compared to Cell 3 (134.6 to $142.3 \mu\text{m}$) may be related to the presence of external pressure, which might hinder the expansion of the particles to a certain degree. Another reason for the increased cathode thickness for Cell 3 is delamination, but this might also be an artifact from CSP preparation.

Overall, it can be concluded that the anode suffers from aging phenomena such as lithium plating, rather than from morphological changes. In contrast, the cathode shows significant morphological degradation along the grain boundaries (cracking), which probably contributes to the loss of cell capacity. The cathodes of the unbraced cell in the area of the ripples show enhanced particle cracking close to the surface. Although the SEM surface images suggested that the anode made a more significant contribution to cell aging, the SEM cross sections revealed as the cathode particles also shows significant morphological degradation during cycling. The negative impact of these cathode morphological changes on the cell performance is discussed in Section 2.2.3.

To examine the impact of lithium plating and cathode degradation, inductively coupled plasma optical emission spectroscopy (ICP-OES) is performed (in duplicate) on a sample from each electrode and each cell. The amount of lithium in the anode, in mole per square centimeter, is converted into milliamp hour per square centimeter to provide a value that is more tangible and thus easier to relate to the capacity losses. The areal lithium content increases in the anode during cycling as shown in Figure 7a. The anode of the unaged reference cell has a lithium content of $0.5 \pm 0.01 \text{ mAh cm}^{-2}$, which is 4.9% of the total lithium in the anode and cathode. This lithium is associated with the SEI and any remaining lithium ions inside the graphene layers. The share of lithium in the anode is 13.9% for Cell 2 (aged, braced) and 15.6% for Cell 3 (aged, unbraced). One possible reason for the lithium gain is the lithium plating on the anode during the aging test. Additionally, the growth of the SEI during aging consumes lithium which further increases the amount in the anode. These results demonstrate the loss of lithium inventory inside the battery cell due to lithium plating and SEI growth, which causes capacity reduction. A small amount of the lithium increase can be explained by a different degree of lithiation at cell opening due to different overpotentials, although an extensive CV step at 2.7 V at the end of discharge is intended to minimize this effect. The unbraced Cell 3 shows the highest lithium loss due to increased plating, which coincides with the results from analytical investigations discussed in the previous sections. It should be noted that for ICP-OES, anode samples with excessive visible lithium plating were not chosen in order to obtain representative values for Cell 3.

Based on the ICP-OES results, the composition of the cathode active material of Cell 1 (reference cell) is estimated as $\text{Li}_{1.0} \text{Ni}_{0.4} \text{Co}_{0.3} \text{Mn}_{0.3} \text{O}_2$, where the oxygen content is inferred from the crystal structure. The cathode active material composition of aged Cell 2 (braced) is estimated to be $\text{Li}_{0.84} \text{Ni}_{0.4} \text{Co}_{0.3} \text{Mn}_{0.3} \text{O}_2$, while that of Cell 3 (unbraced) is estimated to be $\text{Li}_{0.86} \text{Ni}_{0.4} \text{Co}_{0.3} \text{Mn}_{0.3} \text{O}_2$. For Cell 3, areas with and without ripples were studied but no notable differences in the metal ion contents were observed. It should be noted that the seemingly higher stoichiometric amount of lithium in the

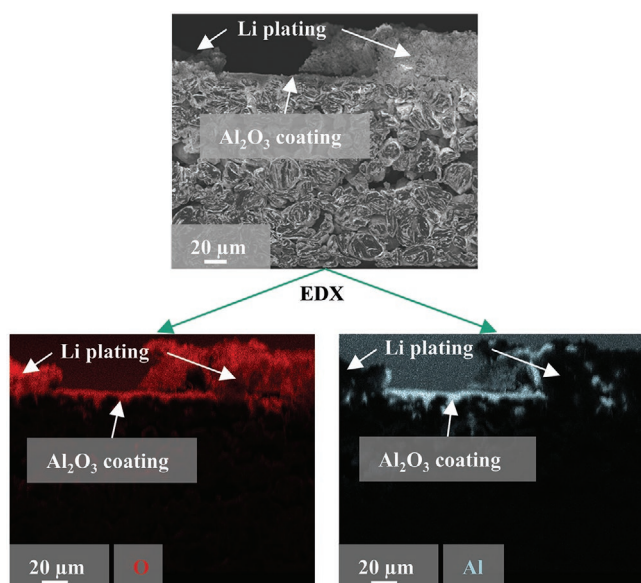


Figure 5. Cross section and SEM-EDX mapping (only O and Al displayed) of Cell 3: unbraced, with Li plating.

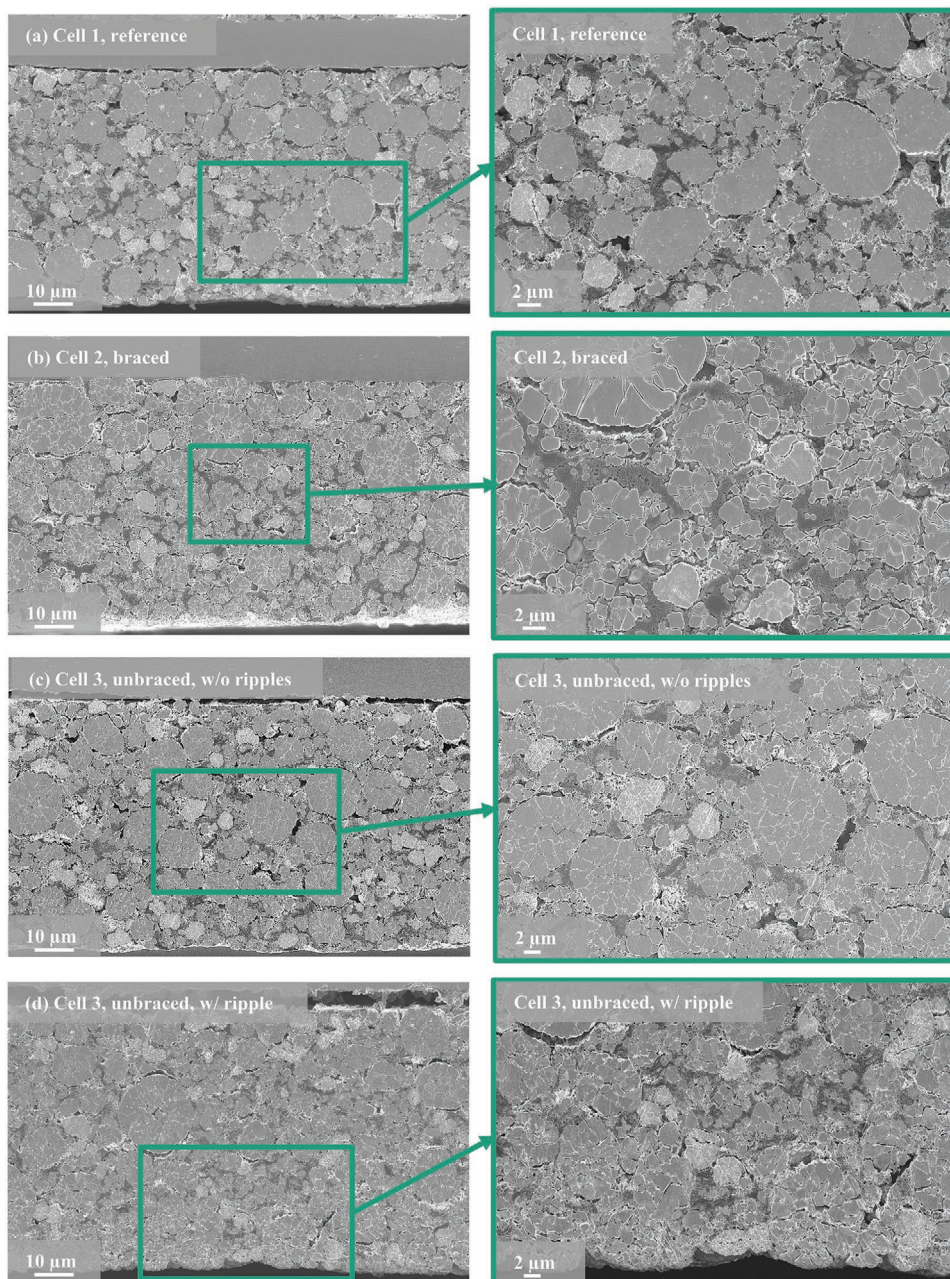


Figure 6. SEM cross sections of the differently aged cathodes. a) Cell 1, reference, b) Cell 2, braced, c) Cell 3, unbraced, w/o ripples, d) Cell 3, unbraced, w/ ripple. On the pictures on the left side the current collector can be seen at the top, and the electrode area near the surface at the bottom.

unbraced cell as compared to the braced is related to the calculation of the value itself. This is because the stoichiometric amount of lithium is based on the ratio of lithium to the sum of nickel, cobalt, and manganese. Since the amount of transition metals decreases more in the cathode of the unbraced cell than in the braced cell, the resultant proportion of lithium is higher in the unbraced cell.

The transition metal content in the anode is shown in the Figure 7b. The manganese content is higher in the anode after cycling and follows the lithium content in the anode. This gain is related to the enhanced SEI formation on the anode during aging.^[61–63] Mn disproportionation ($2\text{Mn}^{3+} \rightarrow \text{Mn}^{4+} + \text{Mn}^{2+}$)

may occur, which would accelerate the formation of complexes between the Mn^{2+} ions and the carbonate-based electrolyte. The Mn^{2+} ions are transported to the anode and subsequently can trap further lithium ions in the SEI.^[61,64–66] This causes a further loss of lithium inventory. The amount of cobalt and nickel in the anode also increases but not as much as for manganese. The ICP-OES results mirrors the data presented in the previous sections and underscores the positive effect of the bracing on the cell performance. The lithium and the transition metal content in the anode is slightly higher for the cell without external bracing (Cell 3), which can be related to lithium plating and SEI growth. Only the Mn content is slightly higher for the

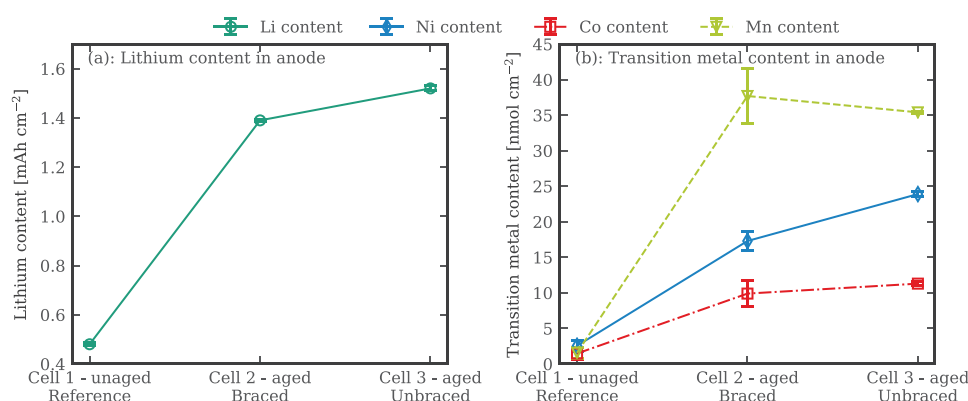


Figure 7. Lithium (a) and transition metal content (b) in anode for reference and aged cells. The lines are a guide for the eye only.

braced cell, albeit with a higher error. This result might be related to increased cracking of the particles, and thus also to the increased disproportionation of Mn^{3+} ions and subsequent trapping of lithium ions in the SEI.

X-Ray diffraction (XRD) analyses were performed (Figure 8) to further investigate the structural degradation of the aged cathodes. Rietveld analysis was used to perform the structure refinement. No significant phase changes due to aging could be detected. Previous studies showed changes from $R\text{-}3m$ layered to $Fd\text{-}3m$ spinel and to $Fm\text{-}3m$ rock salt structure during aging.^[64,67] A closer examination of the lattice parameters obtained from the Rietveld analysis, for example, a/c (lattice parameter), R (intensity ratio), crystallite size, and lattice strain (Table 2) indicates an increased structural degradation of the layered cathode materials for the aged braced cell (Cell 2) and for the aged unbraced cell in the areas with ripples (Cell 3: with ripples). The aged unbraced cell in the area without ripples (Cell 3: without ripples) shows less structural degradation.

A high $I(003)/I(104)$ ratio represents a “well-layered” structure and low level of Ni^{2+} and Li^+ cation mixing in the crystal

structure.^[64,68] The reference Cell 1 and Cell 3: without ripples have a higher $I(003)/I(104)$ ratio than Cell 2 and Cell 3: with ripples. It should be noted that the intensity ratio should only be used as an indication for degradation of the active material, rather than quantitative measure as the ratio can be affected by the variations in the experimental setup.^[68] A better indication of Ni^{2+} and Li^+ cation mixing of is the intensity ratio R ($(I(006) + I(102))/I(101)$), introduced by Dahn.^[69] High R values, as observed for Cell 2 and Cell 3 with ripples, indicate increased cation mixing as the intensity peak of (101) is lower when Ni atoms occupy Li sites in the layered structure.^[70] The broadening of the peaks in the XRD pattern is a further indication of structural damage within the cathode active material lattice size and can be correlated with the crystallite size and the lattice strain of the particles.^[71,72] The cathode particles of the aged cells show decreased crystallite size and slightly increased lattice strain for Cell 2 and Cell 3: with ripples. The active particles of Cell 3: without ripples have enhanced crystallite size compared to the particles of the other aged cells and also slightly lower lattice strain compared to the particles of the reference cell.

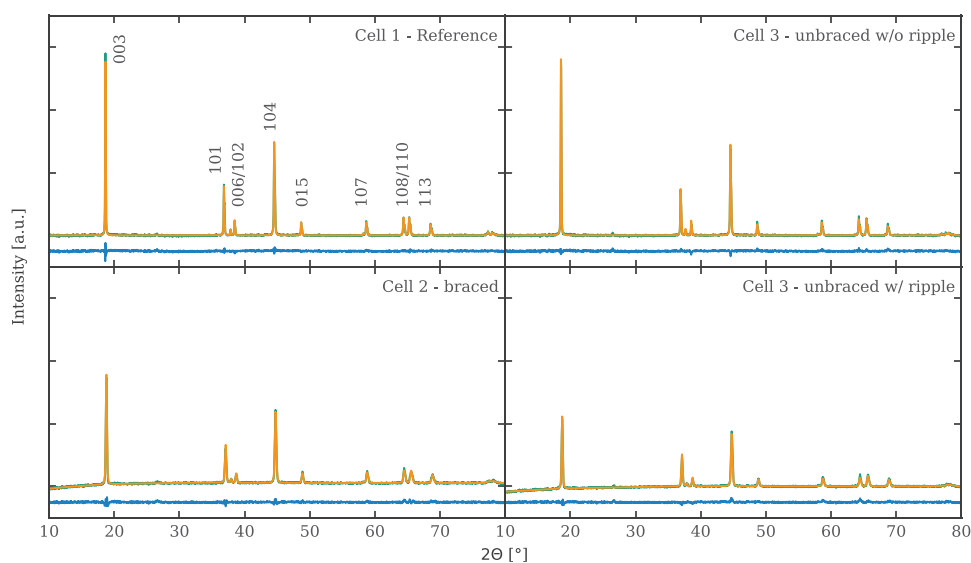


Figure 8. Observed (green), calculated (orange), and difference (blue) XRD patterns of the differently aged cathode materials.

Table 2. Lattice parameters for cathodes obtained from the Rietveld analysis.

Cell	a [Å]	c [Å]	$I(003)/I(104)$	$R: (I(006) + I(102))/I(101)$	Crystallite size [Å]	Lattice strain [%]
Cell 1: unaged, reference	2.857	14.250	2.03	0.74	1357	0.08
Cell 2: aged, braced	2.849	14.308	1.52	0.92	388	0.11
Cell 3: aged, unbraced, without ripples	2.849	14.304	2.23	0.73	994	0.06
Cell 3: aged, unbraced, with ripples	2.848	14.327	1.26	0.88	387	0.10

The XRD results suggest a correlation of the crystallite size and applied pressure on the electrodes. Higher pressure on the electrodes (Cell 2 and Cell 3: with ripples) increase the damage of the layered structure and the cation mixing compared to the electrodes which were not subjected to such high pressure (Cell 3: without ripples or Cell 1). The increased pressure arises from the external bracing or from the internal volume changes through ripples on the cathode and hence lithium plating on the anode. Moreover, cathodes with small crystallite size show an increased lattice strain and also more pronounced Ni^{2+} and Li^+ cation mixing. External pressure seems to increase the aging of the cathode (particle cracking). Without external pressure, (Cell 3) different areas of the electrodes exhibit different characteristics: areas without ripples show only minor aging (Cell 3: without ripples), while areas with ripples shown much more significant aging (Cell 3: with ripples).

2.2.3. Electrochemical Testing

To substantiate the results related to cathode and anode electrode degradation, electrochemical tests were performed in three electrode laboratory cells with electrodes from selected areas of the prismatic cells. Electrical impedance spectroscopy (EIS) was conducted after 5 cycles (2×0.1 and 3×0.2 C) at 100% state of charge (SOC) to correlate the morphological and structural changes with electrochemical phenomena. The results are shown in Nyquist plots presented in **Figure 9**. The individual spectra of the anode and cathode half cells consist of several features which can be described as follows: a high-frequency intercept due to ohmic resistances in the cell ($R_{a,s}$ and $R_{c,s}$) and a semicircle at high frequencies related to the surface film on the particles ($R_{a,sei}$ and $R_{c,f}$). The a and c in the subscripts refer to the anode and cathode half cells, respectively. For the anode half cells, a second semicircle at medium frequencies is related to the charge transfer resistance ($R_{a,ct}$) and a third semicircle at low frequencies is detected ($R_{a,d}$). The third semicircle has been reported to appear only for high and low SOC_s,^[72] where solid-state diffusion in the electrode plays a role but may not be detectable. For the cathode half cells, the second semicircle at medium frequencies is related to the electrical conductivity of the active material along with the metallic lithium/electrolyte interface ($R_{c,e}$) and the third semicircle at low frequencies is correlated to the charge transfer resistances ($R_{c,ct}$).^[73–75] The inclined line is related to solid-state diffusion for both electrodes. These features were fitted with an appropriate model (Figure 9c).

The EIS study of the anode half cells revealed an increase of the impedances (Table S2, Supporting Information) between the reference cell and the aged cells as can be seen in Figure 9a.

For instance, the SEI resistance ($R_{a,sei}$) increases from $6.0 \Omega \text{ cm}^2$ in the reference cell to $>19.0 \Omega \text{ cm}^2$ in the aged cells. This is consistent with the findings of the ICP-OES analysis, which showed a pronounced TM content on the anode after cycling that is likely associated with a thicker SEI, due to transition metal dissolution. The resistances dramatically increase, a factor of ≈ 5 ($R_{a,sei}$ by a factor of ≈ 10), for the anodes of Cell 3 containing visible lithium plating. This is in agreement with the results from previous sections, showing lithium plating as the main cause of performance degradation.

The results of the EIS of the cathode half cells (Figure 9b and Table S3, Supporting Information) are also in accordance with the data presented in previous sections, as the cathodes from Cell 2 and Cell 3: with ripples show increased resistances than Cell 1 and Cell 3 without ripples. For instance, $R_{c,e}$, which is correlated with the electrical conductivity of the active material and the lithium metal/electrolyte interface resistance, is higher in the aged cells than the reference cell. As the lithium metal/electrolyte interface resistance should be more or less the same for all cells, the change in the resistance can be attributed to the electrical conductivity of the active material particles. For the cathode of Cell 3: with ripples, the resistance is the highest. These electrode areas exhibited significant particle cracking and separation between the particles (Figure 6d), which would result in the most inhibited conductivity inside the secondary particles. The charge transfer resistance $R_{c,ct}$, as expected, is lowest in Cell 1 (reference cell) and increases in the aged cells. $R_{c,ct}$ is larger for the cathodes with the high applied pressure (Cell 2 and Cell 3: with ripples) as compared to Cell 3: without ripples. This might also be related to the lower crystallite size (Table 2) and hence to the more pronounced cracking of the active particles due to higher internal and external pressure on the particles. For the surface film resistance $R_{c,f}$ and the ohmic resistance $R_{c,s}$, no clear trend is visible indicating little relationship with the aging processes. The incomplete first semicircle and also the variation of $R_{c,s}$ in some measurements might be related to cable resistances.

The results from half-cell EIS measurements enable a better understanding of the resistances inside the prismatic cells. The anode likely makes the most significant contribution to the resistance of the full cell. The higher resistances in the unbraced cell can be attributed to lithium plating. The increase of the surface layer resistance in the aged cells compared to the reference cell is probably mainly caused by the anode, whereas the larger the charge transfer resistance probably can be attributed to both electrodes.

Figure 10 shows the C-rate capability test of the electrodes harvested from the prismatic cells. Anode and cathode samples obtained from the prismatic cells are tested either individually in half cells or together in full cells (laboratory cells). After the

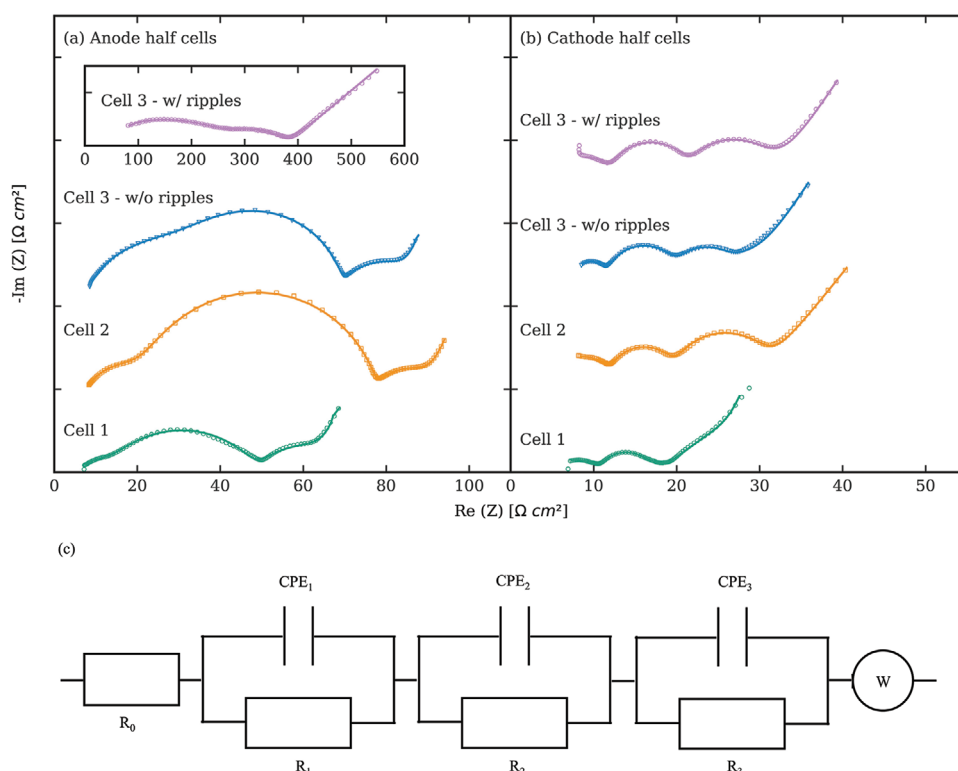


Figure 9. Nyquist plot of anode- (a) and cathode half cells (b) obtained from different prismatic cells. EIS measurements performed at 100% SOC. The markers correspond to the measured data and the line presents the fit of the data. The individual spectra are shifted along the y-axis for better visibility. Data shown from 1 MHz to 10 mHz. c) Equivalent circuit model used for fitting.

initial 0.1 C (referring to the reference cell) charge and discharge cycles, the cells are charged with 0.2 C and discharged as described in the experimental section. No significant capacity deviations occur between samples taken from different regions of the JR, for example, inner and outer part of the JR or between different locations in one electrode sheet (Figure S6, Supporting Information). Therefore, only the mean values are shown. Only for Cell 3, a distinction between different areas of the electrodes (areas with and without ripples) has been made. For the full cell tests (laboratory scale), large capacity variations between the reference cell (Cell 1, for example, 2.6 mAh cm^{-2} at 0.2 C) and the aged cells (Cell 2 + 3, for example, 1.9 and 1.8 mAh cm^{-2} at 0.2 C) are observed, which are comparable to the differences in the long-term cycling test described in Section 2.1. The anode and cathode half cells have smaller capacity differences between the reference cell and the aged cells than is evident in the full cell test. This indicates little degradation of the electrodes, in terms of a capacity reduction, during cycling.

During the full cell test, the reference cell has a $\approx 28\%$ higher capacity compared to the braced cell and $\approx 32\%$ higher capacity compared to the unbraced cell, for example, 2.5 mAh cm^{-2} for Cell 1 compared to 1.9 mAh cm^{-2} for Cell 2 and 1.7 mAh cm^{-2} for Cell 3 at 1.1 C. This loss reflects the capacity difference between the aged prismatic BEV cells with its nominal capacity before the cycling of $\approx 24\%$ for the braced prismatic cell and $\approx 33\%$ for the unbraced prismatic cell (Figure 2). As it remains unclear if the capacity loss of the cells in the full-cell test is

initiated by the cathode, anode, or both of them, the half-cell tests are examined to study the impact of the individual electrodes.

For the anode half cell tests, no capacity fading is detected up to 74 mA (1.1 C); the capacity decreases only with further increasing currents. For the highest current rate of 2.2 C, the capacity shows the largest drop among all currents, which is also partly related to the diffusion limitations of the lithium counter electrode in combination with the carbonate-based electrolyte.^[76] The electrodes from the braced cell (e.g., 2.6 mAh cm^{-2} at 1.1 C) have only a slightly lower capacity of 3% compared to the reference cell (e.g., 2.7 mAh cm^{-2} at 1.1 C). This reveals only little degradation in terms of capacity reduction for the anodes from the braced cell. The electrodes from the unbraced cell show the lowest capacity (e.g., 2.4 mAh cm^{-2} at 1.1 C), that is, 11% lower capacity compared to the reference cell, and the highest standard deviation over the whole test. This demonstrates the pronounced degradation of the anode in the unbraced cell due to the increased lithium plating.

The cathode half cells test show a linear discharge capacity fading until 11 mA (1.6 C), with an increased capacity drop at 14.7 mA due to the high current. Interestingly, the cathodes from the unbraced cell (6% lower capacity compared to reference cell, for example, 2.3 to 2.5 mAh cm^{-2} at 1.1 C) have a slightly higher capacity compared to those of the braced cell (11% lower capacity compared to reference cell, for example, 2.2 mAh cm^{-2} at 1.1 C) confirming that the applied external pressure along with the rising internal pressure results in

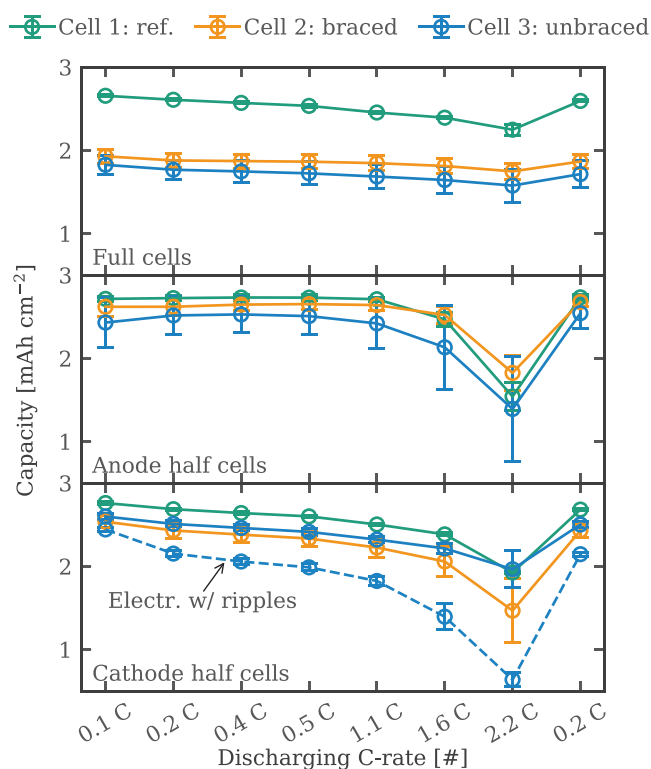


Figure 10. C-rate-capability test of laboratory electrodes harvested from the prismatic cells. The C-rate relates to the reference cell.

pronounced structural cathode degradation. The areas from the cathode of Cell 3: with ripples (unbraced) show more significant capacity fading than the other cathode half cells, which supports the hypothesis that the electrical conductivity and the charge transfer inhibit the performance.

The results of the C-rate test show that the capacity fade of the full cells is primarily attributed to the loss of lithium inventory and to a smaller extent, by the individual electrodes. The loss of lithium for the intercalation into the electrodes is mainly caused by lithium plating and increased SEI formation, as is shown in Figures 3 and 4. The examination of the laboratory electrodes from the braced cell show that the anode suffers only little from capacity reduction compared to the reference cell, whereas the cathode suffers from significant mechanical degradation through the high pressure. In comparison, the laboratory cells derived from the unbraced cell reveal that the capacity fading is also related to the loss of lithium inventory and structural cathode degradation, but the aging of the anode plays a more significant role due to the substantial lithium plating. It can be concluded that external pressure is beneficial for the overall performance in prismatic cells, as it leads to decreased anode degradation even if the cathode suffers more from the high pressure. The bracing also results in a more homogeneous degradation over the complete cell, in terms of morphological and structural changes, lithium plating, and capacity reduction compared to the unbraced cell. In the unbraced cell a variety of different local aging mechanisms, for example, ripples on the cathode, widespread lithium plating, or crumbled coatings, occur.

2.3. Mechanical State of Health

The new concept of the mechanical SOH is introduced in this section. It shall correlate the capacity reduction with the mechanical degradation of, for example, the electrode particles or other cell components. Although these aspects also play a role in the more general term “state-of-health”, the concept of mechanical SOH is intended to focus more on the mechanical characteristics of the materials and cell components and their influence on the capacity loss. Compared to temperature and current, the mechanical effects on the cycle life of a battery cell are rather unexplored, but play a vital role in the lifetime of batteries, particularly as the volumetric energy density (related to the space for the battery) is continually increased. The mechanical SOH is derived from the processes inside the battery cell/electrodes (particle cracking or volumetric expansion/contraction, to name a few). Electrodes with a good mechanical SOH should have low structural and irreversible volume changes and also a low capacity reduction. In comparison, electrodes with a poor mechanical SOH have large structural changes, for example, particle cracking, high irreversible volumetric growth in combination with a significant capacity fading. In this sense, changes in mechanical SOH are not directly initiated by external effects like applied pressure, etc., but are certainly affected by them. This work illustrates this point through the effect of fixed bracing, for example, on the particle cracking in the cathodes.

As discussed above (Figure 6), the cathodes of the braced cell and of the unbraced cell in the areas of the ripples suffer, in particular, from cracking. These visible results are confirmed by XRD-measurements (Figure 8 and Table 2) and indicate a reduced mechanical SOH in those areas. The cathodes of the unbraced cell in the areas without ripples have a higher mechanical SOH, which is also confirmed by electrochemical investigations (Figures 9 and 10). The change in thickness (only considering the electrode material) compared to the reference cathode is lower for the braced cell compared to the unbraced cell, thus also contributing to the lower mechanical SOH.

The mechanical SOH of the anode of the aged cells is only slightly lower than that of the reference cell. There is negligible increase in cracking (Figure S4, Supporting Information) and only a small capacity loss (Figure 10). The higher capacity loss of the anode without external bracing is possibly related to lithium plating and not to effects which have an impact on the mechanical SOH. Nevertheless, the anodes of the braced prismatic cell show a lower change in thickness as the anodes of the unbraced prismatic cells at EOL.

In total, the mechanical SOH can be used as an indication for the degradation of an electrode material. In this work, the reduction of the mechanical SOH of the aged cathodes is associated with particle cracking and volumetric expansion, while for the anode, only the volumetric expansion may contribute to the lower mechanical SOH. Further studies need to be conducted with specialized sensor technology, for example, ultrasound, to gain a deeper understanding of the correlation between changes in the mechanical characteristics of the materials and components and the capacity reduction. With this additional information, it may be possible

to integrate the mechanical SOH into battery management systems.

3. Conclusion

The cycling tests of braced and unbraced automotive prismatic BEV cells for more than 7000 cycles reveal different aging phenomena, which are investigated using post-mortem analysis. The externally-braced prismatic cells exhibit an enhanced cycling performance during the aging test, reaching the threshold of 80% SOH 900 cycles later compared to the unbraced cells. This result demonstrates the importance of external bracing, and more specifically a homogeneous pressure distribution for lithium-ion cells. During this aging test, the change in cell thickness of the braced cell is $\approx 2.5\%$ while the unbraced cell expanded $\approx 17.5\%$. This expansion is associated with lithium plating, electrode delamination, and electrode swelling. Further post-mortem studies revealed that the morphological and structural cathode degradation, for example, particle cracking and cation mixing, has a reasonable impact on the cell performance reduction for the braced cell, whereas the impact of the anode on the performance loss is small. For the unbraced cell the effect of the anode on the capacity loss is clearly increased as the anode suffers from lithium plating due to insufficient contact between the components within the electrode stack. Nevertheless, the C-rate test of the laboratory cells revealed that the main factor contributing to the capacity reduction of the prismatic BEV cells is the loss of lithium inventory.

The concept of a mechanical SOH as an indicator for electrode degradation due to mechanical effects is introduced in this work. The cathode suffers from a reduced mechanical SOH due morphological and structural degradation, whereas the anode exhibits a relatively stable mechanical SOH during aging. One explanation is the higher Young's modulus of the polycrystalline NCM (≈ 200 GPa) as compared to graphite (≈ 100 GPa) in the lithiated state.^[77–79] The high modulus in combination with the volumetric expansion leads to stress and hence cracking inside the particles. Thus, external bracing results in a reduced mechanical SOH for the cathode material, but a more uniform aging over the entire cell and less localized degradation.

4. Experimental Section

Prismatic Cells: Figure 11a shows the cells tested in this study and Table S4, Supporting Information, gives information about the cells. These prismatic cells are designed for BEV applications.

A total of 4 cells were cycled (Table S5, Supporting Information), whereby two cells were cycled without external pressure and the other cells were cycled under braced conditions. Two form-fitted metal plates are used to brace the front and back of the battery cell (Figure 11b). The pressure is applied with fixed bracing. At the beginning of the cycling experiment, the plates are positioned at the sides of the battery cell and the spacing of the plates corresponds to the thickness of the prismatic cell. With the plates in place, further expansion of the battery cell is severely limited. An exact pressure determination over the entire cell is not possible, since the cell has an additional housing at the top and bottom of the battery cell (Figure 11 and Figure S1, Supporting Information).

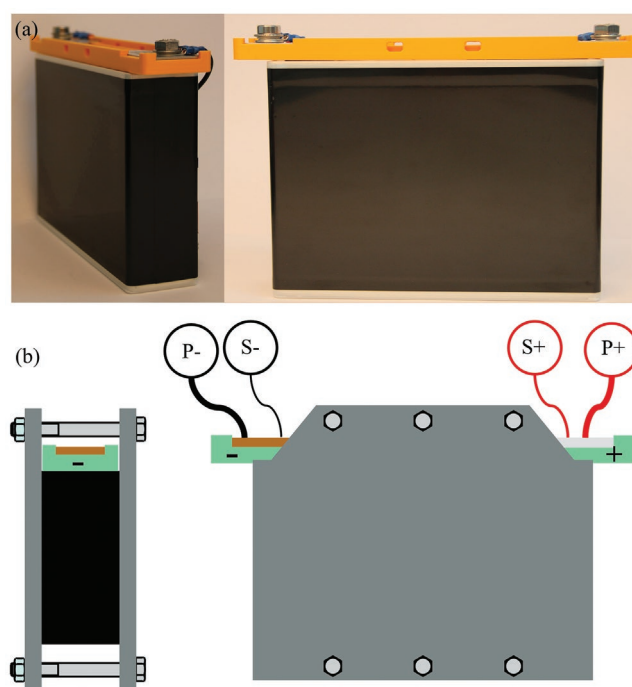


Figure 11. a) 94 Ah prismatic cell and b) schematic view of cell bracing. The dimension of the cell is 174 mm \times 45 mm \times 133 mm (length \times width \times height).

Electrochemical Testing: Table S5, Supporting Information, shows the parameters for the electrochemical testing of the prismatic cells. All cells were cycled (BaSyTec GmbH) at room temperature using an adapted aging protocol with elevated discharge currents of 188 A (2.0 C, related to nominal capacity). The discharging procedure used a constant current (CC) step with an end criterion of 2.7 V. The charging procedure used a constant current–constant voltage (CCCV) procedure with a current of 94 A and an end criterion of current $I < 0.1$ C at 4.15 V. Every 250 cycles, the cycling procedure was paused to measure the width (DIGI MET, HELIOS-PREISSER GmbH) in the center of the cell.

The DCIR is determined with the current switch method^[80] every 500 cycles. The DCIR is calculated by the difference in the voltage divided by the difference in the current. The difference is the result of the last charging voltage or current value at 100% SOC and the voltage or current value after 10 s of discharge. The DCIR has to be corrected with a temperature factor to account for the fluctuating temperature during cycling. The uncorrected DCIR value at 1000 cycles is set as the reference value for the correction, since the temperature is known to be ≈ 25 °C. This correction is based on the Arrhenius equation and the assumption that between cycle 1000 and 1500 the change of the DCIR is negligible. Figure S5, Supporting Information, visualizes the impact of the temperature on the DCIR.

Table 3. History of prismatic cells examined via post-mortem techniques.

	Cell 1 (Reference cell)	Cell 2	Cell 3
Bracing Condition	–	Externally braced	No external bracing
Cycles ^{a)}	None	7250	7500
EOL capacity ^{a)} [Ah]	–	72.0	63.2
Actual capacity ^{b)} [Ah]	97.0	80.5	71.6

^{a)}(1.0 C charge/2.0 C discharge); ^{b)}(0.05 C charge/0.05 C discharge).

Post-Mortem Analysis: Table 3 summarizes the history of the cells which were studied with post-mortem techniques. Two of the cells were electrochemically aged under different bracing conditions (Table S5, Supporting Information) and one unaged cell was used as a reference (Cell 1).

Prior to post-mortem characterization the cells were cycled for 2 cycles with 4.7 A (0.05 C) from 2.7 to 4.15 V to determine the actual capacity. Afterwards, the cells were discharged with a CCCV step with 4.7 A (0.05 C) in CC step until 2.7 V and then held at 2.7 V for 12 h to ensure that the lithiation state was similar for all cells. The prismatic cell casing was removed and the four JR were detached from the casing. For each JR, the anode, cathode, and separator were separated and examined inside the glovebox. Prior to the following investigations, the samples were washed with dimethyl carbonate (DMC).

Morphological analysis of the electrodes was done with a SEM (Auriga 60, Carl Zeiss Microscopy GmbH) and EDX analysis (Element SDD Detector, AMETEK/EDAX). The sample preparation and the transfer into the SEM were carried out in argon atmosphere without contact to the air with a custom-made sample holder. The cross-section preparation was conducted with a CSP (Ion Milling System IM4000Plus, Hitachi High-Tech Corporation). The samples for the CSP were handled in air and the visualization was done with the SEM.

The electrode and separator thickness were determined by a displacement sensor (GT2-H12K, KEYENCE Corporation). After washing the samples inside the glovebox and drying in the antechamber at room temperature under vacuum, the electrodes and the separators were handled in air for the thickness measurements. To calculate the mean and standard deviation of each sample (e.g., cathode thickness of Cell 2, aged, braced), measurements were taken on two different jelly rolls, where measurements were made on two different sheets and on different areas of the sheet. At least 24 measurements were made for each sample to calculate the mean values.

The chemical composition of the anode and cathode samples was determined with ICP-OES. The specimens were weighed after washing and drying, and then digested using aqua regia (mixture of hydrochloride acid and nitric acid, vol% 1:3). The dispersion was filtered and the filtrate was then characterized with ICP-OES (Vista-PRO radial, Varian Inc.). The graphite and the binder remained as a solid residue. A more detailed explanation of the ICP-OES procedure is described by Bach et al.^[39] The carbon and oxygen content of the solid residue was examined by C-Leco and ONH-Leco (LECO C744 and LECO ONH836, LECO Corporation).

XRD of the cathode material was performed with a SmartLab diffractometer (Rigaku Corporation) in the range of $2\theta = 10\text{--}80^\circ$ and at a scan rate of $0.5^\circ/\text{min}$. Powder samples were collected by carefully scratching the active material from the current collector with a scalpel, followed by drying and grinding by hand in a mortar and pestle.

For the electrochemical tests, laboratory test cells (PAT-Core, EL-Cell GmbH) with a three-electrode set-up were built from electrodes harvested at different areas of the JR. A drawing of the electrodes and the locations for sampling can be seen in Figure S6, Supporting Information. The electrodes were harvested from: 1) the center of the electrode sheet from the inner and outer part of the electrode; and 2) from the top, bottom, side and center from the middle part of the jelly roll. The selection of these positions was intended to provide a representative picture of the jelly roll electrode as a whole.

The active material was carefully removed from one side of the electrode to enable electrical contact with the current collector. The separator was a 220 μm thick double-layered separator made up of a nonwoven polypropylene (PP) cloth and a microporous PE membrane (FS-5P, EL-Cell GmbH). LP 57 (Gotion Inc.), a 1 M LiPF_6 in EC/EMC = 30/70 wt% solution, was used as the electrolyte. Either half cells with a working electrode from the JR and lithium metal (380 μm thick, Merck KGaA) as counter electrode, or full cells with a cathode working electrode and an anode counter electrode from the JR were built. For the EIS measurements only cathode and anode half cells from the center part of an electrode sheet were used. The EIS was performed at 100% SOC due to the fact that the electrodes were at a state of maximum expansion resulting in the pressure peak inside the cell. The impedance

spectra were recorded in a frequency range of 1 MHz to 10 mHz with a 5 mV root-mean-square perturbation. For all EIS measurements at least two cells were built. The rate capability test was applied to all cells with three initial charging and discharging (formation) cycles with a current density of 0.29 mA cm^{-2} . After formation, the cells were charged with 0.58 mA cm^{-2} CCCV ($I < 0.13 \text{ mA cm}^{-2}$) and discharged with 0.58, 0.96, 1.45, 2.89, 4.33, 5.78, and 0.58 mA cm^{-2} CC sequentially. It should be noted that the same current densities were applied for all cells and refer to the C-rate from the initial 0.1 C formation cycles of the electrodes harvested from the reference cell. The rate test consisted of the following: 0.2 C charging and 0.2, 0.4, 0.5, 1.1, 1.6, 2.2, and 0.2 C discharging. The full cells were cycled between 2.7 and 4.2 V, the cathode half cells between 3.0 and 4.3 V and the anode half cells between 0.01 and 1.0 V. At least 8 cells were built in different areas of the JR (Figure S6, Supporting Information) for the aged cells and at least 3 cells (only from the center part of the electrode sheets) for the unaged reference cell.

Supporting Information

Supporting Information is available from the Wiley Online Library or from the author.

Acknowledgements

The authors gratefully acknowledge the funding of this work by the Federal Ministry for Economic Affairs and Energy (BMWi) of Germany in the project ReVISED-Batt (grant number 03ETE004A). They also want to thank the members of the Fraunhofer R&D Center Electromobility at Fraunhofer ISC for fruitful discussions, scientific support; and especially Ajana Gebel, Viliija Anfimoivaite, Franziska Stahl, Elena Fleder, Werner Stracke, and Richard Olsowski for technical support.

Open access funding enabled and organized by Projekt DEAL.

Conflict of Interest

The authors declare no conflict of interest.

Data Availability Statement

The data that support the findings of this study are available from the corresponding author upon reasonable request.

Keywords

aging, bracing, mechanical state of health, post-mortem, prismatic cells

Received: August 10, 2021

Revised: November 5, 2021

Published online: December 4, 2021

[1] A. Energiewende, Lifecycle Analysis of Electric Vehicles, **2019**, <https://www.agora-verkehrswende.de/en/publications/lifecycle-analysis-of-electric-vehicles-study-in-german-with-english-executive-summary/> (accessed: October 2020).

[2] D. Hall, N. Lutsey, Effects of Battery Manufacturing on Electric Vehicle Life-Cycle Greenhouse Gas Emissions, **2018**, <https://the-icct.org/publications/EV-battery-manufacturing-emissions>.

- [3] B. Scrosati, J. Garche, *J. Power Sources* **2010**, *195*, 2419.
- [4] G. Zubi, R. Dufo-López, M. Carvalho, G. Pasaoglu, *Renewable Sustainable Energy Rev.* **2018**, *89*, 292.
- [5] S. Campanari, G. Manzolini, F. L. Garcia de Iglesia, *J. Power Sources* **2009**, *186*, 464.
- [6] M. Prussi, M. Yugo, L. De Prada, M. Padella, Edwards, *JEC Well-to-Tank Report V5*, **2020**, <https://ec.europa.eu/jrc/en/publication/eurscientific-and-technical-research-reports/jec-well-wheels-report-v5> (accessed: January 2021).
- [7] G. Berckmans, M. Messagie, J. Smekens, N. Omar, L. Vanhaverbeke, J. Van Mierlo, *Energies* **2017**, *10*, 1314.
- [8] B. Nykvist, M. Nilsson, *Nat. Clim. Change* **2015**, *5*, 329.
- [9] F. Larouche, F. Tedjar, K. Amouzegar, G. Houlachi, P. Bouchard, G. P. Demopoulos, K. Zaghbi, *Materials* **2020**, *13*, 801.
- [10] G. Harper, R. Sommerville, E. Kendrick, L. Driscoll, P. Slater, R. Stolkin, A. Walton, P. Christensen, O. Heidrich, S. Lambert, A. Abbott, K. Ryder, L. Gaines, P. Anderson, *Nature* **2019**, *575*, 75.
- [11] B. Huang, Z. Pan, X. Su, L. An, *J. Power Sources* **2018**, *399*, 274.
- [12] W. Lv, Z. Wang, H. Cao, Y. Sun, Y. Zhang, Z. Sun, *ACS Sustainable Chem. Eng.* **2018**, *6*, 1504.
- [13] J. Heelan, E. Gratz, Z. Zheng, Q. Wang, M. Chen, D. Apelian, Y. Wang, *JOM* **2016**, *68*, 2632.
- [14] U.S. Geological Survey, *Mineral Commodity Summaries 2020*, U.S. Geological Survey **2020**, p. 200, <https://doi.org/10.3133/mcs2020>.
- [15] E. A. Olivetti, G. Ceder, G. G. Gaustad, X. Fu, *Joule* **2017**, *1*, 229.
- [16] J. Speirs, M. Contestabile, Y. Houari, R. Gross, *Renewable Sustainable Energy Rev.* **2014**, *35*, 183.
- [17] H. Vikström, S. Davidsson, M. Höök, *Appl. Energy* **2013**, *110*, 252.
- [18] S. Abada, G. Marlair, A. Lecocq, M. Petit, V. Sauvart-Moynot, F. Huet, *J. Power Sources* **2016**, *306*, 178.
- [19] P. Andersson, P. Blomqvist, A. Lorén, F. Larsson, *Fire Mater.* **2016**, *40*, 999.
- [20] Y. Fu, S. Lu, K. Li, C. Liu, X. Cheng, H. Zhang, *J. Power Sources* **2015**, *273*, 216.
- [21] Q. Wang, P. Ping, X. Zhao, G. Chu, J. Sun, C. Chen, *J. Power Sources* **2012**, *208*, 210.
- [22] R. Korthauer, *Handbuch Lithium-Ionen-Batterien*, Springer Berlin Heidelberg, Berlin, Heidelberg **2013**.
- [23] H. Budde-Meiwes, J. Drillkens, B. Lunz, J. Muennix, S. Rothgang, J. Kowal, D. U. Sauer, *Proc. Inst. Mech. Eng., Part D* **2013**, *227*, 761.
- [24] T. Horiba, *Proc. IEEE* **2014**, *102*, 939.
- [25] J. Cannarella, C. B. Arnold, *J. Power Sources* **2014**, *245*, 745.
- [26] M. Wünsch, J. Kaufman, D. U. Sauer, *J. Energy Storage* **2019**, *21*, 149.
- [27] Volkswagen AG, Battery and Charging Options, **2020**, <https://www.volkswagen-newsroom.com/en/the-new-id3-6240/battery-and-charging-options-6247> (accessed: July 2020).
- [28] Dr. Ing. h.c. F. Porsche AG, The Battery: Sophisticated Thermal Management, 800-Volt System Voltage, **2020**, <https://newsroom.porsche.com/en/products/taycan/battery-18557.html> (accessed: January 2021).
- [29] Tesla Inc, Battery Cell Production Begins at the Gigafactory, **2017**, https://www.tesla.com/de_DE/blog/battery-cell-production-begins-gigafactory (accessed: July 2020).
- [30] R. E. Ciez, J. F. Whitacre, *J. Power Sources* **2017**, *340*, 273.
- [31] D. Andre, S.-J. Kim, P. Lamp, S. F. Lux, F. Maglia, O. Paschos, B. Stiaszny, *J. Mater. Chem. A* **2015**, *3*, 6709.
- [32] Mazda Motor Corporation, *Mazda MX-30*, **2019**, <https://www.mazda.com/en/new-generation/mx-30/> (accessed: January 2021).
- [33] R. S. Rubino, H. Gan, E. S. Takeuchi, *J. Electrochem. Soc.* **2001**, *148*, A1029.
- [34] P. Daubinger, F. Ebert, S. Hartmann, G. A. Giffin, *J. Power Sources* **2021**, *488*, 229457.
- [35] D. Sauerteig, S. Ivanov, H. Reinshagen, A. Bund, *J. Power Sources* **2017**, *342*, 939.
- [36] M. Bauer, M. Wachtler, H. Stöwe, J. V. Persson, M. A. Danzer, *J. Power Sources* **2016**, *317*, 93.
- [37] M. Hahn, H. Buqa, P. W. Ruch, D. Goers, M. E. Spahr, J. Ufheil, P. Novák, R. Kötz, *Electrochem. Solid-State Lett.* **2008**, *11*, A151.
- [38] B. Rieger, S. Schlueter, S. V. Erhard, J. Schmalz, G. Reinhart, A. Jossen, *J. Energy Storage* **2016**, *6*, 213.
- [39] T. C. Bach, S. F. Schuster, E. Fleder, J. Müller, M. J. Brand, H. Lorrman, A. Jossen, G. Sxetl, *J. Energy Storage* **2016**, *5*, 212.
- [40] A. S. Mussa, M. Klett, G. Lindbergh, R. W. Lindström, *J. Power Sources* **2018**, *385*, 18.
- [41] V. Müller, R.-G. Scurtu, M. Memm, M. A. Danzer, M. Wohlfahrt-Mehrens, *J. Power Sources* **2019**, *440*, 227148.
- [42] F. Ebert, G. Sxetl, M. Lienkamp, **2017**, <https://ieeexplore.ieee.org/abstract/document/7935871> (accessed: November 2020).
- [43] J. E. Harlow, X. Ma, J. Li, E. Logan, Y. Liu, N. Zhang, L. Ma, S. L. Glazier, M. M. E. Cormier, M. Genovese, S. Buteau, A. Cameron, J. E. Stark, J. R. Dahn, *J. Electrochem. Soc.* **2019**, *166*, A3031.
- [44] S. Hahn, S. Theil, J. Kroggel, K. P. Birke, *J. Energy Storage* **2021**, *40*, 102517.
- [45] A. Adam, J. Wandt, E. Knobbe, G. Bauer, A. Kwade, *J. Electrochem. Soc.* **2020**, *167*, 130503.
- [46] B. Ng, P. T. Coman, E. Faegh, X. Peng, S. G. Karakalos, X. Jin, W. E. Mustain, R. E. White, *ACS Appl. Energy Mater.* **2020**, *3*, 3653.
- [47] P. Berg, J. Soellner, M. Herrmann, A. Jossen, *J. Energy Storage* **2020**, *28*, 101246.
- [48] M. Lewerenz, D. U. Sauer, *J. Energy Storage* **2018**, *18*, 421.
- [49] A. S. Mussa, A. Liivat, F. Marzano, M. Klett, B. Philippe, C. Tengstedt, G. Lindbergh, K. Edström, R. W. Lindström, P. Svens, *J. Power Sources* **2019**, *422*, 175.
- [50] M. Dubarry, B. Y. Liaw, M.-S. Chen, S.-S. Chyan, K.-C. Han, W.-T. Sie, S.-h. Wu, *J. Power Sources* **2011**, *196*, 3420.
- [51] K. W. Knehr, T. Hodson, C. Bommier, G. Davies, A. Kim, D. A. Steingart, *Joule* **2018**, *2*, 1146.
- [52] L. C. Casals, M. Rodríguez, C. Corchero, R. E. Carrillo, *World Electr. Veh. J.* **2019**, *10*, 63.
- [53] M. H. Lipu, M. A. Hannan, A. Hussain, M. M. Hoque, P. J. Ker, M. H. M. Saad, A. Ayob, *J. Cleaner Prod.* **2018**, *205*, 115.
- [54] E. Wood, M. Alexander, T. H. Bradley, *J. Power Sources* **2011**, *196*, 5147.
- [55] J. Liu, M. Kunz, K. Chen, N. Tamura, T. J. Richardson, *J. Phys. Chem. Lett.* **2010**, *1*, 2120.
- [56] G. Zhang, C. E. Shaffer, C.-Y. Wang, C. D. Rahn, *J. Electrochem. Soc.* **2013**, *160*, A610.
- [57] F. Ebert, M. Spielbauer, M. L. Maximilian, (preprint) <https://doi.org/10.20944/preprints202011.0232.v1> (accessed: May 2021).
- [58] M. M. Besli, S. Xia, S. Kuppan, Y. Huang, M. Metzger, A. K. Shukla, G. Schneider, S. Hellstrom, J. Christensen, M. M. Doeff, Y. Liu, *Chem. Mater.* **2019**, *31*, 491.
- [59] L. de Biasi, B. Schwarz, T. Brezesinski, P. Hartmann, J. Janek, H. Ehrenberg, *Adv. Mater.* **2019**, *31*, 1900985.
- [60] F. Schipper, E. M. Erickson, C. Erk, J.-Y. Shin, F. F. Chesneau, D. Aurbach, *J. Electrochem. Soc.* **2017**, *164*, A6220.
- [61] J. A. Gilbert, I. A. Shkrob, D. P. Abraham, *J. Electrochem. Soc.* **2017**, *164*, A389.
- [62] T. Joshi, K. Eom, G. Yushin, T. F. Fuller, *J. Electrochem. Soc.* **2014**, *161*, A1915.
- [63] H. Zheng, Q. Sun, G. Liu, X. Song, V. S. Battaglia, *J. Power Sources* **2012**, *207*, 134.
- [64] P. Teichert, G. G. Eshetu, H. Jahnke, E. Figgemeier, *Batteries* **2020**, *6*, 8.
- [65] I. Buchberger, S. Seidlmayer, A. Pokharel, M. Piana, J. Hattendorf, P. Kudejova, R. Gilles, H. A. Gasteiger, *J. Electrochem. Soc.* **2015**, *162*, A2737.

- [66] S. Solchenbach, G. Hong, A. T. S. Freiberg, R. Jung, H. A. Gasteiger, *J. Electrochem. Soc.* **2018**, *165*, A3304.
- [67] L. Liang, W. Zhang, F. Zhao, D. K. Denis, F. u. Zaman, L. Hou, C. Yuan, *Adv. Mater. Interfaces* **2020**, *7*, 1901749.
- [68] M. Bianchini, M. Roca-Ayats, P. Hartmann, T. Brezesinski, J. Janek, *Angew. Chem., Int. Ed. Engl.* **2019**, *58*, 10434.
- [69] J. Dahn, *Proc. Symp. Mater. Adv. Batteries Fuel Cells* **1990**, *44*, 87.
- [70] E.-J. Lee, Z. Chen, H.-J. Noh, S. C. Nam, S. Kang, D. H. Kim, K. Amine, Y.-K. Sun, *Nano Lett.* **2014**, *14*, 4873.
- [71] A. A. Al-Tabbakh, N. Karatepe, A. B. Al-Zubaidi, A. Benchaabane, N. B. Mahmood, *Int. J. Energy Res.* **2019**, *43*, 1903.
- [72] V. Ovejas, A. Cuadras, *Batteries* **2018**, *4*, 43.
- [73] M. Hofmann, F. Nagler, M. Kapuschinski, U. Guntow, G. A. Giffin, *ChemSusChem* **2020**, *166*, A5313.
- [74] U. Nisar, R. Amin, R. Essehli, R. A. Shakoor, R. Kahraman, D. K. Kim, M. A. Khaleel, I. Belharouak, *J. Power Sources* **2018**, *396*, 774.
- [75] M. Hofmann, M. Kapuschinski, U. Guntow, G. A. Giffin, *J. Electrochem. Soc.* **2020**, *167*, 140512.
- [76] X.-B. Cheng, R. Zhang, C.-Z. Zhao, Q. Zhang, *Chem. Rev.* **2017**, *117*, 10403.
- [77] E. J. Cheng, K. Hong, N. J. Taylor, H. Choe, J. Wolfenstine, J. Sakamoto, *J. Eur. Ceram. Soc.* **2017**, *37*, 3213.
- [78] Y. Qi, H. Guo, L. G. Hector, A. Timmons, *J. Electrochem. Soc.* **2010**, *157*, A558.
- [79] K. Min, E. Cho, *Phys. Chem. Chem. Phys.* **2018**, *20*, 9045.
- [80] H.-G. Schweiger, O. Obeidi, O. Komesker, A. Raschke, M. Schiemann, C. Zehner, M. Gehnen, M. Keller, P. Birke, *Sensors* **2010**, *10*, 5604.



Supporting Information

for *Adv. Energy Mater.*, DOI: 10.1002/aenm.202102448

Impact of Bracing on Large Format Prismatic Lithium-Ion
Battery Cells during Aging

*Philip Daubinger, Matthias Schelter, Ronny Petersohn,
Felix Nagler, Sarah Hartmann, Matthias Herrmann, and
Guinevere A. Giffin**

Supporting Information

Impact of Bracing on Large Format Prismatic Lithium-Ion Battery Cells During Aging

*Philip Daubinger, Matthias Schelter, Ronny Petersohn, Felix Nagler, Sarah Hartmann, Matthias Herrmann, Guinevere A. Giffin**

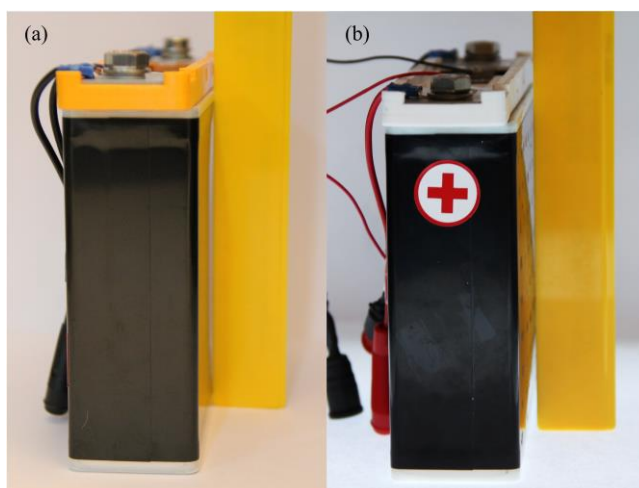


Figure S1. Photographs of (a) reference cell 1 and (b) aged cell 3 (unbraced, 7500 cycles).



Figure S 2. Photograph of anode facing a cathode with ripples. Metallic lithium plating on the surface of the anode is visible.

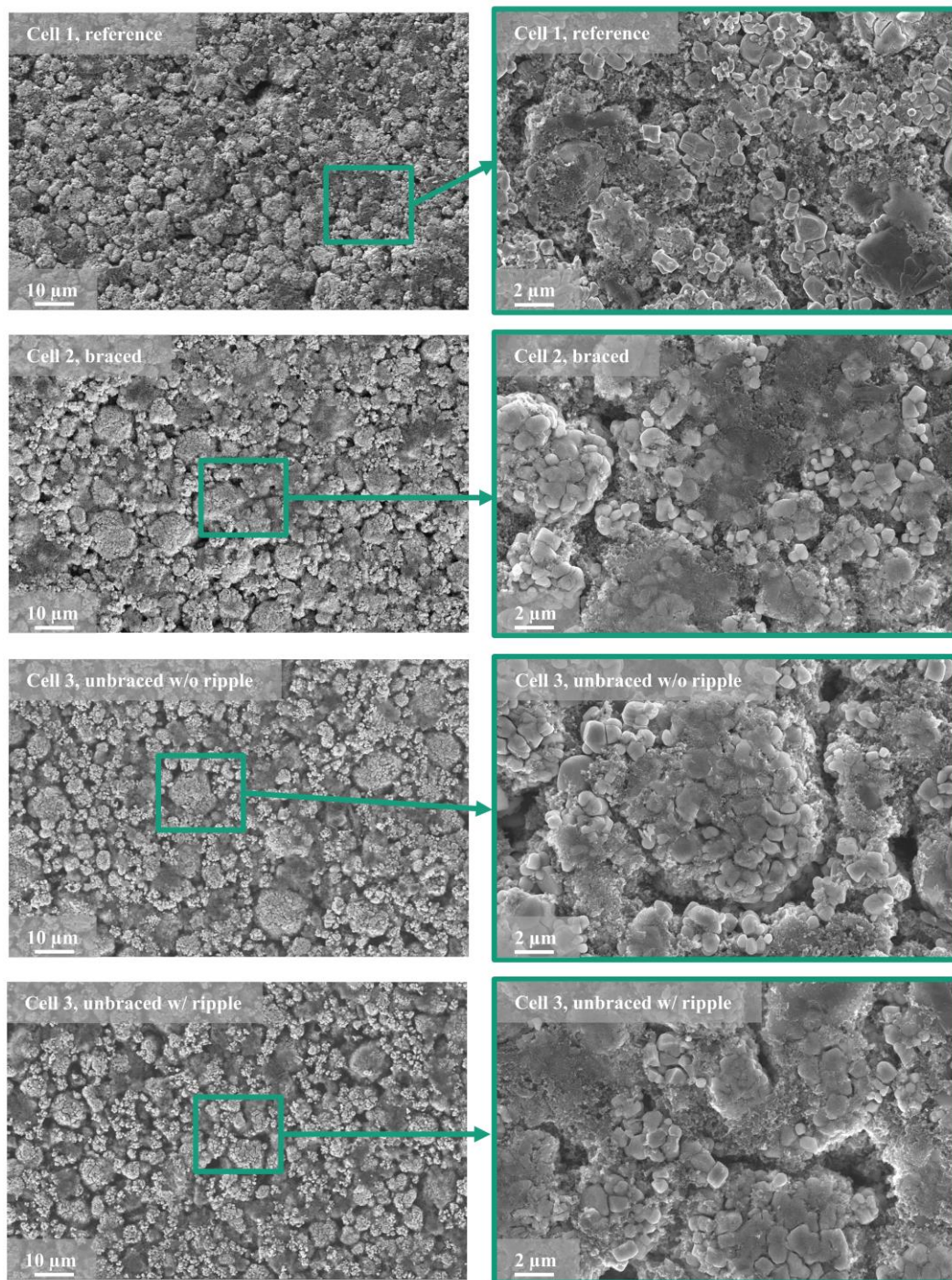


Figure S3. SEM pictures of cathodes' surfaces of the reference and aged cells.

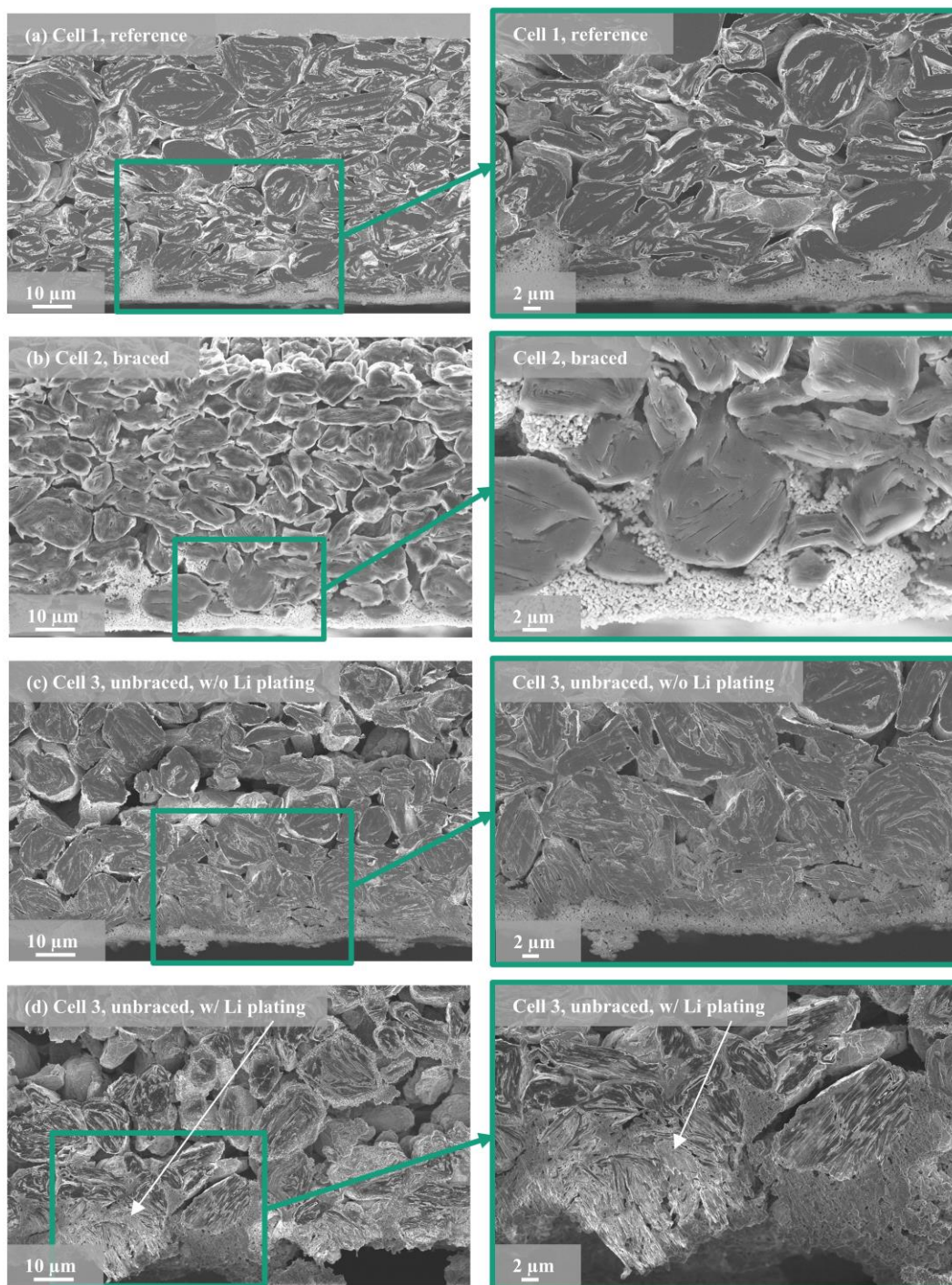


Figure S4. SEM cross sections of the reference and aged anodes. On the pictures on the left side the current collector can be seen at the top, and the electrode area near the surface at the bottom.

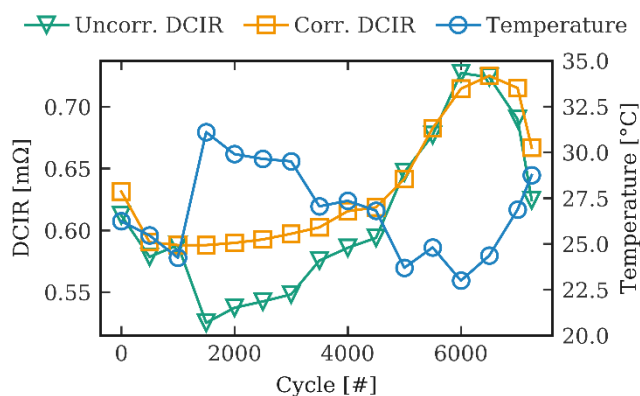


Figure S5. Uncorrected DCIR, corrected DCIR and temperature values of Cell 2. The corrected DCIR is based on the Arrhenius equation and the assumption of negligible resistance change between cycle 1000 and 1500. The lines are only intended as a guide for the eye.

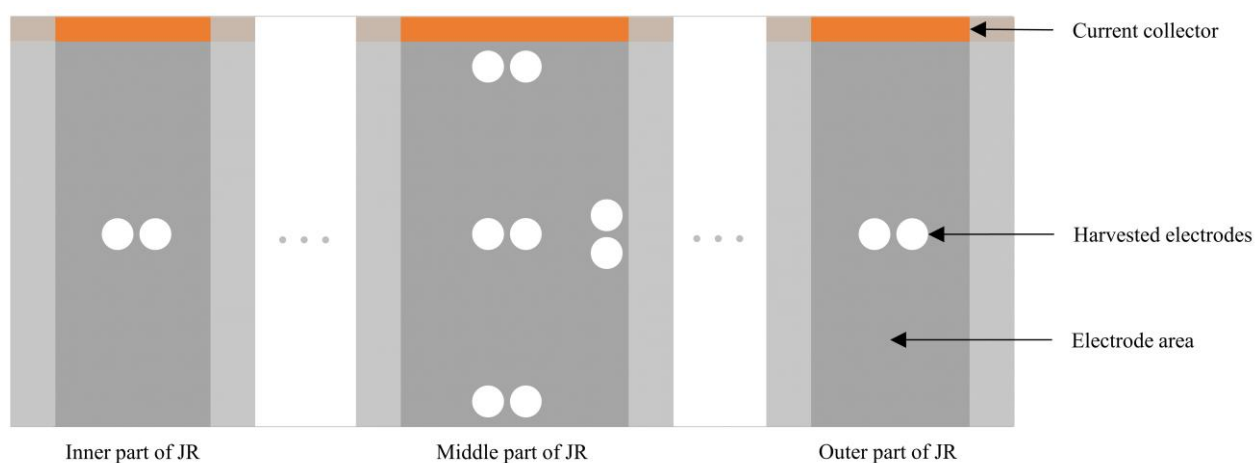


Figure S6. Schematic presentation of locations for harvesting electrodes of a Jelly Roll.

Table S1. Summary of measurements as displayed in the master chart (Figure 1) along with the main result from each one.

Section	Investigated parameter	Testing method	Main result
Aging of differently braced 94 Ah prismatic cells (section 2.1)	Capacity retention	Cycling	Braced cells show enhanced performance, especially in the region of 80% SOH
	Internal resistance	DCIR	Increase of the DCIR for the unbraced cells in the region of 80% SOH
	Cell expansion	Thickness change	Unbraced cells have a significant increase of around 20% at EOL
Post-mortem analysis (section 2.2)	Visible degradation	Cell opening	Significant visible degradation (lithium plating, crumbled coatings) mainly in the unbraced cell
	Morphology	CSP/SEM/EDX	Significant particle cracking on the aged cathode electrodes
	Electrode and separator thickness	Displacement sensor	Increased electrode thickness in aged cells
	Chemical composition	ICP-OES	Enhanced lithium and transition metal content in the anode of the unbraced cell
	Cathode structure	XRD	Correlation between cathode particle size and applied pressure
	Loss of lithium inventory	C-rate capability test (full cells)	Capacity reduction mainly attributed to loss of lithium inventory
	Degradation of anode active material	C-rate capability test/ EIS (anode half cells)	Electrodes from the braced cell show that the anode suffers only little from capacity reduction compared to the reference cell

	Degradation of cathode active material	C-Rate capability test/ EIS (cathode half cells)	The cathodes from the braced cell show higher capacity reduction compared to unbraced cell
--	--	--	--

Table S2. Resistances obtained from fitting the anode half cells EIS at 100% SOC.

Cell	$R_{a:s}$ [Ω cm ²]	$R_{a:SEI}$ [Ω cm ²]	$R_{a:ct}$ [Ω cm ²]	$R_{a:d}$ [Ω cm ²]
Cell 1 – unaged, reference	6.0	6.0	37.0	17.1
Cell 2 - aged, braced	7.2	19.1	52.3	13.9
Cell 3 – aged, unbraced, w/o ripples	7.6	19.9	40.9	14.5
Cell 3 – aged, unbraced, w/ ripples ^{a)}	29.1	57.2	187.9	100.9

^{a)} with lithium plating on the surface**Table S3.** Resistances obtained from fitting the cathode half cells EIS at 100% SOC.

Cell	$R_{c:s}$ [Ω cm ²]	$R_{c:f}$ [Ω cm ²]	$R_{c:e}$ [Ω cm ²]	$R_{c:ct}$ [Ω cm ²]
Cell 1 – unaged, reference	5.3	5.9	4.9	1.3
Cell 2 - aged, braced	6.5	6.4	6.9	8.5
Cell 3 – aged, unbraced, w/o ripples	7.6	4.6	7.0	5.6
Cell 3 – aged, unbraced, w/ ripples	5.7	5.7	9.5	7.6

Table S4. Parameters of prismatic cells.

Nominal Capacity [Ah]	94
Chemistry	Cathode: Li(Ni _{0.4} Mn _{0.3} Co _{0.3})O ₂ (NCM433), elemental composition obtained from ICP-OES (section 2.2.2) Separator: Trilayer PP/PE/PP Anode: Graphite with Al ₂ O ₃ coating
Number of Jelly Rolls	4
Sheets	Cathode: 4 x 30 (double-sided coating) Separator: 8 x 36 Anode: 4 x 32 (double-sided coating)
Area of electrodes [cm²]	Cathode: 4 x 9425 Separator: 8 x 5983 Anode: 4 x 10500
Cell dimensions (Length x Width x Height) [mm³]	174 x 45 x 133 (uncycled cell)
Mass [kg]	2.1

Table S5. Electrochemical tested cells.

	Braced cells	Unbraced cells
Number of tested cells	2	2
Applied current (charging / discharging)	94 A (1.0 C) / 188 A (2.0 C)	94 A (1.0 C) / 188 A (2.0 C)
Cycles ('first cell' / 'second cell')	7250 / 13000	7500 / 8500
Post-mortem analysis	Yes w/ 'first cell'	Yes w/ 'first cell'

Interplay between Elastic and Electrochemical Properties during Active Material Transitions and Aging of a Lithium-Ion Battery

Simon Feiler^{+, [a]} Philip Daubinger^{+, [a]} Lukas Gold,^[a] Sarah Hartmann,^[a] and Guinevere A. Giffin^{*[a, b]}

The interplay between the internal mechanical properties and external mechanical conditions of a battery cell, e.g., Young's modulus and thickness change, has a crucial impact on the cell performance and lifetime, and thus, needs to be fully understood. In this work, 12 Ah lithium-ion battery pouch cells were studied during cycling and aging by non-invasive operando ultrasonic and dilation measurements. The effective Young's modulus increases and the thickness varies the most within a

single cycle during the graphite transition from stage 1L to 4, at the beginning of the 2 to 1 stage transition and at the phase transition of the nickel-rich NCM from H2 to H3. After 1000 cycles of aging, the overall effective Young's modulus of the lithium-ion battery decreases by ~11%–12% and the cell thickness increases irreversibly by ~3%–4%, which is mostly related to a thicker and possibly softer, more porous solid electrolyte interphase layer.

Introduction

For today's lithium-ion batteries (LIBs), lifetime and reliability play an increasingly important role in the environmental impact, performance, safety and costs. In addition to the well-studied effects of current and temperature on the longevity of LIBs, another key element to consider is the mechanical and electrochemical interplay of the batteries. This interplay, between, e.g., electrode expansion,^[1–4] changes in elastic properties such as Young's modulus^[5,6] and changes in porosity^[7–9] during cycling and aging, can have a significant impact on the performance and degradation of LIBs. Along with the importance of the internal mechanical properties on the lifetime of LIBs, the external mechanical conditions, e.g., bracing, also have a significant impact. An external mechanical pressure applied on the batteries can be beneficial as it, e.g., counteracts contact losses of electrodes with the separator.^[9–12]

A method to study the mechanical changes inside a LIB during cycling that has become more popular in recent years is the use of ultrasound.^[13–15] In this method, an ultrasonic

transducer is acoustically coupled to the battery and the transmitted or the reflected signal is recorded and analyzed. Changes in thickness or stiffness of the whole cell, e.g., caused by changes in the lattice structure of the electrodes during cycling, result in changes in the measured signal. One obtainable parameter from the ultrasonic measurements is the time of flight (ToF), defined as the time it takes for the ultrasonic wave to travel through a battery. Together with the thickness d of the cell, the mean sound velocity c of the whole cell can be calculated:

$$c = \frac{d}{\text{ToF}} \quad (1)$$

The sound velocity is dependent on the effective Young's modulus E_{eff} , defined as:^[16]

$$c = \sqrt{\frac{E_{\text{eff}}}{\rho}} \quad (2)$$

where ρ is the overall density of the battery cell. The effective Young's modulus is a unit of measure for the stiffness of the cell. A lower modulus indicates a softer cell and leads to a lower sound velocity.


The term *effective modulus* was proposed by Knehr et al.^[16] to summarize the elastic interactions of the different layers into a single parameter for the cell as a whole. This effectively treats the cell as an isotropic medium which is justifiable by the fact that the ultrasonic wavelength used is much larger than the thickness of the individual layers.^[17] In this definition, the shear modulus is neglected for simplicity. It also includes emergent effects on the sound velocity that arise from the layered structure, e.g., as described in Ref. [18].


It has been shown that ultrasonic testing, and in particular the ToF, is sensitive to mechanical battery degradation. An

[a] S. Feiler,⁺ P. Daubinger,⁺ L. Gold, Dr. S. Hartmann, Dr. G. A. Giffin
Fraunhofer R&D Center Electromobility
Fraunhofer Institute for Silicate Research
Neunerplatz 2, 97082 Würzburg (Germany)
E-mail: guinevere.giffin@isc.fraunhofer.de

[b] Dr. G. A. Giffin
Julius-Maximilians-Universität Würzburg (JMU)
Faculty of Chemistry and Pharmacy
Chemical Technology of Materials Synthesis
Röntgenring 11, 97070 Würzburg (Germany)

[*] These authors contributed equally to this work.

 Supporting information for this article is available on the WWW under <https://doi.org/10.1002/batt.202200518>

 © 2023 The Authors. Batteries & Supercaps published by Wiley-VCH GmbH. This is an open access article under the terms of the Creative Commons Attribution License, which permits use, distribution and reproduction in any medium, provided the original work is properly cited.

increase in the ToF is observed during the first 300 or less cycles.^[19–22] Knehr et al.^[16] measured a rapid increase in ToF and dilation of the cell during the first 12 cycles which they attributed to the initial swelling of the graphite anode and changes in its elastic modulus. They observed that this trend continues, albeit much slower, up to 100 cycles. However, there is no long-term data available to confirm whether this trend continues during the typical lifetime of today's batteries. Bommier et al.^[23] measure a ToF increase during the first 700 cycles, however, without measuring the thickness of the cells. Thus, a conclusion cannot be drawn whether the effect is due to a thickness increase or a decrease in elastic modulus or both. In general, the survey of the published literature has shown that the relevant mechanical changes in a LIB cell are either studied for a small number of cycles or without taking the thickness change into account.

In this work, the dependence of the mechanical properties on the state-of-charge (SoC) in commercial 12 Ah LIB cells are studied with ultrasound and dilatometry. The correlation of the ultrasonic signal with the electrode transitions is examined. Furthermore, the mechanical changes are examined during an aging test with 1000 cycles. The correlation between the change in the capacity, thickness and ToF is shown.

Results and Discussion

Figure 1 shows the initial reference performance test (RPT) of the 12 Ah LIB pouch cell. During charging and discharging (at 0.04 C), the thickness of the LIB cell varies by ~ 0.13 mm, which corresponds to $\sim 2.0\%$ of the total value of ~ 6.5 mm (Figure 1a and b). A plateau in the thickness can be seen at ~ 3.7 V, which can probably be associated with the graphite anode. The graphite electrode undergoes small thickness changes during the 3L-2 stage transition that occurs around 50% SoC.^[3,4,24,25] The cathode has a thickness change that is an order of magnitude smaller in the SoC 0–80% region.^[4,25,26] At high SoCs, starting at ~ 4.1 V, a decline in thickness of the cell is detected. Here, the nickel-rich NCM cathode contracts, as the c-lattice parameter in the rhombohedral crystal structure of the layered oxide cathode declines.^[4,25–27] Even though the cell is expanding during charge, the ToF decreases (Figure 1c). This is initially counterintuitive as the cell is getting thicker and the signal needs to traverse a greater distance. However, it can be explained by an increase in the sound velocity (Figure 1d), which leads to the decrease in the ToF [Equation (1)]. The change in the sound velocity is dependent on the change in stiffness of the electrodes inside the cell [Equation (2)]. The anode is mostly responsible for the increased stiffness during charging,^[6] which results in an increase in the effective Young's modulus of $\sim 9\%$ of the whole cell (Figure 1e). The cathode also shows a change in effective Young's modulus, but this change is less pronounced when compared to the anode.^[28] During discharge, the reverse process takes place.

Overall, it can be concluded that the ultrasonic measurements detect mechanical changes inside a battery during cycling. A more detailed examination of the correlation

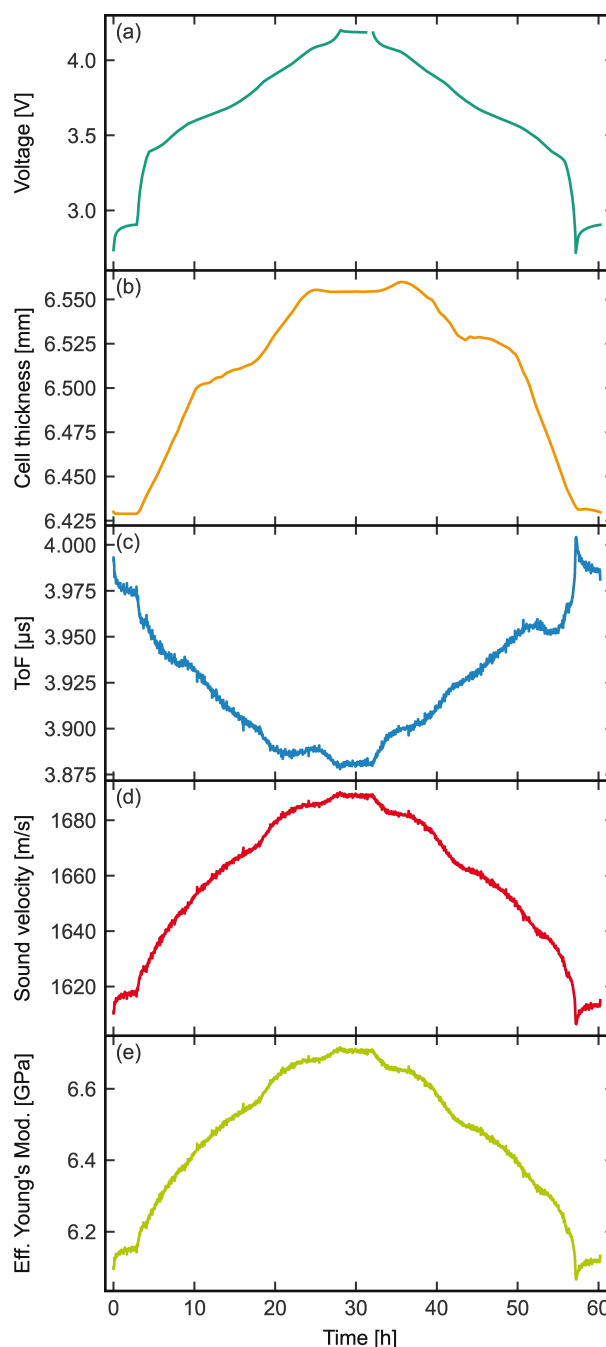


Figure 1. Parameters of an initial single cycle at 0.04 C of a 12 Ah LIB: a) voltage, b) cell thickness, c) ToF, d) sound velocity and e) effective Young's modulus as a function of time.

between the change in the capacity, thickness and ToF will be discussed later.

After the initial RPT, the cells are cycled for 1000 cycles with a C-rate of 1.0 C. After every 200 cycles, a RPT is performed (Figure 2). The cells have a relatively high-capacity retention of $\sim 95\%$ after 1000 cycles. The discharge capacity, when comparing the initial and final RPT, drops by $\sim 10\%$, with the largest drop occurring between the initial RPT and that at cycle 200. This is probably due to incomplete wetting of the electrodes, and hence, further solid electrolyte interphase (SEI) growth,

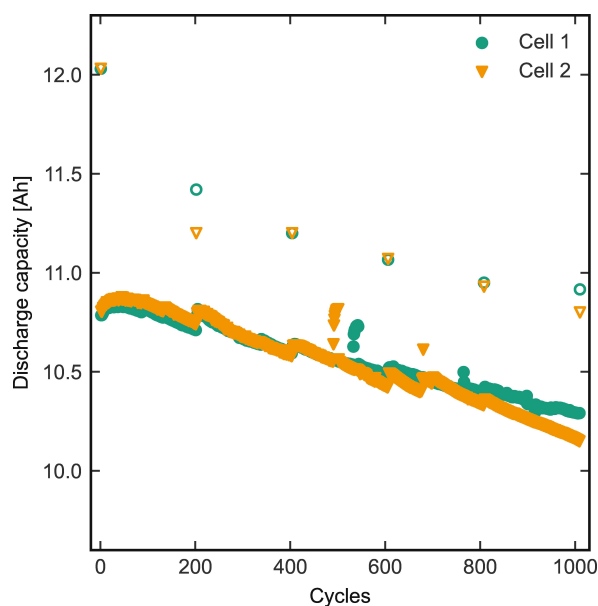


Figure 2. Discharge capacity of the 12 Ah LIB cell during aging at 1.0 C. The unfilled circles correspond to capacity measurements from the RPT at 0.04 C. Cells were aged with a bracing of 10 kPa.

most likely in the first few of the 200 cycles, which consumes cyclable lithium causing the capacity to fade. The capacity increases during the first ca. 60 cycles at 1.0 C, which may be related to the cracking of the active materials leading to shorter diffusion pathways within the particles. Therefore, at this high C-rate, more active material takes part in the electrochemical reaction leading to an increase in capacity.

To further examine the SEI formation and the capacity reduction during the aging test, electrochemical impedance spectroscopy (EIS) was performed during the RPT cycles at SoC 50% (Figures 3 and S1). The data was fitted with the equivalent circuit model shown in Figure S2. Figure 3 shows that the decrease of the resistance after the initial RPT is mostly caused by the drop of the SEI resistance (R_{SEI}). It should be noted that R_{SEI} includes the resistance of the surface layers on the anode and cathode, although the contribution of anode SEI layer is dominant. The decline in the R_{SEI} after the initial RPT may seem counterintuitive, particularly in association with the SEI growth as described above. However, the particle cracking and filling of pores not yet wetted with electrolyte leads to an increase in the electrochemically active surface area. The exposure of more surface area reduces the resistance and increases the capacity in the initial ~60 cycles at 1.0 C (Figure 2). Figure 3b shows that after cycle 200, the R_{SEI} starts to increase slightly due to thickening of the SEI. This effect probably started earlier but was concealed by the exposure of fresh active material surface area. The trends in the impedance data further substantiate the explanation of incomplete wetting during formation.^[16] The ohmic resistance (R_S) increases constantly from ~2.0 m Ω to ~2.3 m Ω during aging. The charge transfer resistance (R_{CT}) is more or less constant at ~0.9 m Ω in the first 400 cycles, followed by an increase up to ~1.4 m Ω at cycle 1000.

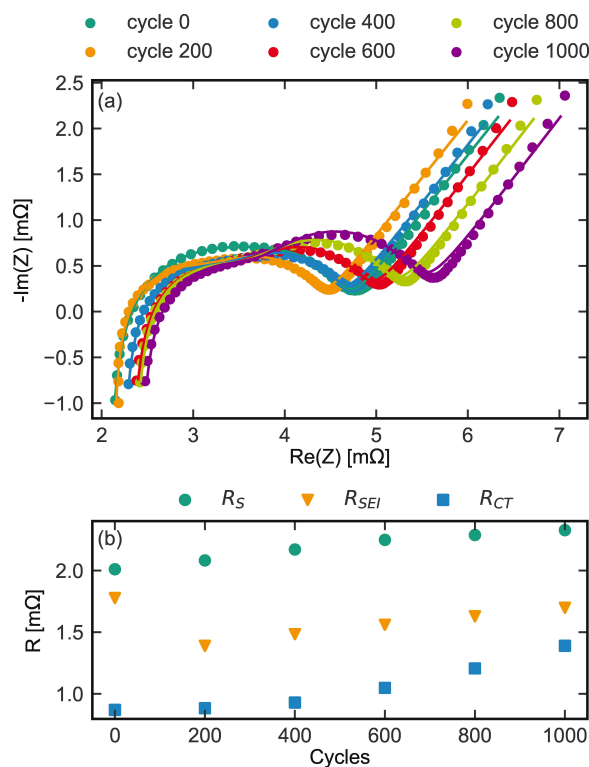


Figure 3. Evolution of the EIS measurement parameters during cycling of Cell 1: a) Nyquist plot and b) ohmic (R_S), SEI (R_{SEI}) and charge transfer resistance (R_{CT}) over the cycles.

After evaluating the capacity reduction and the impedance growth during aging, a closer examination of the changes of the mechanical parameters during the RPTs is performed. Figure 4a shows the differential voltage analysis, while the incremental capacity analysis for the RPTs during the aging study is seen in Figures S3 and S4. For peak identification, electrode material was harvested from a fresh cell and laboratory full cells with a lithium reference electrode were built. The results can be seen in Figures S5 and S6. The first peak (I, Figure 4a) can mainly be attributed to the transition of graphite stages 1L-4. The next two peaks are both a superposition of a cathode phase transition and a graphite stage transition, i.e., H1-M with 3-2 (II) and M-H2 with 2-1 (III), respectively. The last one (IV) can be solely attributed to the H2-H3 phase transition.^[29] As the most mechanical changes are expected from the anode, the graphite stage transitions are overlaid in different colors in Figure 4 to serve as an orientation. Cycle 0 shows a large deviation in dQ/dV from the other cycles. This is likely due to break-in effects where the electrolyte further infiltrates the porous electrodes. The capacity increase during the initial cycles and the decrease in SEI resistance support this claim. Afterwards, the changes are less drastic (Figures 2, 3 and 4a). During RPT of cycles 200 through 1000, the first three peaks in the dQ/dV plot shift to higher voltages (a delta of ~20 mV in total) and decrease in height as the cell ages (Figure 4a). This can be attributed to the loss of cyclable lithium, which is associated with SEI growth, and is evident in an increase in SEI resistance. Less cyclable

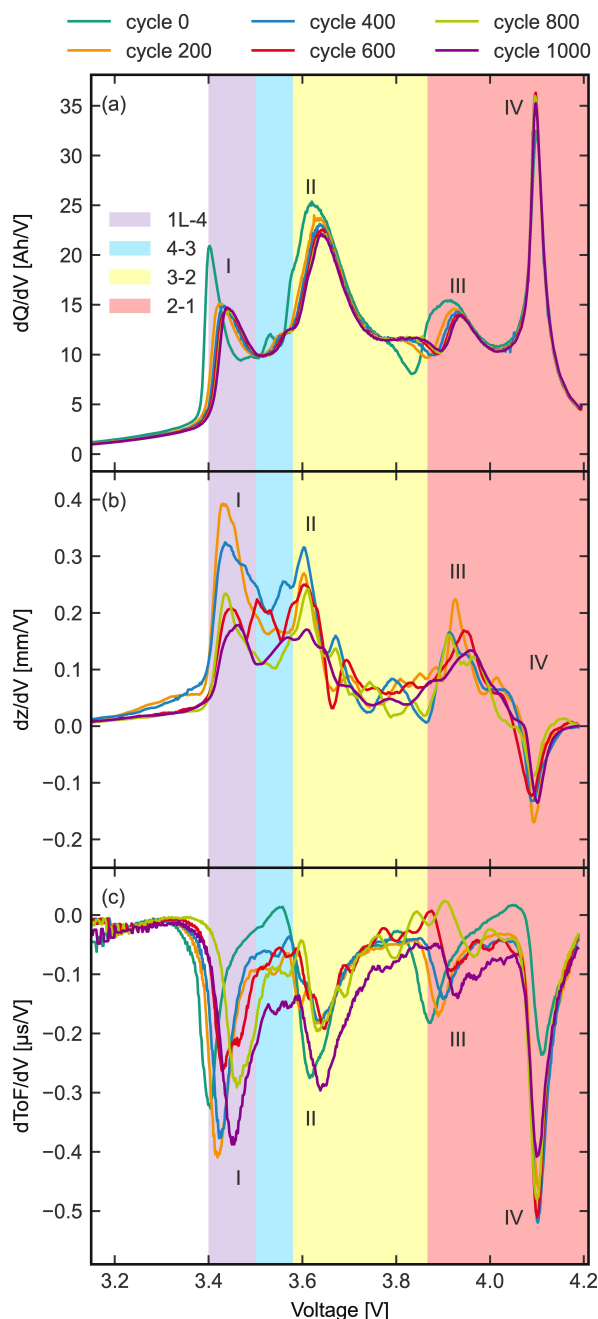


Figure 4. Differential analysis of a) capacity, b) dilation and c) ToF for 0.04 C cycles during RPT over cell voltage of Cell 1. The colored overlay shows the staging of the graphite estimated from three electrode laboratory cells (Figures S5 and S6).

lithium leads to a less lithiated anode at a given voltage, therefore shifting the intercalation stages of graphite to higher cell voltages. The last peak is not affected as it can purely be attributed to the NCM.^[29]

Figure 4b shows the incremental dilation analysis of the RPT cycles 200–1000. For cycle 0, there was no data recorded. When comparing the increase in thickness with the stages of graphite, it can be observed that a major contribution of the cell expansion stems from the graphite stages 1L through 3. For the 3-2 stage transition, the change in thickness decreases.

The 2-1 transition also leads to a major increase in thickness but is counteracted by the decrease in thickness of the H2-H3 phase transition of the nickel-rich NCM. This explains the upward trend at around 3.9 V (III) followed by the decrease in differential thickness at around 4.1 V (IV). This can also be seen in the overall thickness change (Figure 1b). During the aging of the cell, the clearest trend is the decrease of reversible thickness gain during the 1 L-3 transition, i.e., between ~3.4–3.5 V. This could be due to particle cracking on the cathode and/or SEI formation on the anode. Both processes can lead to higher porosity that can accommodate part of the expansion. It should be noted that the oscillations of the signals stem from stick and slip effects of the profile rail guides from the bracing setup.

Figure 4c shows the differential ToF over voltage. Four peaks can be observed, (I–IV) in Figure 4c. The second peak (II) mainly stems from a voltage plateau, that mathematically leads to a larger absolute $d\text{ToF}/dV$, rather than a significant change in ToF. This is confirmed by the absence of this peak in the $d\text{ToF}/dQ$ plots in Figure S3c. A negative differential ToF (ToF is decreasing) can be caused by a decrease in thickness (negative dz/dV) and/or by an increase in stiffness and therefore an increase in sound velocity. A peak in the differential ToF means that the changes in stiffness and/or thickness are confined or enhanced in a specific region, in our case a specific voltage range. In a battery, changes in the lattice structure of the electrodes, e.g., stage or phase transitions due to lithium intercalation, are therefore expected to cause peaks in the ToF.

The first peak (I) stems from the 1L-4 transition of graphite. The peak is caused by a stiffening of the graphite anode. The reason cannot be a decrease in thickness because the anode is expanding (Figure 4b) in that stage. The same logic applies to the third peak (III) that occurs right after the completion of stage 2. The shifting and position of the peak suggest that this is an effect of the anode, although a contribution of the M–H2 phase transition of the NCM cathode cannot be ruled out. With the completion of stage 2, lithium-ions start to intercalate between every graphene layer. Therefore, the mechanical properties, e.g., the Young's modulus (thus, ToF) and the thickness of the graphite electrode change drastically at this point. The peak does not span over the whole 2-1 transition but is located at the start of the stage transition. This indicates that the major part of the mechanical changes during this transition are taking place in the initial lithium-ion intercalation of the 2-1 stage transition. The last peak (IV) stems mainly from the cathodic H2-H3 phase transition. Here, it must be distinguished whether the peak is an effect of the decreased thickness or of the increase in stiffness. Assuming a constant sound velocity of 1680 m/s, the differential dilation of ~ -0.15 mm/V would only lead to a differential ToF of -0.1 $\mu\text{s}/\text{V}$ for the last peak, but a change of ~ -0.5 $\mu\text{s}/\text{V}$ is measured. Thus, this change in ToF is mostly caused by an increase in effective Young's modulus during this H2-H3 transition and not due to a decline in cell thickness. During aging, the peaks of the graphite anode (I and III) shift to higher voltages and decrease in magnitude due to loss of cyclable lithium. The peak of the H2-H3 transition does not change notably. It should be

noted that in cycle 1000, the ultrasonic measurement was conducted at a different spot on the cell, due to coupling problems. An inhomogeneous thickness increase of the cell led to an insufficient coupling of the ultrasonic wave into the battery cell on the previous measuring spot. The result is that the data is not fully comparable to the prior RPTs.

The absolute ToF is shown in Figures 5(a) and S7 for the RPT cycles. It can be seen that the ToF increases from cycle 0 to cycle 1000. During aging, the cell undergoes an irreversible thickness growth from ~ 6.5 mm before cycling to ~ 6.75 mm at cycle 1000. This results in a longer sound path for the ultrasonic signal through the battery that would account for ~ 0.15 μs of travelling time, assuming an unchanged sound velocity from cycle 0. Nevertheless, the total increase in ToF is ~ 0.4 μs . Thus, the additional increase must be related to a reduction of the overall stiffness of the cell, which can be seen in Figure 5b. The effective Young's modulus decreases by 0.7 GPa–0.8 GPa, which corresponds to 11%–12%. The reversible modulus change between charged (SoC 100%) and discharged state (SoC 0%) also decreases from around 0.58 GPa to 0.43 GPa, when comparing the initial cycle to cycle 1000. This reveals that the cell is not only getting thicker but also softer during aging. The decrease in Young's modulus can be related to a possibly softer and more porous SEI over aging.^[30–32] A higher porosity leads to a lower sound velocity in the medium. This mechanism is well known in geophysics.^[33,34] Larger pores deform more easily under stress, implying that they are softer and thus, lower the

sound velocity. It should be noted that the values of cycle 0 is from a different unaged reference cell, because logging of the dilation, which is needed for determining the effective Young's modulus [Equations (1) and (2)] was introduced at cycle 200.

Conclusion

Ultrasonic and dilation measurements on commercial 12 Ah LIB pouch cells reveal mechanical changes inside the cell. During a single cycle, an increase in the effective Young's modulus of $\sim 9\%$ from fully discharged (SOC 0%) to fully charged state (SOC 100%) is measured. This change probably stems in large part from the graphite anode and the H2-H3 phase transition of the NCM. Most of the ToF decrease and hence stiffening of the cell is observed during the graphite transition 1L-4, at the beginning of 2-1 transition and at the phase transition of the nickel rich NCM from H2-H3. The largest increase in thickness during a cycle of the cell is observed during the graphite transitions 1L-3 and at the beginning of 2-1 followed by a decrease in thickness from the H2-H3 transition.

During aging, the reversible change in thickness decreases, while the irreversible thickness of the cell increases, probably mostly due to SEI formation and cracking. This leads to a higher porosity of the cell that can partially accommodate the expansion of the electrodes during cycling. The magnitude of the differential ToF during cycling is decreasing, mostly in SoC regions where the anode has stage transitions. The differential ToF during the cathodic H2-H3 transition does not experience significant changes during aging. From cycle 0 to 1000 a decrease in the cells effective Young's modulus of 11%–12% is measured. This softening can probably mostly be attributed to the graphite anode. The irreversible thickness increase combined with an increase in SEI resistance is an indication of a growing SEI layer on the anode. The SEI is possibly softer and more porous than the rest of the cell, which lowers the overall cell modulus and increases ToF. A schematic of the findings of this work are shown in Figure 6. The methodology demonstrated presents a chance for a fundamentally different perspective towards battery diagnostics by studying mechanical parameters instead of electrical ones which might be more sensitive and/or easier to implement in certain conditions. Analyzing the time of flight has been shown to reliably correlate with capacity fading of the cell and staging of the graphite anode over 1000 cycles.

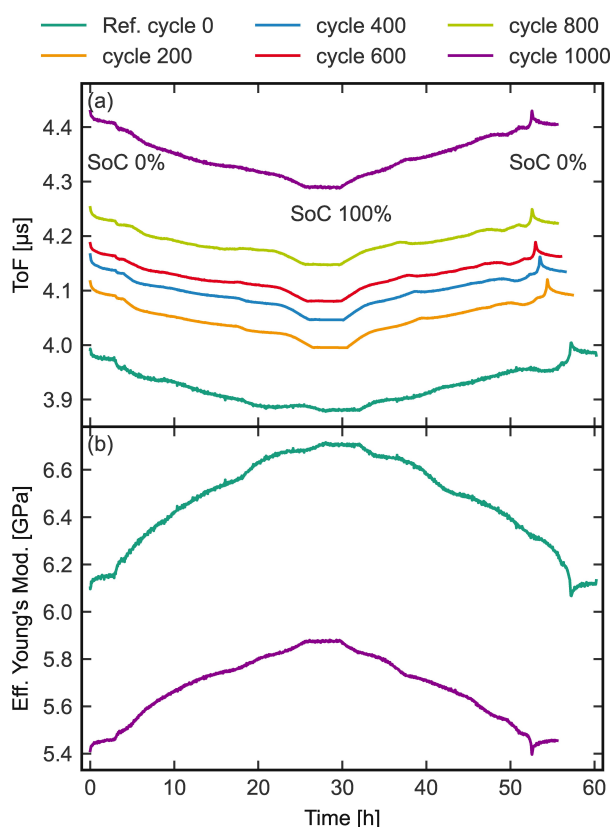


Figure 5. a) Evolution of ToF and b) effective Young's modulus as a function of time during RPTs of Cell 1.

Experimental Section

Electrochemical testing: For all experiments, two LIBs with a nominal capacity of 12 Ah from Kokam (SLPB065070180, Kokam Co., Ltd.) were used. The cell consists of a graphite anode and a nickel-rich NCM cathode. It is known from the data sheet that the electrolyte is a mixture of lithium hexafluorophosphate (LiPF_6) in ethylene carbonate (EC)/ethyl methyl carbonate (EMC), but the exact composition is not given. The battery cells have an active area dimension (excluding sealing and tabs) of $67 \text{ mm} \times 165 \text{ mm}$ (width \times height). The thickness of the battery cell is $6.5 \text{ mm} \pm$

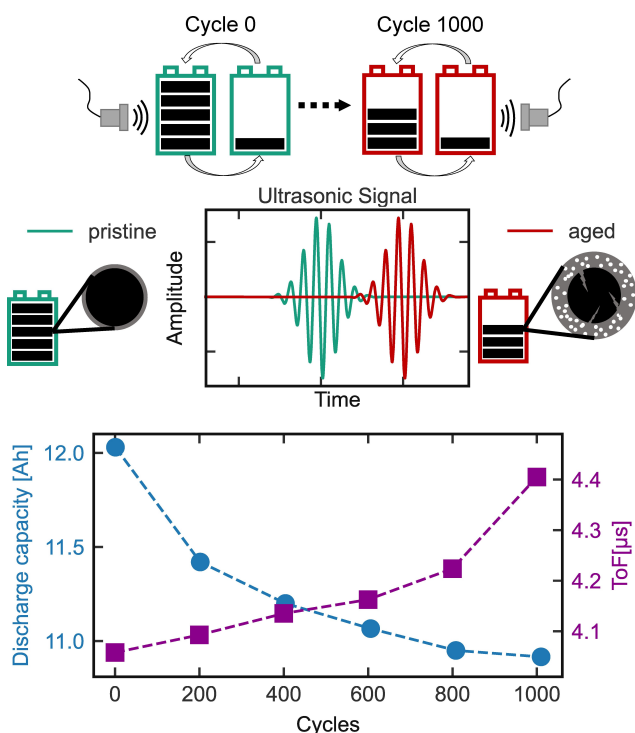


Figure 6. Schematic of the findings of this work, which illustrates the generalization of morphological changes on the particle level.

0.05 mm at SoC 30%. The RPT was performed in self-built experimental setup (Figure 7). The applied external pressure was 10 kPa and the cycling was performed within the voltage range of 2.7 V to 4.2 V. The C-rate during constant current constant voltage

(CCCV) charging and CC discharging in the RPT (measured with a Biologic SP-240, BioLogic Sciences Instruments) was 0.04 C (0.48 A). The cut-off criterion in the constant voltage step during charge was a current $I < 0.01$ C at 4.2 V. After reaching the charging cutoff criterion, a 3 h rest period was included. During the accelerated aging tests, the cells were braced in a separate spring braced device at a pressure of 10 kPa and cycled from 2.7 V to 4.2 V at a rate of 1.0 C (12.0 A) also using a CCCV charge and CC discharge procedure (Maccor Series 4000, Maccor Inc.). The cut-off criterion during charging in the voltage step was a current $I < 0.1$ C at 4.2 V. After charging and discharging, a 10 minute rest step was included.

Experimental setup: A sketch of the test setup is shown in Figure 7. The pressure was applied through two springs (38.15 N/mm, 13330, SODEMANN Industrifjedre A/S) to ensure a control of the pressure by ± 1 kPa. The cells were braced between two 25 mm thick aluminum plates in order to apply a homogeneous pressure distribution. A pressure sensor (KM38-2 kN load cell, ME-Systeme GmbH) was used to measure the force applied on the battery cell. The expansion of the battery cell was measured with a dilation sensor (IL-S065, KEYENCE DEUTSCHLAND GmbH) paired with an amplifier unit (IL-1000, KEYENCE DEUTSCHLAND GmbH). The ultrasonic transducers (U2P10, United NDT GmbH) had a center frequency of 2.0 MHz and a diameter of 10 mm. The transducers were mounted flat on the backside of each metal plate, facing each other. To enhance the coupling, and thus reduce reflections at the different interfaces (transducer-metal plate, metal plate-battery), canola oil was used as a coupling agent.

Ultrasonic measurements: For all excitation pulses and recordings, a single-channel ultrasonic frontend (PCUS pro Single, Fraunhofer Institute for Ceramic Technologies and Systems IKTS) was used. The excitation voltage of the applied rectangular pulse was set to 200 V with a pulse length of 500 ns. The excited ultrasonic signal passes through the metal plates and the LIB and was recorded by

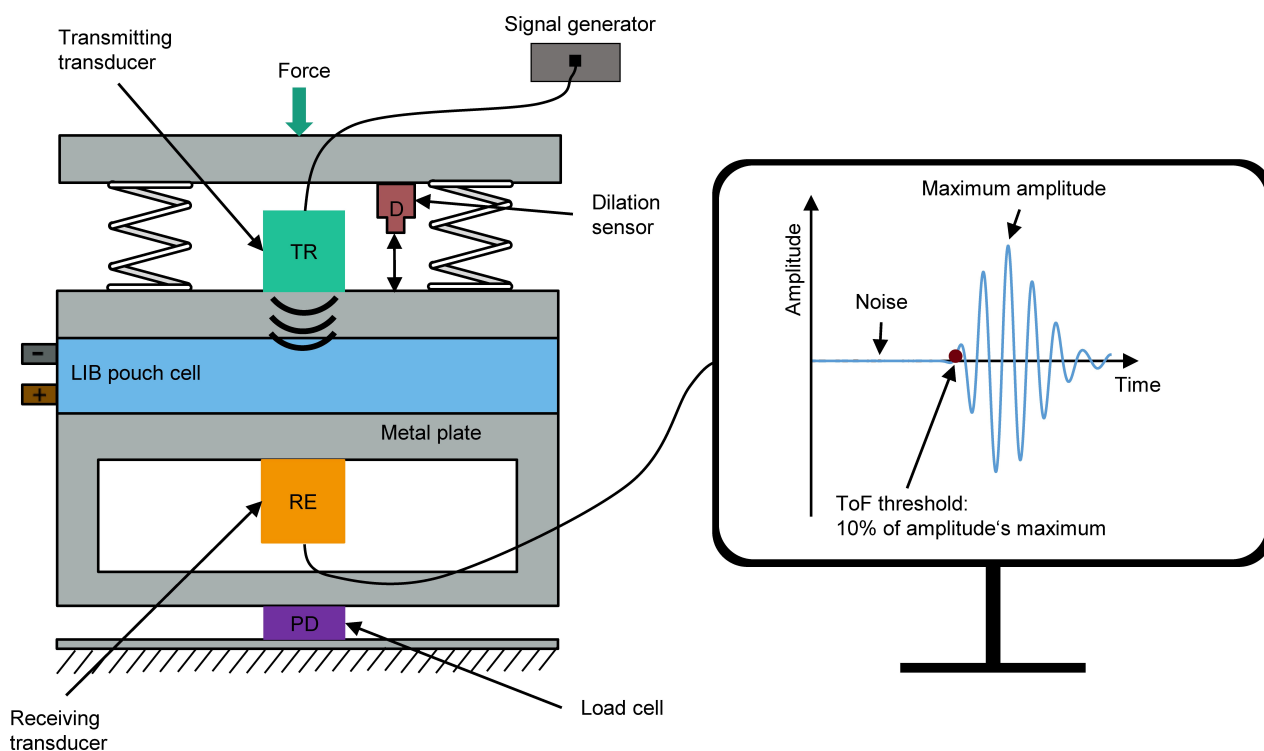


Figure 7. Scheme of experimental setup and an exemplary incoming ultrasonic signal.

the PCUS analog digital converter with a sampling rate of 100 MHz. On the right hand side of Figure 7, an exemplary ultrasonic signal is shown. To evaluate the ToF, a thresholding method was used (Figure 7). The ToF is taken as the first datapoint of the entry exceeding the threshold. The threshold was set to 10% of the maximum amplitude. The value was chosen as a good compromise between detecting the signal as early as possible and staying well above the noise level. Scaling the threshold with the maximum amplitude ensures that the ToF is independent of the scale of the signal as the intersection of the threshold with the signal is located at the same point in time for two differently scaled signals. The signals are prefiltered by a hardware filter with center frequency at 2 MHz and detrended by subtracting a linear least-squares fit from the data. To enhance the resolution of the ToF beyond the 10 ns (limited by the 100 MHz sampling rate) of the A/D converter, the signal was linearly interpolated between the first datapoint exceeding the threshold and the previous datapoint. The ToF of the LIB is determined by a subtraction of the ToFs through the setup with and without the LIB.

Electrochemical impedance spectroscopy

EIS measurements were conducted for SoC 0%, 50% and 100%. SoC 0% is defined as the recommended discharge cut-off voltage at 2.7 V. SoC 100% is the charge cut-off voltage at 4.2 V. SoC 50% is defined as the state of the cell at 3.7 V, which was determined from the open circuit potential of a fresh cell charged to half of the initial discharge capacity. To reach a given SoC, the cells were brought to the cutoff voltage with a 0.04 C (0.48 A) constant current, constant voltage step with a CV cutoff of $I < 0.01$ C. Impedance data was acquired with a potentiostatic EIS measurement with an amplitude of 5 mV (Biologic SP-240, BioLogic Sciences Instruments). Frequencies were recorded between 7 MHz and 10 mHz. The measurements were averaged for a given frequency and 11 points were measured per frequency decade. Data points below $\text{Im}(Z) < 1 \text{ m}\Omega$ were neglected due to occurrence of skin effect at high frequencies. A simplified equivalent circuit, represented by Equation 3 and shown in Figures S2, e.g., as used in Ref. [34], was used to fit the data. The real and imaginary impedance data were raveled/flattened and a least square fit was conducted. The capacitances were approximated as constant phase elements and the Warburg element Y_0 was extended by an additional angle parameter γ .

$$Z = i\omega L + R_s + \frac{1}{\frac{1}{R_{SEI}} + (i\omega)^\beta C_{SEI}} + \frac{1}{\frac{1}{R_{CT} + \frac{1}{Y_0 \sqrt{i\omega}^\gamma}} + (i\omega)^\alpha C_{CT}} \quad (3)$$

Author Contributions

S. F. and P. D. contributed equally to this work. Conceptualization, Investigation, Methodology, Visualization and Writing – original draft was done by S. F. and P. D. Investigation, Supervision and Writing – review & editing was performed by L. G., S. H. and G. G.

Acknowledgements

The authors gratefully acknowledge the funding of this work by the European Union's Horizon 2020 Research & Innovation program in the SPARTACUS project (grant number 957221) and

the Federal Ministry of Education and Research (BMBF) of Germany in the project MAD³AM4Life (grant number 03XP0327). We also want to thank the members of the Fraunhofer R&D Center Electromobility and the Center Smart Materials and Adaptive Systems at Fraunhofer ISC for fruitful discussions and scientific support. Open Access funding enabled and organized by Projekt DEAL.

Conflict of Interest

The authors declare no conflict of interest.

Data Availability Statement

The data that support the findings of this study are available from the corresponding author upon reasonable request.

Keywords: aging · lithium · phase transition · ultrasound · Young's modulus

- [1] D. Sauerteig, S. Ivanov, H. Reinshagen, A. Bund, *J. Power Sources* **2017**, 342, 939.
- [2] B. Rieger, S. Schlueter, S. V. Erhard, J. Schmalz, G. Reinhart, A. Jossen, *J. Energy Storage* **2016**, 6, 213.
- [3] P. Daubinger, F. Ebert, S. Hartmann, G. A. Giffin, *J. Power Sources* **2021**, 488, 229457.
- [4] F. B. Spingler, S. Kücher, R. Phillips, E. Moyassari, A. Jossen, *J. Electrochem. Soc.* **2021**, 168, 40515.
- [5] K. Min, E. Cho, *Phys. Chem. Chem. Phys.* **2018**, 20, 9045.
- [6] Y. Qi, H. Guo, L. G. Hector, A. Timmons, *J. Electrochem. Soc.* **2010**, 157, A558.
- [7] S. A. Channagiri, S. C. Nagpure, S. S. Babu, G. J. Noble, R. T. Hart, *J. Power Sources* **2013**, 243, 750.
- [8] G. Sikha, B. N. Popov, R. E. White, *J. Electrochem. Soc.* **2004**, 151, A1104.
- [9] M. Göttlinger, P. Daubinger, W. Stracke, S. Hartmann, G. A. Giffin, *Electrochim. Acta* **2022**, 419, 140354.
- [10] P. Daubinger, M. Schelter, R. Petersohn, F. Nagler, S. Hartmann, M. Herrmann, G. A. Giffin, *Adv. Energy Mater.* **2022**, 12, 2102448.
- [11] J. Cannarella, C. B. Arnold, *J. Power Sources* **2014**, 245, 745.
- [12] M. Wünsch, J. Kaufman, D. U. Sauer, *J. Energy Storage* **2019**, 21, 149.
- [13] L. Gold, T. Bach, W. Virsik, A. Schmitt, J. Müller, T. E. M. Staab, G. Sextl, *J. Power Sources* **2017**, 343, 536.
- [14] A. G. Hsieh, S. Bhadra, B. J. Hertzberg, P. J. Gjeltema, A. Goy, J. W. Fleischer, D. A. Steingart, *Energy Environ. Sci.* **2015**, 8, 1569.
- [15] R. J. Copley, D. Cumming, Y. Wu, R. S. Dwyer-Joyce, *J. Energy Storage* **2021**, 36, 102406.
- [16] K. W. Knehr, T. Hodson, C. Bommier, G. Davies, A. Kim, D. A. Steingart, *Joule* **2018**, 2, 1146.
- [17] J. M. Carcione, *J. Acoust. Soc. Am.* **1996**, 99, 2655.
- [18] G. E. Backus, *J. Geophys. Res.* **1962**, 67, 4427.
- [19] J.-Y. Kim, J.-H. Jo, J.-W. Byeon, *Microelectron. Reliab.* **2020**, 114, 113859.
- [20] P. Ladpli, F. Kopsaftopoulos, F.-K. Chang, *J. Power Sources* **2018**, 384, 342.
- [21] Y. Wu, Y. Wang, W. K. C. Yung, M. Pecht, *Electronics* **2019**, 8, 751.
- [22] G. Davies, K. W. Knehr, B. van Tassell, T. Hodson, S. Biswas, A. G. Hsieh, D. A. Steingart, *J. Electrochem. Soc.* **2017**, 164, A2746–A2755.
- [23] C. Bommier, W. Chang, J. Li, S. Biswas, G. Davies, J. Nanda, D. I. Steingart, *J. Electrochem. Soc.* **2020**, 167, 20517.
- [24] M. Bauer, M. Wachtler, H. Stöwe, J. V. Persson, M. A. Danzer, *J. Power Sources* **2016**, 317, 93.
- [25] H. Pegel, O. von Kessel, P. Heugel, T. Deich, J. Tübke, K. P. Birke, D. U. Sauer, *J. Power Sources* **2022**, 537, 231443.
- [26] L. de Biasi, A. O. Kondrakov, H. Geßwein, T. Brezesinski, P. Hartmann, J. Janek, *J. Phys. Chem. C* **2017**, 121, 26163.

- [27] P. Kargl, V. Drews, P. Daubinger, O. Schweighofer, M. Marinaro, G. A. Giffin, M. Wohlfahrt-Mehrens, A. Thaler, *J. Power Sources* **2022**, *548*, 232042.
- [28] R. Xu, H. Sun, L. S. de Vasconcelos, K. Zhao, *J. Electrochem. Soc.* **2017**, *164*, A3333–A3341.
- [29] R. Jung, M. Metzger, F. Maglia, C. Stinner, H. A. Gasteiger, *J. Electrochem. Soc.* **2017**, *164*, A1361–A1377.
- [30] P. Guan, L. Liu, X. Lin, *J. Electrochem. Soc.* **2015**, *162*, A1798–A1808.
- [31] S. K. Heiskanen, J. Kim, B. L. Lucht, *Joule* **2019**, *3*, 2322.
- [32] W. Huang, P. M. Attia, H. Wang, S. E. Renfrew, N. Jin, S. Das, Z. Zhang, D. T. Boyle, Y. Li, M. Z. Bazant, B. D. McCloskey, W. C. Chueh, Y. Cui, *Nano Lett.* **2019**, *19*, 5140.
- [33] C. M. Sayers, L. D. den Boer, *Geophys. Prospect.* **2021**, *69*, 1733.
- [34] M. R. J. Wyllie, A. R. Gregory, L. W. Gardner, *Geophys.* **1956**, *21*, 41.

Manuscript received: December 1, 2022
Revised manuscript received: January 25, 2023
Version of record online: February 13, 2023

Batteries & Supercaps

Supporting Information

Interplay between Elastic and Electrochemical Properties during Active Material Transitions and Aging of a Lithium-Ion Battery

Simon Feiler⁺, Philip Daubinger⁺, Lukas Gold, Sarah Hartmann, and Guinevere A. Giffin*

RESEARCH ARTICLE

Interplay between Elastic and Electrochemical Properties during Active Material Transitions and Aging of a Lithium-Ion Battery

Simon Feiler^[a], Philip Daubinger^[a], Lukas Gold^[a], Sarah Hartmann^[a] and Guinevere A. Giffin^{*[a], [b]}.

[a] P. Daubinger, S. Feiler, L. Gold, Dr. S. Hartmann, Dr. G. A. Giffin
Fraunhofer R&D Center Electromobility
Fraunhofer Institute for Silicate Research
Neunerplatz 2, 97082 Würzburg, Germany
E-mail: guinevere.giffin@isc.fraunhofer.de

[b] Dr. G. A. Giffin
Julius-Maximilians-Universität Würzburg (JMU)
Faculty of Chemistry and Pharmacy
Chemical Technology of Materials Synthesis
Röntgenring 11, 97070 Würzburg, Germany

+ S.F. and P.D. contributed equally to this work

Supporting Information

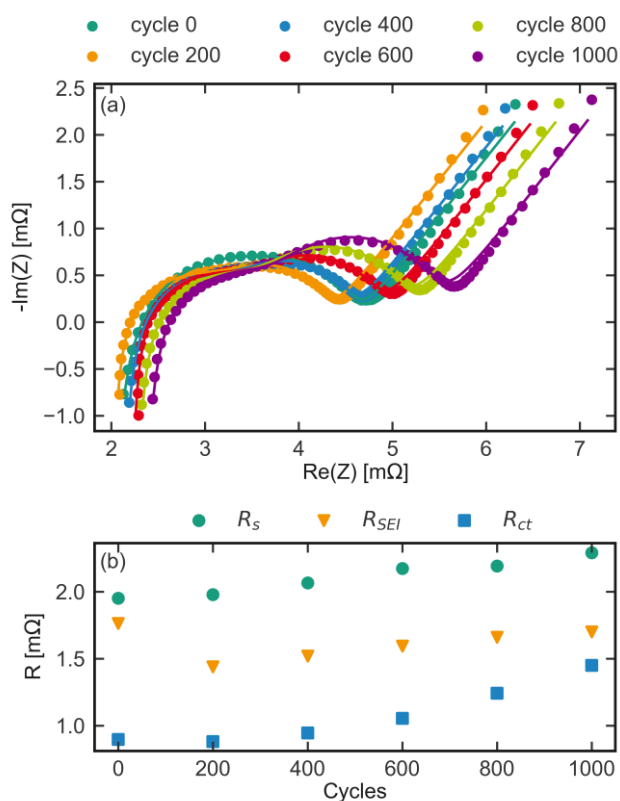


Figure S 1. Evolution of the EIS measurement parameters during cycling of Cell 2. (a) Nyquist plots and (b) ohmic, SEI and charge transfer resistances during the RPT cycles.

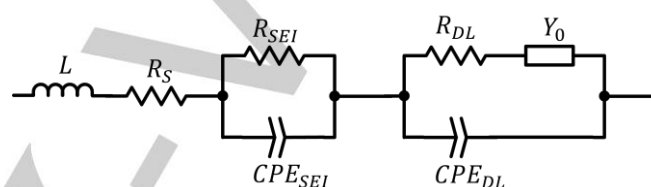


Figure S 2. Equivalent circuit model used for fitting the impedance data.

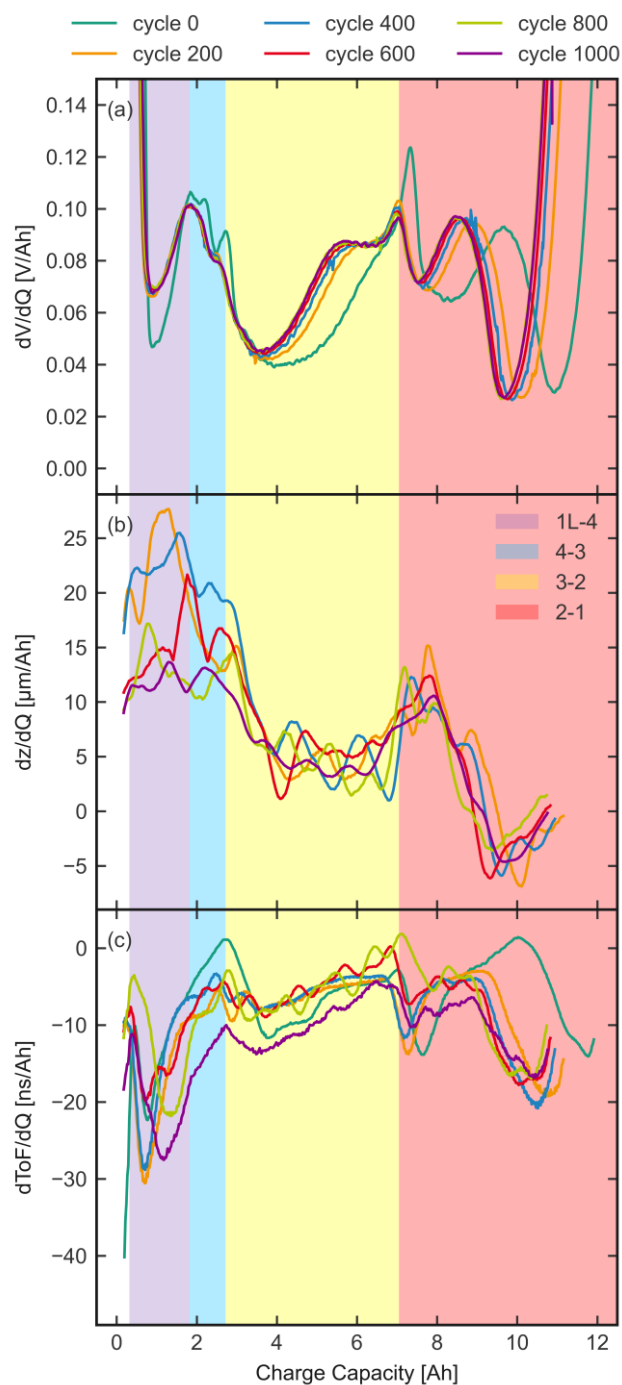


Figure S 3. Differential analysis of a) voltage, b) dilation and c) ToF for 0.04 C cycles during RPT as a function of capacity for Cell 1. The colored overlay shows the staging of the graphite anode estimated from three electrode cells containing electrodes harvested from the 12 Ah cells (Figure S 5 and Figure S 6).

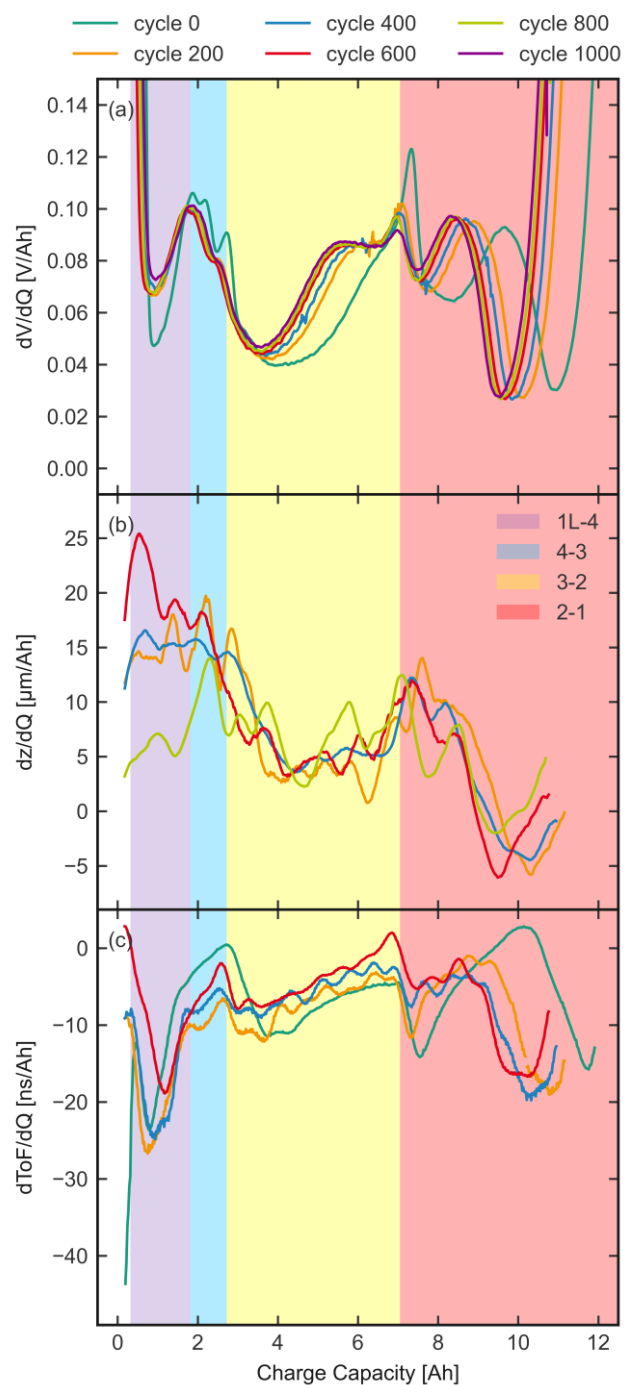


Figure S 4. Differential analysis of a) voltage, b) dilation and c) ToF for 0.04 C cycles during RPT as a function of capacity for Cell 2. The colored overlay shows the staging of the graphite anode estimated from three electrode cells containing electrodes harvested from the 12 Ah cells (Figure S 5 and Figure S 6).

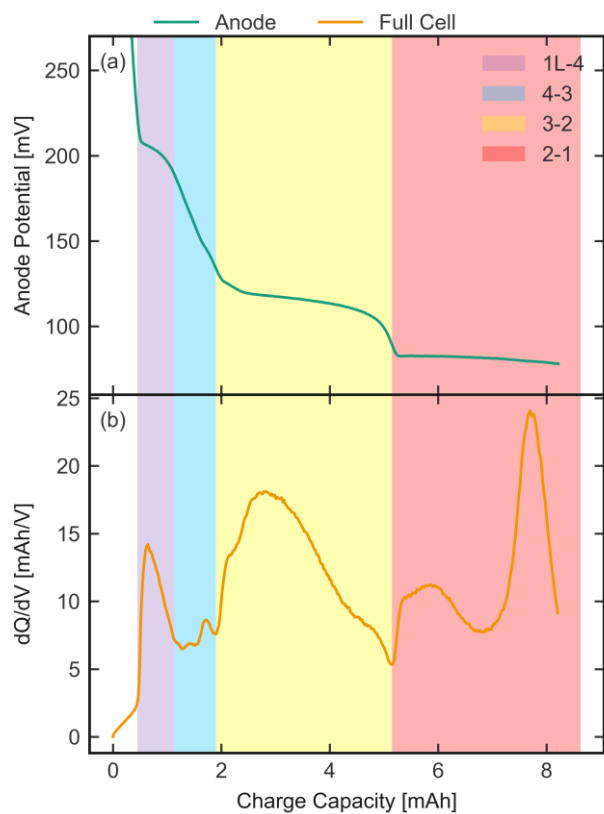


Figure S 5. Anode potential and dQ/dV of the full cell containing electrodes harvested from the 12 Ah cells in a 3-electrode setup. Stages identified from the voltage plateaus according to Ref. [35].

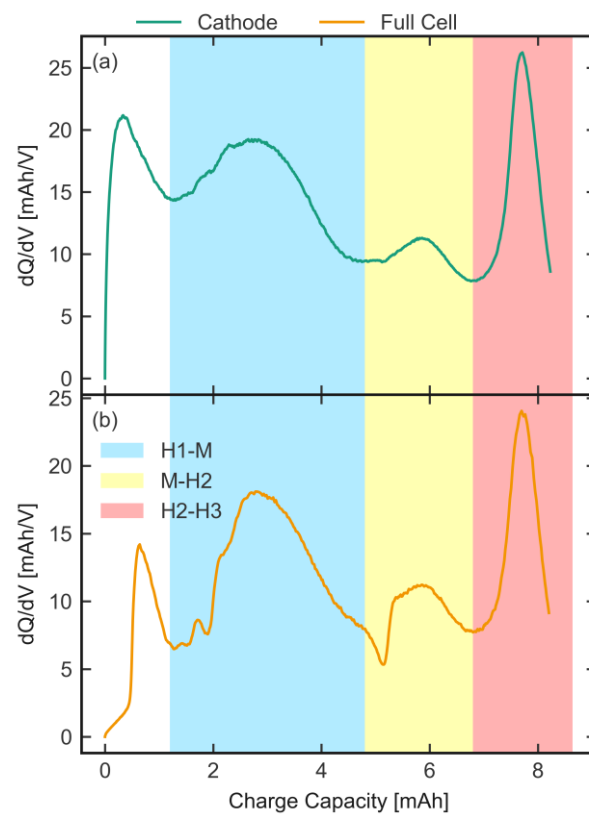


Figure S 6. dQ/dV of (a) the cathode potential and (b) the full cell potential for cells containing electrodes harvested from the 12 Ah cells in a 3-electrode setup. Phase transition identified according to Ref. [29].

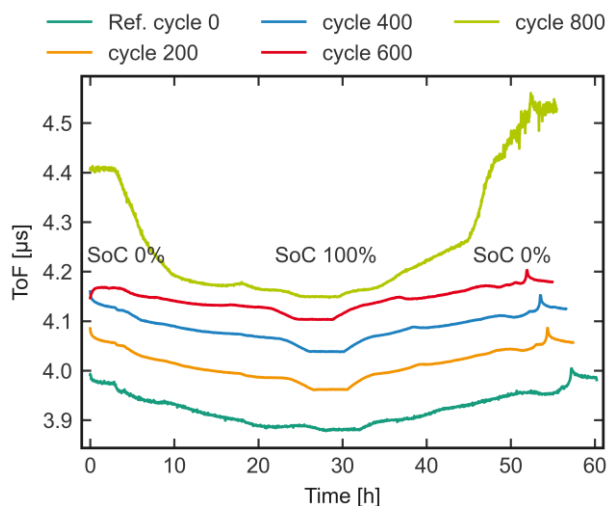


Figure S 7. Evolution of ToF as a function of time during RPTs of Cell 2.

References:

- [29] R. Jung, M. Metzger, F. Maglia, C. Stinner, H. A. Gasteiger, *J. Electrochem. Soc.* 2017, 164, A1361-A1377.
 [35] J. Asenbauer, T. Eisenmann, M. K., A. Kazzazi, Z. Chen, D. Bresser, *Sustainable Energy & Fuels* 2020, 4, 5387.

Consequences of Different Pressures and Electrolytes on the Irreversible Expansion of Lithium Metal Half Cells

Philip Daubinger,^[a] Mara Göttlinger,^[a] Sarah Hartmann,^[a] and Guinevere A. Giffin.*^[a, b]

Lithium metal is considered as the 'holy-grail' among anode materials for lithium-ion batteries, but it also has some serious drawbacks such as the formation of dendritic and dead lithium. In this study, the interplay of external pressure and different carbonate- and ether-based electrolytes on the (ir)reversible expansion of lithium metal during cycling against lithium titanate and lithium iron phosphate is studied. In carbonate-based electrolytes without any additives, lithium metal shows tremendous irreversible expansion and significant capacity

reduction at elevated current densities due to the formation of mossy and dead lithium. The addition of fluoroethylene carbonate can reduce irreversible expansion and capacity reduction, especially when a high external pressure is applied. When an ether-based electrolyte is used, the irreversible dilation of the lithium metal is suppressed when applying increased external pressures. Overall, increased external pressure appears to reduce the formation of mossy and dead lithium and improve the performance.

Introduction

The demand for higher energy densities in lithium-ion batteries (LIB) leads to the search for materials with high theoretical capacities. Lithium metal is considered the 'holy-grail' of lithium-based batteries, as it has the highest theoretical specific capacity with 3860 mAh g^{-1} and the lowest reduction potential of -3.04 V vs. the standard hydrogen electrode of all possible candidates for the negative electrode.^[1,2] By replacing the state-of-the-art (SoA) anode material graphite with lithium metal in a LIB with a transition metal cathode, the specific energy could be increased from $\sim 250 \text{ Wh kg}^{-1}$ up to $\sim 440 \text{ Wh kg}^{-1}$.^[2] However, there are many obstacles for the widespread use of lithium metal as an anode material, such as poor cyclability, high reactivity, volumetric expansion and safety concerns.^[3-6] The dissolution (stripping) and deposition (plating) processes during cycling cause the formation of dendrites. New lithium tends to be deposited at the defect sites of the lithium surface due to the altered electric field and the high atomic mobility of lithium.^[7-9] This means that lithium deposition does not necessarily occur at the tip of the dendrites, but at the site with the lowest surface energy.^[10] Hence, continuous stripping and plating of lithium leads to the formation of a 'mossy-like'

lithium layer on top of the bulk lithium. Further cycling promotes the formation of 'dead' lithium. Dead lithium is a metal that is electrically isolated from the substrate or bulk lithium and thus, no longer takes part in the cycling.


The tremendous volume change during cycling ($\sim 4.9 \mu\text{m}$ for every mAh cm^{-2})^[2] and the related cracking of the solid electrolyte interphase (SEI) result in high surface area lithium and the formation of a fresh metal surface. Severe side reactions occur due to the high reactivity of lithium which consume lithium and electrolyte. Hence, the thickness of the SEI increases, which in combination with the mossy and dead lithium, increases the ion transport resistance in the double layer. Additionally, dendrite growth can cause short circuits between anode and cathode, which poses a risk for thermal runaway.^[3,4] One possible way to tackle the issue of the lithium dendrite formation during cycling is to apply an external mechanical force to the cell which also results in increased pressure onto the surface of the lithium metal. Mechanical pressure, which is also known to enhance the performance of SoA LIB,^[11-14] may restrict lithium dendrite formation and extend cycle life.^[15-18]


The use of carbonate-based electrolytes in combination with lithium metal results in a short cycle life due the poor deposition morphology of lithium in this electrolyte combined with the high chemical reactivity of the carbonate components with Li, particularly at high current rates.^[6,19,20] With the use of ether solvents like dimethoxyethane (DME) in combination with salts like lithium bis(fluorosulfonyl)imide (LiFSI), high rate performance can be achieved in symmetrical lithium cells even at high current densities of 10 mA cm^{-2} .^[21]

In this work, the behavior of lithium metal is studied using different external pressures in combination with different carbonate- and ether-based electrolytes. To do this, lithium metal is cycled against the 'zero-strain' electrode lithium titanate (LTO) and lithium iron phosphate (LFP) to minimize the impact of the counter electrode on the total expansion. The volumetric expansion due to the combined effects of the

[a] P. Daubinger, M. Göttlinger, Dr. S. Hartmann, Dr. G. A. Giffin.
Fraunhofer R&D Center Electromobility
Fraunhofer Institute for Silicate Research
Neunerplatz 2, 97082 Würzburg, Germany
E-mail: guinevere.giffin@isc.fraunhofer.de

[b] Dr. G. A. Giffin.
Chemical Technology of Materials Synthesis
Faculty of Chemistry and Pharmacy
Julius-Maximilians-University Würzburg
Roentgenring 11, 97070 Würzburg, Germany

 Supporting information for this article is available on the WWW under <https://doi.org/10.1002/batt.202200452>

 © 2022 The Authors. Batteries & Supercaps published by Wiley-VCH GmbH. This is an open access article under the terms of the Creative Commons Attribution License, which permits use, distribution and reproduction in any medium, provided the original work is properly cited.

formation of the SEI, the deposition of mossy and formation of the dead lithium is investigated in an *operando* dilation cell. Additionally, pressure and electrolyte dependent cycling experiments in a laboratory-scale pouch cell system is done to demonstrate the beneficial impact of certain electrolytes and external mechanical pressure on the performance of the cells.

Results and Discussion

Dilation and preselection of the electrodes

In order to find a counter electrode with limited expansion, the dilation behavior of various SoA and next-generation electrodes was investigated (Figures 1 and S1). Table 1 shows the measured capacity, dilation and the areal capacity related dilation during lithiation and delithiation. From the results, it can be seen that the cell configuration with NCM111 vs. LTO undergoes almost no expansion during cycling. This is consis-

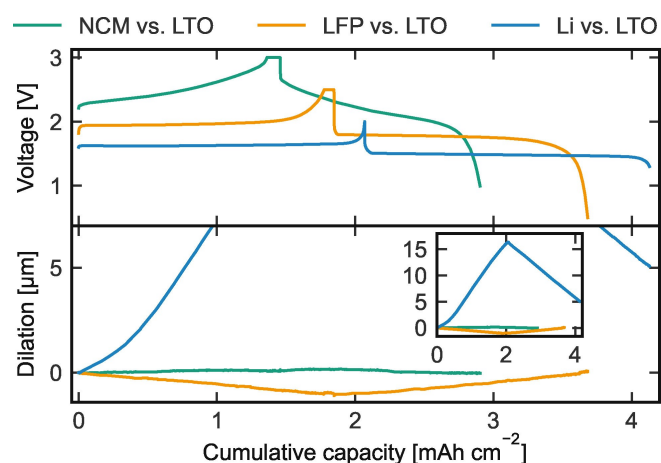


Figure 1. Dilation behavior of NCM111 vs. LTO, LFP vs. LTO and Li vs. LTO during cycling. Voltage and dilation as a function of cumulative capacity. The cells were cycled with Celgard 2500 as separator, LP57 as electrolyte and 0.05 MPa external applied pressure. The current was 2.0 mA cm^{-2} ($\sim 1.0 \text{ C}$).

tent with the literature, where LTO is known to be a zero-strain material and NCM111 shows little expansion ($\sim 1\%$) during cycling.^[22–25] LFP contracts during delithiation and expands during the lithiation. The dilation of $\sim 0.5 \mu\text{m per mAh cm}^{-2}$ is relatively small compared to the other electrodes (Table 1). Lithium metal has the largest expansion during plating of $\sim 7.9 \mu\text{m per mAh cm}^{-2}$. This expansion cannot be explained solely by the theoretical expansion of the metal during plating ($\sim 4.9 \mu\text{m per mAh cm}^{-2}$, calculated by using Faraday's law, assuming the deposition of a dense, homogeneous lithium layer).^[2] Further increases in the thickness are associated with the SEI and with the deposition of less dense, i.e., dendritic or mossy, lithium. The contraction during stripping is $\sim -5.4 \mu\text{m per mAh cm}^{-2}$, which also is larger than theoretically expected, thus implying stripping of mossy lithium. The irreversible dilation is $\sim 2.5 \mu\text{m per mAh cm}^{-2}$, as determined from the difference between the two half cycles, and is associated with the SEI growth and the formation of dead lithium. Although this normally would lead to a loss of a capacity in the cell, the lithium excess in the anode is sufficient to compensate this loss.

To give a more direct comparison of the expansion of lithium metal to that of other SoA and next-generation electrodes, further configurations were examined (Figure S1). The silicon vs. NCM111 cell has also a significant expansion during lithiation and delithiation (Figure S1 and Table 1). Assuming the negligible cell thickness change of NCM111, the expansion of silicon is $\sim 9 \mu\text{m}$ which corresponds to a thickness change of $\sim 50\%$ (related to film thickness of the silicon electrode). This is lower than expected based on the theoretically estimated expansion of 280% (on the particle level and assuming full lithiation to $\text{Li}_{15}\text{Si}_4$).^[26,27] Thus, the lower expansion can be related to the high porosity of the electrode ($\sim 75\%$) and the limited utilization of the electrode ($\sim 72\%$). The graphite configurations with LTO or NCM have similar expansion values of $3.2\text{--}3.4 \mu\text{m}$ ($\sim 5\%$ expansion, related to film thickness of the graphite electrode). The expansion of the used graphite is lower compared to the theoretical value of $\sim 10\%$ as the capacity is not fully utilized ($\sim 78\%$) and due to the porosity

Table 1. Measured areal capacity, dilation and the dilation per areal related capacity of the investigated cells during lithiation and delithiation of the negative electrode.

	Lithiation			Delithiation			Full cycle
	Areal capacity [mAh cm^{-2}]	Dilation [μm]	Areal capacity related dilation [$\mu\text{m per mAh cm}^{-2}$]	Areal capacity [mAh cm^{-2}]	Dilation [μm]	Areal capacity related dilation [$\mu\text{m per mAh cm}^{-2}$]	Irreversible dilation [μm]
NCM111 vs. LTO	1.46	0.10	0.07	1.44	-0.10	-0.07	0
LFP vs. LTO	1.85	-1.00	-0.54	1.83	1.05	0.57	0.05
Lithium vs. LTO	2.07	16.30	7.89	2.06	-11.20	-5.43	5.1
Graphite vs. NCM111	1.74	3.20	1.84	1.72	-3.03	-1.76	0.17
Graphite vs. LTO	1.75	3.44	1.96	1.74	-3.44	-1.98	0
Silicon vs. NCM111	1.83	8.90	4.87	1.74	-8.42	-4.85	0.48

of the electrode (~35%). From the results shown in Figures 1 and S1, lithium metal has both the highest reversible and irreversible expansion with 11.2 μm and 5.1 μm , respectively, during cycling at 0.05 MPa external pressure. The irreversible expansion for the other cell configurations is smaller (Table 1). The cells with NCM111, LFP and graphite vs. LTO show negligible irreversible expansion during this cycle. The graphite vs. NCM111 cell shows a small irreversible expansion of 0.17 μm , which can probably be related to some lithium plating on the anode. The silicon vs. NCM111 cell demonstrates a noticeable irreversible expansion of 0.48 μm during one full cycle. This can be explained by the reduced capacity during delithiation of the silicon anode and probably also due to degradation effects, e.g., particle cracking, during the lithiation of the silicon.

To study the impact of the electrolyte and the external applied pressure on the performance and (irreversible) expansion of the lithium metal cells, LTO and LFP were chosen to be the counter electrodes. These two electrodes undergo only a small dilation during cycling and have a good cyclability. Therefore, it may be assumed that LTO and LFP will have only a small impact on the overall expansion of the lithium metal cell. In comparison, NCM111 also has a small dilation, but it is known to be unstable (aluminum corrosion) in contact with the LiFSI-based electrolyte due to its higher potential compared to LFP.^[28,29]

Irreversible dilation of lithium metal cells

Figure 2 shows the pressure-dependent discharge capacity of the cells with lithium metal against LTO or LFP and three different electrolytes (i.e., 1 M LiPF₆ in ethylene carbonate (EC)/ethyl methyl carbonate (EMC) 3/7 wt% (LP57), LP57 with 5 wt% fluoroethylene carbonate (FEC) and the ether-based 1 M LiFSI in DME) during cycling. The cells with the carbonate-based electrolytes (LP57 and LP57 with 5 wt% FEC) show a different cycling behavior in terms of capacity retention compared to the cells with the ether-based electrolyte. In the initial six cycles (three formation cycles at 0.2 mA cm⁻²/0.1 C and three 1.0 mA cm⁻²/0.5 C cycles), the capacity remains constant at ~2.2 mA h cm⁻² and only a small capacity reduction due to the different current densities is visible. A significant capacity reduction, especially when the low external pressure is applied, is seen for the cells with the carbonate-based electrolytes at higher currents (2.0 mA cm⁻²/1.0 C). The cells with LP57 (w/o FEC) also show sudden capacity fading at higher pressure, but later in the cycling experiment. For the cells with LP57 w/ 5 wt% FEC, the capacity fading is clearly reduced at elevated pressures, particularly at the highest pressure of 1.0 MPa. When cycling lithium metal with the ether-based electrolyte, no significant capacity reduction is detectable during the cycling experiment regardless of the applied external pressure. This clearly demonstrates a positive impact of both elevated pressure and the replacement of a carbonate-based LP57 electrolyte on the performance of lithium metal half cells. The capacity reduction during cycling is decreased for the cells with

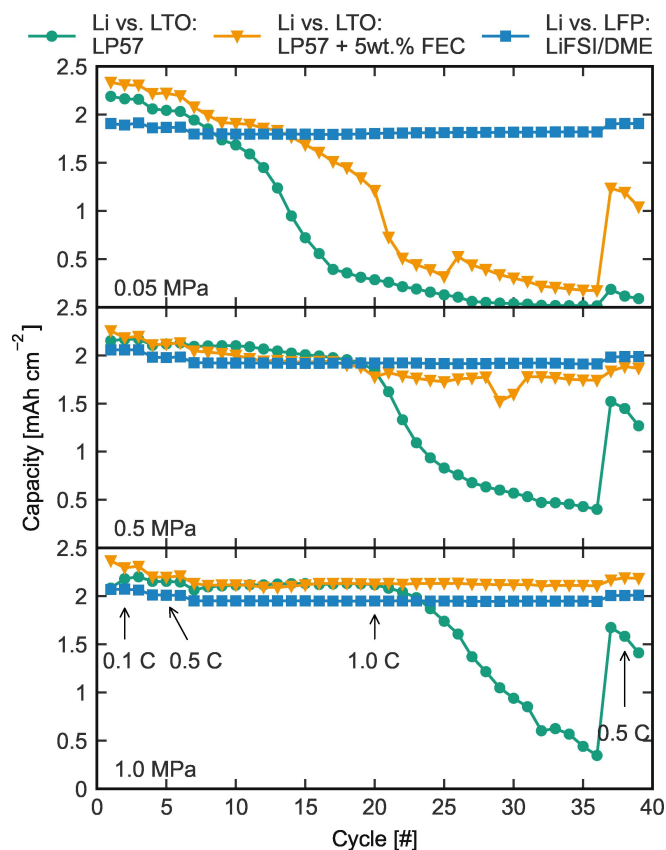


Figure 2. Pressure dependent performance of Li vs. LTO or LFP with three different electrolytes (LP57, LP57 with 5 wt% FEC and 1 M LiFSI in DME). The lines are a guide for the eye only. It should be noted that the LTO electrodes have a slightly higher actual capacity (~2.2 mA h cm⁻² to ~2.0 mA h cm⁻²) and hence the discharge capacities are higher compared to the capacities of the LFP electrodes.

LP57 w/ 5 wt% FEC and 1 M LiFSI in DME at elevated pressures, which shows decreased aging phenomena on the lithium metal. A more detailed discussion of the aging phenomena can be found in the following sections.

The dilation of the different cell configurations during cycling is shown in Figure 3. Figures S2–S4 show the dilation of the cells for one 1.0 mA cm⁻²/0.5 C cycle (Cycle 6). It should be noted that the dilation of the Li vs. LTO cells initially decreases below 0 μm as the LTO electrode gets lithiated at the beginning of the formation. Hence, the lithium ions get stripped from the lithium metal electrode and the total cell thickness decreases. For the Li vs. LFP cells, the LFP electrode is first delithiated in the formation and hence are the lithium ions plated on the lithium metal electrode. In the initial three cycles (0.2 mA cm⁻²/0.1 C), the reversible dilation is dominant and the irreversible dilation is comparably small. This is also true for the following three cycles (1.0 mA cm⁻²/0.5 C) for the cells with higher external pressure (0.5 MPa and 1.0 MPa). In contrast, the cells with the lowest pressure have a noticeable irreversible expansion already at this current density. Furthermore, a pressure dependency in the total expansion can be seen. The cells with the lowest external pressure have the highest expansion of ~14–17 μm , while the cells with the highest

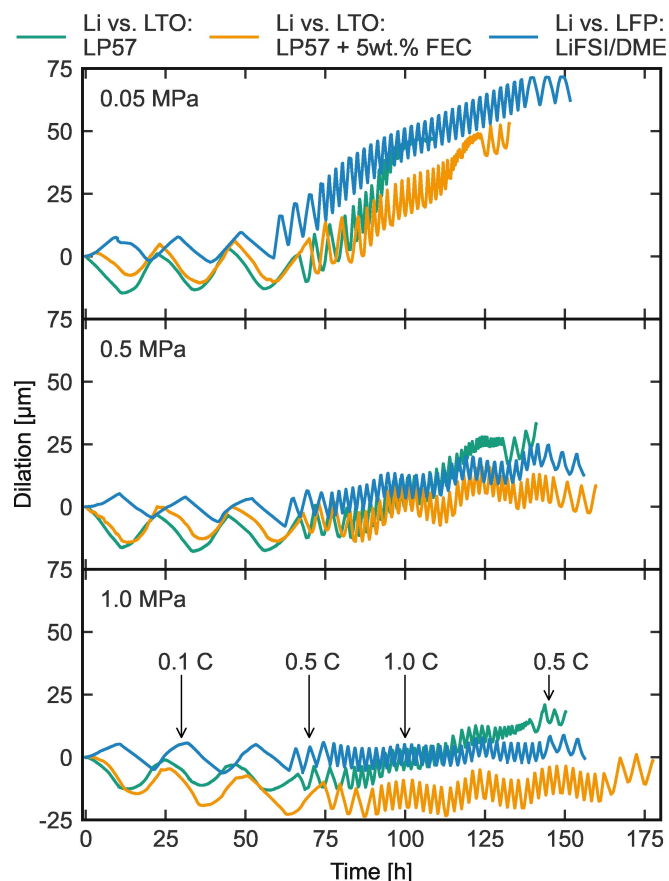


Figure 3. Pressure dependent dilation of Li vs. LTO or LFP with three different electrolytes (LP57, LP57 with 5 wt% FEC and 1 M LiFSI in DME). 1.0 C refers to 2.0 mA cm^{-2} .

pressure show the smallest expansion of $\sim 9\text{--}11 \mu\text{m}$ (Figures S2–S4). This can probably be explained by the reduced formation of mossy and dead lithium at higher pressures. Here, the high pressure probably leads to reduced electrical isolation of the mossy lithium during stripping and hence reduced formation of dead lithium. Furthermore, the high pressure may also reduce the ability of the lithium metal to expand, which may affect the plating morphology.

The cells with LP57 have the most significant irreversible dilation increase at the highest current density of 2.0 mA cm^{-2} at all applied pressures (e.g., $33.2 \mu\text{m}$ for the pure LP57 cells compared to $8.2 \mu\text{m}$ for the FEC cells at the end of the test at 0.5 MPa). In contrast, the cells with the FEC additive and ether-based electrolyte only show this behavior at the lowest applied pressure. Interestingly, even though the ether-based cells show a large irreversible expansion at the lowest pressure, the capacity fading is negligible (Figure 2). The reason for this result is not fully understood, but may be related to the morphology and nature of the SEI and needs further investigation. For the higher applied pressures, only a small (0.5 MPa) or negligible (1.0 MPa) irreversible expansion is visible for the cells with FEC additive and ether-based electrolyte. A pressure dependency is evident as the irreversible dilation decreases with increasing external applied pressure for all investigated cells. The cells

cycled at the lowest pressure show an irreversible expansion of $> 47 \mu\text{m}$ for all electrolytes and only little expansion at the highest pressure, i.e., $\sim 18 \mu\text{m}$ for the cells with LP57 and $\sim 0 \mu\text{m}$ for the other cells. The pressure dependency can be mostly related to the reduced formation of mossy and dead lithium at higher pressures due to the better electrical contact of the mossy lithium and the bulk lithium.

Impact of external pressure and electrolyte on the performance

To study the pressure and electrolyte dependent performance of the lithium metal cells for a longer time period, cycling experiments were conducted in laboratory pouch cells with an external bracing device. Figure 4 shows the capacity upon cycling for lithium vs. LTO or LFP. Both systems are cycled with two different electrolytes, the common electrolyte LP57 (both LTO and LFP configurations) and additionally LP57 with 5 wt% FEC and 1 M LiFSI in DME for the lithium vs. LTO system and the lithium vs. LFP system, respectively.

The cells with LP57 show a significant reduction performance in comparison to the cells with both other electrolytes. The lithium vs. LTO cells with LP57 show stable cycling for around 35 cycles, followed by a sudden capacity reduction, which is consistent with the results in the dilation cell (Figure 2). The slope of the capacity drop is pressure dependent, i.e., the cells with no external bracing show the highest slope whereas the cells with the highest pressure have the flattest slope. The threshold of 80% initial capacity is reached by cells without external pressure first, followed by the cells with 0.5 MPa and last by the cells with 1.0 MPa. The lithium vs. LTO cells with LP57 with 5 wt% FEC demonstrate an enhanced performance compared to those with LP57. The capacity retention is around 95.8% after 250 cycles for the cells with 1.0 MPa external bracing. The stable performance for hundreds of cycles is related to the more stable SEI on the lithium metal and the reduced formation of dead lithium.^[30–36] The cells show a capacity drop shortly before reaching 80% of the initial capacity, followed by a short phase of recovery before the capacity fades again. This capacity fading–recovery–fading phenomenon is present for all applied external pressures, but is shifted to later cycles in the cells with the highest pressure. It should be noted that the standard deviation is higher for the cells with 0.5 MPa as this behavior occurs for one cell at ~ 200 cycles and for the other cell at ~ 250 cycles.

For a better understanding of this phenomenon and to check if there is an electrolyte or separator dependency, cells with a lower amount of electrolyte and a different separator were built (Figure 5). The capacity fading–recovery–fading phenomenon is present for all cells built but with some variations in terms of the cycling stage and the intensity of fading. The cells with $100 \mu\text{L}$ electrolyte show the phenomenon at an earlier stage in the cycling compared to the cells with $300 \mu\text{L}$. For the cells with a $260 \mu\text{m}$ glass fiber separator (Whatman GF/C) and $200 \mu\text{L}$ electrolyte the initial capacity fading is mitigated but still visible. The varying cycling stage

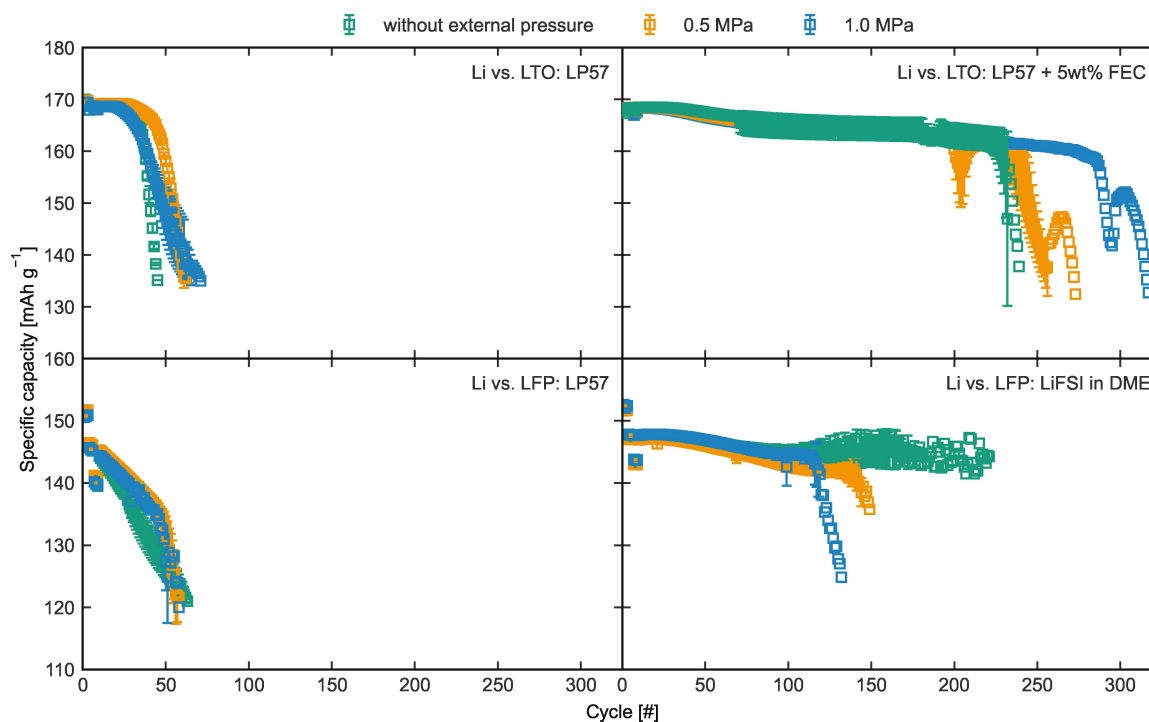


Figure 4. Specific capacity as a function of cycle for the cycling of lithium vs. LTO or LFP with different electrolytes (LP57, LP57 with 5 wt% FEC and 1 M LiFSI in DME) and various external applied pressures (without external pressure, 0.5 MPa and 1.0 MPa).

and intensity of the fading indicates that the specific amount of FEC ($\text{mol}_{\text{FEC}}/\text{g}_{\text{electrode}}$) is responsible for this phenomenon. Jung et al. showed enhanced performance of lithium vs. silicon cells containing an increased amount of FEC additive in the cells compared to cells with a lower amount of additive in the electrolyte.^[32] Saltira et al. showed a capacity fading and recovery of lithium vs. NCM cells with a FEC-based electrolyte.^[31] The initial capacity fading might then be related to the consumption of the FEC in the cell, which can explain the earlier appearance of the capacity fading phenomenon in the cells with the lower amount of electrolyte. The decomposition of the electrolyte when FEC is present is almost exclusively related to FEC, as it is easier to decompose compared to EC or EMC. FEC has a lowest unoccupied molecular orbital (LUMO) that is lower in energy than that of EC and EMC with values of -0.87 eV, -0.38 eV and -0.26 eV, respectively.^[33,37] As a result, the SEI has an increased LiF content, which makes the SEI thick and more stable when FEC is present.^[32,33,38] The capacity recovery, after the FEC has been consumed, might then be a result of SEI cracking, followed by the formation of a new, thinner SEI due to the reduction of EC/EMC. The newly-formed SEI might be initially thinner, but is more unstable for continuously cycling. As a result, the capacity recovers for some cycles before the dead lithium and the dendrite growth, likely facilitated by a less robust or stable SEI, lead to the capacity fading. Higher external pressure reduces the formation of mossy and dead lithium, and hence, also the side reactions and consumption of the electrolyte with the lithium metal. Hence, the capacity fading-recovery-fading phenomenon is shifted to a later phase during cycling.

To determine the impact of the LiFSI-based electrolyte and the effect of the counter electrode on the pressure-dependent performance of the lithium metal cells LFP was chosen as a second counter electrode. When the carbonate-based electrolyte LP57 is used, the lithium vs. LFP cells yield similar results as the LTO cells, i.e., the 80% capacity threshold is reached after around 60 cycles (Figure 4c). For around 50 cycles, the cells with higher pressure have an increased capacity retention compared to the cells without external applied pressure. Nevertheless, the cells with the high external pressure have a sudden capacity drop after ~ 50 cycles, whereas the cells without external pressure do not show this sudden capacity fading behavior.

The lithium vs. LFP cells with 1 M LiFSI in DME show stable cycling up to around 100 cycles, but there is no evidence of a dependence on pressure in this experiment (Figure 4d). The capacity retention after 100 cycles is $\sim 98\%$. This proves that a relatively stable SEI is present on the lithium metal with the ether-based electrolyte, which limits the formation of dead lithium.^[9,39] After around 100 cycles, the capacity of the individual cells starts to scatter, which is probably related to drying due to consumption of the electrolyte. The consumption of the electrolyte, which in this case leads to gassing (Figure S5), is a significant degradation mechanism, which makes it difficult to cycle the cells longer than ~ 100 cycles. Overall, the results in this section show that while the influence of the counter electrode on the performance of the lithium metal cells is small, whereas the choice of electrolyte and external pressure play a more dominant role.

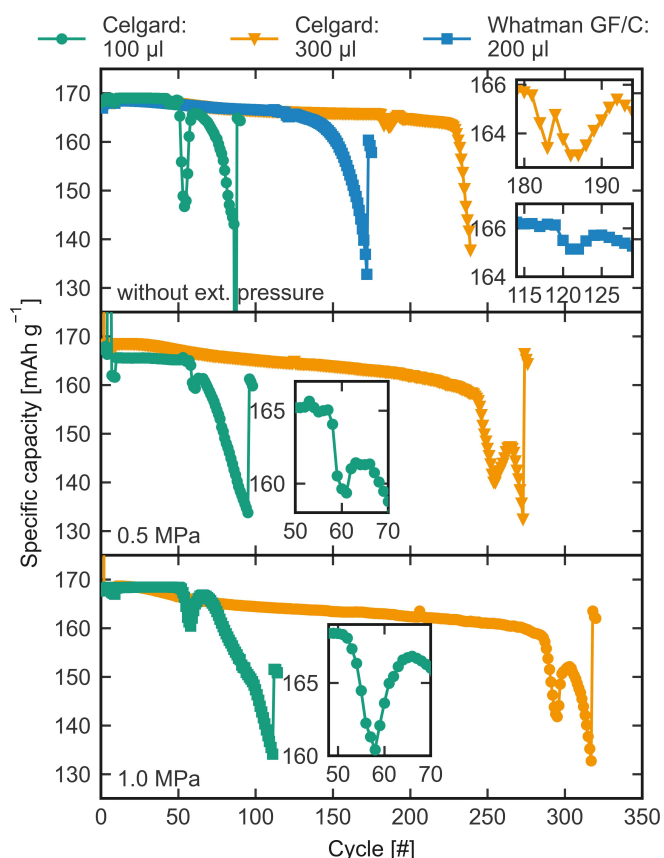


Figure 5. Capacity fading-recovery-fading phenomenon of representative lithium vs. LTO cells with different amounts of electrolyte, different separators and different applied external pressures. For better visibility, only one representative cell is shown for each parameter.

Figure 6 shows the pressure evolution of the cells with an external applied pressure over the time. Regardless of the applied pressure or electrolyte used, the pressure increases for all cells over cycling. Nevertheless, the cells with an initial applied pressure of 0.5 MPa show a more significant increase of the pressure compared to the cells with 1.0 MPa, e.g., by a factor of at least 2, which can be related to the more significant increase of the irreversible expansion of the lithium metal (Figure 3). This is further evidence for the reduced formation of mossy and dead lithium in cells with a high applied external pressure.

The pressure increase is also influenced by the type of electrolyte. The use of the LP57 (carbonate-based electrolyte without an additive) results in a tremendous increase of the pressure during cycling at high current densities ($>1.0 \text{ mAcm}^{-2}$). The cells with the FEC additive still have a significant increase of the pressure, but this increase is less pronounced than the cells without additive. After 1000 h of cycling the pressure on the electrodes increased from 0.5 MPa and 1.0 MPa up to only $\sim 0.8 \text{ MPa}$ and $\sim 1.1 \text{ MPa}$, respectively. Subsequently, a significant pressure change is visible after $\sim 1100 \text{ h}$ (0.5 MPa) and $\sim 1580 \text{ h}$ (1.0 MPa). At this point (Cycle 204 at 0.5 MPa and cycle 295 at 1.0 MPa), the capacity starts to recover from the initial capacity fading (Figures 4 and 5) as part

of the capacity fading-recovery-fading phenomenon. This behavior is further evidence that at this point the FEC has been consumed and that reduction of the EC/EMC has started. Combined with the results above, this shows the beneficial impact of the FEC on a stable SEI, which suppresses the formation of dead lithium. The cells with ether-based electrolyte undergo the highest pressure increase over the cycling. However, this result is probably a combination of several effects and gassing likely plays the most significant role (Figure S5).

Conclusion

The cycling of lithium metal half cells in an *operando* dilation cell and in laboratory-scale pouch cells reveal the beneficial effect of external pressure on the cycling performance. The thickness of lithium stripped and plated is much higher than theoretically expected at low applied external pressures. The difference comes from SEI formation and the deposition morphology that is not homogeneous which leads to formation of mossy and dead lithium. The irreversible expansion of lithium is significantly reduced with increasing external pressure on the cells. The smaller irreversible expansion is most likely related to the reduced formation of mossy and dead lithium at higher pressures due to enhanced electrical contact between the bulk and mossy lithium.

Another significant factor in the performance of the lithium metal half cells is the choice of the electrolyte. Standard carbonate-based electrolytes show a high pressure or irreversible dilation increase and poor performance. The addition of an additive like FEC or the use of ether-based electrolytes can significantly reduce the pressure or irreversible expansion increase over the cycling, which is mostly related to a stable SEI. Furthermore, the specific amount of the FEC additive in the carbonate-based electrolyte is an important aspect. The cells with a larger amount of FEC performed significantly better than those with a smaller amount of FEC. The continuous formation of SEI on fresh lithium during stripping and plating leads to the consumption of the FEC. When all the FEC has been consumed, the capacity of the cell fades due to the poorer stability of the newly-formed SEI resulting from the reduction of the other carbonates in the electrolyte.

Overall, this work shows the importance of pressure and electrolyte choice for lithium metal cells. This result is not only important for future battery systems, but also for SoA battery research. When testing electrodes in half-cells, the limitation of the lithium metal should also be considered, especially at high current rates and when a low external pressure is applied. The addition of a sufficient amount of FEC to standard carbonate electrolytes can also help to reduce the impact of lithium metal on the performance of electrodes in half-cells.

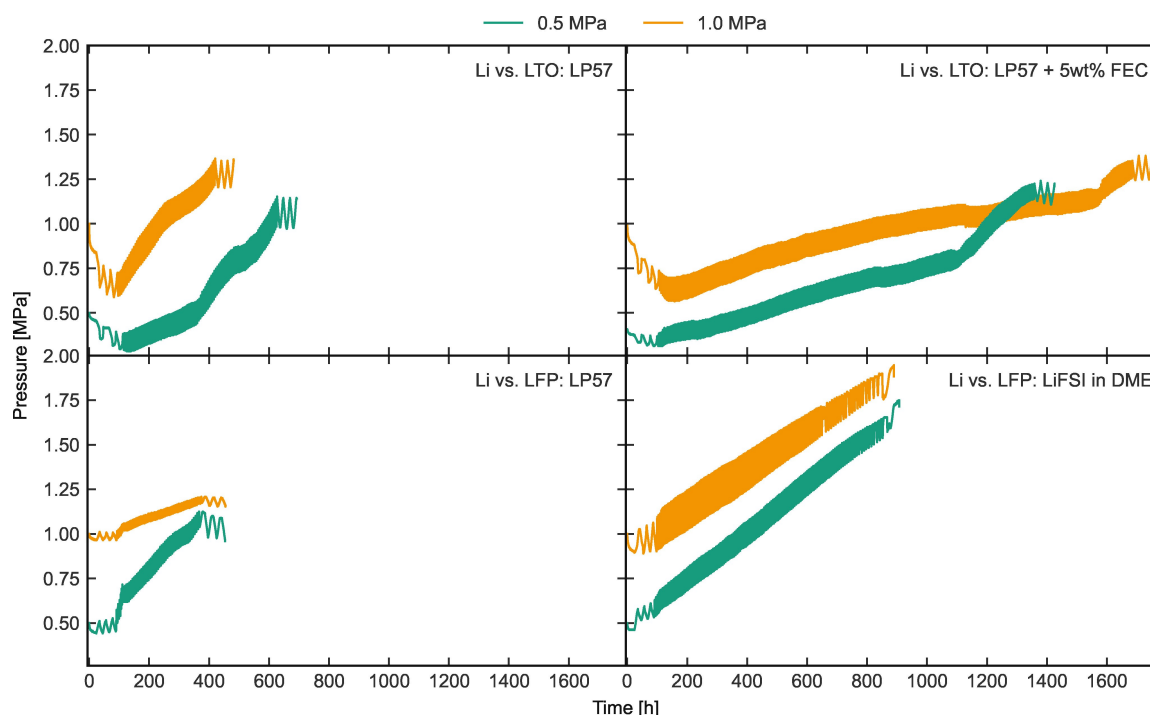


Figure 6. Pressure as a function of time for the cells with 0.5 MPa and 1.0 MPa initially applied external pressure. For better visibility, only one representative cell is shown for each parameter.

Experimental Section

Materials

Lithium metal, $\text{Li}_4\text{Ti}_5\text{O}_{12}$ (LTO), LiFePO_4 (LFP), graphite, $\text{LiNi}_{0.33}\text{Co}_{0.33}\text{Mn}_{0.33}\text{O}_2$ (NCM111) and silicon were used as electrodes (Table 2). The loading of the electrodes were between 2.0 and 2.2 mAh cm^{-2} for the commercial electrodes and $\sim 2.5 \text{ mAh cm}^{-2}$ for the silicon electrodes fabricated in house. It should be noted that the actual capacity utilized is around 72% for the silicon electrodes. Before using lithium as an anode material, the surface was cleaned by scraping off the passivation layer with a ceramic knife and then flattened with a roll to obtain a flat and smooth surface. Before the cycling experiments, the electrodes were punched into 18 mm discs (silicon: 16 mm) and then dried in a glovebox oven at 120 °C for 12 hours under vacuum. The lithium metal was punched into 18 mm discs for the dilation cell and to approx. 20 × 20 mm pieces for the pouch cells. CG2500 (Celgard LLC) with a thickness of 25 μm and porosity of 55% was used as separator in all experiments, unless otherwise noted. The separator was dried in a

glovebox oven at 50 °C for 12 hours under vacuum. Three different types of electrolytes were used in this work: (1) 1 M LiPF_6 in ethylene carbonate (EC)/ethyl methyl carbonate (EMC) 3/7 wt% (LP57, Gotion Inc.), (2) LP57 with 5 wt% fluoroethylene carbonate (FEC, BASF SE) and (3) the ether-based 1 M LiFSI (Arkema) in DME (Merck KGaA).

Dilation cell and bracing cell

The expansion behavior of the electrodes was measured in a dilatometry setup.^[41] In this setup, the expansion of an electrode stack was measured under various applied mechanical forces. For more detailed information about the dilation cell, the reader is referred to the following Ref. [41]. The electrode stack consists of two 18 mm electrodes and a 21.6 mm separator. The applied external mechanical pressures were 0.05 MPa, 0.5 MPa and 1.0 MPa. The amount of electrolyte was 200 μL .

To investigate the impact of the external applied pressure on the cell performance, laboratory pouch cells were built with lithium metal as the working electrolyte, LTO or LFP as counter electrodes and CG2500 (approx. 33 × 33 mm) as separator. Two 20 mm stainless steel spacers (placed between the electrode and the current collector tab) were used to homogenize the pressure distribution on the electrode stack. The amount of electrolyte was 100 μL for the cells with LP57 and 300 μL for the cells with LP57 with 5 wt% FEC and 1 M LiFSI in DME. The higher electrolyte amount for the LP57 with 5 wt% FEC and 1 M LiFSI in DME was used to prevent rapid drying out of the electrolyte in the cell. The pouch cells were placed in a self-built bracing device, where an aluminum plate presses against the cell and a load cell measures the pressure.^[40] The external applied pressures were 0.5 MPa and 1.0 MPa. Furthermore, pouch cells without external pressure were cycled. The internal pressure from the vacuum sealing of the pouch cells is in the range of 0.05–0.1 MPa and hence comparable to the

Table 2. Properties (i.e., areal loading, thickness of the active material, porosity and distributor) of the electrodes used in this study.

Electrode	Areal loading [mAh cm^{-2}]	Thickness [μm]	Porosity [%]	Distributor
Lithium	–	380	–	Merck KGaA
LTO	2.0	115	64	Customcells Holding GmbH
LFP	2.0	88	51	Customcells Holding GmbH
Graphite	2.2	71	35	Customcells Holding GmbH
NCM111	2.0	100	40	Customcells Holding GmbH
Silicon	~ 2.5	~ 18	~ 75	Self-fabricated ^[40]

performance with the cells in the dilation cell with an external pressure of 0.05 MPa.

Electrochemical measurements

The experiments with the dilation cell were conducted inside an argon-filled glovebox (O_2 and $H_2O < 1$ ppm, M. BRAUN Inertgas-Systeme GmbH) to avoid the infiltration of air into the cell. The electrochemical tests were performed with a ModuLab XM MTS System (Solartron Analytical), where the applied pressure and the dilation were recorded along with the full cell voltage. For the initial investigation of the electrode expansion and the selection of the counter electrode for subsequent testing, different electrode combinations were cycled (graphite vs. NCM111, NCM111 vs. LTO, LFP vs. LTO, Li vs. LTO, graphite vs. LTO and Si vs. NCM111). The applied pressure was 0.05 MPa, CG 2500 was used as separator and LP57 and LP57 + FEC (silicon vs. LTO) were used as the electrolyte. The current was 2.0 mA cm^{-2} . During the irreversible dilation measurements of lithium vs. LTO or LFP, all cells were cycled with three initial 0.1 C (0.2 mA cm^{-2}) formation cycles, followed by three 0.5 C (1.0 mA cm^{-2}) cycles, 30 1.0 C (2.0 mA cm^{-2}) cycles and again three 0.5 C (1.0 mA cm^{-2}) cycles. The C-rate was related to the nominal capacity of the counter electrodes, which was 5.09 mAh (i.e., $2.0 \text{ mAh cm}^{-2} \times 2.545 \text{ cm}^2$). The temperature was set to 25°C and controlled with a self-built temperature device during the measurement. The lithiation of the LTO and the delithiation of the LFP ('discharging' for LTO - and 'charging' for LFP system) was conducted in a constant current constant voltage (CCCV) mode, with a cut-off criterion during the CV step of $I < 0.04 \text{ C}$ for 0.1 C and 0.5 C and $I < 0.1 \text{ C}$ for 1.0 C, respectively, at the cutoff voltage. The Li vs. LTO cells were cycled between 1.3 V and 2.0 V and the Li vs. LFP cells were cycled between 2.5 V and 3.8 V. All cell combinations were built at least twice.

The electrochemical tests for the pouch cells were performed with a Maccor Series 4000 battery tester (Maccor Inc.) in a climate chamber at 25°C . The cells (i.e., Li vs. LTO/LFP) were cycled with three initial 0.1 C (0.2 mA cm^{-2}) formation cycles, followed by three 0.5 C (1.0 mA cm^{-2}) cycles, three 1.0 C (2.0 mA cm^{-2}) cycles and then cycled with 0.5 C (1.0 mA cm^{-2}) until 80% of the initial 0.1 C capacity is reached. The lithiation of the LTO and the delithiation of the LFP was also conducted with CCCV procedure, with a voltage cutoff of 1.3 V and 3.8 V, respectively, and a cutoff of 10% of the applied current (e.g., $I < 0.1 \text{ C}$ for 1.0 C). All cells with standard deviation shown were obtained from at least two separate cells.

Acknowledgements

The authors gratefully acknowledge the funding of this work by the Federal Ministry for Economic Affairs and Climate Action (BMWK) of Germany in the project ReViSEDBatt (grant number 03ETE004 A) and the Bavarian Ministry of Economic Affairs and Media, Energy and Technology for funding the Fraunhofer R&D Center for Electromobility Bavaria FZEB (Grant number: 43-6629/86). We also want to thank Prof. Dr. Gerhard Sxlt and the members of the Fraunhofer R&D Center Electromobility at Fraunhofer ISC for fruitful discussions, scientific support, proof-reading and especially the technical support of Ajana Gebel, Vilija Anfimovaite, Franziska Stahl. Open Access funding enabled and organized by Projekt DEAL.

Conflict of Interest

The authors declare no conflict of interest.

Data Availability Statement

The data that support the findings of this study are available from the corresponding author upon reasonable request.

Keywords: electrochemistry · dead lithium · dilation · lithium · lithium metal cell · pressure

- [1] M. Winter, B. Barnett, K. Xu, *Chem. Rev.* **2018**, *118*, 11433.
- [2] D. Lin, Y. Liu, Y. Cui, *Nat. Nanotechnol.* **2017**, *12*, 194.
- [3] C. Fang, X. Wang, Y. S. Meng, *Trends Chem.* **2019**, *1*, 152.
- [4] X.-B. Cheng, R. Zhang, C.-Z. Zhao, Q. Zhang, *Chem. Rev.* **2017**, *117*, 10403.
- [5] W. Xu, J. Wang, F. Ding, X. Chen, E. Nasybulin, Y. Zhang, J.-G. Zhang, *Energy Environ. Sci.* **2014**, *7*, 513.
- [6] G. A. Giffin, *Nat. Commun.* **2022**, *13*, 5250.
- [7] X. Gao, Y.-N. Zhou, D. Han, J. Zhou, D. Zhou, W. Tang, J. B. Goodenough, *Joule* **2020**, *4*, 1864.
- [8] K. N. Wood, M. Noked, N. P. Dasgupta, *ACS Energy Lett.* **2017**, *2*, 664.
- [9] Y. Xu, K. Dong, Y. Jie, P. Adelhelm, Y. Chen, L. Xu, P. Yu, J. Kim, Z. Kochovski, Z. Yu, W. Li, J. LeBeau, Y. Shao-Horn, R. Cao, S. Jiao, T. Cheng, I. Manke, Y. Lu, *Adv. Energy Mater.* **2022**, *12*, 2200398.
- [10] J. Steiger, G. Richter, M. Wenk, D. Kramer, R. Mönig, *Electrochem. Commun.* **2015**, *50*, 11.
- [11] P. Daubinger, M. Schelter, R. Petersohn, F. Nagler, S. Hartmann, M. Herrmann, G. A. Giffin, *Adv. Energy Mater.* **2021**, *12*, 2102448.
- [12] M. Wünsch, J. Kaufman, D. U. Sauer, *J. Energy Storage* **2019**, *21*, 149.
- [13] F. Ebert, G. Sxlt, M. Lienkamp **2017**, <http://ieeexplore.ieee.org/servlet/opac?punumber=7933062>.
- [14] J. Cannarella, C. B. Arnold, *J. Power Sources* **2014**, *245*, 745.
- [15] L. Qin, K. Wang, H. Xu, M. Zhou, G. Yu, C. Liu, Z. Sun, J. Chen, *Nano Energy* **2020**, *77*, 105098.
- [16] C. Niu, H. Lee, S. Chen, Q. Li, J. Du, W. Xu, J.-G. Zhang, M. S. Whittingham, J. Xiao, J. Liu, *Nat. Energy* **2019**, *4*, 551.
- [17] X. Zhang, Q. J. Wang, K. L. Harrison, K. Jungjohann, B. L. Boyce, S. A. Roberts, P. M. Attia, S. J. Harris, *J. Electrochem. Soc.* **2019**, *166*, A3639-A3652.
- [18] X. Yin, W. Tang, D. Im Jung, K. C. Phua, S. Adams, S. W. Lee, G. W. Zheng, *Nano Energy* **2018**, *50*, 659.
- [19] M. Ue, K. Uosaki, *Curr. Opinion Electrochem.* **2019**, *17*, 106.
- [20] Y. Li, Z. Yang, Z. Wu, J. Li, J. Zou, C. Jiang, J. Yang, L. Wang, X. Niu, *Proc. Symposium on Materials for Advanced Batteries and Fuel Cells* **2018**, *324*, 144.
- [21] J. Qian, W. A. Henderson, W. Xu, P. Bhattacharya, M. Engelhard, O. Borodin, J.-G. Zhang, *Nat. Commun.* **2015**, *6*, 6362.
- [22] H. Yan, D. Zhang, Qilu, X. Duo, X. Sheng, *Ceram. Intern.* **2021**, *47*, 5870.
- [23] L. de Biasi, A. O. Kondrakov, H. Geßwein, T. Brezesinski, P. Hartmann, J. Janek, *J. Phys. Chem. C* **2017**, *121*, 26163.
- [24] D. Sauerteig, S. Ivanov, H. Reinshagen, A. Bund, *J. Power Sources* **2017**, *342*, 939.
- [25] M. Nagayama, K. Ariyoshi, Y. Yamamoto, T. Ohzuku, *J. Electrochem. Soc.* **2014**, *161*, A1388-A1393.
- [26] M. N. Obrovac, V. L. Chevrier, *Chem. Rev.* **2014**, *114*, 11444.
- [27] K. Feng, M. Li, W. Liu, A. G. Kashkooli, X. Xiao, M. Cai, Z. Chen, *Small* **2018**, *14*, 1702737.
- [28] T. R. Jow, K. Xu, O. Borodin, M. Ue, *Electrolytes for Lithium and Lithium-Ion Batteries*, Springer New York, New York, NY **2014**.
- [29] K. Xu, *Chemical reviews* **2014**, *114*, 11503.
- [30] P. Zhai, L. Liu, X. Gu, T. Wang, Y. Gong, *Adv. Energy Mater.* **2020**, *10*, 2001257.
- [31] G. Salitra, E. Markevich, M. Afri, Y. Talyosef, P. Hartmann, J. Kulisch, Y.-K. Sun, D. Aurbach, *ACS Appl. Mater. Interfaces* **2018**, *10*, 19773.

- [32] R. Jung, M. Metzger, D. Haering, S. Solchenbach, C. Marino, N. Tsiouvaras, C. Stinner, H. A. Gasteiger, *J. Electrochem. Soc.* **2016**, *163*, A1705-A1716.
- [33] X.-Q. Zhang, X.-B. Cheng, X. Chen, C. Yan, Q. Zhang, *Adv. Funct. Mater.* **2017**, *27*, 1605989.
- [34] R. Petibon, V. L. Chevrier, C. P. Aiken, D. S. Hall, S. R. Hyatt, R. Shunmugasundaram, J. R. Dahn, *J. Electrochem. Soc.* **2016**, *163*, A1146-A1156.
- [35] H. Shin, J. Park, A. M. Sastry, W. Lu, *J. Electrochem. Soc.* **2015**, *162*, A1683-A1692.
- [36] K. Schroder, J. Alvarado, T. A. Yersak, J. Li, N. Dudney, L. J. Webb, Y. S. Meng, K. J. Stevenson, *Chem. Mater.* **2015**, *27*, 5531.
- [37] X. Shen, P. Li, X. Liu, S. Chen, X. Ai, H. Yang, Y. Cao, *Chem. Sci.* **2021**, *12*, 9037.
- [38] Z.-C. Wang, J. Xu, W.-H. Yao, Y.-W. Yao, Y. Yang, *ECS Trans.* **2012**, *41*, 29.
- [39] H. Wu, H. Jia, C. Wang, J.-G. Zhang, W. Xu, *Adv. Energy Mater.* **2021**, *11*, 2003092.
- [40] M. Göttlinger, P. Daubinger, W. Stracke, S. Hartmann, G. A. Giffin, *Electrochim. Acta* **2022**, *419*, 140354.
- [41] P. Daubinger, F. Ebert, S. Hartmann, G. A. Giffin, *J. Power Sources* **2021**, *488*, 229457.

Manuscript received: October 14, 2022
Revised manuscript received: November 18, 2022
Version of record online: December 16, 2022

Batteries & Supercaps

Supporting Information

Consequences of Different Pressures and Electrolytes on the Irreversible Expansion of Lithium Metal Half Cells

Philip Daubinger, Mara Göttliger, Sarah Hartmann, and Guinevere A. Giffin.*

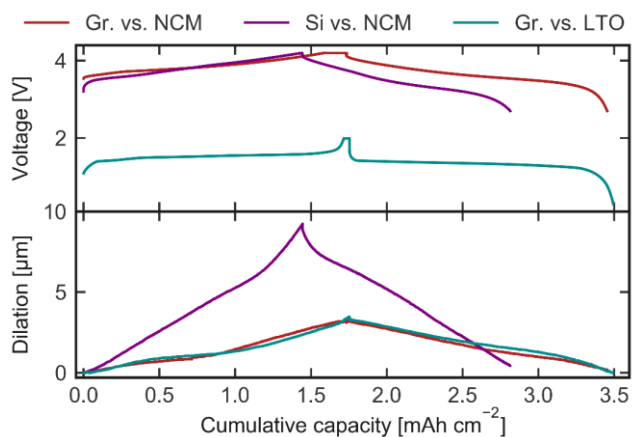


Figure S 1: Dilation behavior of graphite vs. NCM111, silicon vs. NCM111 and graphite vs. LTO during cycling. Voltage and dilation as a function of cumulative capacity. The cells were cycled with Celgard 2500 as separator, LP57 as electrolyte (silicon vs. NCM111: LP57 with 5wt% FEC) and 0.05 MPa external applied pressure. The current was 2.0 mA cm^{-2} ($\sim 1.0 \text{ C}$).

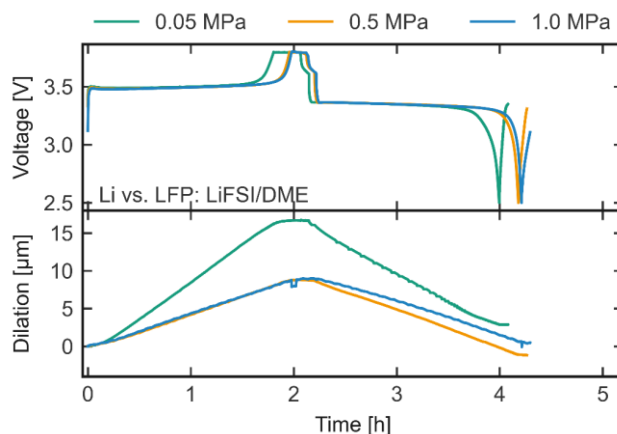


Figure S 4: Voltage and dilation as a function of time during the sixth cycle (1.0 mA cm^{-2}) for Li vs. LFP with 1M LiFSI in DME as electrolyte and three different applied external pressures (0.05, 0.5 and 1.0 MPa).

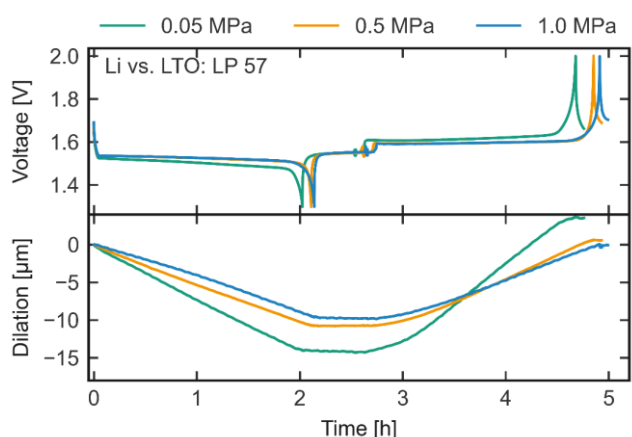


Figure S 2: Voltage and dilation as a function of time during the sixth cycle (1.0 mA cm^{-2}) for Li vs. LTO with LP57 as electrolyte and three different applied external pressures (0.05, 0.5 and 1.0 MPa).

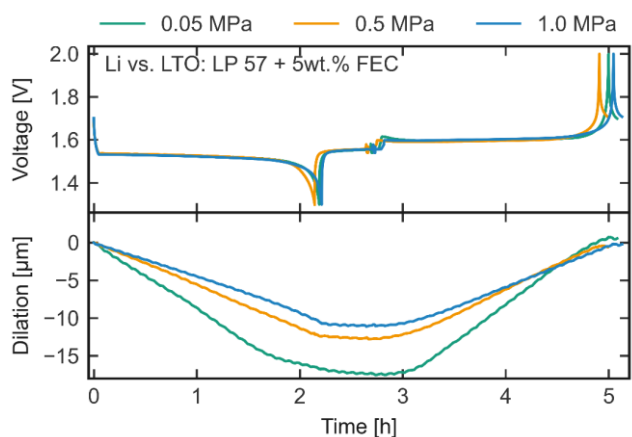


Figure S 3: Voltage and dilation as a function of time during the sixth cycle (1.0 mA cm^{-2}) for Li vs. LTO with LP57 with 5wt% FEC as electrolyte and three different applied external pressures (0.05, 0.5 and 1.0 MPa).

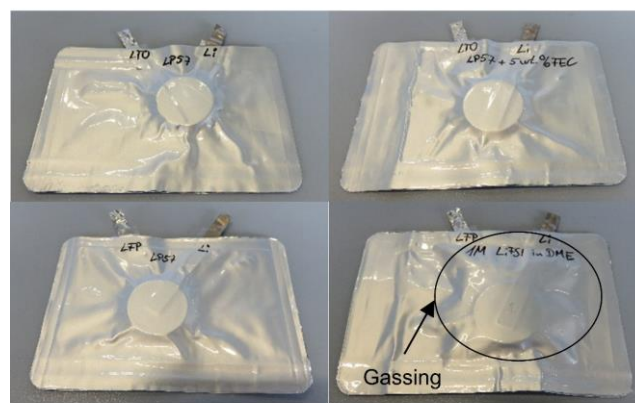


Figure S 5: Representative pouch cells after cycling. Top row: Li vs. LTO with LP57 and LP57 with FEC as electrolyte. Bottom row: Li vs. LFP with LP57 and 1M LiFSI in DME as electrolyte. The LiFSI in DME cell shows gassing.

Personal Contribution to Articles



Erklärung zur Autorenschaft

Impact of electrochemical and mechanical interactions on lithium-ion battery performance investigated by operando dilatometry, Daubinger, P., Ebert, F., Hartmann, S., & Giffin, G. A., Journal of Power Sources, 2021, 488, 229457.

Detaillierte Darstellung der Anteile an der Veröffentlichung (in %)

Angabe Autoren/innen (ggf. Haupt- / Ko- / korrespondierende/r Autor/in) mit Vorname Nachname (Initialen)

Philip Daubinger (PD), Fabian Ebert (FE), Sarah Hartmann (SH), Guinevere A. Giffin (GG)						
Autor	PD	FE	SH	GG	∑ in Prozent	
Dilatationszelldesign	1%	8%	0%	0%	9%	
Validierung der Dilatationszelle	12%	2%	1%	7%	22%	
Dilations- und Impedanzversuche	20%	3%	1%	15%	39%	
Verfassen der Veröffentlichung	15%	0%	0%	0%	15%	
Korrektur der Veröffentlichung	0%	1%	1%	8%	10%	
Koordination der Veröffentlichung	1%	0%	0%	4%	5%	
Summe	49%	14%	3%	34%	100%	

Erklärung zur Autorenschaft

Impact of Bracing on Large Format Prismatic Lithium-Ion Battery Cells during Aging, Daubinger, P., Schelter, M., Petersohn, R., Nagler, F., Hartmann, S., Herrmann, M., & Giffin, G. A., Advanced Energy Materials, 2021, 2102448.

Detaillierte Darstellung der Anteile an der Veröffentlichung (in %)

Angabe Autoren/innen (ggf. Haupt- / Ko- / korrespondierende/r Autor/in) mit Vorname Nachname (Initialen)

Philip Daubinger (PD), Matthias Schelter (MS), Ronny Petersohn (RP), Felix Nagler (FN), Sarah Hartmann (SH), Matthias Herrmann (MH), Guinevere A. Giffin (GG)								
Autor	PD	MS	RP	FN	SH	MH	GG	Σ in Prozent
Elektrische und Physikalische Messungen an prismaticen Vollzellen	0%	5%	4%	0%	0%	1%	0%	10%
Zellöffnung von prismaticen Automotive Batterien	8%	0%	0%	0%	0%	0%	5%	13%
Physikalisch-Chemische und Elektrochemische Untersuchungen von Bestandteilen aus geöffneten Zellen	23%	1%	0%	2%	2%	1%	18%	47%
Verfassen der Veröffentlichung	15%	0%	0%	0%	0%	0%	0%	15%
Korrektur der Veröffentlichung	0%	1%	1%	0%	1%	1%	6%	10%
Koordination der Veröffentlichung	2%	0%	0%	0%	0%	0%	3%	5%
Summe	48%	7%	5%	2%	3%	3%	32%	100%

Erklärung zur Autorenschaft

Interplay between Elastic and Electrochemical Properties during Active Material Transitions and Aging of a Lithium-Ion Battery, Feiler, S., Daubinger, P., Gold, L., Hartmann, S., & Giffin, G. A., Batteries & Supercaps, 2023, Seite

Detaillierte Darstellung der Anteile an der Veröffentlichung (in %)
Angabe Autoren/innen (ggf. Haupt- / Ko- / korrespondierende/r Autor/in) mit Vorname Nachname (Initialen)

Simon Feiler (SF), Philip Daubinger (PD), Lukas Gold (LG), Sarah Hartmann (SH), Guinevere A. Giffin (GG)						
Autor	SF	PD	LG	SH	GG	∑ in Prozent
Ladezustandsabhängige Ultraschalluntersuchungen	6%	6%	1%	0%	2%	15%
Alterung von Pouchzellen mit regelmäßigen Check-up Zyklen	11%	11%	0%	1%	1%	24%
Alterungsabhängige Auswertung der mechanischen Parameter	14%	14%	1%	0%	2%	31%
Verfassen der Veröffentlichung	7%	7%	1%	0%	0%	15%
Korrektur der Veröffentlichung	0%	0%	0%	1%	9%	10%
Koordination der Veröffentlichung	1%	1%	0%	0%	3%	5%
Summe	39%	39%	3%	2%	17%	100%

Erklärung zur Autorenschaft

Consequences of Different Pressures and Electrolytes on the Irreversible Expansion of Lithium Metal Half Cells, Daubinger, P., Goettlinger, M., Hartmann, S., & Giffin, G. A., Batteries & Supercaps, 2023, vol. 6, no. 2.

Detaillierte Darstellung der Anteile an der Veröffentlichung (in %)
Angabe Autoren/innen (ggf. Haupt- / Ko- / korrespondierende/r Autor/in) mit Vorname Nachname (Initialen)

Philip Daubinger (PD), Mara Göttlinger (MG), Sarah Hartmann (SH), Guinevere A. Giffin (GG)						
Autor	PD	MG	SH	GG	∑ in Prozent	
Ausdehnungsversuche unterschiedlicher Elektrodenmaterialien	8%	1%	1%	6%	16%	
Druck- und elektrolytabhängige Performance Untersuchungen von Lithium-Metall Zellen in Dilatationszelle	21%	2%	1%	9%	33%	
Druck- und elektrolytabhängige Performance Untersuchungen von Lithium-Metall Zellen in Verspannvorrichtung	4%	6%	1%	10%	21%	
Verfassen der Veröffentlichung	14%	1%	0%	0%	15%	
Korrektur der Veröffentlichung	0%	1%	2%	7%	10%	
Koordination der Veröffentlichung	3%	0%	0%	2%	5%	
Summe	50%	11%	5%	34%	100%	

